DESIGN AND EVALUATION OF ULTRAFAST ELECTRON-OPTICAL STREAK AND FRAMING CAMERAS

Yueping Liu

A Thesis Submitted for the Degree of PhD
at the
University of St Andrews

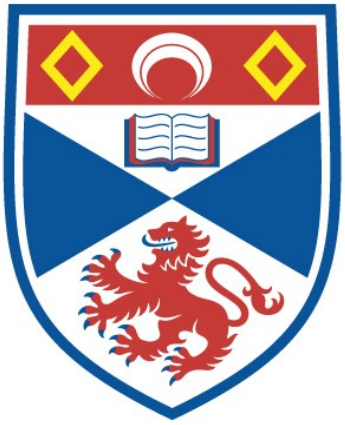

1993

Design And Evaluation Of Ultrafast Electron-Optical Streak And Framing Cameras

Thesis submitted for the degree of Doctor of Philosophy to the

University of St. Andrews

by

Yueping Liu, B.Sc, M.Sc

The J. F. Allen Physics Research Laboratories

Department of Physics and Astronomy

University of St. Andrews

North Haugh

St. Andrews, Fife

KY16 9SS, Scotland

October 1992

Declaration

I, Yueping Liu, hereby certify that this thesis has been composed by myself, that it is a record of my own work, and that it has not been accepted in partial or complete fulfilment of any other degree or professional qualification.

Signed Date 29. Sept. 1992

I was admitted to the Faculty of Science of the University of St. Andrews under Ordinance General No 12 on 1st October, 1988 and as a candidate for the degree of Ph.D. on 1st October, 1988

Signed Date 29. Sept. 1992

Certificate

I hereby certify that the candidate has fulfilled the conditions of the Resolution and Regulations appropriate to the Degree of Ph.D.

Signature of Supervisor Date 29 Sept 92.

Copyright

In submitting this thesis to the University of St.Andrews I understand that I am giving permission for it to be made available for use in accordance with the regulations of the University Library for the time being in force, subject to any copyright vested in the work not being affected thereby. I also understand that the title and abstract will be published, and that a copy of the work may be made and supplied to any bona fide library or research worker.

Dedicated to

my parents

ABSTRACT

The assessment of the performance of ultrafast electron-optical cameras operating in single-shot, synchroscan streak modes and framing mode has been accomplished and it has provided a better understanding of the limiting factors in the performance of these systems. The characterisation of a Photochron IV streak camera in synchroscan operation has been carried out and this has indicated that apart from the limiting time resolution of the streak tube itself, the amplitude and phase noise in laser sources and electronic circuitry also represent significant limitations to the overall system performance. The simulation of space-charge effects in the single-shot operation of streak cameras has demonstrated that space-charge effects are the key factor that limits the dynamic range. The use of travelling-wave deflection systems has been shown to offer a high deflection sensitivity over a broad frequency range.

To achieve femtosecond time resolutions from both synchroscan and single-shot streak cameras, the design of a Photochron V streak tube having optimised electron-optical focusing and deflection systems has been discussed. Analyses have indicated that a limiting time resolution of 250 fs is to be expected. Preliminary tests on an experimental version of a Photochron V tube operating in a synchroscan mode have shown a recorded pulse duration of 3.8 ps. Quantitative theoretical studies of output temporal responses of this tube for different input temporal profiles have indicated that it can reproduce temporal structures of input signals with high fidelity for both synchroscan and single-shot operations in a timescale of around 1ps.

The analysis of the Picoframe type of framing cameras has led to the refinements of the dynamic performance. For the future development, proposals have been made for the designs of a new streak tube having high dynamic range and a new framing tube having frame times less than 10 ps with potential applications in medical diagnosis.

CONTENTS

Chapter 3

Chapter 4

Chapter 5

Chapter 6

Chapter 7

Chapter 8

Chapter 9

Chapter 1

INTRODUCTION

Recent advances in laser technology have enabled ultrashort laser pulses to be generated throughout the ultraviolet, visible and infrared regions of the spectrum. The developments in laser designs, nonlinear optical materials and optical fibres have resulted in approaches for producing ultrashort light pulses which have a wide range of pulse durations, tunability, average and peak powers at various repetition rates. The advent of these methodologies has offered useful tools to study dynamic processes in real time in picosecond and femtosecond regimes for a large number of scientific applications. Consequently, it is vital to provide pulse monitoring systems that exhibit time resolutions adequate for characterising such laser sources and to allow time-resolved analysis of the excitation processes that these ultrashort light sources may induce.

Techniques for the measurement of ultrashort pulses can be classified into two categories. One relates to the so-called nonlinear optical methods which utilise the nonlinear behaviour exhibited by optical media while the other involves the use of electron-optical devices. The former is indirect and can provide time resolutions in the sub-10 fs region whereas the latter is a direct, linear approach with time resolutions currently around 1 ps. Considerable effort in developing both diagnostics have been made in the past two decades and a brief review of these techniques will be given in this chapter

1.1 Generation of ultrashort laser pulses

The majority of systems used to generate ultrashort laser pulses rely on the technique of modelocking. Since the first demonstration of modelocking of lasers in the mid-1960's[1], there have been some remarkable advances in the generation of ultrashort light pulses[2]. Using passive modelocking regime, the direct generation of laser pulses as short as 19 fs has been achieved from a continuously pumped passive modelocked ring dye laser in visible spectral

region[3] and pulses with sub-200 fs time durations have been produced from colour-centre lasers in the near-infrared range[4]. Additional extracavity amplification and temporal compression has resulted in light pulses having durations as short as 6 fs at 630 nm[5] and 9 fs at 800-840 nm[6].

Most notably in recent years, new methods for ultrashort pulse generation with solid-state lasers have been discovered and have provided the possibility of producing the shortest light pulses over a wide spectral accessibility range[7,8,9]. In particular, the modelocked Ti:sapphire laser has received considerable attention due to its broad tunable spectral range from 680 nm to 1100 nm, a much broader range than any of its dye or colour-centre competitors, and due to its capability of producing pulses with durations as short as those from CPM dye lasers (eg. sub-30 fs)[10,11,12]. In addition to its greater tunability, the average power capability can be several orders of magnitude larger than that of femtosecond dye lasers. While a CPM dye laser can produce average powers of tens of milliwatts, a self-modelocked Ti:sapphire laser can produce femtosecond pulses at average powers in excess of 1W[13]. The energy-storage characteristics of solid-state materials make it possible to produce compact, high peak power lasers[14] and using the chirped-pulse amplification technique terawatt peak powers have been demonstrated[15,16,17]. In addition to Ti:sapphire, other solid-state materials such as Cr:Mg_2SiO_4, the diode-pumpable Nd:YLF, Cr:$LiCaAlF_6$, Cr:$LiSrAlF_6$ and Cr:$LiSrCaAlF_6$ gain media[18,19,20,21,22] have also shown great potentiality and they offer very interesting possibilities as high power femtosecond sources for time-domain spectroscopy in the near-infrared spectral region[16,23].

The availability of such a variety of ultrashort pulse sources has become increasingly important in many branches of pure and applied scientific research including fundamental studies in physics, chemistry, biology and laser-induced thermonuclear fusion, high-speed electronics, communications, information systems as well as the non-invasive probing of miniature integrated electronic circuits[24,25]. Also, with high intensity femtosecond lasers it is possible to create plasmas with near solid densities which can provide valuable information on the dynamics of dense hot solids and can be used as sub-picosecond x-ray pulse sources. The

availability of such x-ray bursts can have a significant impact in the field of plasma and solid-state physics. Experiments have been performed with time-resolved optical pump and probe techniques and with x-ray diagnostics to obtain a better understanding of femtosecond laser-matter interaction.

1.2 Nonlinear optical measurement techniques for ultrashort light pulses

The rapid growth in ultrashort pulse generation and related applications has stimulated the development of ultrafast optical diagnostic techniques in the past decade and as a result a variety of pulse characterisation methods have emerged[26]. These techniques are based on the correlation of multiple replicas of the input pulse via first-, second- or third-order nonlinear optical interactions in a material and the theoretical aspects of their operating principles have been treated extensively in the literature[7,26].

The most popular schemes involve second-harmonic generation (SHG) in a nonlinear crystal[27]. As an example, the basic elements of a second-order autocorrelator are displayed in Fig.1.2.1.

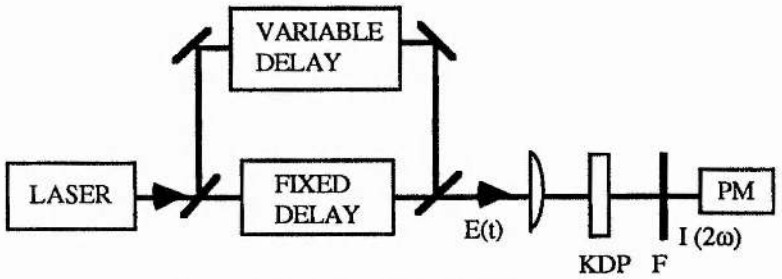

$$E(t) = \{\xi(t-\tau)e^{j\phi}\}e^{j\omega t} + \xi(t)\, e^{j\omega t}$$

$$I(2\omega) = \int |E^2|^2\, dt$$

Fig.1.2.1 A second-order autocorrelator setup

The measured pulse train is split into two beams and after passing through a fixed and an adjustable optical delay respectively, the two beams are combined in the nonlinear crystal (typically KDP) where the second harmonic intensity is generated. Adaptation of these schemes to split and recombine the beams, methods to scan the optical delay and the choice of detectors

can lead to different measurement approaches. These include intensity autocorrelation, interferometric autocorrelation, first-order and second-order cross-correlations, spectral interferometry and so on.

The intensity autocorrelation is the most-commonly used method and has become a standard tool for pulse duration measurements providing time resolutions as short as 6 fs[5]. Unfortunately, intensity autocorrelation does not provide information on pulse shape nor on the phase modulation. This disadvantage is implemented by interferometric autocorrelation achieved by utilising broad band frequency response detector which is sensitive to pulseshape and frequency chirps[28]. By using iterative fit technique, which utilises interferometric autocorrelation envelope together with pulse intensity autocorrelation and spectrum data, it is possible to characterise pulseshape and chirp information. But such technique requires previous knowledge or assumption of the pulseshape and has difficulties in constructing complex pulseshapes and modulations[29].

In order to measure pulseshape and frequency chirp detail, Diels et al demonstrated an asymmetric correlator which involves intensity cross-correlation of the measured pulse with its broadened form by adding a dispersive delay line into one of the interferometer arms[30,31]. The amplitude and phase information on the dispersed pulse can be extracted from the interferometric cross-correlation and the original pulse to be measured can then be recovered by applying the reverse transform to the dispersed pulse. This requires a complete knowledge of the dispersive process and involves post-data processing.

Methods based on spectral interferometric have also been reported in order to measure optical phase of chirped pulses after propagation through optical fibres[32,33]. To enhance sensitivity and efficiency for the measurement of pulse phase information, researchers employed the first order cross-correlation in the Fourier space[34,35] which can be used for complete characterisation of single pulses. The disadvantage that these methods have in common is that their usable spectral range is limited to wavelengths above 450 nm. To overcome this drawback, the combination of Treacy compressors and a streak camera has been employed which provides single-shot pulse measurements in the spectral range from the near-

infrared to the ultraviolet[36]. In this technique, by temporally stretching the input pulse in a controlled manner the use of a streak camera with picosecond time resolution became possible. It is especially convenient for the analysis of Gaussian pulses and the result is free from fluctuation influence. Again difficulty arises in the treatment of pulses with arbitrary shape which requires numerical methods in the determination of pulse chirp. Another way to measure ultrafast UV light pulses is to use the two-photon-excited excitonic fluorescence of BaF_2 as a phase-sensitive detector of an autocorrelator[37].

In principle, successive optical correlations of increasing order (> 2) provide a complete characterisation of ultrashort pulses but it is generally considered that the requirements for higher-order correlations for both a high intensity and a broad bandwidth are inconvenient. Nevertheless, high-order nonlinear optical techniques such as degenerate four-wave mixing[38] and third-order correlation[39] have demonstrated their potential. The former uses the correlation of three replicas of the input pulse while the latter uses two consecutive second-order nonlinear interactions of replicas of the input pulse in a dielectric crystal. They are especially useful for UV probes which can not be diagnosed by the previously mentioned schemes.

Another useful method for measuring the temporal history of various ultrafast processes in semiconductor materials is the optical sampling technique where the measured events are monitored with the use of temporally-correlated trains of light pulses[40]. The basic measurement principle is based on pump-and-probe configuration and autocorrelation technique where two pulse trains with consecutive pulses of slightly different temporal spacing are used as the pump and probe beams respectively.

These optical diagnostic methods have high time resolution (<100fs) and are cheap to perform. In particular, the intensity autocorrelation technique is very simple and convenient to use. However, when pulseshape information is required, they tend to involve nonlinear process and require post-data processing.

1.3 Linear measurements of ultrashort light pulses using electron-optical streak cameras

The popularity of ultrafast streak cameras as a diagnostic tool originates from their ability to measure directly and unambiguously the intensity of a light pulse as a function of time. The femtosecond resolving ability of streak cameras was recognised in the 60's[41] but the time resolution was limited to 50 ps until the early 70's when a fine-mesh electrode was introduced close to the photocathode[42]. The use of such a mesh electrode allowed a very high electric field to be applied to the photocathode and brought time resolution down to 1ps[43,44,45]. Since then, electron-optical streak cameras have advanced into a well-established technology producing a variety of devices for many different purposes and applications.

For the temporal measurements of single-shot pulses, single-shot streak cameras have been developed to provide subpicosecond time resolution (the best results recorded so far have been 300 fs in an experimental camera[46] and 600 fs in a commercial device[47]) and high dynamic range with real-time image recording systems[48]. For diagnosing very weak repetitive ultrashort pulse signals, streak cameras have been made capable of operating in a repetitive or "synchroscan" mode which offers the best performance when low noise laser and electronic systems are involved[49,50]. The characterisation of two-dimensional ultrafast events are enabled by the development of refined framing cameras which provide picosecond frame times and high spatial resolutions[51,52]. The spectral response has been extended to cover IR/ visible/ UV/ X-ray[53,54,55,56,57]. Image recordings and data acquisitions have also been simplified by the availability of self-intensified electronic imaging devices[58,59]. The number of applications of streak cameras have been continuously growing in research fields involving ultrafast optical phenomena that include laser physics, laser plasma physics, solid state physics, chemical physics, chemistry, biochemistry, biology, biomedical diagnosis[24,60,61,62,63].

As this trend in growth continues, a need emerges for a better understanding of the design principles and operation of these electron-optical ultrafast cameras in order to further improve their performance and to meet the increasing demands of their applications. Although numerous

publications have been presented in which the design and performance characterisation of such devices have been discussed, it is necessary to provide a more systematic and thorough study such that the potential of further improvements can be assessed.

Electron-optical devices themselves form a complex subject area which covers several aspects that include optics, electron lenses, photocathodes, phosphor screens, intensification, fibre-optic and microchannel plates, high-frequency techniques, electronics and electronic imaging devices[64]. Each of these can be a major research subject in its own right and as such they can not be covered in detail within this thesis. The main objective here is to explain the performance of ultrafast electron-optical cameras, the physical mechanisms giving rise to such performance, the limitations arising from the basic physics and the components used, and design considerations. Emphasis will be placed upon the key element which is the streak/framing image tube of camera systems in different modes of operations.

Chapter 2 begins with an introduction to the theoretical basics on which the performance of streak/framing cameras can be assessed with due regard to the influence of each component used. In doing so, factors giving rise to the temporal dispersions in input optics, photocathode, electron-optical focusing lens and deflection systems are analysed. The contributions of phosphor screen, optical coupling methods, image intensifiers and readout devices to the camera performance are also considered. In order to achieve quantitative characterisation of the performance of a streak/framing tube, a suite of computer programs have been developed and described. Using these programs, the potential distributions of electron-optical systems, photoelectron trajectories, image qualities, spatial and temporal modulation transfer functions (MTF) of the tube have been simulated.

Chapter 3 is devoted to the analysis of a streak tube in synchroscan operation. In this operation, apart from the limited time resolution of the streak tube, significant problems arise from the amplitude and phase noise inherent in laser and electronic circuitry. The evaluation of a synchroscan camera with consideration of these noise sources is provided and it is identified that the improvement of both streak tube time resolution and the stability of laser and electronic circuitry is desirable if a femtosecond time resolution is to be achieved. Another problem is

multipacting effects associated with the application of high power RF signals to the deflection system. The theoretical analysis of such effects indicates that it is possible to prevent such deleterious influence.

The design considerations and performance characterisation of a Photochron V streak tube are presented in chapter 4. This streak tube has a theoretically predicted limiting time resolution of 250 fs at an overall operating voltage of 10 kV. Preliminary tests on an experimental sub-specification version of this tube provided a static spatial resolution of 50 lp/mm at a 5 kV overall operating voltage and 3.8 ps streaked pulse duration for less than 1 W RF power in its synchroscan operation.

In chapter 5, emphasis is placed upon the single-shot operation of streak tubes where high streak speed and good dynamic range are the main concerns. The deflection system evaluation showed that meander-type travelling wave deflectors offer a better high frequency deflection response and the design of such systems is presented. In the determination of tube dynamic range, the simulation of space-charge effects is carried out. The experimental evaluation of a streak tube with travelling-wave deflectors is also described briefly where an output streak duration of 300 fs has been recorded.

In order to examine the fidelity of the temporal information provided by a streak camera, in Chapter 6 the output responses of the Photochron V tube for a variety of input signals under synchroscan/single-shot operation conditions are investigated. Theoretical data indicate that the streak tube can identify temporal structures of input pulses in timescales around 1 ps and can give pulse duration data for input signals in timescales between 400fs and 1 ps.

Following a brief introduction to various framing techniques, the analysis and design considerations of Picoframe framing tubes are described and possible refinements are discussed in chapter 7. It is predicted that for an improved design of the tube, frame times of less than 60 ps are achievable with 15 lp/mm spatial resolution for UV illuminations and 10 lp/mm for X-ray radiations. Based on this work, a framing tube having less than 10 ps frame

times for near-infrared and visible light sources is proposed which will be applicable to medical diagnosis.

1.4 References

1 Bradley D J, Topics in Applied Physics 18, Edited by S. L. Shapiro (New York: Springer-Verlag, 1977)

2 Simon J D, Rev. Sci. Instrum., Vol.60 (12), pp.3597-3624 (1989)

3 Finch A, Chen G, Sleat W E, and Sibbett W, J. Mod. Optics, Vol.35, pp.345-354 (1988)

4 Kean P, Zhu X, Crust D W, Grant R S, Langford N, Sibbett W, Opt. Lett., Vol.14, pp.39-41 (1989)

5 Fork R L, Brito-Cruz C H, Becker P C, Shank C V, Opt. Lett., Vol.12, pp.483-485 (1987)

6 Becker P C, Fragnito H L, Fork R L, Beisser F A, Shank C V, Proc. IQEC'88, Post-dead line paper PD-15, p.36 (1988)

7 Spence D E, PhD Thesis, Department of Physics and Astronamy, University of St. Andrews, (1992)

8 Mollenauer L F, Stolen R H, Opt. Lett, Vol.9, pp.13-15 (1984)

9 Spence D E, Kean P N, Sibbett W, Opt. Lett., Vol.16, pp.42-44 (1991)

10 Krausz F, Spielmann Ch, Brabec T, Wintner E, Schmidt A J, Opt. Lett., Vol.17 (3), pp.204-206 (1992)

11 Huang C P, Kapteyn H C, McIntosh J W, Murnane M M, Opt. Lett., Vol.17 (2), pp.139-141 (1992)

12 Liu Y M, Sun K W, Prucnal P R, Lyon S A, Opt. Lett., Vol.17 (17), pp.1219-1221 (1992)

13 Squier J, Mourou G, Laser Focus World, Vol.28(6), pp.51-60 (1992)

14 Maine P, Strickland D, Bado P, Pessot M, Mourou G, IEEE J. Quantum Electron., Vol.24 (2), pp.398-403 (1988)

15 Kmetec J D, Macklin J J, Young J F, Opt. Lett., Vol.16 (13), pp.1001-1003 (1992)

16 Salin F, Squier J, Mourou G, Opt. Lett., Vol.16 (24), pp.1964-1966 (1991)

17 8th International Conference on Ultrafast Phenomena, Technical Digest (France, June 1992)

18 Sennaroglu A, Carrig J, Pollock C R, Opt. Lett., Vol.17 (17) pp.1216-1218 (1992)

19 Malcolm G P A, Ferguson A I, Opt. Lett., Vol.16 (24) pp.1967-1969 (1991)

20 Moore D S, Schmidt S C, Opt. Lett., Vol.12 (7), pp.480-482 (1987)

[21] Huang C P, Asaki M, McIntosh J W, Murnane M M, Kapteyn H C, in Digest of Conference on Lasers and Electro-Optics (Optical Society of America, Washington, D C., 1992)

[22] Evans J M, Spence D E, Sibbett W, Chai B H T, Miller A, Opt. Lett., Vol.17 (20) pp.1447-1449 (1992)

[23] Sibbett W, Inst. Phys. Conf. Ser. No.126: Section I, Int. Symp. on Ultrafast Processes in Spectroscopy, pp.1-8 (Bayreuth, 1991)

[24] Topics in Applied Physics 18, Edited by S. L. Shapiro (New York Springer-Verlag, 1977)

[25] Miller A, Sibbett W, J. Modern Opt. Vol.35 (12), pp.1871-1890 (1988)

[26] Ippen E P, Shank C V, in Topics in Applied Physics Vol.18, Ultrashort Light Pulses, Picosecond Techniques and Applications, Ed. S L Shapiro, Springer-Verlag, Berli-Heidelberg, New York, pp.83-102 (1977)

[27] Weber H P, J. Appl. Phys., Vol.38, pp.2231-2236 (1966)

[28] Diels J-C M, Fontaine J J, McMichael I C, Simoni F, Appl. Opt., Vol.24 (9), pp.1270-1282 (1985)

[29] Naganuma K, Mogi K, Yamada H, IEEE J. Quantum Electron. QE-25 (6), pp. 1225-1233 (1989)

[30] Diels J C, Laser Focus World, Vol.25, pp.95-100 (1989)

[31] Yan C, Diels J C, J. Opt. Soc. Am. B, Vol.8 (6), pp.1259-1263 (1991)

[32] Reynaud F, Salin F, Barthelemy A, Opt. Lett., Vol. 14 (5), pp.275-277 (1989)

[33] Rothenberg J E, Grischkowsky D, Opt. Lett., Vol.12 (2), pp.99-101 (1987)

[34] Chilla J L, Martinez O E, Opt. Lett., Vol.16 (1), pp.39-41 (1991)

[35] Lai M, Diels J C, Opt. Commun., Vol.88, pp.319-325 (1992)

[36] Szabo G, Muller A, Bor Z, Opt. Commun., Vol.82, pp.56-62 (1991)

[37] Blanc S P L, Szabo G, Sauerbrey R, Opt. Lett., Vol.16, pp.1508-1510 (1991)

[38] Janszky J, Corradi G, Opt. Commun., Vol.60 (4), pp.251-256 (1986)

[39] Paulter N G, Rev. Sci. Instrum., Vol.62(3), pp.567-578 (1991)

[40] Raski F, Heuer W, Zacharias H, Opt. Commun., Vol.86, pp.1-6 (1991)

[41] Zavoisky E K, Fanchenko S D, Applied Optics, Vol. 4 (9), pp. 1155-1167 (1965)

[42] Bradley D J, UK Patent Spec. 31167/70 (1970)

[43] Bradley D J, Liddy B, Sleat W E, Opt. Commun., Vol.2, pp.391-395 (1971)

[44] Sibbett W, PhD Thesis, Department of Pure and Applied Physics, the Queen's University of Belfast, (1973)

[45] Bradley D J, Sibbett W, Appl. Phys. Lett., Vol.27, pp.382-384 (1975)

[46] Finch A, Liu Y, Niu H, Sleat, W E, Sibbett W, Yang Q L, Zhang H, Proc. 18th ICHSPP, SPIE Vol. 1032, pp.622-627 (1988)

[47] Hamamatsu Photonic Systems (advertisement), Laser Focus World, Vol.26, No.5, p.220 (1990)

[48] Bradley D J, Bryant S F, Sibbett W, Rev. Sci. Instrum., Vol. 51, No. 6, pp.824-831 (1980)

[49] Sibbett W, Proc. 15th ICHSPP, SPIE Vol. 348, pp. 15-26 (1982)

[50] Walker D R, Crust D W, Sleat W E, Sibbett W, IEEE J. Quantum Electron., Vol. 28, No. 1, pp. 289-296 (1992)

[51] Eagles R T, Freeman N J, Allison J M, Sibbett W, Sleat W E, Walker D R, "100ps UV/X-ray framing camera", Proc. 32nd International Symposium on Optical and Optoelectronic Applied Science and Engineering(San Diego), pp.193-220 (1988)

[52] Sibbett W, Walker D R, Sleat W E, Eagles R T, Freeman N J, "Four-frame UV/X-ray Picoframe II framing camera", Proc. 33rd International Symposium on Optical and Optoelectronic Applied Science and Engineering, SPIE Vol. 1155, pp.406-414 (San Diego, 1989)

[53] Tsuchiya Y, Suzuki H, Koishi M, Kinoshita K, Nakamura T, SPIE Vol.569, High Speed Photography, Videography, and Photonics, pp.181-188 (1985)

[54] Schiller N H, SPIE Vol.348, High Speed Photography, pp.280-282 (1982)

[55] Kuroda H, Nakano N, SPIE Vol.491, High Speed Photography, pp.108-112 (1984)

[56] Stradling G L, Proc.18th ICHSPP, SPIE Vol.1032, pp.194-212 (1988)

[57] Chevokin V K, Sov. J. Quantum Electron., Vol.20 (9), pp.1013-1044 (1990)

[58] Tsuchiya Y, Horiguchi C, Iida H, and Kamiya K, Proc. 14th ICHSPP., pp.350-354 (1980)

[59] Cavailler C, Genoud M, Fleurot N, Launspach J, Mazataud D, Mens A, Proc. 16th ICHSPP, SPIE. Vol. 491, pp.693-701 (1984)

[60] Campillo A. J., Shapiro S. L., IEEE Journal of Quantum Electronics, QE-19 (4), pp.585-603 (1983)

[61] Fujimoto J G, Salour M M, SPIE Vol.322 Picosecond Lasers and Applications, pp.137-165 (1982)

[62] Tsuchiya Y, IEEE J. Quantum Electron., QE-20 (12), pp.1516-1528 (1984)

[63] Schelev M Ya, Proc. 13th ICHSPP, pp.142-150 (1978)

[64] Lavin H P, "Photoelectronic imaging devices", Vol.1&2, Plenum Press, New York (1971)

Chapter 2

THE BASIC CONCEPTS IN THE THEORETICAL ANALYSIS OF ELECTRON-OPTICAL STREAK CAMERAS

2.1 Introduction

The most important parameters for describing the performance of a streak/framing camera are **time resolution, spatial resolution,** and **dynamic range**[1]. Time resolution is used to specify the time resolving ability of a streak camera and is normally defined as the full width at the half maximum (FWHM) of its output temporal response to a delta intensity input pulse. In experimental evaluations, the actual value of the temporal resolution is normally derived from the ratio of dynamic spatial resolution and deflection streak speed at the phosphor screen which is calibrated by using a pair of quasi-delta pulses separated by a known time interval. This time resolving ability is limited by factors such as the energy and angle spreads of photoelectron emission at the photocathode, defraction-limited input slit size, finite photocathode response time, nonuniformity of deflection field distributions, space-charge effects in the case of single-shot/framing operation, phase noise in synchroscan operation and so on.

As in any imaging devices, the concept of spatial resolution is used to characterise the image quality of streak/framing cameras. The overall spatial resolution in the ultimate recording is determined primarily by the geometrical aberrations present in the electron-optical lens and deflectors and also by the spatial resolutions of the phosphor screen, image intensifier and readout system. Under dynamic deflection (i.e. sweeping) conditions, further degradation occurs, and hence the term, dynamic spatial resolution, is used.

When a streak camera is used for recording picosecond/femtosecond light events, a high transient photoelectron current density (in the order of 100 mA/cm^2 or even higher) may be

drawn from the photocathode in order to obtain an adequate light intensity for recording. At such high current densities, the time resolution can deteriorate significantly due to Coulombic repulsion between photoelectrons[2] while a low incident intensity can give rise to an output that is too noisy to record[3]. Therefore, the range of the incident light intensities which can be measured with adequate fidelity by a streak/framing camera is limited by these extremes. For this reason, the concept of dynamic range is defined to characterise this feature. The dynamic range is taken as the ratio of the acceptable upper limit to the lower noise limit of the input light intensity. The upper limit is taken as that where a 20% temporal broadening in the recorded duration relative to the incident pulse occurs and the lower limit is commonly set as the overall noise level of the system.

An optimised design of streak cameras requires the assessment of these parameters, thus the quantitative analyses of the limitations to these parameters have been an important research subject relating to the development of streak cameras. With the availability of large-scale computers, theoretical evaluation techniques with sufficient accuracy have been developed which have enabled us to predict the dynamic performance of a pre-designed streak camera with great confidence.

2.2 The configuration and operation of a streak camera

A time-resolving electron-optical camera basically consists of input optics, streak image tube, output image intensifier, electrical deflection signal generator and readout medium[4] (see fig. 2.2.1).

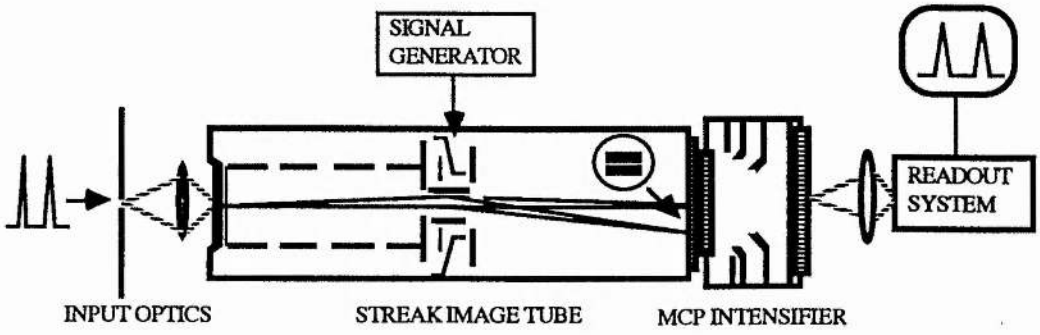

Fig.2.2.1 The operating principle of a streak camera

It can operate in any one of four modes which include single-shot, repetitive synchronous scanning (i.e. synchroscan), circular-scan and framing. In single-shot and synchroscan streak operations, the input optics comprises a narrow input slit and an optical lens. A streak image tube typically consists of photocathode, acceleration mesh, electron-optical focusing lens, deflection system and phosphor screen. In circular-scan operation mode, the input object is a small spot and the streak tube has two sets of deflection systems which are perpendicular to each other and are driven simultaneously 90° out of phase. Such cameras have been developed for spaceborne laser ranging measurement[5] and the design criteria are similar to those for single-shot or synchroscan tube. In the framing operation, two-dimensional information is recorded and hence no input slit is used. A second pair of deflectors is generally required in this type of image tube in order to compensate for image smear. Details of the framing mode of operation will be described in Chapter 7, but the theoretical simulation techniques described in this chapter are applicable to all of these four types of camera.

In the operation of a streak camera, a light signal to be studied is incident on a narrow slit (typically 20 μm) and imaged by the optical lens onto the photocathode of the image tube. The photocathode then converts the slit image into a packet of photoelectrons that replicates the spatial and temporal information of the input light signal. These emitted photoelectrons are accelerated and focused by the electron-optical lens onto the phosphor screen where the photoelectron signal is reconverted into a light signal for subsequent recording. To resolve the temporal information carried by the photoelectrons, a linear time-varying voltage ramp is applied to the deflection system in synchronisation with the arrival of photoelectrons such that the photoelectrons which arrive at different times are deflected correspondingly to different positions on the phosphor screen. The deflection direction is chosen in an orientation orthogonal to the slit length direction and thus the slit width direction of the recording image on the phosphor screen can represent the temporal profile of the input light signal provided that the slit width influence can be neglected. This deflection process thus translates the temporal information into a spatial profile which can be readily recorded by suitable readout techniques.

The operation of the streak camera implies that the linearity of the output response is dependent upon the following conditions being satisfied. These are that (i) the input optical lens only induces negligible temporal or spatial error to the input light signal, (ii) the width of the input slit image is very small compared with the recorded signal duration so that its influence on the streaked image becomes insignificant, (iii) the photocathode has a linear response to light signals, (iv) the temporal and spatial aberrations induced in the electron-optical lens system are negligible in comparison with the temporal and spatial structure dimensions of the measured light signal, (v) the deflection system provides a linear time-varying deflection, (vi) the linearity of deflection voltage ramp lasts during the transit time of the photoelectrons through the deflectors, (vii) the photoelectron/photon transformation at the phosphor screen is linear, (viii) the image intensifier (if required) does not introduce any non-linearities (i.e. it has sufficiently high gain and good spatial resolution with acceptable signal-to-noise ratio), (ix) the recording medium provides either a linear-response recording or that a suitable analytical procedure is available to recover the input signal information. In practice, not all of these conditions can be satisfied simultaneously and compromises have to be made. In order to have a quantitative understanding of how well a streak camera can perform and to achieve an optimised design, a thorough theoretical evaluation of the system has become imperative. This has been accomplished by developing a suite of computer programs which enable various performance parameters of streak camera systems to be evaluated.

It is the streak image tube that enables a linear measurement of time information of ultrafast light events and is thus of key importance in determining the performance of the entire camera. It follows, therefore, that the analysis and design of streak image tubes are of particular interest to this area of research. It is necessary to give an overview of each component that comprises the camera as a whole and to have a qualitative knowledge of how each component influences the overall performance of the system.

2.3 Input optics

The input optics by which the slit image is relayed to the photocathode may induce a temporal distortion of the incident event due to the finite width of the slit, the limited spectral bandwidth and inherent chromatic and geometric aberrations of the optical lens.

Ideally, the input slit width should tend towards being infinitely small. However, due to manufacturing difficulties and resolution limitations arising from diffraction, there is a minimum practical slit width. This slit width is mostly chosen in the range of 10 - 30 μm depending on the features of a particular system. For example, if the input optical lens has a demagnification of 3, the streak image tube provides a magnification of x3 and a streak speed of 3×10^8 m/s, then a minimum temporal resolution would appear to be approximately 70 fs for a 20 μm input slit. For time resolutions greater than 300 fs this is negligible whereas for time resolutions less than 200 fs a narrower slit image should be considered.

When the optical lens focuses the desired slit image onto the photocathode, the photon arrival times at the photocathode depend upon the optical bandwidth, geometrical and chromatic aberrations of the lens. The limited bandwidth of ordinary refractive photographic lenses can cause a time dispersion of around 10 fs - 100 fs[6]. Due to chromatic and geometric aberrations, rays originating from the same object point may not meet at the same point at the image plane. Such spreads in optical path lengths result in a temporal broadening of the input light signal. Due to the finite size of the object, rays from object points on-axis may also have different path lengths from those emitted from off-axis points and this induces time distortion in the measured signal. The detailed computation of the physical time resolution of refractive optical lenses has not been considered in this work. It has been suggested that in the femtosecond regime, the time dispersion and distortion introduced by input optics can be significant. To overcome such defects, a specially-designed optical lens with time dispersion and distortion compensation has been reported[7].

2.4. Photocathode

Photocathodes are used to transform an optical signal into an electron signal in image devices. For the application in ultrahigh speed streak cameras, photocathodes are required to have prompt response times (i.e much shorter than measured pulse duration), wide spectral responses (IR/NIR/visible/UV/X-ray), small emission energy and angle spreads, low transverse surface resistivities and high quantum efficiencies. To satisfy these requirements, it is desirable to examine the performance of photocathodes so as to choose the most suitable photocathode.

2.4.1 Photoemission

The mechanisms of photoemission in different photocathode materials may differ and the explanation of them is not a simple matter. Schematically, photoemission can be considered as a three-step process[8] which includes the excitation of electrons from the valence band to conduction band, the transport of the excited electrons from the point of liberation to the surface, escape from the surface to vacuum. The minimum energy necessary for electrons to emerge from a photocathode is set by the energy band gap between the valence band and the conduction band plus the surface electron affinity. Due to the energy loss during the transport of electrons from the excitation point to the surface, some of the excited electrons may arrive at the surface without enough residual energy to overcome a positive electron affinity and to escape from the surface. The energy loss process is considered to result from lattice scattering and pair production. In lattice scattering, the energy loss per collision is small due to the large difference between electron and atom mass of the material. In pair production, the energy loss is substantial and requires a minimum energy which is more than twice the bandgap above the conduction-band bottom. For example, the bandgap of the multialkali photocathodes is of the order of 1.0 eV and the threshold energy for pair production is around 3.3 eV. If the photon energy is less than 3.3 eV, the energy loss is caused mainly by lattice scattering whereas for illuminations with energies more than 3.3 eV, pair production becomes the dominating cause of energy loss. Because the energy loss by lattice scattering is small, electrons may experience

many collisions before emerging from the photocathode surface and so the average escape path is much longer than that for pair production. Typically, the average escape path is around 30 nm for lattice scattering and is only around 3 nm for pair production[9]. In reality, the mechanism of photoemission is much more complicated than this, there is no precise quantitative explanation for it and most analyses to date are rather qualitative in character.

2.4.2 Spectral response

Photocathode materials can be divided into two categories __ metal-type and semiconductor-type and they can cover spectral ranges extending from NIR to X-ray. The choice of photocathodes depends mainly on the spectral range of operation[10]. For near-infrared applications, the most-commonly used photocathode is S1 type (i.e. A_g-C_s-O). For visible light sources, multialkali type photocathodes (e.g. (Na_2KSb)Cs) are most extensively used due to their high quantum efficiencies (up to 0.4 electron/photon) and broad spectral responses extending up to near-infrared region.

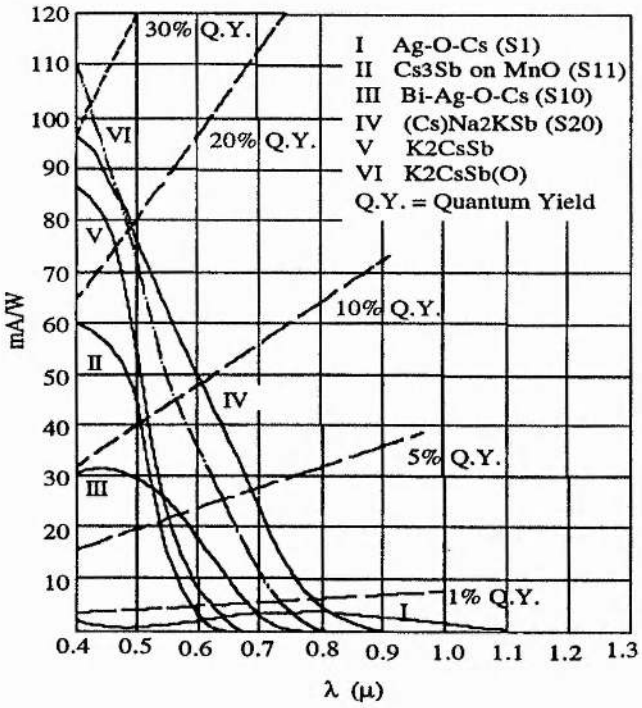

Fig.2.4.1 Spectral response of photocathodes commonly used for visible and near infrared light sources

For UV, X-ray applications, both metal-type and semiconductor-type photocathodes can be used. The semiconductor type of photocathodes can be further classified as negative and

positive electron affinity photocathodes of which the latter is of our particular interest. As an example, typical spectral responses expressed in quantum efficiency of visible- and infrared-sensitive semitransparent photocathodes are shown in Fig. 2.4.1.

2.4.3 Response time of photocathodes

There are two factors which affect the response time of photocathodes to input light signals. One is the finite spectral response range associated with the physical response time limited by Heisenberg uncertainty principle $\Delta\omega \cdot \Delta\tau \sim 1$. The other is the inherent time of the photoemission process itself.

The bandwidth of a typical antimony-caesium semitransparent photocathode is about 300 nm and the induced physical response time is 10^{-15} s. Different photocathodes may have different spectral sensitivity ranges and therefore their corresponding response times will differ. General theoretical considerations indicate that the inherent time of photoeffect should be shorter than 10^{-14} s [6].

The response time induced by photoemission process is more difficult to predict. Attempts to measure experimentally have been reported[11], but they tend to be rather complicated. For the estimate of the order of magnitude of this response time, a simpler method can be used by considering the time for an excited electron to lose all of the energy in excess of that needed for escaping to the vacuum interface. Obviously, electrons generated within the bulk of the photocathode material at a maximum escape depth are likely to take a longer time and lose more energy before emerging than those with equivalent energy generated closer to the vacuum surface.

If the average velocity of the electrons is assumed to be 3×10^7 cm/s, then the average response time of the photocathode is approximately 100 fs for lattice-scattering-dominated photoemission which has the average escape path of 20 - 30 nm. It is 5 - 40 fs for pair-production-dominated photoemission which gives an average escape path of 1.5 - 10 nm. Near-infrared photocathodes tend to have longer response times since the photoemission is dominated by lattice scattering. This intrinsic response time can be minimised by using very

thin photocathodes such as 1 - 10 nm and by utilising the photocathode at its long-wave length sensitivity threshold. The associated low sensitivity can be compensated, at least to some extent, by utilising a high efficiency phosphor screen and incorporating a high gain intensifier which is especially recommended in single-shot operation.

2.4.4 Initial energy and angle distributions of photoelectrons

Fig.2.4.2 shows the schematic energy band diagram of photocathodes where E_G, E_A denote for the energy bandgap and electron affinity of the photocathode material respectively, E_M is the lowest energy level in the valence band from which an electron can be excited into the conduction band by a photon of energy hν.

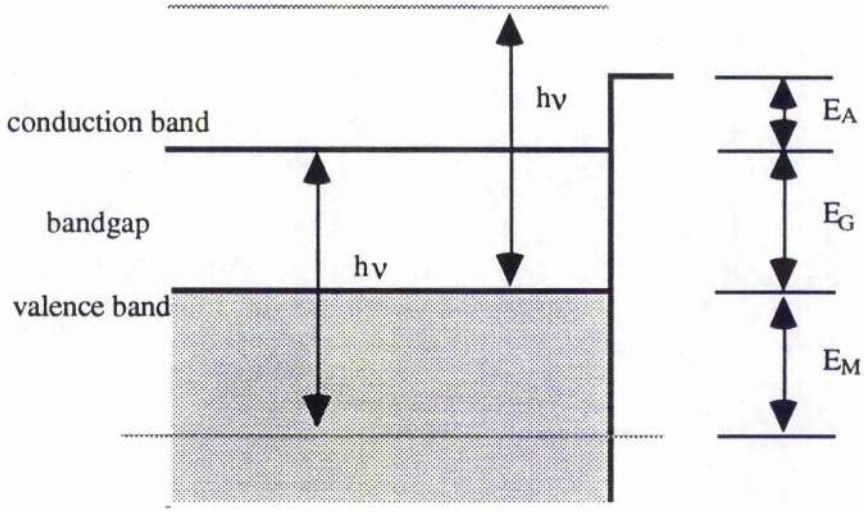

Fig.2.4.2 The energy band diagram for a photocathode

It implies that as a light signal at frequency, ν, illuminates a photocathode, photoelectrons having initial energies between a minimum of zero and a maximum of $\varepsilon = h\nu - E_G - E_A$ can be emitted. As previously mentioned, in propagating from the point of excitation to the photocathode surface, photoelectrons tend to collide with lattice or electrons and this leads to variations in their initial energies and angles as well as emitting times. Due to different energy levels in the valence band and due to the intrinsically large bandwidths of ultrashort light sources, a further spread in the energy of conduction electrons may arise. The values and distributions of the energy and angle spreads depend upon the type of photocathodes and the

signal wavelength and are random in nature. For a particular photoelectron at a specific observation time, the values of these parameters appear in a random manner, but over a long observation period and for a large number of photoelectrons, they may be described by certain distribution functions. When assuming a linear temporal response of the photocathode (i.e. having response time much shorter than the input pulse durations), the initial temporal distribution of the electrons should have the same shape as the incident light pulse. Simulations for initial energy distribution have been carried out by both experimental measurements and Monte-Carlo calculations and they are rather sophisticated processes[12]. A simpler way is to use a Beta or Maxwellian function as an estimate which is adequate for the purpose of streak image tube designs. The angular distribution of photoemission has been generally predicted to obey Lambertian's law which has been confirmed in experiments for alkali material[13]. In the spatial domain, the photoelectrons are assumed to be uniformly distributed within a resolution element.

2.4.5 Photocathode surface resistivity

In streak cameras, especially in single-shot/framing operation, photocurrents in excess of 100 mA/cm^2 may be drawn from photocathodes. For the photocathodes having high surface resistivity, such high photoelectron currents can cause charge saturation in the photocathode and induce changes in photocathode surface potential. This will give rise to image distortion and in extreme cases, may damage the photocathode permanently. Commonly-used photocathodes such as multialkali type have surface resistivity in the order of 10^6 Ω/square which gives a saturation current of only about 1 mA/cm^2[2,14,15].

Such a limitation can be overcome by utilising semitransparent conducting substrates upon which a photocathode can be deposited. The choice of conducting substrate materials is governed by conditions such as being compatible with the photocathode material and processing procedure, having adequate transmission to incident light signal and low inherent surface resistivity as well as having the least deleterious influence on image quality. The achievement of high time resolutions demands low substrate surface resistivity. In this respect, several materials have been found suitable and are listed below together with their properties:

Substrates	S_nO_2[16] or InO_2	Palladium[17]	Pressed-on Mesh[18]	Opto-etched Mesh[19]
Compatible cathodes	S1, S9, S11	S1, S9, S11, S20	S1, S9, S11, S20	S1, S9, S11, S20
Transmission	>80%	~ 25%	35 - 50%	> 60%
Resistivity	< 100 Ω/square	< 100 Ω/square	< 0.3 Ω/square	< 60 Ω/square
Effects	none	none	Moire fringes	pattern-dependent

Theoretical calculations of the influence of photocathode surface resistivity on the performance of streak image tubes have suggested[20] that to achieve femtosecond time resolution, a substrate with a surface resistivity of less than 100 Ω/square is required. It can be seen that S_nO_2 coating or opto-etched random-pattern meshes offer the best compromise. Considering that opto-etching procedures require appropriate pattern design and involve complicated manufacturing technique, the simple S_nO_2 or I_nO_2 coating is generally preferable.

2.5 Electron-optical system and its theoretical numerical simulation

In a streak image tube, one of the most important aspects is the design of the electron-optical system because it plays a fundamental role in the determination of the ultimate temporal and spatial resolutions and dynamic range. The availability of high-speed computers and efficient numerical techniques has enabled a thorough simulation of electron-optical systems and hence the achievement of optimised spatial and temporal performance has become possible.

Commonly-used electron-optics in streak cameras are of the electrostatic type which consists of electrostatic focusing lens and deflection systems. The focusing lens is typically composed of multiple cylinder electrodes and the deflectors are usually a pair of parallel plates. To evaluate such configurations, the detailed calculations of potential distributions, electric field distributions, electron trajectories are essential.

2.5.1 The computation of potential distribution

For the purpose of our camera designs, the programs have been developed for dealing with electrostatic electron-optics. Such systems are normally plane or axially symmetric and under the condition of negligible space-charge effects, their potential distributions satisfy Laplace equation[21] :

$$\frac{\partial^2 V}{\partial x^2}+\frac{\partial^2 V}{\partial y^2}+\frac{\partial^2 V}{\partial z^2}=0 \qquad (2.5.1.1)$$

For an axially symmetric arrangement, this can be recast in cylindrical coordinates as

$$\frac{\partial^2 V}{\partial r^2}+\frac{1}{r}\frac{\partial V}{\partial r}+\frac{\partial^2 V}{\partial z^2}=0 \qquad (2.5.1.2)$$

where V(r,z) represents the potential at the point (r, z), r and z are the radial and axial coordinates. For a planar system this becomes

$$\frac{\partial^2 V}{\partial x^2}+\frac{\partial^2 V}{\partial z^2}=0 \qquad (2.5.1.3)$$

Using a prior knowledge of the boundary conditions of the system, the potential distribution V(r, z) or V(x, z) can be numerically computed by means of either a finite difference method or a finite element method. The latter is very efficient in dealing with non-symmetrical, irregular, open boundary problem but it is more complicated and requires enormous memory space. For our particular image tubes, the former is more practical.

Because our streak tubes have axial or planar symmetry, the potential distribution can be described by the potential distribution on a plane cross-section of the system along its axis. Therefore, the problem is reduced to a two-dimensional one.

Regarding the distinct feature of different parts of the system, the computation of the potential can be carried out in several stages. The first stage is the photocathode-mesh region which is isolated by the mesh from the succeeding region. Because the gap between the two surfaces is much smaller compared to their surface areas, the potential distribution in this

region can be approximated to be linearly dependent on the axial distance and it can be therefore expressed analytically. The second region is bounded by mesh and anode electrodes. The potential distribution in this region is rotationally symmetric and so only half of its cross-section needs to be considered. The potential distribution is given by the solution of equation (2.5.1.2). The third part of the system is the deflection region which has planar-symmetry about the axis and is bounded by anode aperture and a rear aperture and its potential distribution is represented by the solution of equation (2.5.1.3). The last part lies between the deflector rear aperture and phosphor screen. This region has a constant potential and so it is a field-free zone.

To establish a closed boundary in the focusing and deflection regions, interpolation methods are employed to estimate the unknown potential values in the gaps between electrodes assuming a linear or logarithmic variation of potentials between the sides of electrodes. For simplicity, in the focusing region the mesh electrode is taken as its constant potential boundary and the microlensing effects due to the small potential variation within mesh-holes are ignored. This may be justified when considering that the mesh size is only about 20 μm whereas the grid size is often much greater (typically 100 μm). The two apertures are taken as the boundary of the deflection region and the influence of the apertures can be neglected.

These closed potential regions can then be mapped onto a two-dimensional grid with rectangular-shaped meshes so that the potential distribution over the region can be digitised into a data matrix. Applying finite difference method to the partial equations (2.5.1.2) or (2.5.1.3), a set of difference equations can be deduced where the potential on every grid point is directly related to those on the four neighbouring grid points. Each difference equation corresponds to one grid point. For a region containing N grid points, there will be N corresponding difference equations. The solution of these equations represents the potential distribution of this region. To solve these equations, a successive over-relaxation iterative method is used which has been described in detail elsewhere[20]. Once the potentials on all grid points are obtained, the electric field at each point can be deduced from relation $E = -\nabla V$ by taking a Taylor series expansion

and using the Lagrange interpolation method. Knowing the electric field distribution, the trajectories of electrons can be readily achieved by solving the appropriate equations of motion.

2.5.2 The computation of electron trajectories

Without considering the relativistic effects, the equations of motion of photoelectrons in general can be written in Cartesian coordinates as:

$$\frac{d^2x}{dt^2} = -\frac{e}{m}E_x \qquad (2.5.2.1a)$$

$$\frac{d^2y}{dt^2} = -\frac{e}{m}E_y \qquad (2.5.2.1b)$$

$$\frac{d^2z}{dt^2} = -\frac{e}{m}E_z \qquad (2.5.2.1c)$$

where e, m are electron charge and mass respectively and the coordinate z represents the axial displacement. These equations define the electron trajectories within the given electric fields. It should be pointed out that for more accurate calculations the relativistic effects should be included and this will be presented in chapter 5.

In the photocathode-mesh region, the electric field formed between the two parallel surfaces can be assumed to be uniform along the z direction provided that the diameters of photocathde and mesh are much larger than their separation. Therefore the electric field can be described as

$$E_x = 0 \qquad (2.5.2.2a)$$

$$E_y = 0 \qquad (2.5.2.2b)$$

$$E_z = \frac{(V_m - V_c)}{d} \qquad (2.5.2.2c)$$

where d is the distance between photocathode and mesh, V_c, V_m stand for photocathode and mesh voltages respectively.

Equations (2.5.2.2a), (2.5.2.2b), (2.5.2.2c) can be substituted into equations (2.5.2.1a), (2.5.2.1b), (2.5.2.1c) respectively. Then for a photoelectron emitted at position (x_c, y_c, z_c)

and time t_c with velocity (v_{xc}, v_{yc}, v_{zc}) from photocathode, its velocity, transit time and coordinates at the mesh can be derived as

$$v_{xm} = v_{xc} \tag{2.5.2.3a}$$

$$v_{ym} = v_{yc} \tag{2.5.2.3b}$$

$$v_{zm} = \sqrt{v_{zc}^2 + \frac{2e}{m}V_m} \tag{2.5.2.3c}$$

$$t_m = t_c + \frac{2d}{v_{zm} + v_{zc}} \tag{2.5.2.4}$$

$$x_m = x_c + v_{xc}\,(t_m - t_c) \tag{2.5.2.5a}$$

$$y_m = y_c + v_{yc}\,(t_m - t_c) \tag{2.5.2.5b}$$

$$z_m = d \tag{2.5.2.5c}$$

where v_{xc}, v_{yc}, v_{zc} are determined by the initial emitting conditions of photoelectrons.

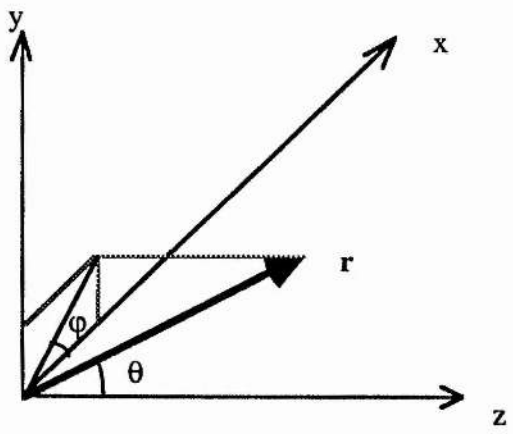

Fig.2.5.1 The notion of initial emission angles

The emission direction of a photoelectron can be described by two angular parameters θ and φ which are designated as tangential and sagittal angles. If the scalar velocity of a photoelectron at the photocathode is v, then in a Cartesian coordinate system as shown in Fig. 2.5.1 we have

$$v_{xc} = v_c \cos\varphi \sin\theta \tag{2.5.2.6a}$$

$$v_{yc} = v_c \sin\varphi \sin\theta \tag{2.5.2.6b}$$

$$v_{zc} = v_c \cos\theta \qquad (2.5.2.6c)$$

where $v_c = \sqrt{\frac{2eE_0}{m}}$, E_0 is the initial energy of the photoelectron in eV.

In the focusing region, equations (2.5.2.1a), (2.5.2.1b), (2.5.2.1c) can only be solved by using numerical integration. Taking parameters given in equation (2.5.2.3a) - (2.5.2.5c) as the initial conditions of the photoelectron, then the photoelectron trajectory in this region can be computed by employing a third-order Runge-Kutta method[4].

Taking the velocity, position coordinates and the transit time of an electron at the anode aperture plane as the initial conditions, the electron trajectory in the deflection region can be achieved in the same manner as in the focusing region. In the dynamic sweep operation, a linear voltage ramp for single-shot/framing mode and a sinusoidal waveform for synchroscan mode is applied to the deflectors. The potential distribution and fields are thus no longer static and to accommodate this time dependency, the multiplicative feature of potential and electric fields is adapted. This means that the potential and field distributions can be calculated under static condition with one unit volt DC signal applied to the deflection plates and a time variation $V(t) = V_0 + K(t - \frac{z}{c})$ or $V(t) = V_0 \sin(\omega t - \frac{z}{c})$ (K denotes the gradient of the linear ramp and c denotes the speed of light) can be introduced as a multiplicative factor to the field distributions.

From the deflector rear aperture plane to the phosphor screen, there is no potential variation and so the electric field is zero. Therefore the photoelectron trajectory is a straight line and the coordinates of the photoelectron at phosphor screen can be easily derived as

$$x_p = x_{ap} + \frac{L}{v} v_x \qquad (2.5.2.7a)$$

$$y_p = y_{ap} + \frac{L}{v} v_y \qquad (2.5.2.7b)$$

$$z_p = z_{ap} + \frac{L}{v} v_z \qquad (2.5.2.7c)$$

where L is the distance between the aperture plane and phosphor screen, x_{ap}, y_{ap}, z_{ap} are the coordinates of the electron at the aperture and $v = \sqrt{v_x^2 + v_y^2 + v_z^2}$.

2.6 The assessment of spatial and temporal performance of electron-optical systems

Focusing parameters such as spatial aberrations, magnification, spatial distortion are generally used to describe the imaging performance of a streak image tube whereas time dispersion, time distortion and ultimate time resolution are also required to evaluate its temporal performance. With the aid of the above computation techniques, these parameters can be readily produced for the specification of both static and dynamic performance of an electron-optical system.

2.6.1 Time dispersions and distortions

2.6.1.1 Time dispersions

Photoelectrons emitted simultaneously from the same point on the photocathode may arrive at the deflectors at different transverse locations and times. The time differences between these photoelectrons constitute time dispersions. The values of such time dispersions depend upon the emission energies and angles of the photoelectrons and upon the focusing lens construction, and can be calculated by tracing the photoelectron trajectories through the entire image tube. For simplicity, in the design of a streak tube only a small number of photoelectrons in the extreme cases are traced. For example, the maximum time dispersion for an object point at the photocathode can be obtained by taking the maximum time difference of photoelectrons with energies and angles varying from zero to a maximum (e.g. 90 degree angle and maximum initial energy spread). Because of the temporal-spatial transformation via deflection, time dispersions are only relevant in the region between photocathode and the entrance of the deflectors after which spatial dispersions are more meaningful.

From a knowledge of the time dispersions in different regions, deflection sweep speed and static spatial resolution, the overall time resolution, τ, can be estimated by using Gaussian approximation as follows[22]

$$\tau = (\Delta t_i^2 + \Delta t_c^2 + \Delta t_m^2 + \Delta t_a^2 + \Delta t_d^2 + \Delta t_s^2)^{1/2}$$

where Δt_i is the input pulse duration, Δt_c is the time response of photocathode, Δt_m is the time dispersion caused in photocathode mesh-region, Δt_a is the time dispersion induced in mesh-anode region, Δt_d is the time dispersion given rise to by deflection region and Δt_s is determined by static spatial resolution, δ, and sweep speed, v, via relation $\frac{1}{v\delta}$. This approximation has been widely used for time resolution evaluation.

In the photocathode-mesh region, the time dispersion, Δt_m, can be obtained analytically from equations (2.5.2.3c) and (2.5.2.4). To minimise the time dispersions caused by initial conditions, a planar mesh electrode is inserted in close proximity to the photocathode in order that a high extraction electric field can be produced at the photocathode. The photoelectrons can thus be accelerated to very high velocities soon after emission and the initial velocity differences become less influential. However, there is a limit to the photocathode electric field that can be applied due to increased background noise and induced problems such as electrical breakdown. It has been suggested that a maximum electric field of 10 kV/mm can be applied in practice by very careful design and manufacture of the photocathode-mesh construction. A further improvement of the time resolution can be achieved by the use of a very thin photocathode operating at its long wavelength sensitivity threshold with the aim of reducing the initial energy spreads of photoelectrons to a minimum.

In the mesh-anode region, photoelectrons having different trajectories do not experience the same electric fields and hence an additional spread in their transit times is present when they arrive at the anode. The design of the focusing arrangement must, therefore, be made such that time dispersions induced in this region are minimised. By using multiple electrode structures with high operating voltages and hence minimum transit times, time dispersions can be minimised to less than 50 fs.

The existence of intrinsic fringe-field effects at the entrance and exit of the conventional deflectors have the effect that photoelectrons at various transverse positions and arrival times experience different electric fields in both axial and radial directions. It gives rise to the degradation of spatial resolution and streak speed nonlinearity. The elimination of such effects

requires careful design of the deflection system in order that the fringe-fields are reduced to a minimum. To achieve this, the deflector length, the separations both between the anode aperture and the deflector entrance and between the deflector exit and the rear aperture as well as the gap between deflector plates need to be reduced. With due consideration of these factors including the deflection sensitivity, the electron beam size and the possibility of RF electrical breakdown associated with high voltage across a small gap, a compromise between these parameters is inevitably required.

2.6.1.2 Time distortions

Photoelectrons emitted from different points with the same initial energies and angles at the photocathode give rise to further variation in the transit times owing to the variation in their trajectories. Photoelectrons from off-axis points take longer transit times than those from on-axis points as their path lengths are longer. Such time differences are referred to here as time distortions. As a consequence, the streaked image of a straight input slit can appear curved on the phosphor screen. It is possible to reduce this type of distortion by employing a spherical photocathode and mesh[23], but such a construction makes it extremely difficult to provide a high extraction field and so its time resolution is limited to the picosecond regime. For the femtosecond regime, the planar photocathode and mesh structure is more suitable. Compensation for the inevitable time distortions can be achieved by using an input optical lens with corresponding negative temporal distortions[7] and the effectiveness of this approach has been demonstrated[24,25]. Another possible approach to avoid temporal distortion effects is to use a computer processing method to eliminate the curvature of the recorded image.

2.6.2 Focusing properties

In the evaluation of the focusing properties of an electron-optical system, typical photoelectron trajectories from different object points at the photocathode are calculated and from each point 8 photoelectrons are selected and assigned with initial angles $\varphi = 0$ and $\varphi = \frac{\pi}{2}$ respectively for $\theta = 0, \frac{\pi}{18}, \frac{\pi}{2}, -\frac{\pi}{2}$ at a fixed maximum initial energy (e.g. 0.4 eV for S20, 0.2 eV for S1).

The location of the Gaussian image plane z_p is defined by the position where a photoelectron, emitted on axis with initial angles $\varphi = 0$ and $\theta = \frac{\pi}{18}$, meets the axis after travelling through the electron-optical system. The location of the limiting image plane z_m is defined to be the position where a photoelectron, emitted on axis with initial angles $\varphi = 0$ and $\theta = \frac{\pi}{2}$, meets the axis after going through the electron-optical system. The optimised image plane location can then be given as $z_f = z_m + \frac{1}{4}(z_p - z_m)$. The magnification is derived from the ratio of the image height to the object height defined by two photoelectrons of which one is emitted from an on-axis point and the other is emitted from an off-axis point on the photocathode with the same initial conditions.

The calculation of the trajectories of photoelectrons emitted from the same point with different emission energies and angles shows that at the image plane, they appear scattered over a disk area with certain diameter rather than meet at one point. This is due to the geometric and chromatic aberrations inherent in electron-optical systems. According to different initial conditions, these aberrations can be theoretically divided into chromatic and spherical aberrations, coma, astigmatism, curvature of the image field and spatial distortion. By the careful design of an electron-optical system, these aberrations can be minimised to provide an optimum spatial resolution of better than 50 lp/mm at the phosphor screen. The main limitation to the ultimate spatial resolution in a streak tube is imposed by the dynamic deflection operation and the obtainable input slit size in the streak direction.

2.6.3 Spatial and temporal modulation transfer functions (MTFs)

Although time dispersions and spatial aberrations are very efficient and useful parameters for the design and preliminary performance evaluation of a streak image tube, they cannot represent its ultimate performance precisely. A more thorough evaluation method is to use optical transfer functions (OTF) which were developed from communication theory combined with optical diffraction theory[26]. Under the assumption that an electron-optical system can be taken as a linear low frequency pass filter, its output response to a sinusoidal signal with a spatial frequency f_x will also be sinusoidal with the same frequency or a frequency reduced by

the factor due to the tube magnification, but with lower contrast and a phase shift in comparison with the input object. The contrast ratio of the intensity of the image to that of the object is defined as the modulation. Both the modulation and phase shift varies with input frequency. The curves of modulation and phase shift versus spatial frequency represent the modulation and phase transfer functions respectively. Optical transfer function is the complex of the two functions. The modulation transfer function (MTF) is the modulus of the OTF, and the phase transfer function (PTF) is the phase of the OTF. The important feature of the OTF evaluation is that it includes all the influential factors that relate to the performance of a streak image tube[27].

The procedure for the calculation of electron-optical OTF includes (i) the simulation of photoelectron initial conditions, (ii) the determination of point spread function (PSF), (ii) the deduction of line spread function (LSF) and (iv) the computation of MTF and PTF.

As has been clearly mentioned, due to the initial emission energy and angle spreads, photoelectrons emitted from a point at photocathode do not meet at a single point on the phosphor screen but are dispersed spatially and form a disk image. The diameter of this disk is dependent upon the most probable initial energy and angle spread values. Taking the phosphor screen as the x-y plane, then the photoelectron distribution versus x and y coordinates can be established as the point spread function i.e. I (x,y). The line spread function (LSF) is the integration of the point spread function along x or y direction, i.e. the infinitesimally small object point is replaced by an infinitesimally narrow line object (line delta function). Because the delta function line object for LSF contains equal amplitude sine waves of all frequencies, the OTF can be obtained from the Fourier transform of the LSF. The MTF is a very important defining characteristic function in the evaluation of streak image tubes. The PTF is a measure of the asymmetry of the LSF and is normally not computed.

2.6.4 The Monte Carlo simulation of initial emission conditions

As previously stated, the emission conditions of photoelectrons can be described by parameters including initial emission times, angles, energies and spatial coordinates at the

photocathode. It has been recognised that the fundamental limitation on the temporal and spatial resolution of streak cameras is imposed mainly by the initial energy and angle spreads of photoelectrons from photocathodes. These initial emission energy and angle differences cause the photoelectrons emitted at the same point and same instant to have different radial and axial velocities and the axial velocity differences cause a spread in the transit time of the photoelectrons. The different radial velocities make photoelectrons travel through different paths such that spatial dispersions arise which degrade the dynamic spatial resolution due to the existence of the geometrical aberrations of electron-optical lens and the nonuniformity of deflection field distributions. All these time and space dispersions intermix with the original temporal distribution of photoelectrons and become unwanted information in the recorded output. To overcome these defects, it is of great importance to simulate the distribution functions of the initial emission parameters of the photoelectrons realistically so that a good understanding of the system operation can be reached.

Conventionally, the simulation of these distributions is produced by dividing the energy and angle into a number of equally spaced strips, each of which can be represented by a single electron trajectory with appropriate weight factor[27]. Obviously, this method can not cover every possible combination of initial energies, angles, times and positions. More importantly, it cannot replicate the statistical features in the photoemission conditions and such features should not be neglected in situations where the number of input photoelectrons is low and where the statistical noise could thus be significant. Therefore, a more realistic simulation method is required and the solution is to use Monte-Carlo statistical simulation techniques. The Monte Carlo simulation is a technique, using uniform random or pseudorandom numbers, for the generation of random variants which describe statistical processes or deterministic processes that resemble some stochastic processes[28].

2.6.4.1 Random number generation

The so-called uniform random or pseudorandom numbers used by Monte Carlo simulation are essentially independent random variables uniformly distributed over the interval [0,1]. Based

on uniform random numbers, the generation of random variates from a variety of distributions, such as electron angles, energies and so on, can be carried out.

There are several techniques available for generating random numbers. Some of these are based on random phenomena, others on deterministic recurrence procedures. The requirements for a good random generating method are that it is fast and requires minimum memory capacity and that the produced random numbers are uniformly distributed, statistically independent and reproducible. The most commonly used present-day method for generating pseudorandom numbers is one that produces a nonrandom sequence of numbers according to some recursive formula based on calculating the residues modulo of some integer *m* of a linear transformation. Although these processes are completely deterministic, the numbers generated by the sequence appear to be uniformly distributed and statistically independent. A congruential method is selected for our simulation and it is based on a fundamental congruence relationship, which may be expressed as

$$X_{i+1}= (a\, X_i + C)(\text{mod } m),\quad i=1, 2, ..., n \qquad (2.6.4.1)$$

where the multiplier, a, the increment, C, and the modulus, m, are non-negative integers. The modulo notation(mod m) means that

$$X_{i+1}=a\, X_i + C - m\, K_i \qquad (2.6.4.2)$$

where $K_i=((a\, X_i + C)/m)$ denotes the largest positive integer in $(a\, X_i + C)/m$.

Given an initial starting value X_0, equation (2.6.4.2) yields a congruence relationship (modulo m) for any value, i, of the sequence, $\{X_i\}$. Generators that produce random numbers according to (2.6.4.1) are called mixed congruential generators. The random numbers on the unit interval (0,1) can be obtained by

$$U_i = X_i/m \qquad (2.6.4.3)$$

Because of the deterministic character of the sequence, such a sequence will be periodic and the period cannot exceed modulo, m, the so-called full period. Since most computers utilise a binary or a decimal digit system, we select $m = 2^\beta$ or $m = 10^\beta$, respectively where β denotes the word-length of the particular computer.

For our particular application, a mixed congruential generator is utilised on a SUN Station computer system where the full word size is equal to 32 bits with 1 bit reserved for algebraic sign. Therefore a suitable choice for m is 2^{31}.

2.6.4.2 Random variant generation of initial conditions

Several methods are available for generating random variants having different distributions and they are mainly based on the following three methods: inverse transform method, composition method and acceptance-rejection method[28]. These methods can be applied to almost any variants with any distributions. For our particular applications, the choice of the technique is based on the condition that is simple.

2.6.4.2.1 Initial temporal distribution

In most cases, the temporal shape of an incident light pulse can be assumed to be a Gaussian function given by

$$f(t) = \frac{1}{\sigma\sqrt{2\pi}}\exp\left(-\frac{(t-\mu)^2}{2\sigma^2}\right) \qquad -\infty < t < \infty \qquad (2.6.4.4)$$

and is denoted by $N(\mu,\sigma)$ where μ is the mean value and σ is the variance. Let $t = \mu + \sigma Z$, then the variant, Z, has a distribution ~ $f(Z) = \frac{1}{\sqrt{2\pi}}\exp\left(-\frac{Z^2}{2}\right)$ which is denoted by N(0,1).

According to the central limit theorem, if X_i, i= 1,...,n, are independent and identically distributed random variants with $E(X_i) = \mu$, $Var(X_i) = \sigma^2$, then

$$Z = \frac{\sum_{i=1}^{n} X_i - n\mu}{n^{1/2}\sigma} \qquad (2.6.4.5)$$

converges asymptotically with n to N(0,1).

Consider the particular case when all X_i (i=1,...,N) are uniformly distributed in unit region (0,1), then $\mu = \frac{1}{2}$, $\sigma = \frac{1}{\sqrt{12}}$. Therefore we can have

$$Z = \frac{\sum_{i=1}^{n} X_i - \frac{n}{2}}{\sqrt{\frac{n}{12}}} \qquad (2.6.4.6)$$

By using a variant transformation $t = \mu + \sigma Z$, the distribution $N(\mu,\sigma)$ can then be obtained.

The **algorithm** of such a procedure can be outlined as follows:

1. Generate N uniformly distributed random variants, X_1, ..., X_N from unit region (0,1).

2. Compute Z from equation (2.6.4.6).

3. $\mu + \sigma Z \rightarrow t$

In the case of more than one photoelectrons, the procedure is repeated from step 1.

2.6.4.2.2 Initial energy spread distribution

The initial energy of a photoelectron at photocathode can be taken as a variant which is stochastically distributed in a given function. In our case, for instance, a beta function is assumed such that:

$$f(x) = \frac{\Gamma(\alpha+\beta)}{\Gamma(\alpha)\Gamma(\beta)} x^{\alpha-1} (1-x)^{\beta-1} \qquad (2.6.4.7)$$

where $\alpha > 0$, $\beta > 0$, $0 \le x \le 1$ and values $\alpha = 5$, $\beta = 5$, $x = \frac{\Delta\varepsilon}{\varepsilon_m}$ (i.e. the ratio of photoelectron initial energy to the maximum value) are selected.

The simplest way to produce such a variant is to use the theory of order statistics. Let U_1, U_2, ..., $U_{\alpha+\beta-1}$ be random variants uniformly distributed in unit region (0,1), then the αth order statistic, $U_{(\alpha)}$, is from $Be(\alpha,\beta)$. The procedure for generating such a variant can be summarised as follows.

1. Generate $(\alpha + \beta - 1)$ uniform random variants, U_1, U_2, ..., $U_{\alpha+\beta-1}$, from unit region (0,1).

2. Find $U_{(\alpha)}$, which is from $Be(\alpha,\beta)$.

3. $\varepsilon_m \cdot U_{(\alpha)} \rightarrow \Delta\varepsilon$

To produce more such variants, simply repeat the procedure from step 1.

2.6.4.2.3 Initial angles

Under the assumption that the emission of photoelectrons obeys the Lambertian law, the radial angle θ of a photoelectron emitted from photocathode varies as a cosine function and its sagittal angle φ is uniformly distributed in the region (0,2π). Mathematically, the probability distributions for these two angles can be given respectively as:

$$f(\theta) = \begin{cases} \cos\theta & 0 \le \theta \le \pi/2 \\ 0 & \text{the other} \end{cases} \tag{2.6.4.8}$$

$$f(\varphi) = \begin{cases} \dfrac{1}{2\pi} & 0 \le \alpha \le 2\pi \\ 0 & \text{the other} \end{cases} \tag{2.6.4.9}$$

For the generation of variant θ, an inverse transform method can be used which gives

$$\cos\theta = \max(r_1, r_2) \tag{2.6.4.10a}$$

$$\sin\theta = \sqrt{1-\cos^2\theta} \tag{2.6.4.10b}$$

where r_1, r_2, are uniform variants from unit region (0,1). The computing procedure can be written as follows.

1. Generate two uniform random variants independently from unit region (0,1).

2. Compute cosθ and sinθ from expression (2.6.4.10a), (2.6.4.10b) respectively.

As for the generation of variant φ, an acceptance-rejection method can be employed. Let r_1, r_2 be uniform random variants generated from unit region (0,1), then we have

$$\cos\varphi = \frac{u^2-v^2}{u^2+v^2} \tag{2.6.4.11a}$$

$$\sin\varphi = \frac{2uv}{u^2+v^2} \tag{2.6.4.11b}$$

where $u = r_1$, $v = 2r_2 - 1$ and it requires $u^2 + v^2 < 1$. The **algorithm** can be stated as follows.

1. Generate uniform random variants r_1, r_2 from unit region (0,1).

2. $r_1 \rightarrow u$, $2r_2-1 \rightarrow v$.

3. If $u^2+v^2 > 1$, go back to step 1, otherwise compute cosφ, sinφ from expressions (2.6.4.11a), (2.6.4.11b).

2.6.4.2.4 Initial spatial distributions

It is impossible to predict the spatial shape of the incident object being tested. For the sake of theoretical evaluation, such information must be given. In the computation of time and space resolutions, it is assumed that the photoelectrons are uniformly distributed within a slit width dimension. Such a uniform random variant can be readily produced using the techniques described earlier.

To demonstrate the effectiveness of the Monte-Carlo simulation method described above, the simulation results of initial energy and angle distributions are displayed in Fig. 2.6.1 where the solid lines represent analytical results. It is clear that the Monte-Carlo modelling data are in good agreement with those of the predicted analytical distributions.

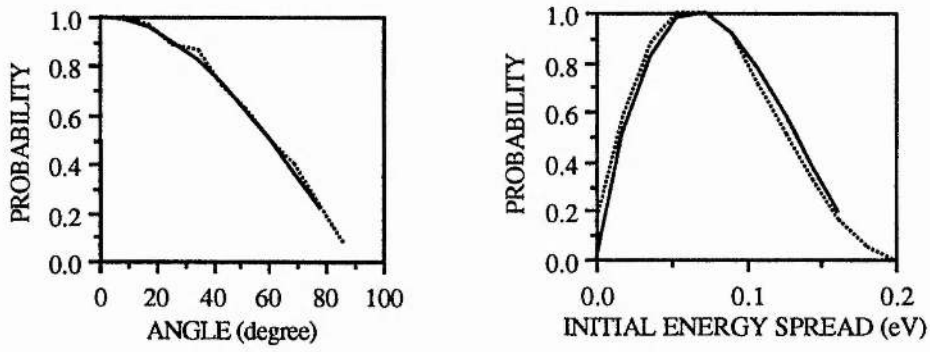

Fig.2.6.1 The simulated results of angle and energy distributions

2.6.5 The evaluation of LSF

To produce a smooth point spread function, 1000 electrons (the more the better) are traced through the image tube from a chosen point on the photocathode to a chosen location. The point spread function is represented by the photoelectron positions at the chosen plane. To achieve the LSF along y direction from such a discrete distribution, the photoelectron distribution region is divided into a fixed number of strips across the y direction. In each strip, the number of photoelectrons are added up along the x direction and taken to be the LSF value at the y position of the centre of this strip. Therefore the values of photoelectron numbers on all strips form the LSF distribution against y position.

2.6.6 The calculation of spatial and temporal MTFs

Once the LSF is produced, the OTF at a frequency f_y can be readily calculated from the Fourier transformation of the LSF:

$$MTF(f_y) = (A_1 + A_2)^{1/2}$$

$$PTF(f_y) = \tan^{-1}(\frac{A_2}{A_1})$$

where

$$A_1 = \frac{\int_{-\infty}^{\infty} LSF_y \cos(2\pi f_y y)\, dy}{\int_{-\infty}^{\infty} LSF_y\, dy}$$

$$A_2 = \frac{\int_{-\infty}^{\infty} LSF_y \sin(2\pi f_y y)\, dy}{\int_{-\infty}^{\infty} LSF_y\, dy}$$

Since the LSF_y has non-zero values barely within the photoelectron beam spot, the integration is only performed across the spot size.

The temporal MTF of a streak image tube prior to deflection have the same expressions as its spatial MTF except that the spatial frequency f_y is replaced by temporal frequency f_t and the space variable y is replaced by time t. After deflection, the spatial MTF at the phosphor screen is calculated first and then the ultimate temporal MTF is produced by transfering the space frequency and variable of the spatial MTF into time frequency and variable via the deflection sweep speed. The spatial resolution is taken as the spatial frequency where the SMTF falls to a value of 5% which is near the limit of discrimination by the human eye[29]. Similarly the time resolution is defined as the temporal frequency where the TMTF shows a 5% contrast. The MTF provides a very important property which is that if several incoherently linked systems are used together, the MTF of the whole system is simply equal to the product of the MTFs of each individual component.

A problem which may occur in the evaluation of MTFs is the generation of spurious spectra referred to as aliasing[30]. This originates from both the finite number of electrons sampled, and the fact that the LSF is produced using only a limited number of strips to sample the true LSF. This can cause the onset of an MTF increase at high frequencies (oscillation). Particularly in single-shot operation where the number of photoelectrons are limited by the space-charge effects, this problem becomes significant.

2.7 The performance of phosphor screen

At the phosphor screen, the temporal information has already been transferred into a spatial profile, hence there is no special requirement on its temporal response property and only its spatial resolution needs to be taken into account. It is the phosphor screen that carries out the conversion from a photoelectron signal to a light signal, so its response fidelity has a direct influence on the accuracy of the ultimate information.

A phosphor screen is typically formed by depositing a layer of phosphor upon a glass or optic-fibre faceplate backed with a thin aluminium film. The Al film serves to prevent light feedback from the output screen through the anode aperture to the photocathode and subsequently to enhance the forward light emission. The performance parameters of phosphor screen include quantum efficiency, linearity of response and spatial MTF. The quantum efficiency is dependent on many factors including phosphor material, processing technique, thickness, substrate, the thickness of Al backing layer and incident electron energy. High quantum efficiency requires larger phosphor particles, higher electron energy and thinner Al coating. However, larger phosphor particles induce lower spatial resolution, thinner Al coating may cause higher background noise. Higher electron energy implies lower deflection sensitivity. Therefore a compromise has to be made between these parameters. A P11 phosphor screen with appropriate Al backing layer may provide 500 photons per 18 keV electron[31]. A high gain intensifier or an internally-incorporated MCP may be employed to compensate low quantum efficiency.

The theoretical analysis has shown that under pulse operation, the maximum electron density allowed for linear response can be much higher than that under static conditions. The phosphor screen can be considered as a linear component. This implies that the total MTF of an image tube can be taken as the product of the MTFs of electron-optical system and the phosphor screen.

It has been experimentally indicated that the MTF of a P20 phosphor can be expressed by[32]

$$MTF(f) = \exp(-(\frac{f}{f_c}))^n$$

where n=1.1 and f_c is the frequency constant deduced from fitting the experiment data. This can also be used to approximate the MTF of P11 type phosphor. For P20, f_c = 24~48 lp/mm, for P11, f_c = 48.7 lp/mm. The main effect of the phosphor screen is to reduce the modulation at high frequencies. When the modulation has fallen to a low value, the modification caused by the phosphor is relatively small.

In order to minimise veiling glare and to couple the tube directly with readout media or an intensifier, the phosphor screen deposited on a fibre-optic window is often chosen. As the geometrical positions and dimensions of phosphor particles and fibres are completely independent of each other, the MTF of the screen on the fibre-optic is a combination of the phosphor screen MTF and fibre-optic MTF and can be degraded significantly. This can be overcome by intagliating phosphor particles in holes excavated in each elementary fibre at the input of the fibre-optic plate and the spatial resolution can be improved from 60 lp/mm to 85 lp/mm for a 10 μm pitch fibre-optic plate[33]. Actually the spatial resolution of a streak image tube is normally limited to no better than 50 lp/mm at the phosphor screen which is lower than that of phosphor screen and so the spatial resolution requirement in streak image tubes can easily be satisfied.

It is well-known that to ensure a linear response of a phosphor screen under DC operating condition, the maximum electron current density is limited to about 150 $\mu A/cm^2$. Obviously, this could be a problem for a streak tube as in pulse operation the electron current density required for adequate recording is much higher (e.g. $1mA/cm^2$ ~ $1A/cm^2$) than this value.

Fortunately, studies on the linearity of phosphor screen under dynamic pulse operation have indicated that the maximum current density in such mode can be much higher than in DC mode[34]. The difference is in that a quantum efficiency loss (4 times reduction for P11 and 6 times for P20) was observed for pulse durations shorter than 1ns. It is considered that P46 and P47 phosphors are the better choice for high speed detection since they have much shorter rise and fall times (less than 1 μs) than those of P11 and P20 (several hundred μs)[35].

2.8 MCP and intensifiers

In the operation of streak cameras, it is essential to ensure that the photocurrent densities are adequate for readout recording. This is especially true in single-shot/framing operations. To prevent the photocurrent density reaching levels where significant space-charge effects can occur which will lead to serious degradation of the temporal performance of the streak camera, high gain intensification is required. Such intensification can be provided in either external or internal configurations. Internal intensification is realised by incorporating a microchannel plate (MCP) directly into the streak image tube in proximity to the phosphor screen while the external intensification is provided by coupling an image intensifier onto the output screen of the streak image tube. Internal intensification has the merits of convenience, elimination of coupling loss and absence of spatial resolution degradation whereas the use of an external intensifier gives flexibility and can exhibit less gain saturation problems[36].

The basic requirement of the intensification scheme are that it should provide a sufficient gain ($> 10^4$), a spatial resolution considerably better than the dynamic spatial resolution of the streak image tube (e.g. 50 lp/mm) and a good signal to noise ratio. The gain of MCP is dependent on the electric field applied across the channel plate, the ratio of the length to diameter of each channel and the secondary emission characteristics of the channel wall[37]. Typical value of the length-to-diameter ratio of an MCP is around 60 - 100. At a potential difference of a few kilovolts, gains of up to 10^5 are achievable with the advantage that by adjusting this potential the gain may be controlled without affecting the focusing properties. MCPs can also be easily gated by modulating the applied voltage and this is often desirable for reducing background noise. For electrostatically focused MCP image intensifiers, spatial

resolutions of up to 50 lp/mm can be obtained. A typical noise figure is about 40 which is 4 times higher than cascade type of intensifiers due to MCP's finite open area (e.g. 50%) and detection efficiency (50%)[38]. Nevertheless, the electrostatically focused MCP image intensifier is considered as the most appropriate type of device because of its capacity to providing high gain, good spatial resolution, low background noise in a relatively compact and robust structure. Its high noise figure can be compensated to some extent by using direct fibre-optic coupling onto the output screen of streak image tube instead of lens coupling thereby improving the coupling efficiency from around 2.2% to 25%.

When an MCP is internally incorporated into a streak image tube it has to be noted that channel saturation effect may arise because a short duration electron pulse strips electrons from the walls of channels too fast to be replaced by the charging current[37]. The accumulated charges on the channel walls will then reduce the electric field within the channels thereby reducing the gain and inducing a nonlinear response. Obviously, for synchroscan operation this is not a problem but in single-shot/framing operations external intensification is generally preferred.

2.9 Output readout systems

To carry out the output data acquisition, storage and image processing, a suitable output recording medium is required. This can be facilitated by the use of either high speed photographic film recording[39] or photoelectronic readout systems. The requirements for the performance of a readout device are that it should have a spatial resolution and a dynamic range greater than that of the streak camera and it should also have low inherent background noise. Photographic film recording can provide two-dimensional image analysis and good spatial resolution. But due to its low dynamic range and complications associated with the nonlinearity of its response, it requires necessary calibration. This involves lengthy processing procedures for data access including chemical processes and microdensitometering of the streak records[40], it has therefore been increasingly replaced by photoelectronic readout systems that provide linear response. These readout systems include an image isocon TV camera tube interfaced to a microprocessor display unit[41] and silicon intensified target (SIT) vidicon cameras connected to

a one[42] or two dimensional optical multichannel analyser (OMA)[43], solid state integrated photodiode arrays (Reticon™) coupled to an oscilloscope[44] and charge coupled device (CCD) cameras[45,46]. OMAs can be used to measure and display the intensity of the incident light on the detector head as a function of position and so they provide direct linear readout of streak images. Compared to a CCD camera, an OMA has the disadvantages of being bulky, expensive and providing limited dynamic range (370 or less for single-shot operation)[3].

Two dimensional CCD cameras have been developed to fulfil the streak camera demands. Also a CCD component incorporated inside a streak image tube in place of phosphor screen as an electron detector has been reported. This was only partially successful as the device suffered from damage during photocathode activation and demonstrated an unacceptably low dynamic range (about 10)[47]. Most electronic readout devices suffer from either poor spatial resolution (typically 25 μm detector pixel size)[42] or small video field. This can make them difficult to use with a single-shot camera and become one of the main factors limiting time resolution in femtosecond regime. Despite this, they represent useful data acquisition systems for streak cameras.

2.10 Summary

The streak camera has long been considered as a unique direct, linear ultrafast diagnostic technique, however, its application is restricted due to the limitations to its instrumental performance. In order to understand and hence to overcome the limiting factors, a thorough analysis of such systems is increasingly desirable. The characteristics of the operating performance of a streak camera are normally described by systematic parameters such as temporal and spatial resolutions, and dynamic range. Each component of a streak camera has contributions to the limitations of these parameters. A linear output response from a streak camera, therefore, requires that each such component must exhibit a linear response.

The analysis of the overall operating characteristics of streak cameras has been carried out by considering the performance of all the components including input optics, streak image tubes, image intensification and readout systems in every aspect. These studies have identified

that presently the deficiencies in the image streak tubes represent, in general, the major limitation to the further improvement of the instrumental performance of a streak camera system. Therefore, the main emphasis of this work has been upon the theoretical evaluation techniques of a streak image tube. For the simulation of photoelectron trajectories faithfully, Monte-Carlo statistics have been employed to simulate the initial energy and angular spreads of photoelectrons. Such techniques have the advantage of taking the statistical feature of photoemission process into account which is of great importance in the single-shot operation of a streak camera. Therefore, the essence of the theoretical evaluation of a streak image tube has been established to provide most of the data on both its static and dynamic performance. On the basis of such theory, the optimisation of streak camera design can be carried out.

It has been identified that the initial energy and angle spreads of photoelectrons and deflection fringe-field effects are the vital limiting factors in streak image tubes. The former induces spatial aberrations and time dispersions in photoelectrons while the later causes degradation of dynamic spatial resolution and limits the streak speed. The possibilities of minimising the influence of these factors have been discussed briefly and more details will be given in chapter 4. In single-shot/framing operations, space-charge effects arise which has become the primary obstacle to their extensive applications in researches and the detailed simulation and analysis of such effects will be presented in chapter 5.

The simulation methods described here have been adopted in new design of streak image tubes and have also formed the theoretical base on which further studies of streak cameras can be carried out.

2.11 References

1 "Workshop on picosecond streak cameras", Proc. 16th ICHSPP, SPIE Vol. 491, pp.374-375 (1984)

2 Bradley D J, Liddy B, Roddie A G, Sibbett W, Sleat W E, Adv. Elect. and Elect. Phys., Vol. 33B, pp.1145-1156 (1972)

3 Bryant S F , PhD Thesis, Imperial College of Science and Technology, London University (1978)

4 Baggs M R, PhD Thesis, Imperial College of Science and Technology, London, University, (1983)

5 Sibbett W, Sleat W E, and Taylor J R, Proc. 16th ICHSPP, SPIE Vol.491, pp.76-81 (1984)

6 Zavoisky E K, Fanchenko S D, Applied Optics, Vol. 4, No. 9, pp. 1155-1167 (1965)

7 Huang Y J, Liu J Q, Guo M Y, Proc. 18th ICHSPP, SPIE Vol. 1032, pp.91-93 (1988)

8 Ghosh C, Phys. Rev. B, Vol. 22, No. 4, pp.1972-1979 (1980)

9 Spicer W E, Wooten F, Proc. of IEEE, Vol.51, pp.1119-1126 (Aug. 1963)

10 Sommer A H, "Photoemissive Materials", Ed. by R. E. Krieger, Wiley, New York (1968)

11 Duchet M, Adv. Electron. Electron. Phys., Vol.22A, pp.499-506 (1966)

12 Wooten F, Hernandez J P, Spicer W E, J. Appl. Phys., Vol. 44, No. 3, pp.1112-1117 (1973)

13 Ives H E, Olpin A R, Johnsrud A L, Phys. Rev., Vol. 32, pp.57-80 (1928)

14 Ahmad N, Gale B C, Key M H, Adv. Elect. and Elect. Phys., Vol. 28B, pp.999-1010 (1969)

15 Stewart G W, Waniek R W, Rev. Sci. Instrum., Vol. 34, pp.512-515 (1963)

16 Gex F, Alexandre R, Horville D, Cavailer C, Fleurot N, Nail M, Mazataud D, Mazataud E, Rev. Sci. Instrum., Vol. 54, No. 2, pp.161-164 (1983)

17 Zhang X Q, Pang Q C, Lei Z Y, Adv. Elect. Elect. Phys., Vol. 64B, pp 385-391 (1085)

18 Garfield B R C, Folks J R, Liddy B T, Adv. Elect. & Elect. Phys., Vol. 28A, pp.375-380 (1969)

19 Niu H, Zhang H, Yang Q L, Liu Y P, Wang Y C, Reng Y A, Zhou J L, Proc. 18th ICHSPP, SPIE Vol. 1032, pp.472-480 (1988)

[20] Thomas B R, Adv. Elect. & Elect. Phys., Vol. 33B, pp.1119-1129 (1972)

[21] Weber C, Philips Research Reports Supplement, No. 6 (1967)

[22] Kalibjian R, McConaghy C F, and Coleman L W, Rev. Sci. Instrum., Vol. 45, pp.776-778 (1974)

[23] Niu H, Proc. 15th ICHSPP, SPIE Vol. 348, pp.231-236 (1982)

[24] Kolesov G V, Korzhenevich I M, Lebedev V B, Stepanov B M, Proc. 16th ICHSPP, SPIE Vol. 491, pp.657-658 (1984)

[25] Huang Y J, Guo M Y, Jiang L P, Acta Photonica Sinica, Vol.21 (1), pp.61-66 (1991)

[26] Stark A M, Lamport D L, Woodhead A W, Adv. Elect. & Elect. Phys., Vol. 28B, pp.567-575 (1969)

[27] Niu H, Sibbett W, Baggs M R, Rev. Sci. Instrum., Vol. 53, pp.563-569 (1982)

[28] Rubinstein R Y, "Simulation and the Monte-Carlo method", Wiley, New York (1981)

[29] Rose A, "Vision, human and electronic", Plenum Press, New York (1974)

[30] Lavin H P, "Photoelectronic imaging devices", Vol.1, Plenum Press, New York (1971)

[31] Sleat W.E, PhD Thesis, The Queen's University of Belfast (1974)

[32] Johnson C B, Adv. Elect. & Elect. Phys., Vol. 33B, pp.579-584 (1972)

[33] Fouassier M, Duchenois V, Dietz J, Guillemet E, and Lemonier, Adv. Elect. & Elect. Phys., Vol. 74, pp.315-322 (1988)

[34] Majumdar S, Majumdar Samprasad, Serdyuchenko Y, Platonov V, SPIE Vol. 1155, Ultrahigh Speed and High Speed Photography, Photonics, and Videography '89, pp.375-382 (1989)

[35] Boutot J P, Goret R, Jatteau M, Paulin J, Richard J C, Adv. Electron. & Electron Phys., Vol.64A, pp.113-122 (1985)

[36] Sibbett W, Sleat W E, Taylor J R, Willson J P, Proc. 15th ICHSPP, SPIE Vol. 348, pp.217-221 (1982)

[37] Manley B W, Guest A, and Holmshaw R T, Adv. Elect. & Elect. Phys., Vol. 28A, pp.471-486 (1969)

[38] Schagen P, "Advances in image pickup and display", Academic Press, New York, Vol. 1 (1974)

[39] Bird P R, Bradley D J, and Sibbett W, Adv. Elect. & Elect. Phys., Vol. 40A, pp.51-58 (1976)

[40] Bryant S F, Taylor J R, Sibbett W, and Bradley D J,Proc. 13th ICHSPP., pp.476-479 (1978)

[41] Cavailler C, Fleurot N, Mazatud D, Verrecchia R, Proc. 14th ICHSPP., pp.347-349 (1980)

[42] Bradley D J, Bryant S F, and Sibbett W, Rev. Sci. Instrum., Vol. 51, pp.824-831 (1980)

[43] Tsuchiya Y, Horiguchi C, Iida H, and Kamiya K, Proc. 14th ICHSPP., pp.350-354 (1980)

[44] Cheng J C, Thomas S W, Storm E K, McLerran W R, Tripp G R, Coleman L W, Proc. 12th ICHSP., SPIE. Vol. 97, pp.311-316 (1976)

[45] Cavailler C, Genoud M, Fleurot N, Launspach J, Mazataud D, Mens A, Proc. 16th ICHSPP, SPIE. Vol. 491, pp.693-701 (1984)

[46] Zhang R, Proc. 18th ICHSPP, SPIE Vol. 1032, pp.749-755 (1988)

[47] Weiss P B, Black P, Oona H, and Sprouse L, Proc. 16th ICHSPP, SPIE. Vol. 491, pp.679-684 (1984)

Chapter 3

SYNCHROSCAN OPERATION OF STREAK CAMERAS

3.1 Introduction

When observing repetitive signals, the synchronously scanned version of streak cameras has some distinct advantages when compared with the single-shot version[1]. First of all, it has the capability, due to signal integration, to detect very weak light signals without any requirement for additional intensification which may degrade its spatial resolution. Secondly, it is essentially immune to any defects associated with space-charge effects. Thirdly, it has very high dynamic range and good signal-to-noise ratio. Fourthly, it does not require a single laser pulse or electronic pulse selection which adds complexity to the experiments. The synchronisation between its deflection signal and detected optical signal is relatively straightforward. Furthermore, it is compatible with relatively weak sources of repetitive light signals such as CW mode-locked lasers and finally, its streak output can be conveniently recorded, stored and analysed using available one- or two- dimensional readout devices.

Problems do exist, however, in the development of such cameras. The existence of amplitude noise and timing jitter (phase noise) in available laser sources in addition to the intrinsic noise in the electronic circuitry leads to inaccurate synchronisation. Another problem can be the multipacting discharge in the deflection system associated with high RF power at high frequencies (e.g. 100 to 500 MHz) resulting in RF power loss and spurious signals. These problems have limited the time resolution of existing synchroscan streak cameras to around 1 ps[2,3] while the time resolution of single-shot cameras has reached 300 fs[4]. Schemes to overcome these problems have been the main issue in the development of femtosecond synchroscan streak cameras.

3.2 Operating principle and performance characteristics

3.2.1 Principle of operation

In the synchroscan operation of a streak image tube, a sinusoidal waveform voltage signal at a high frequency (e.g. ≥ 100 MHz) is applied to the deflection system synchronously with the repetitive input light signal on the photocathode. When the deflection signal frequency is equal to or multiple of the repetition frequency of the input light signal and is correctly phased, the streak images are superimposed and become integrated in intensity on the phosphor screen. A schematic of the operating principle is indicated below in Fig.3.2.1.

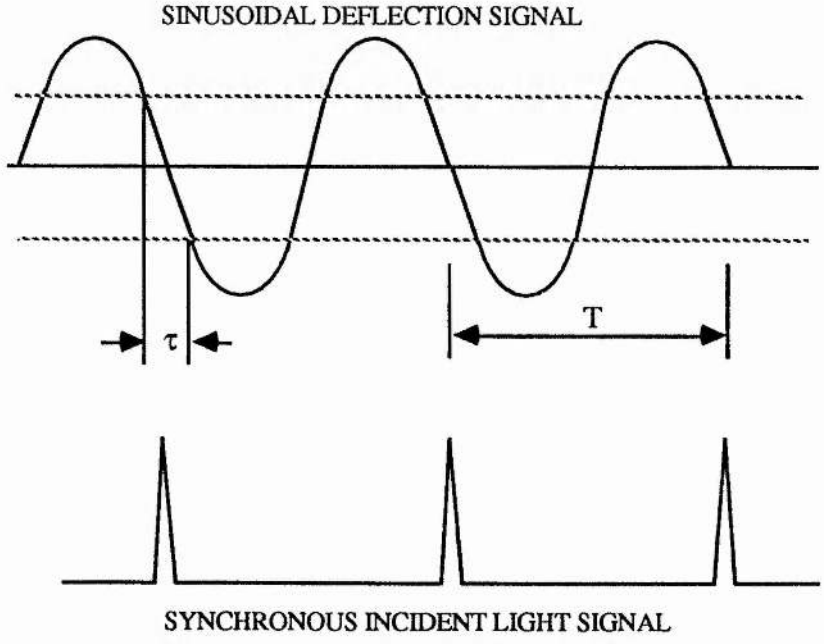

Fig. 3.2.1 Synchroscan operation principle

It is seen that if the time duration of the streaked images does not exceed the time window for the linear sweep of the deflection signal, the instrumental time or spatial resolution should be the limiting resolution of the streak image tube itself.

3.2.2 Linearity of the sinusoidal deflection

The duration of the linear time window depends on the requirement of linearity in particular applications. The nonlinearity can be defined as

$$L_n=\frac{(V_t-V_t')}{V_t}=1-\frac{\sin(\omega t)}{\omega t} \qquad (3.2.1)$$

The meaning of the variables are shown in Fig. 3.2.2a. Nonlinearity values at given time windows (i.e. photoelectron transit time in the deflectors) and deflection signal frequencies can be calculated by using expression (3.2.1) and are plotted in Fig.3.2.2b. It is seen clearly that higher deflection frequencies imply shorter time windows for a required linearity.

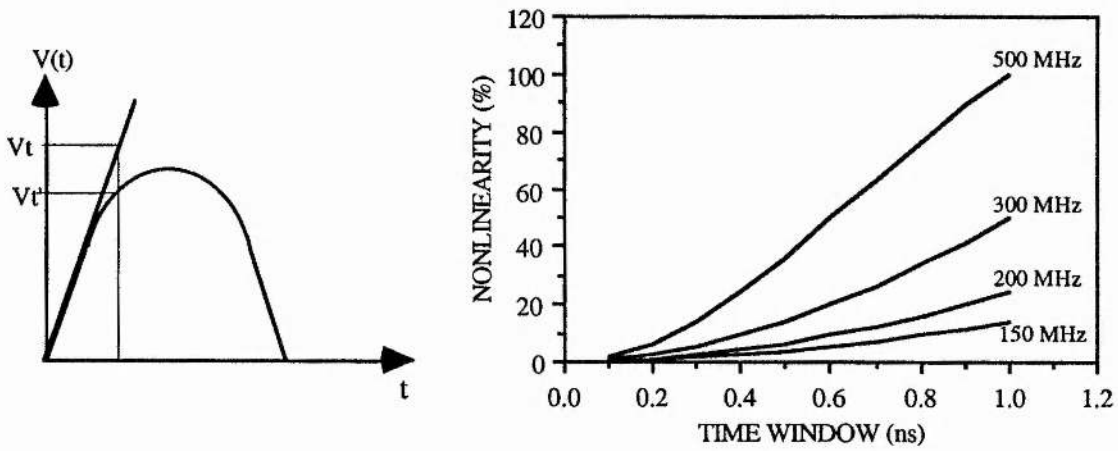

(a) **(b)**

Fig.3.2.2 The nonlinearity of synchroscan deflection

For example, to ensure less than 5.0 % nonlinearity of deflection speed, the time window is required to be no longer than 833 ps for 200 MHz and to be only 333 ps for 500 MHz. For high deflection frequency operation, a shorter deflector length is necessary to ensure adequate linearity of the deflection speed and under no circumstances should the transit time of the photoelectrons exceed a half period of the deflection signal. There is, therefore, a trade-off between deflection sensitivity and repetitive frequency of operation which implies that an increase of deflection sweep speed can not be reached solely by increasing the operating frequency.

3.2.3 Dynamic range of synchroscan streak cameras

Since the resultant output image in synchroscan streak cameras is achieved by superimposing successive streak traces at a frequency of up to several hundred megahertz, the effective system gain for a single pulse can be as high as 10^7 to 10^8 whereas in single-shot cameras the use of intensifier can only provide 10^3 to 10^5. Thus the minimum acceptable current density for synchroscan streak cameras even without using an intensifier can be a factor of 10^2 to 10^5 less than that for single-shot cameras and the use of an intensifier would further extend its lower limit of detectable current density. Also the photocurrent limit associated with space-charge induced pulse broadening is no longer the limiting factor in the dynamic range of synchroscan streak cameras. Instead it is parameters such as phosphor screen saturation, damage thresholds and the dynamic range of the readout system chosen that establish the dynamic range of a synchroscan camera system. Therefore, the dynamic range of such systems is expected to be several orders of magnitude higher than that of single-shot cameras[5,6].

3.3 Experimental evaluation setup

From the operating principle it is seen that the time resolution in synchroscan streak cameras is dependent not only upon the time performance of the streak tube but also upon the synchronisation stability within the operating time window. Any amplitude and phase fluctuations existing in the laser source and the electronic circuitry will give rise to the degradation of the overall time resolution because they result in variations in the streak image positions on the phosphor screen. Therefore, in the evaluation of synchroscan camera performance, it is very important to choose an experimental setup with minimum inherent amplitude and phase noise.

In one of our early experiments on the synchroscan operation of Photochron IV image tube, the laser signal was used directly to produce the electronic deflection signal so that the timing jitter in the laser source can be followed by the deflection signal and a more precise synchronisation between the two signals can be ensured[7,8]. Fig.3.3.1 illustrates the experimental arrangement for the evaluation of a Photochron IV streak image tube carried out at

St. Andrews University. In this setup, a dispersion compensated, passively mode locked, colliding pulse ring dye laser was employed to provide femtosecond pulses (at 630 nm) at a repetition rate of 100 MHz. The laser dye was rhodamine 6G (Rh6G) and saturable absorber was 3-3'-diethyloxadicarbo-cyanine iodide (DODCI), both dissolved in ethylene glycol.

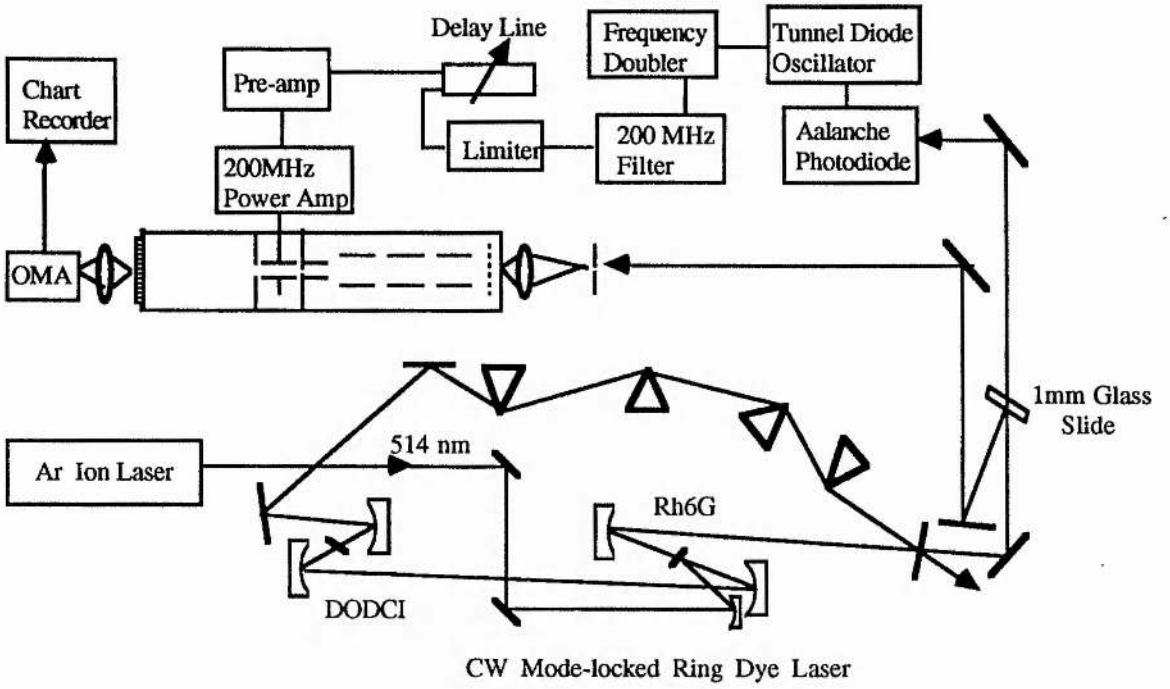

Fig.3.3.1 Experimental setup for the evaluation of synchroscan operation of a femtosecond streak image tube

The 100 MHz electrical signal, detected by a fast avalanche photodiode (with risetime ≤ 250 ps), was frequency-doubled and passed through a 200 MHz bandpass filter. The output from this filter was fed to a limiting amplifier which removes any laser-related amplitude fluctuations. The filtered signal was then fed via a variable delay line to a broadband preamplifier and then further amplified by a narrow band power amplifier tuned to 200 MHz. A stable 200 MHz sinusoidal waveform signal was thus produced with a power of up to 20 W as the deflector input signal. To obtain a sufficiently high deflection voltage at this moderate RF power, the electrical signal was coupled into the deflectors through a resonant LC network which provided a high Q factor (> 50). A maximum deflection voltage was ensured by adjusting the coupling until a minimum standing-wave ratio (SWR) in the transmission line from the amplifier was reached. Two calibration pulses separated by 10 ps were obtained from

the quasi-normal reflections of the two surfaces of a glass slide with 1 mm thickness. An optical multichannel analyser having a silicon-intensified target (SIT) vidicon readout device was lens-coupled onto the phosphor screen of the streak camera for the acquisition of the streaked output.

The tube was operated at an overall voltage of 15 kV and a photocathode electric field strength of 2.1 kV/mm for a photocathode-mesh separation of about 4 mm. The static spatial resolution was measured to be 50 lp/mm at the photocathode (electron-optical magnification of 2) and the deflection sensitivity was measured to be 3.7 cm/kV.

Using this setup, streaked time durations of 1.2 ps (FWHM) were recorded at a RF power of 15W using an optical shutter period of 1 ms to limit low frequency phase noise[3]. Without shuttering, the time resolution was 1.3 ps. When operating at a streak speed of 0.67×10^8 m/s with an input slit size of 5 μm, the theoretically predicted limiting time resolution at the photocathode centre was 600 fs for this tube. Taking into account that a slit size of 20 μm was used in the experiment, the obtained single-shot experimental result of 800 fs time resolution[9] may represent a more realistic limiting time resolution value for this particular tube. The fact that the limiting temporal resolution was not achieved in synchroscan operation of this tube indicated the influence of phase and amplitude noise present in the RF electrical and laser light signals. This will be discussed in the following section.

3.4 Amplitude and phase noise and their effects on the ultimate time resolution in synchroscan streak cameras

Although synchroscan streak cameras do not suffer from space charge effects, the precise integration of streak images on the phosphor screen without any loss of temporal resolution is not possible in practice. The output pulses in a practical mode-locked laser generally exhibit some random changes in pulse amplitude and periodicity and these fluctuations are present as phase noise in the signal. Such noise exists both in the laser pulse signal and in the deflection sinusoidal signal. The key components of the noise include pulse-to-pulse timing jitter (i.e.

phase noise), pulse duration and amplitude fluctuations. As a result, the synchronisation between the light and deflection signal varies with time and thus the ultimate recorded time duration of the streaked image is broadened. In order to reduce these factors and to improve the time resolution of a synchroscan streak camera, it is of vital importance to identify and characterise these optical and electrical noise sources.

The analysis of these noise sources is a rather complex subject and it is not possible to give a detailed treatise here. It should be useful, however, to give a brief introduction because an understanding of the noise sources and the mechanism of their influence on the temporal performance of the system provides some insight as to how such limitations may be alleviated.

3.4.1 The amplitude and phase noise in laser sources

When a completely regular pulse train (with no fluctuations) from a perfectly-mode-locked laser is monitored using a suitable combination of a high-speed photodetector and a spectrum analyser, the output power spectrum comprises a regular series of delta-function-like frequency components at integral multiples of 1/T (c/2L) where T is the pulse repetition, L is the optical path length between the laser cavity mirrors and c is the speed of light. Due to the inherent statistical fluctuations in photoemission and thermal effects on laser cavity length, optical components and environmental noise, the output of a laser system tends to have inherent noise. This noise appears as fluctuations in the laser pulse amplitudes, pulse intervals and pulse durations.

The intensity of a pulse train from a practical mode-locked laser can be approximated as a series of Gaussian pulses with timing and amplitude fluctuations and expressed as

$$I(t) = I_0\, T\, (1 + N(t)) \sum_{n=-\infty}^{n=+\infty} \frac{1}{\sqrt{2\pi}\sigma_t} \cdot \exp\{-[t-T_0-nT-J(t)]^2/2\sigma_t^2\} \qquad (3.4.1)$$

where I(t) is the laser intensity, I_0 is the beam average intensity, T is the pulse repetition period, σ_t is the rms pulse duration, N(t) is the normalised pulse-intensity fluctuations, J(t) is the timing fluctuation of the pulse train and T_0 is the static time offset of the pulse train. The

fluctuations of the pulse duration here are excluded because pulse duration changes are much less significant compared with the timing jitter of the pulse train and also its inclusion adds much complication to the power spectrum analysis[10].

The assessment of amplitude and phase noise in lasers is normally provided by the measurement of the power spectrum of the light or electric signal intensity. In the power spectral density of the pulse train I(t) expressed in (3.4.1), the amplitude and phase fluctuations give rise to some characteristic broadening of the individual frequency components, i.e. the bases of the δ-function components are broadened[11]. The frequency components in the broadened part is the so-called noise sidebands. Under low noise criteria, the noise sidebands caused by amplitude fluctuations are independent of the harmonic number and the noise components induced by timing fluctuations increase quadratically with the harmonic number. Such difference enables one to distinguish the two types of fluctuations and to determine the phase fluctuations by comparing the frequency-domain spectra of the low-order harmonics (dominated by amplitude fluctuations) with those of the higher-order harmonics where phase noise predominates.

The timing jitter existing in the laser signal may cause inaccurate synchronisation between the light pulses and the deflection signal in the characterisation of synchroscan streak cameras such as to degrade the ultimate time resolution. The influence of the amplitude fluctuations in light signals is relatively insignificant except that when the light signal is used as a driving signal, the amplitude noise can be converted into phase noise in the deflection signal.

3.4.2 Amplitude and phase noise in RF electrical signals

Ideally, the deflection signal should be a clean single frequency sinusoidal wave, but, in reality this is not achievable. Apart from the amplitude and phase fluctuations detected from the laser signal, further amplitude and phase noise can be generated in the deflection electronic circuitry itself due to the intrinsic thermal noise, shot noise, flicker noise in the electronic components used such as photodetectors, power amplifiers, resistors and filters. As a result, the spectrum of the deflection signal appears to be the signal frequency with noise sidebands

sitting on a noise floor. Normally, such noise can be treated as narrow bandwidth white noise and each noise sideband can be described as sinusoidal within the system bandwidth.

Consider a single frequency carrier on which some white noise is superposed. Let V_n, ψ be the instantaneous noise amplitude (voltage) and phase of a single sideband. Then the noise sideband at a frequency $(f_0 + f)$ can be written as[12]

$$V_n(t) = V_n \sin(2\pi(f_0 + f)t + \psi) \tag{3.4.2}$$

The total noise in the electronic circuitry bandwidth $\pm$ B centred on f_0 is the integration of $V_n(t)$

$$V_N(t) = \int_{-B}^{+B} V_n \sin(2\pi(f_0+f)t+\psi)\, H(f)\, df \tag{3.4.3}$$

where H(f) is the frequency response function of the electronic system. The deflection signal with noise sidebands can be expressed as

$$V_D(t) = V_s \sin 2\pi f_0 t + V_N(t) \tag{3.4.4}$$

where V_s is the signal voltage amplitude. By expanding the triangular term in $V_N(t)$, equation (3.4.4) can be rearranged as

$$V_D(t) = a \sin 2\pi f_0 t + b \cos 2\pi f_0 t = V_m \sin(2\pi f_0 t + \theta(t)) \tag{3.4.5}$$

where

$$V_m = \sqrt{a^2 + b^2}, \tag{3.4.6a}$$

$$\tan\theta = \frac{b}{a}, \tag{3.4.6b}$$

$$a = V_s + V_n \int_{-B}^{B} \cos(2\pi ft+\psi) H(f) df, \tag{3.4.7a}$$

$$b = V_n \int_{-B}^{B} \sin(2\pi ft+\psi) H(f) df. \tag{3.4.7b}$$

As a result of these noise effects, both amplitude and phase of the deflection signal are modulated and this induces variations in both synchronisation positions and streak speeds for

individual streaks. Consequently, the streaked image positions and spatial widths on the phosphor screen tend to be dispersed and inevitably the ultimate time resolution of the camera is degraded.

3.4.3 Theoretical simulation of the temporal performance of synchroscan streak cameras with amplitude and phase noise

In principle, the quantitative evaluation of the contribution of the noise effects to the temporal performance of a synchroscan streak camera can be carried out by tracing the trajectories of photoelectrons, generated by the light signal expressed in equation (3.4.1), through the tube when a deflection signal expressed as in equation (3.4.3) is applied. However, it tends to be complicated and in practice the procedure can be simplified.

The timing jitter in the input light signal implies an instability in the synchronisation between the light signal and the electric deflection signal and it can be simply included in the deflection signal by adding a fluctuation term to the time variable. In most cases, the distribution of timing jitter can be modelled as a Gaussian function:

$$p(t) = \frac{1}{\tau\sqrt{2\pi}}\exp(-\frac{t_j^2}{\tau^2}) \qquad (3.4.8)$$

where t_j is the arrival time of an individual pulse and τ is rms value of the timing jitter. If the full width at half maximum of the timing jitter is given to be Δt, then $\Delta t=2.36\tau$. The amplitude fluctuations in the light signal should not affect the time resolution since the pulse intensity level is well below the level where space charge effects arise. When the laser signal is detected by a photodetector to produce an electric driving signal, the amplitude noise can be detected and amplified. It can then have significant contribution to the RF noise in the electrical signal and will influence the temporal performance of the entire system. Such effects can be included in the deflection signal expression.

Amplitude and phase noise is commonly measured in spectral power density relative to the carrier power (i.e. in dBc/Hz) using a spectrum analyser and it is a rather complex matter to

determine the instantaneous noise amplitude from spectral power density. To avoid such difficulties, the noise given by equation (3.4.3) can be more simply written as

$$V_N(t) = V_n(t)\sin(2\pi f_0 t + \phi(t)) \tag{3.4.9}$$

Both $V_n(t)$ and $\phi(t)$ are statistical variables. Their instantaneous values are random but in a long time period of observation they follow a certain distribution. The noise voltage amplitude $V_n(t)$ is normally taken as a Gaussian variant which obeys

$$f(V) = \frac{1}{\Delta V_n\sqrt{2\pi}}\exp(-\frac{V_n^2}{2\Delta V_n^2}) \tag{3.4.10}$$

and $\phi(t)$ can be assumed to be uniformly distributed in the 0-2π space. ΔV_n is the root-mean-square (i.e. rms) value of the instantaneous noise voltage. As the fundamental noise in electronic circuitry is set by Johnson (thermal) noise and shot noise both of which are Gaussian white noise, such simplification should be instructive.

The complete form of deflection signal including RF noise as well as timing jitter can then be expressed by

$$V_D = V_m\sin(2\pi f_0(t+t_j)) + \theta(t)) \tag{3.4.11}$$

where t_j represents the timing jitter in laser signal, V_m and $\theta(t)$ are the same as in equation (3.4.6a), (3.4.6b) but a and b are now given as $a = V_s + V_n\cos\phi(t)$, $b = V_n\sin\phi(t)$.

The statistical values of timing jitter, noise voltage amplitude and phase fluctuations can be simulated by using the Monte-Carlo statistical method described in chapter 2. Using the computation methods for tracing electron trajectories described in chapter 2, the temporal performance of Photochron IV streak camera in synchroscan operation has been theoretically evaluated for a variety of signal-to-noise ratio levels (i.e. snr= $20\log_{10}\frac{V_s}{V_n}$ dB, V_s is the RF signal voltage amplitude) and timing jitters, τ. The results are shown in Fig.3.4.1 which were obtained when the tube was assumed to be operating at a sweep speed of 0.677 x10^8 m/s with an input slit of 5 μm at the centre of the photocathode.

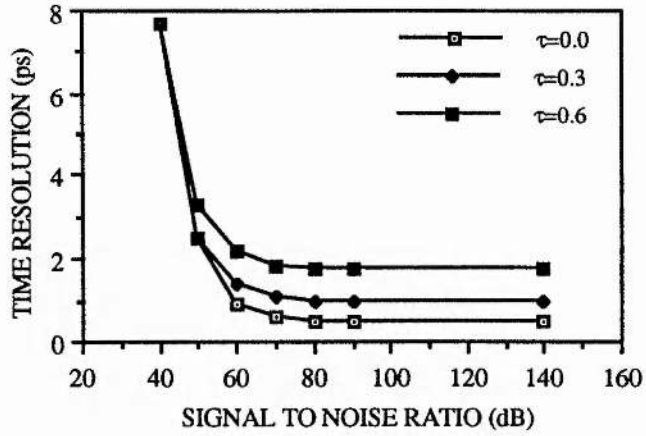

Fig.3.4.1 Time resolution under the influence of RF noise and timing jitter (in ps)

When the signal-to-noise ratio is above 80 dB with no synchronisation timing jitter, the time resolution of the streak tube itself, which is around 600 fs, can be attained. When the SNR decreases to less than 80 dB, the time resolution starts to degrade. For a signal-to-noise ratio of 60 dB to 70 dB, the time resolution is limited to about 1 ps. Considering a slit size of 20 μm with a magnification of x 2 used in the experiments described in section 3.3, this has very close agreement with the experimental results of 1.3 ps. When the synchronisation timing jitter is present, the overall time resolution deteriorates significantly such that the timing jitter becomes the fundamental limitation. For example, when the timing jitter is 0.3 ps, the time resolution is around 1.4 ps for 60 dB to 70 dB signal-to-noise ratio and remains at 1 ps when the SNR is greater than 80 dB. In the experimental setup shown in Fig.3.3.1, the RF signal generator is driven by the laser signal and the RF signal tends to follow the timing jitter in the laser signal to a great extent. Therefore, the synchronisation timing jitter, τ, should be much smaller than the actual timing jitter in the laser signal and t_j in expression (3.4.11) should be negligible. This implies that for this regime further improvement in the instrumental time resolution of synchroscan cameras relies on the SNR enhancement of RF deflection signal and the time resolution improvement of the streak tube.

It should be worthwhile mentioning that the fact that the temporal performance of synchroscan streak cameras varies with the amplitude and phase noise in the laser and electronic sources can be very useful for laser signal noise monitoring[13].

3.4.4 Noise reduction techniques

Apart from synchroscan streak camera measurement, various other time-resolved measurements, including electrooptic sampling[14], photo-enhanced electron-beam probing of integrated circuits[15], carrier dynamics and electromagnetic transient measurements in semiconductors[16], optical waveform sampling[17], and time-resolved spectroscopy[18], also require very stable and low noise mode-locked laser and electronic signal sources. Similarly, in these experiments the instrumental time resolution depends upon the amplitude and phase noise in both laser and electronic systems. Thus the study of the amplitude and phase noise reduction has received considerable attention. A number of attempts have been made to reduce these noise limitations[8,19,20,21,22] and progress in the noise reduction and stabilisation of laser sources has made possible the achievement of subpicosecond time resolution scheme in a synchroscan camera.

Studies[21] have shown that the spurious amplitude noise sidebands observed in a CPM laser source are partly caused by the interaction of the pump laser with the CPM laser and this factor can be removed by operating the pump laser in a pure single longitudinal mode by inserting a single-frequency etalon in the pump laser cavity[23].

Recent work in the phase (i.e. timing) noise characterisation of various ultrashort pulse lasers reported in the literature has provided a better understanding and control of phase noise[24,25,26,27]. One of the phase noise reduction techniques in the laser source is to lock the laser signal frequency to a very stable reference oscillator using electronic feedback and it is claimed that this can reduce the timing jitter of a laser signal to less than 0.3 ps[21,28]. This technique has been used in the experimental evaluation of synchroscan streak cameras where a Photochron IV image tube was employed[19]. In this experiment, the RF signal was generated by a ultrastable quartz oscillator and the laser system was locked on to this oscillator utilising

an electronic feedback circuit. An improved time resolution of 1.05 ps was recorded. For better time resolutions, a further reduction in the timing jitter of the laser signal is required. Although in this arrangement the deflection signal is very stable, the overall time resolution is determined by the timing jitter of the laser signal and hence an improvement of the time resolution is entirely dependent upon the stabilisation of the laser signal.

Difficulty in the laser stabilisation regime results from the amplitude noise in the laser pulse and noise inherent in electronic components such as photodetectors, amplifiers and mixers. The amplitude noise from the laser signal can be detected, amplified and converted into phase noise in the phase detector and this unwanted noise signal together with the intrinsic electronic noise adds to the error signal fed to the cavity control electronics. As a result, the error signal fed to the laser cavity no longer solely represents phase noise in laser signal and this can lead to overcompensation for the phase noise of the laser cavity thereby resulting in timing jitter. To alleviate such problems, it is desirable to choose photodetector, amplifier and mixer types that offer a minimum noise figure. It is also essential to use a pump laser with minimum amplitude noise level or to use noise reduction techniques to eliminate the amplitude noise before the signal is fed to the mixer. Such considerations should be made in the future development of synchroscan streak cameras in addition to the design of a streak image tube having a better time resolution.

3.5 Multipacting and deflector design aspects

3.5.1 Multipacting

In the synchroscan operation of streak image tubes, glowing discharges may occur in the deflection region when a high RF voltage at a frequency of a few hundred MHz is applied to the deflection system[29]. Such effects give rise to an increased background noise accompanying a RF power loss which degrades the signal-to-noise ratio and induces additional RF phase noise. The phenomenon is called multipacting and is caused by secondary emissions at the electrode surfaces between which the electron transit time is an odd number of half cycles of the RF signal[30]. The initiation of multipacting occurs when the following conditions are

satisfied: (i) the electron mean free path is greater than the electrode separation, (ii) the secondary emission ratio at the electrode surface is greater than unity, (iii) the frequency, electrode separation and applied RF potential fall within ranges appropriate to the required electron dynamics. Due to the ionisation (with luminescence) of gas molecules adhering on deflection plate or insulator surfaces by electron bombardment, an increase in background noise and reduction in the life time of the tube result in. More importantly, the accompanying RF power loss dissipates as heat in the electrode surfaces and the induced temperature variation detunes LC resonate circuit due to the 0-50° lag in the phase of the electron current. Consequently, the deflection sweep speed can be influenced.

Such defects can be overcome by suppressing or avoiding multipacting. Several methods have been used[29,31] which include biasing one of the electrodes with a DC potential, imposing a DC magnetic field orthogonal to the RF electric field, letting the multipacting discharge burn until secondary-emission ratio δ falls low enough that the RF potential across the discharge can rise beyond the multipacting zone, applying the RF power abruptly enough that the voltage rises above the multipacting zone before the multipacting current has time to build up, making the secondary emission coefficient $\delta < 1$ either by a proper choice of electrode material or by coating the electrodes with low secondary emission material such as carbon, or reducing the electrode separation below that for half cycle cutoff or subdividing the electrode gap by inserting one or more thin insulator baffles separated by distances less than that for half cycle cutoff. The first four methods require additional equipment and are incompatible with our particular application. Thus the last two become the possible choices. To achieve a design of deflector system which is immune to multipacting problem, it is necessary to understand the basic mechanism of multipacting so as to determine the electrode gap value which can avoid multipacting.

3.5.2 Multipacting theory

To carry out a quantitative analysis of the multipacting discharge, some simplifications[32,33] need to be made. First, it is assumed that the multipacting is the discharge between two parallel surfaces separated by a distance, d, and driven by an RF signal with a voltage amplitude, V_{rf},

at frequency, ω (= $2\pi f$). This will allow the simulation of the motion of electrons. Second, the surfaces are supposed to have identical secondary emission characteristics so that the critical impact voltage for multipacting initiation can be taken as single-valued. When the secondary emission velocity, v_0, is taken into account, it can be treated as a single-valued constant over the range of impact voltages for which the secondary emission ratio δ is greater than unity.

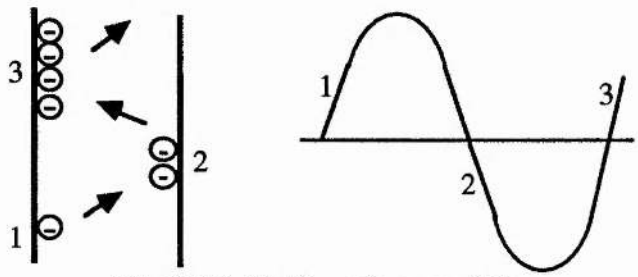

Fig.3.5.1 Multipacting conditions

According to these assumptions, if an electron is released from the left surface shown in Fig.3.5.1 with a velocity v_0 at phase Φ into an RF field $V(t) = V_{rf} \sin(\omega t)$, the equation of the motion of the electron can be expressed as

$$m\frac{d^2x}{dt^2} = e\frac{V_{rf}}{d}\sin(\omega t + \Phi) \tag{3.5.1}$$

where x denotes the position coordinate of the electron in the gap. The integration of this equation gives the expression for the velocity of the electron between the two electrode surfaces as:

$$\frac{dx}{dt} = \frac{e\,V_{rf}}{m\,\omega d}(\cos\Phi - \cos(\omega t)) + v_0 \tag{3.5.2}$$

A second integration produces the position expression for the electron between the surfaces:

$$x = \frac{e\,V_{rf}}{m\,\omega^2 d}((\omega t-\Phi)\cos\Phi - \sin\omega t + \sin\Phi) + \frac{v_0}{\omega}(\omega t-\Phi) \tag{3.5.3}$$

If the transit time to the right surface in Fig.3.5.1 is to be N half cycles (N odd), i.e. $x = d$ at $\omega t = N\pi + \Phi$, then equation (3.4.3) can be rewritten as

$$V_{rf} = \frac{m}{e}\frac{\omega d(\omega d - N\pi v_0)}{N\pi\cos\Phi + 2\sin\Phi} \tag{3.5.4}$$

and from equation (3.5.2), the impact velocity on the right surface can be obtained as:

$$v_i = \frac{2e}{m}\frac{V_{rf}}{\omega d}\cos\Phi + v_0 \tag{3.5.5}$$

which can also be expressed, using (3.5.4), as

$$v_i = \frac{2\omega d\cos\Phi}{N\pi\cos\Phi+2\sin\Phi} + v_0 \tag{3.5.6}$$

When $v_0 = 0$, the impact velocity can be conveniently converted into the equivalent impact voltage as

$$V_i = \frac{2V_{rf}\cos^2\Phi}{N\pi\cos\Phi+2\sin\Phi} \tag{3.5.7}$$

The minimum RF voltage necessary to sustain multipacting will thus occur at the phase that maximises $N\pi\cos\Phi + 2\sin\Phi$ regardless of the value of v_0, that is, $\Phi = \arctan\frac{2}{N\pi}$. The maximum RF voltage at $v_0 = 0$, which gives rise to multipacting, appears at $\Phi = 0$ where a characteristic voltage V_{rf0} is deduced as

$$V_{rf0} = \frac{e}{m}\frac{\omega^2 d^2}{N\pi} \tag{3.5.8}$$

When emission velocity v_0 is non zero, the emission phase angle Φ which leads to a maximum RF voltage for multipacting occurance has a negative value. That means that the initial electric force opposes the motion of the electrons in the x direction (see Fig.3.5.2 below). Their initial velocity v_0 takes them a little distance against this force and they then turn

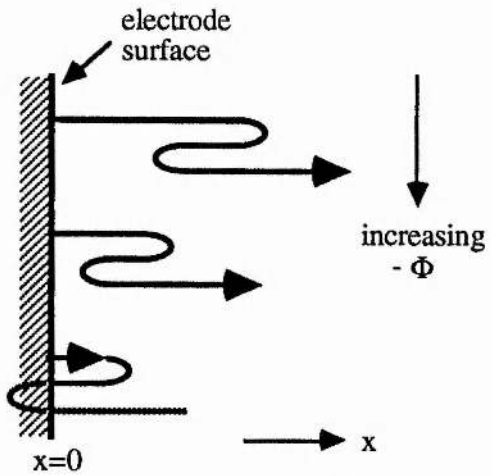

Fig.3.5.2 The propagating path of electrons starting at negative angles

back, accelerating towards x=0 until the force reversal decelerates them and turns them finally to the proper direction. The largest admissible value of $-\Phi$ is that which gives this second turning point at x=0. For larger values the second turning point is for negative values of x which being behind the plate cannot be reached. The electrons in these cases return to the plate with low velocity and are therefore lost. For the limiting case, electrons for which at time $t = -\frac{\Phi}{\omega}$, x=0 and $\frac{dx}{dt} = v_0$ must, at a later time $t = -\frac{\Phi'}{\omega}$, have $x = 0$ and $\frac{dx}{dt} = 0$ which corresponds to the second turning point. This leads to the following conditions:

$$(\Phi' + \Phi)\cos\Phi' = \sin\Phi' + \sin\Phi \tag{3.5.9}$$

$$v_0 = \frac{e\,V_{rf}}{m\,\omega d}(\cos\Phi' - \cos\Phi) \tag{3.5.10}$$

and from (3.5.9) and (3.5.10), we have

$$k = \frac{v_i}{v_0} = \frac{\cos\Phi' + \cos\Phi}{\cos\Phi' - \cos\Phi} \tag{3.5.11}$$

From (3.5.9) and (3.5.11), Φ can be deduced as:

$$\Phi = \sqrt{\frac{1}{A^2} - 1} + \frac{\sin\Phi}{A} - \arccos A \tag{3.5.12}$$

where

$$A = \frac{k+1}{k-1}\cos\Phi$$

$$k = \frac{v_i}{v_0}$$

where Φ is absolute value. From (3.5.5), we have

$$v_i = \frac{\eta\,V_{rf}}{\pi\,df}\frac{k}{k-1}\cos\Phi \tag{3.5.13}$$

This means that for a fixed k and v_0, the impact velocity, v_i, is determined by the RF voltage V_{rf}, the distance between the two surfaces d and the RF frequency f for a certain initial angle value Φ. The RF voltage V_{rf} can also be expressed as:

$$V_{rf} = \frac{\omega^2 d^2}{\eta\left(\frac{k+1}{k-1}N\pi\cos\Phi + 2\sin\Phi\right)} \tag{3.5.14}$$

The minimum V_{rf} will occur when the numerator is maximised at

$$\Phi_{min} = \text{arctg}\left(\frac{k-1}{k+1}\frac{2}{N\pi}\right) \tag{3.5.15}$$

The initial phase angle Φ_{max} where maximum V_{rf} for multipacting emerges can be calculated from equation (3.5.12) by using iterative techniques. Within the initial phase angle range Φ_{min} to Φ_{max}, the minimum and maximum RF voltages for multipacting are determined by the minimum and maximum impact voltages required for the material secondary emission coefficient δ to be greater than unity.

3.5.3 Calculated results and considerations for the deflector construction

On the basis of the above theory, calculations have been made for the determination of multipacting zone and the results are summarised in Fig. 3.5.3. It can be clearly seen that multipacting only occurs within certain regions of RF voltages for a range of RF frequency and

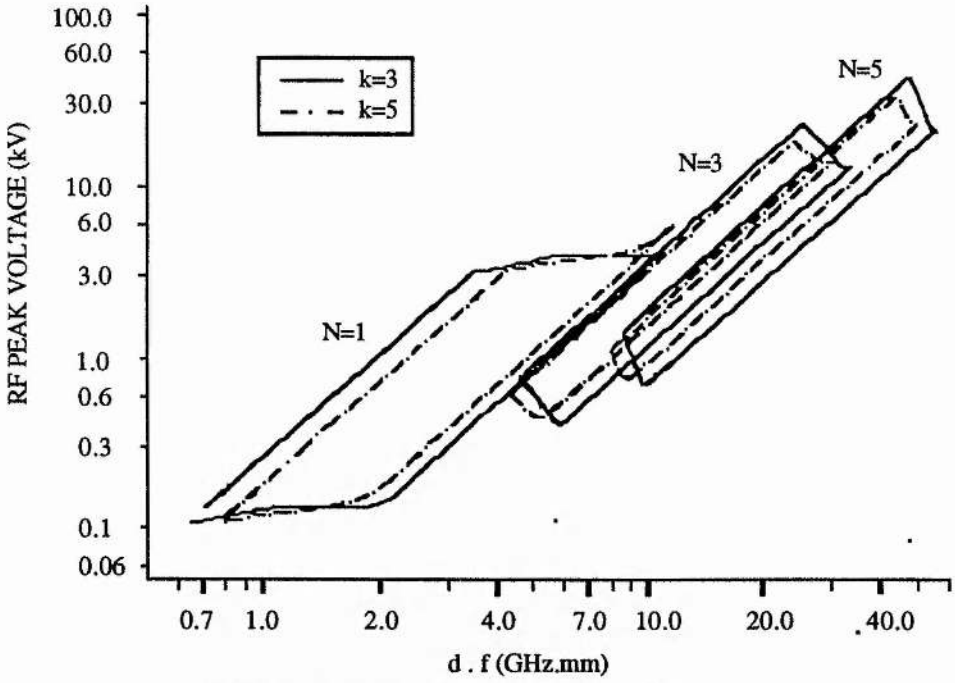

Fig.3.5.3 Multipacting zone of deflection voltage, frequency and electrode surface gaps

electrode separation combinations. For the higher harmonics (i.e. N> 1), the RF multipacting voltage zone moves to a higher value and thus the fundamental harmonics sets the major

multipacting conditions. If multipacting is to be avoided by reducing the electrode separation, judgement needs to be made according to the fundamental harmonic multipacting zone. For example, multipacting can occur in the distance region between 3.7 mm and 38.5 mm for the fundamental harmonic of a 200 MHz RF signal and 1.5 mm to 15.4 mm for 500 MHz RF signal in the impact voltage range between 150 V (the minimum impact voltage to cause $\delta > 1$ among Al, Au, Ag, Cu) and 2 kV. Therefore, it is necessary to design the deflection configuration so that the distances between surfaces can be arranged beyond the multipacting distance region for RF frequency up to 500 MHz. This should be achievable by considering that it is unlikely for the RF voltage to be beyond 2 kV in our application and thus electrical breakdown should not become problematical even at highest required RF deflection voltage. To reduce the possibility of multipacting discharge to minimal, photocathode transfer technology is preferable for the photocathode processing so that contamination in the streak tube can be effectively prevented. In our particular application, the deflector plate material is required to have high conductivity and minimum permitivity so as to produce maximum deflection voltage at minimum RF power loss. This is desirable to overcome frequency drifting caused by deflection system heating effects due to excess power dissipation. To satisfy this requirement, copper coated with silver can be chosen.

3.6 Summary

The outstanding advantages of synchroscan streak cameras over single-shot ones have raised the necessity of improving the performance of such instruments so that they can find a wider range of applications in related research areas. The main objectives in this chapter have been to describe the limiting factors that determine the overall performance of synchroscan cameras and to seek possibilities of improvement.

Theoretical simulations of the temporal performance of Photochron VI streak tube under varied noise conditions have been carried out and have indicated that in synchroscan operation, the main limitations are imposed by amplitude and phase noise in laser source and electronic deflection signal and part of the limitations comes from the streak tube itself. When using a laser signal as the driving signal for the electronic signal generator, the amplitude and phase

noise produced by the electronic circuit are the crucial factors which limit the instrumental time resolution whereas when using the electronic feedback laser stabilisation regime where a very stable electronic signal is taken as the reference which has negligible noise, the timing jitter in laser signal becomes the vital factor. The achievement of a time resolution of better than 500 fs requires a new design of a streak tube with a time resolution better than 300 fs. To this requirement must be added a laser system having low amplitude and phase noise together with electronic circuitry of low noise. For instance, when using the laser signal as a driving signal to the electronic circuitry, a signal-to-noise ratio of better than 70 dB in the deflection signal is desirable. If a quarz oscillator signal is used as a reference signal for active stabilisation of the laser by means of electronic feedback technique, then the requirement for a timing jitter of less than 200 fs in the laser signal as well as a signal-to-noise ratio of over 100 dB in the deflection signal must be satisfied. At this stage, it is difficult to judge which regime can provide better results and it depends upon the availability of low jitter laser sources and low noise photodetectors, amplifiers. Further studies are still required.

When a high power RF signal is applied to the deflectors, multipacting may occur which induces increased background noise and power loss. To prevent such effects, the conditions that initiate multipacting have been investigated by theoretically simulating the behaviour of secondary electrons between two surfaces. Calculations have indicated that it is possible to avoid such effects by carefully manipulating the separations between electrodes and ground surfaces in the deflection region and by preventing any possible contamination of the electrodes.

3.7 References

1 Sibbett W, Proc. 15th ICHSPP, SPIE Vol. 348, pp. 15-26 (1982)

2 Chen J, Li D, IEEE J. Quantum Electron., Vol. 22, No. 1, pp. 153-156 (1986)

3 Finch A, Sleat W E, Sibbett W, Rev. Sci. Instrum., Vol. 60, No. 5, pp. 839-844 (1989)

4 Finch, A., Liu, Y., Niu, H., Sleat, W.E., Sibbett, W., Yang, Q.L., Zhang, H., Proc. 18th ICHSPP, SPIE Vol. 1032, pp.622-627 (1988)

5 Adams M C, Sibbett W, Bradley D J, Opt. Commun., Vol. 26, pp.273-276 (1978)

6 Hadland R, Helbrough K, Huston A E, Adams M C, Sibbett W, Salour M M, Proc. 13th ICHSPP, pp. 443-446 (1978)

7 Niu H, Liu Y P, Yang Q L, Proc. 18th ICHSPP, SPIE Vol. 1032, pp.263-268 (1988)

8 Finch A, Liu Y, Sleat W E, Sibbett W, Chen G, Proc. 18th ICHSPP, SPIE., Vol. 1032, pp. 97-104 (1988)

9 Baggs M R, Eagles R T, Margulis W, Sibbett W, Sleat W E, Adv. Electronics & Electron Physics, Vol. 64B, pp.617-625 (1984)

10 Kluge J, Wiechert D, Linde D von der, Opt. Commun., Vol. 54, No. 4, pp. 271-277 (1984)

11 Linde D von der, Applied Physics B, Vol. 39, pp. 201-217 (1986)

12 Robins W P, Phase Noise in Signal Sources, IEE Telecommunications Series 9, Peter Peregrinus Ltd., London, 1982

13 Spence D E, PhD Thesis, Department of Physics and Astronamy, University of St. Andrews, (1992)

14 Valdmanis J A, and Mourou G, IEEE J. Quantum Electron., Vol. 22, pp. 69-78 (1986)

15 May P G, Halbout J M, and Chiu G L-T, IEEE J. Quantum Electron., Vol. 24, pp. 234-239 (1988)

16 Panchhi P S, and Van Driel H M, IEEE J. Quantum Electron., Vol. 22, pp.101-107 (1986)

17 Weisenfeld J M, Tucker R S, Downey P M, and Bowers J E, Electron. Lett., Vol. 22, pp. 396-397 (1986)

18 Kash J A, Tsang J C, and Hvam J M, in Picosecond Electronics and Optoelectronics, G. A. Mourou, D. M. Bloom and C.-H. Lee, Eds. New York: Springer-Verlag, pp. 87-90 (1985)

19 Walker D R, Crust D W, Sleat W E, Sibbett W, IEEE J. Quantum Electron.. Vol. 28, No. 1, pp. 289-296 (1992)

20 Harvey G T, Heutmaker M S, Smith P R, Nuss M C, Keller U, Valdmanis J A, IEEE J. Quantum Electron., Vol. 27, No. 2, pp.295-301 (1991)

21 Nuss M, Keller U, Harvey G T, Heutmaker, U., Smith, P.R., Opt. Lett., Vol. 15, No. 18, pp. 1026-1028 (1990)

22 Rodwell M J W, Bloom D M, Weingarten K J, IEEE J. Quantum Electron., Vol. 25, No. 4, pp. 817-827 (1989)

23 Nuss M C, Keller U, Harvey G T, Heutmaker M S, Smith P R, Opt. Lett., Vol. 15, No. 18, pp. 1026-1028 (1990)

24 Wilson J P, Sibbett W, Sleat W E, Opt. Commun., Vol. 42, No. 3, pp. 208-210 (1982)

25 Keller U, Soccolich C E, Sucha G, Islam M N, Wegener M, Opt. Lett., Vol. 15, No. 17, pp.974-976 (1990)

26 Keller U, Li K D, Rodwell M, Bloom D M, IEEE J. Quantum Electron., Vol. 25, No. 3, pp.280-288 (1989)

27 Yuan R, Taylor H F, IEEE J. Quantum Electron., Vol. 28, No. 1, pp.109-117 (1992)

28 Rodwell M J W, Weingarten K J, and Bloom D M, Baer T, Kolner B H, Opt. Lett., Vol. 11, No. 10, pp. 638-640 (1986)

29 Kinoshita, K., Shinoda, K., Suzuki, Y., Proc. 16th ICHSPP, SPIE Vol. 348, pp. 227-230 (1982)

30 Hatch A J, Williams H B, J. Appl. Phys., Vol. 25 (4), pp. 417-423 (1954)

31 Hatch A J, Nucl. Instrum. & Methods Vol. 41, pp. 261-271 (1966)

32 Rodney, J., Vaughan, M., IEEE Transactions on Electron Devices, Vol. 35, No. 7, pp. 1172-1180 (1988)

33 Gill E W B, and Engel A von, Proc. Roy. Soc. (London), Vol. A192, pp. 446-463 (1948)

Chapter 4

THE DESIGN AND EVALUATIONS OF PHOTOCHRON V STREAK CAMERA

4.1 Introduction

Despite having limiting time resolutions somewhat inferior to those of nonlinear optical techniques, streak cameras still play a very important role in the time-resolved measurements of ultrafast light phenomena due to their outstanding ability to provide direct, linear spatial and temporal information over a wide spectral range. In research areas such as laser fusion, nuclear physics, plasma physics and non-repetitive light phenomena, a single-shot streak camera offers unique advantages as it provides linear, direct, temporal and spatial or spectral-resolved measurements[1,2]. In other applications such as the studies of mode-locked lasers, optical communications, photobiology, biochemistry, biophysics, solid state physics and so on where the input light signal is repetitive and often very weak for other diagnostic techniques, synchroscan operation of a streak tube becomes a very attractive technique[1,2,3].

Although the Photochron IV streak camera has demonstrated the best synchroscan results reported to date[4,5] the progress in laser noise reduction has indicated that the time resolution inherent in the streak tube itself has become one of the limiting factors to the entire system performance. Single-shot streak cameras have shown time resolution limits of 300 fs in experimental[6] and 600 fs in commercial[7] cameras, thus it is necessary to design a new streak tube with a time resolution that is more compatible with recent developments in mode-locked laser sources. The design of such a new streak tube has been carried out by means of the computational methods described in chapter 2 and the tube is designated as Photochron V. Emphasis has, however, been directed towards the practical considerations associated with factors such as multipacting problems, space-charge effects, robust construction and flexibility

of operation modes, so that a versatile and rugged camera system can be developed as an optical oscilloscope with picosecond and femtosecond time resolutions. When combined with CCD readout technology it will be compatible with computer-based data acquisition and analysis techniques if required. It is, therefore, to be expected that this type of instrument will become quite commonplace within the next generation of standard ultrahigh time resolution diagnostics.

4.2 Design considerations

The analysis of existing streak image tubes, as described in previous chapters, has shown the main factors which must be considered if a better time resolution is to be achieved. These factors include time dispersions in the photocathode-mesh region caused by initial photoelectron energy spread and initial angle distributions, time distortions and spatial aberrations in the focusing system, low deflection sensitivity, space charge effects in single-shot operation, amplitude and phase noise in synchroscan operation.

Time dispersions in the photocathode-mesh region can be reduced by increasing the electric field at the photocathode. Care must be taken in doing this because a high electric field may induce considerable field emission from the photocathode which will give rise to significant background noise. Also the actual electric field, that can be achieved, is very much limited by practical construction difficulties due to electrical discharges. In practice, a gated voltage between the mesh and photocathode will allow electric fields up to 10 kV/mm to be applied provided that the photocathode-mesh electrodes are suitably constructed.

The minimisation of the time dispersions in the focusing region between mesh and anode aperture requires the optimisation of the arrangement of the operating voltages and electrode structure parameters so that the time dispersions, distortions and spatial aberrations are reduced as much as possible. With regard to single-shot operation, the transit time of photoelectrons in this region should be minimal so as to alleviate severe space-charge effects. This implies the reduction of the system length and/or an increase of the overall operating voltages. Inevitably, by doing this, other problems will arise. For instance, high operating voltages result in low

deflection sensitivities and short focusing system length often accompanies high optical magnification and small photocathode working area. To maintain a high deflection sensitivity as well as a short transit time, the anode voltage should be kept relatively low (eg. 10 kV) while the rest of the operating voltages are increased.

In synchroscan operation, a high frequency, high voltage deflection signal is required to achieve the necessarily high streak speed if a femtosecond time resolution is desired. The most effective and commonly-used way to acquire this is to employ the metal-plate deflectors together with a inductor and a tunable capacitor to form a high-Q LC resonant circuit. A high deflection sensitivity demands a low anode voltage, long drift-space length and optimum design of deflection system structure with minimum fringing-fields. Unfortunately, long drift-space length results in a large magnification which degrades the entire dynamic range. Considering the design of the deflector structure, the position of the electron beam waist should be adjusted to be close to the entrance of the deflector so that fringe-field effects can be minimised and the separation between deflector plates can be made minimal. Obviously, a small separation between the deflector plates can provide high deflection sensitivity but it tends to restrict the photocathode effective working area and also it may induce stronger fringe-fields. Longer deflector plates will increase the deflection sensitivity but again it leads to a narrower frequency bandwidth and more severe fringe-field effects. Thus compromise should be made between these conflicts. The diameter of the anode aperture should be as small as possible to minimise the field interaction between focusing and deflection regions which may deteriorate the ultimate dynamic spatial resolution. To reduce the fringing-fields at the ends of the deflector plates and to prevent possible multipacting between electrode surfaces, the anode aperture and rear aperture should be as close as practicable to the ends of the plates. The possible fringing-fields along the sides of the deflector plates can be avoided by using adequately-broad deflector plates without giving rise to an unnecessarily large capacitance which could restrict the upper frequency limit. For single-shot operation, a TWD system should be used to provide high deflection sensitivity and broad frequency bandwidth with minimal fringing-field effects.

4.3 Tube description

On the basis of the considerations described in the previous section, it has been possible to design a new streak image tube. Its basic structure is similar to that of a Photochron IV streak image tube in that it comprises a photocathode, acceleration mesh, four cylindrical electrodes, anode aperture, a deflection system, rear aperture and phosphor screen. It is designed to provide a femtosecond time resolution and more flexible applications.

4.3.1 Focusing system

For synchroscan operation, space-charge effects are no longer the limiting factor and thus the operating voltages can be relatively low which allows high deflection sensitivity. The overall operating voltage of Photochron V has been selected to be 10 kV and other parameters are as shown in Fig.4.3.1.

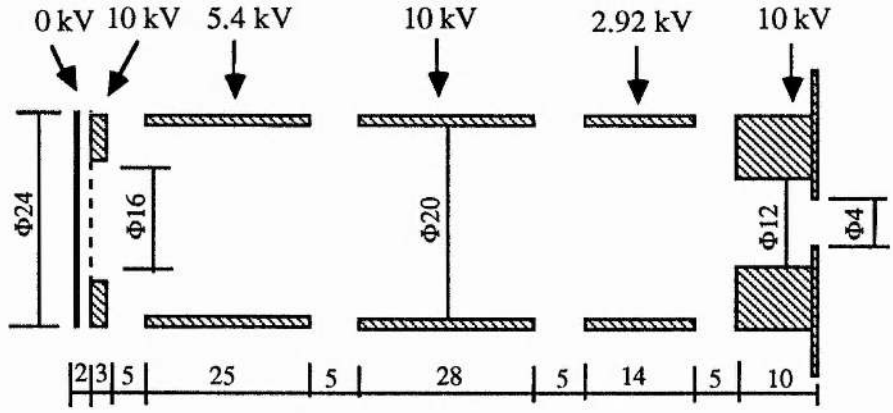

Fig.4.3.1 The configuration of the focusing system

An electric field of 5 kV/mm at the photocathode is provided by applying a 10 kV voltage across a 2 mm gap between the planar photocathode and accelerating mesh electrode. The diameter of the anode aperture is 4 mm. The total length of the tube and the transit time of photoelectrons from photocathode to anode aperture are 300 mm and 2 ns respectively whereas the total length of Photochron IV is 400 mm with 3.5 ns transit time at 15 kV overall operating voltage. These differences are especially significant when the tube is used for single-shot streak operation.

The static spatial resolution is calculated to be better than 70 lp/mm at the centre of the phosphor screen and 40 lp/mm at the edge (referred to photocathode and excluding input slit size) and the electron-optical magnification is 3. The working diameters on the photocathode and on the phosphor screen are Φ6 mm and Φ40 mm respectively.

The influential factors, that determine the temporal performance of this section, include the initial energy and angle spreads, electric field strength at the photocathode and the configuration of the electron-optical focusing lens. Fig. 4.3.2 shows the time dispersions at mesh and anode position versus photocathode electric field values for anode voltage of 10 kV with 0.2 eV rms initial energy spread of photoelectrons.

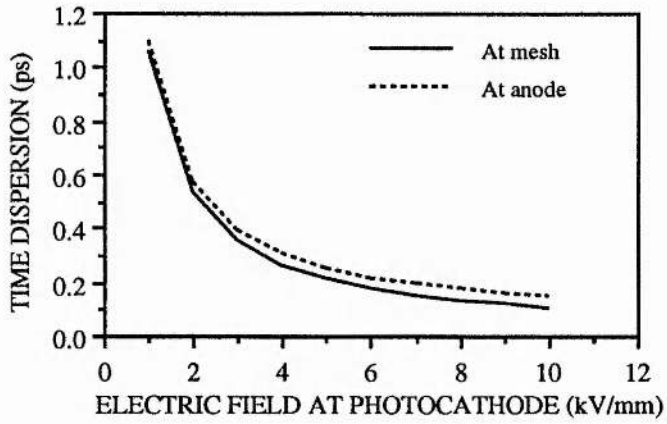

Fig. 4.3.2 Time dispersions at different electric fields at the photocathode

The fact that two curves are very close implies that the time dispersions are mainly induced in the photocathode-mesh region and the focusing system has been adequately optimised. It also suggests that the increase of the photocathode electric field is an effective way to improve the temporal performance of such a tube. For the following performance computations, the photocathode electric field has been chosen to be 5 kV/mm because it can be readily achieved in practice.

Fig.4.3.3 demonstrates the initial energy spread-dependence of the temporal performance of this section.

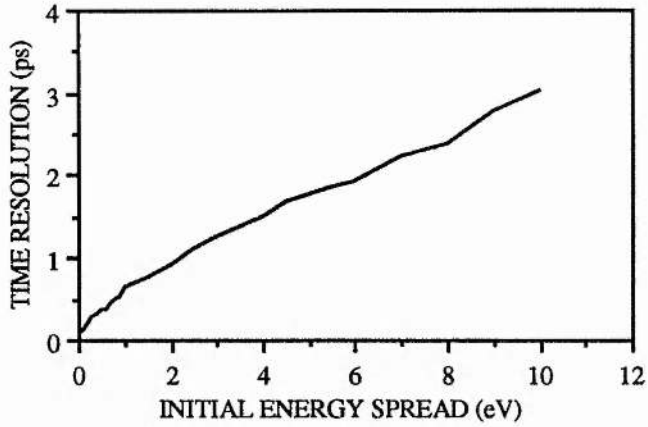

Fig.4.3.3 Time resolution versus initial energy spread

It is seen clearly that the time resolution of this section increases as the initial energy spreads increase. Normally for a given type of the photocathode, the initial energy spread of photoemission is dependent upon the wavelength of the light sources, but it is possible to minimise the initial energy spread value by choosing a thin photocathode having a large energy bandgap at the expense of spectral sensitivity. For NIR light sources, S1 type photocathodes are commonly used and the initial energy spreads are typically 0.1 ~ 0.2 eV for wavelength around 1.06 μm. In this case, the theoretically-predicted time resolution can be better than 200 fs. For visible illuminations, multialkali type of photocathodes are often chosen and they give initial energy spreads of 0.2 ~ 0.6 eV. Thus the time resolution varies from 250 fs to 500 fs. For UV and X-ray illuminations, both metal type and semicondutor type photocathodes can be used and the initial energy spreads are rather large (typically 0.6 ~ 10 eV) depending on the type of photocathode used, so their predicted time resolutions can be in the 500 fs to 3.5 ps range.

Under the operating conditions of 5 kV/mm photocathode electric field and 0.2 eV initial energy spread, the time dispersions and distortions at the mesh and anode electrodes of this tube are calculated and listed in Table 4.4.1. For comparison, data for the Photochron IV tube under the same operating conditions are listed Table 4.4.2 where r stands for the object height, t_{disp} is time dispersion and t_{dist} denotes time distortion.

Table4.4.1 Time dispersions and distortions of Photochron V

h(mm)	0	1	2	3	4	5
t_{disp}(ps)	0.255	0.259	0.261	0.26	0.264	0.293
t_{dist}(ps)	0.	0.38	1.52	3.45	6.17	9.76

Table4.4.2 Time dispersions and distortions of Photochron IV

h(mm)	0	1	2	3	4	5
t_{disp}(ps)	0.265	0.347	0.43	0.51	0.648	0.8
t_{dist}(ps)	0.	0.2	0.826	1.86	3.3	5.2

It is clear that the new streak tube has advantages of uniform and low time dispersions, high deflection sensitivity and shorter transit time compared to the Photochron IV. Its greater time distortions should be easily corrected by means of post-data processing using modern readout system or by specially designing an input optical lens with time-distortion compensation.

When used for single-shot operation, further enhancement of dynamic range is possible by increasing the operating voltages proportionately up to 18 kV. By doing this, the transit time of the photoelectrons can be further reduced without altering the focusing conditions. This may degrade the deflection sensitivity but it is still higher than that of the Photochron IV streak tube.

4.3.2 Deflection system

For the synchroscan tube version, the deflector system consists of two parallel metal plates with 23 mm length and 20 mm width separated by a 3 mm gap. The anode and rear apertures are located 1.5 mm from the ends of the deflector plates. The configuration of the deflection system is displayed in Fig.4.3.4 and it has been designed to provide optimised deflection performance for frequencies up to 500 MHz at anode voltages ranging from 5 kV to 10 kV as illustrated in Fig.4.3.5.

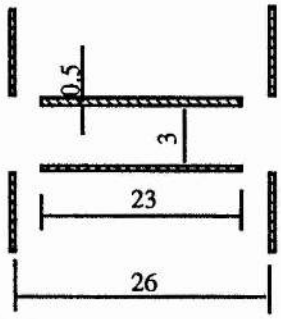

Fig.4.3.4 The configuration of the deflection system

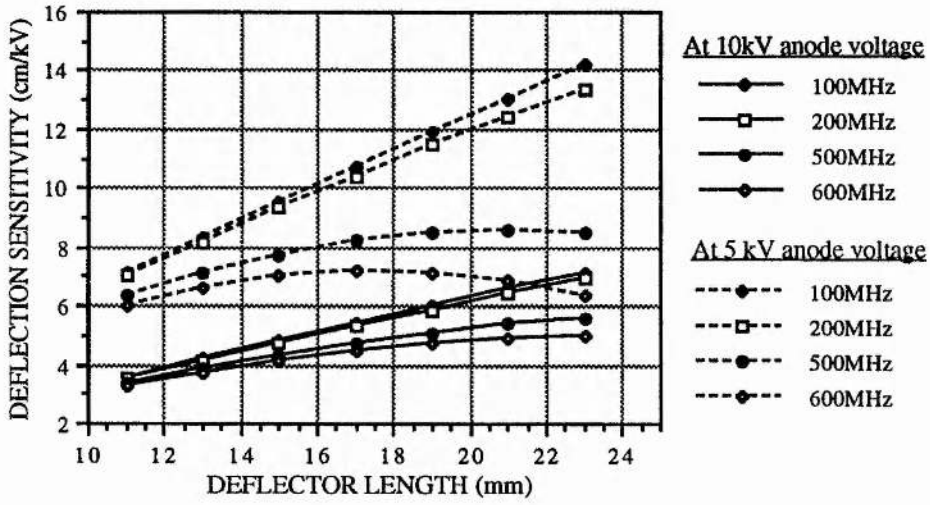

(a) For frequencies 100 MHz to 600 MHz

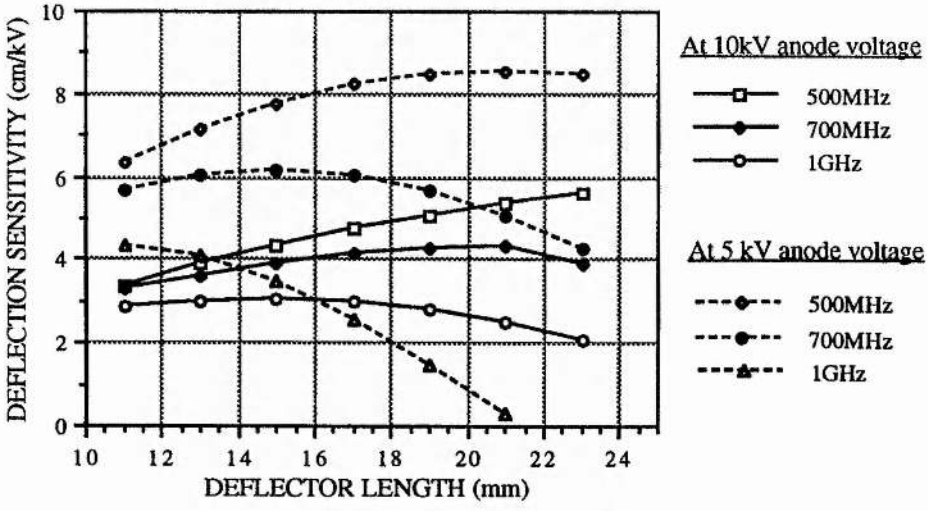

(b) For frequencies 500 MHz to 1GHz

Fig.4.3.5 Deflection sensitivity versus deflector length and frequency

The deflection sensitivity is estimated to be 7.8 cm/kV at 10 kV anode voltage and 5.2 cm/kV at 18 kV anode voltage (3 cm/kV in Photochron IV). The transit time of photoelectrons propagating through the deflector is about 440 ps which implies a synchroscan deflection speed nonlinearity of 1.3% at 200 MHz and 8% at 500 MHz.

For single-shot operation, this metal-plate deflector can be used but to achieve a better performance, travelling-wave deflectors may be a preferred choice which will be discussed later in chapter 5.

4.4 Theoretically-predicted dynamic performance characteristics

Under streak operating conditions, the time resolution of the streak tube may deteriorate due to additional factors such as input slit size, deflection image quality, deflection fringe-field effects and the conversion of spatial aberrations inherent in the focusing system to temporal dispersions by the deflector. To understand how these parameters interact with each other and have a thorough knowledge of the mechanism of the streak tube in dynamic operation, the evaluation of the spatial and temporal performance of Photochron V tube with metal-plate deflector under various realistic operating conditions have been investigated. To produce generalised performance data, the streak operation in the following evaluations has been assessed by applying a linear voltage ramp to the deflector system of the streak tube (for synchroscan operation, the nonlinearity of streak speed could be slightly worse due to the use of sinusoidal deflection waveform but should be insignificant).

The calculated spatial and temporal MTFs of the Photochron V tube are displayed in fig.4.4.1 which were obtained for a zero input slit width at a streak speed of 2.86 $x10^8$ m/s and an initial rms energy spread of 0.2 eV from the centre of the photocathode. The spatial MTF results are referred to the non-streak direction. When the influence of the phosphor screen is excluded, the limiting spatial resolution of the tube can be higher than 100 lp/mm on the phosphor screen. The inclusion of a P11 phosphor screen restricts the spatial resolution to 50 lp/mm.

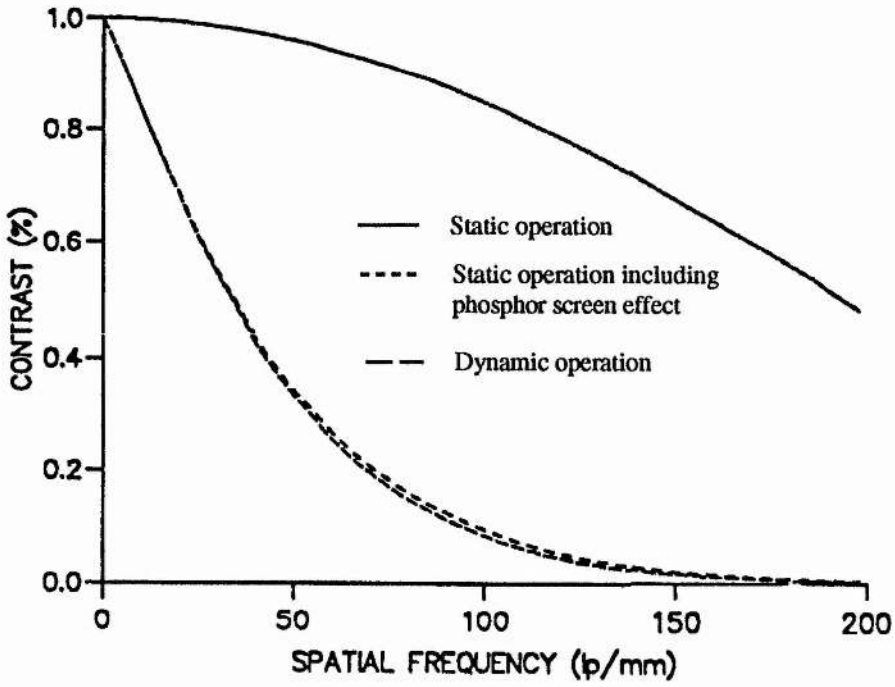

(a) Spatial MTF

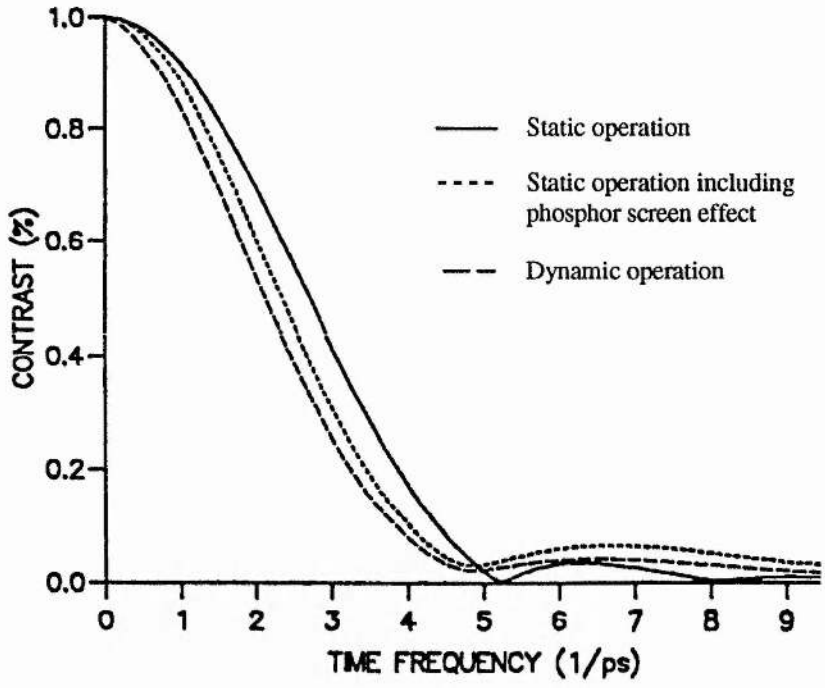

(b) Temporal MTF data

Fig.4.4.1 The calculated spatial and temporal MTFs of the Photochron V streak tube

The dynamic operation of this tube has little influence on the spatial resolution in the non-streak direction. Obviously, in practice, the input slit always has a definite width, for example, 5μm ~

40μm, which will affect the resultant temporal resolution. Generally speaking, at a higher streak speed the slit width has relatively less influence. However, the increase of streak speed will cause other factors to emerge and this can be clearly seen in fig.4.4.2 which displays the time resolution variation with streak speed for different input slit sizes.

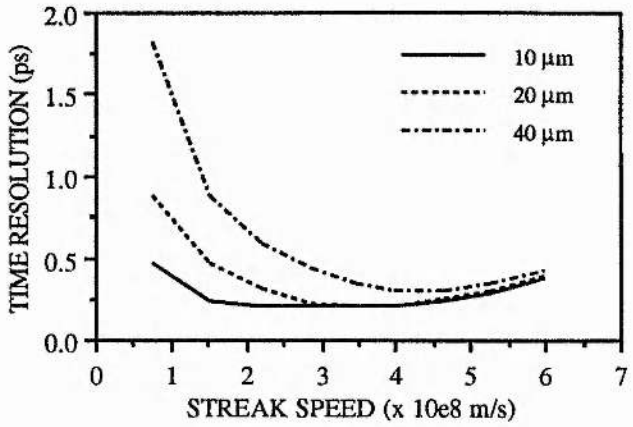

Fig.4.4.2 Time resolution as a function of streak speed for three input slit sizes

It can thus be appreciated that the increase of streak speed does not always improve the time resolution and only over narrow range of streak speed values the best time resolution can be achieved for a fixed slit size. The optimum streak speed range moves towards higher value as the slit size increases. This is because for a fixed slit size at a low streak speed the time resolution is governed by the slit size influence and at a high streak speed the deflector fringe-field effects become more dominant. The minimum streak speed for an optimal time resolution is determined by the input slit size whilst the maximum value is limited by the deflection fringe-field effects. Obviously, it is more advantageous to use the smallest possible slit size but due to practical difficulties, the slit size is often chosen to be 10 ~ 30 μm.

Apart from limiting the streak speed, the fringe-field effects inherent in the metal-plate deflector systems also give rise to nonuniformity of the temporal resolution and the streak speed across the phosphor screen. The image positions of the photoelectrons on the phosphor screen correspond to the synchronisation positions of the photoelectrons on the deflection signal profile when photoelectrons arrive at the deflectors. Different synchronisation positions

imply different voltages to which photoelectrons are subjected and thus different fringe-field effects. Although the fringe-fields at the entrance and exit of the deflectors have a tendency to cancel each other, the changes of the spatial distribution and transverse position of the photoelectron packet during its propagation in the deflection system prevent a complete cancellation. As a result, the nonuniformity of time resolution and streak speed across phosphor screen occurs. The variation of time resolution as a function of image position on the phosphor screen plotted in Fig.4.4.3 where an input slit size of 5 μm was used.

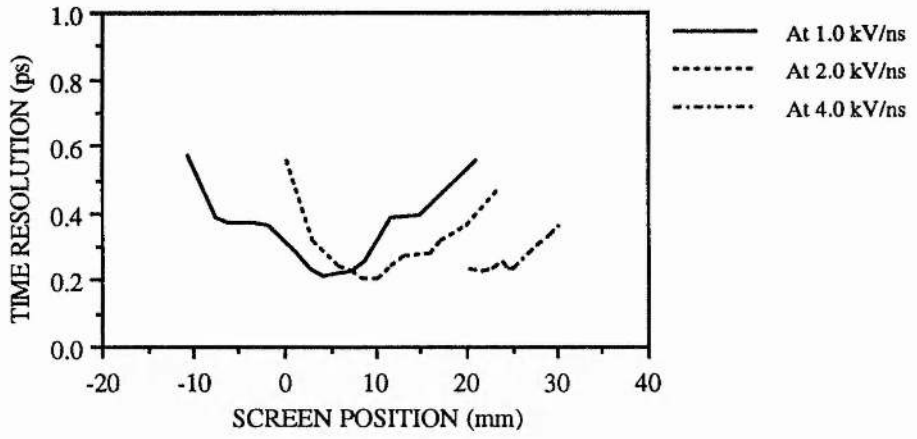

Fig.4.4.3 Time resolution across the screen

It is seen that an optimum position exists where the time resolution reaches its best value. In order to achieve an optimum time resolution, the synchronisation should be adjusted so that the image is located at the optimum position on the screen. At low streak speed, fringe-field effects are less significant and the optimum time resolution occurs near the centre of the screen. When the streak speed increases, this position tends to move further away from the centre of the phosphor screen and to an extreme, the interception of the photoelectrons by the deflectors will occur. Hence the increase of streak speed is restricted in this way.

In order to evaluate the degree of variation, the streak speed nonlinearity is defined in terms of $\frac{v_s - v_{op}}{v_{op}}$ where v_{op} is the streak speed obtained at the optimum screen position. Fig.4.4.4 shows streak speed nonlinearity across phosphor screen. It indicates clearly that the increase of streak speed leads to more pronounced nonlinearity. For example, for a streak speed of around light speed the nonlinearity is in the range of -5% to 12% within an area of 30 mm whereas for

a streak speed of over 5 x 10^8 m/s the nonlinearity is increased up to ± 10% in an area of only 10 mm. This suggests that streak speed should not be any higher than 4 x 10^8 m/s. For the

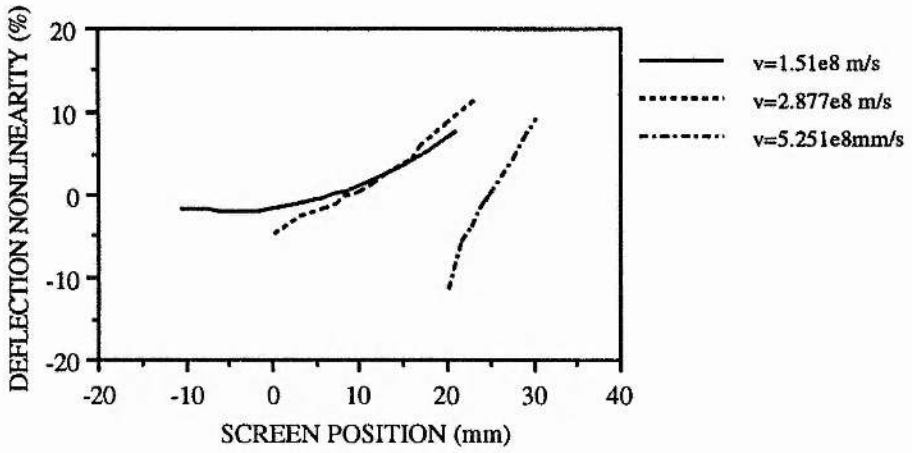

Fig.4.4.4 Streak linearity across the screen

optimum streak speed range of 1.5 ~ 4 x 10^8 m/s, the streak speed nonlinearity across an area of around 15 mm is ± 5%. If a relay optical lens with magnification of 2 is used for coupling onto a readout device, then it will allow a working area of Φ30 mm on the readout system.

4.5 The operation of the Photochron V streak tube

4.5.1 Synchroscan operation mode

The study of synchroscan operation in chapter 3 has indicated that apart from the availability of a streak tube having a femtosecond time resolution, it is equally important to build an electronic circuitry with low RF noise and to have a repetitive femtosecond pulse light source with low timing jitter and amplitude fluctuations in the camera evaluation experiments.

Theoretical evaluation has been made for the Photochron V tube with the consideration of these factors and Fig.4.5.1 shows the calculated results for RF noise in terms of snr (signal to noise ratio in dB) and timing jitter (in ps). For the convenience of comparison, the sweep speed in the calculation was set to be the same as that for the Photochron IV evaluation presented in chapter 3, i.e. 0.677 x 10^8 m/s at 200 MHz frequency. These results reveal that to achieve a time resolution less than 1 ps in the synchroscan operation of this tube, it is necessary for the

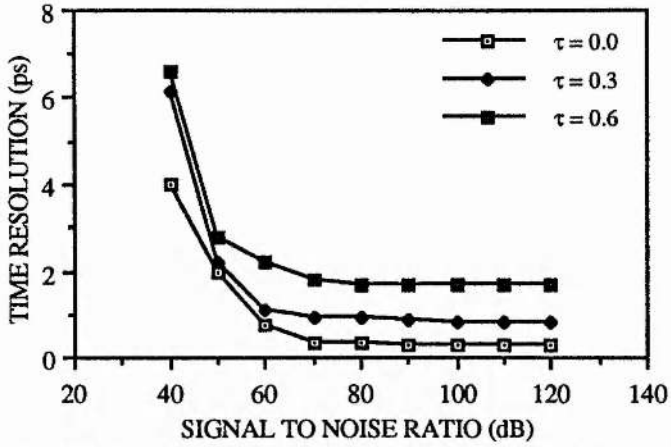

Fig.4.5.1 Time resolution under the influence of timing jitter and RF noise

laser and electronic systems to provide a signal-to-noise ratio better than 70 dB and synchronisation stability of better than 200 fs. A time resolution of better than 300 fs from this streak tube in synchroscan operation requires the timing jitter of the laser system to be less than 100 fs and signal-to-noise ratio of the deflection signal to be better than 100 dB. For example, with a zero timing jitter a time resolution of 250 fs can be produced for a signal-to-noise ratio of 100 dB.

Using the noise reduction techniques where active electronic feedback stabilisation of laser cavity is employed, the timing jitter in passively mode-locked lasers can be reduced to 0.3 ps[5]. This would limit the overall time resolution of this tube to around a picosecond. Thus the relative timing jitter has actually become the fundamental limiting factor to the instrumental time resolution of this streak tube in synchroscan operation.

4.5.2 Circular scan mode

It is also possible to operate the Photochron V streak tube in a circular mode which may be required in applications such as laser ranging[8,9]. This can be obtained by using two sets of metal-plate deflectors located orthogonally to each other with exactly the same deflection sensitivities and identical sinusoidal waveform signals. By adjusting the synchronisation and

phase of the two signals, the photoelectron beam is scanned in a circular trace on the phosphor screen.

4.5.3 Single-shot operation

When operating in a single-shot mode, the dynamic range is one of the major concern. Calculations for evaluation of the dynamic range will be discussed in the next chapter where special attention will be paid to the single shot operation of Photochon V.

4.5.4 Framing mode

This tube can also be revised for a framing operation. To do so, a gating pulse can be applied to the photocathode and/or MCP. If multiple gating signals are used and two staircase electric signals are applied to two sets of deflectors, several frames can be produced on the phosphor screen. To obtain adequate dynamic range, a high gain intensifier is desirable.

4.6 The construction of Photochron V streak tube with metal-plate deflectors

With regard to the construction and manufacture of the tube, the following aspects are important. (i) The mesh electrode should be constructed such that an appropriately high electric field may be applied between the photocathode and mesh. (ii) Ceramic and stainless steel materials for the envelope and electrodes respectively are preferable to ensure precise engineering tolerances and to give rigid structure. (iii) The surface resistivity of the photocathode substrate needs to be a minimum for single-shot operation (< 100 Ω/square) with transmission greater than 50%. (iv) The deflector and its leadthrough material needs to be of low RF resistivity and minimal permeability ($\mu_r \sim 1$) to minimise RF losses and power requirements. (v) The deflection system must be designed and constructed with due regard to multipacting discharge effects. (vi) Transfer photocathode processing is preferred so that discharge problems between the photocathode and mesh and in the deflection region may be avoided. (vii) The vacuum in the tube should be adequately high in order to prevent photocathode deterioration and keep minimum background noise. (viii) Critical attention should

be paid to the tolerance (no bigger than 0.2 mm) for the focusing electrode inner diameters and separations and good alignment should be ensured.

According to the above considerations, practical specifications can be given for the tube construction as follows: (1) accurate alignment, electrode inner diameters and separations (typically -/+ 0.1 - 0.3 mm), (2) avoidance of sharp edges - typical radius 0.5 mm, (3) stainless steel material for electrodes, (4) photocathode substrate having resistivity less than 50 Ω/square for single-shot operation with a transmission of better than 50% and the window material must be nonbirefringent. (5) transfer technique for the manufacture of photocathode to minimise contamination in the tube, (6) Photocathode area of Φ10 - 14 mm and phosphor screen working area of Φ40 mm, (7) high efficiency phosphor screen with better than 60 lp/mm spatial resolution and compatible with the intensifier photocathode spectral response when required for single-shot operation, (8) deflectors with plate gap of 3 + 0.5 mm for the first set and 3.5 + 0.5 mm for the second set (if required for shuttering) for synchroscan or circular modes, (9) a vacuum of better than 10^{-7} Torr which is necessary in the sealed-off tube in order to avoid additional noise, (10) fibre-optic output faceplate so as to ensure efficient input and output optical-coupling, (11) sufficiently clean and smooth electrode and envelope surfaces. To prevent possible ion feedback, photoelectron reflection from phosphor screen, two baffle electrodes are placed in the space between the deflector rear aperture and the phosphor screen.

As discussed in chapter 3, high frequency sinusoidal synchronous drive to the deflection system can lead to multipacting discharge problems in some designs of streak tubes. These discharges have associated additional RF power losses which induce undesirable heating effects and lead to the detuning of the resonant circuits with a consequent drift of image synchronisation. They also result in a serious increase in the parasitic background noise level which degrades the signal-to-noise ratio in the streak tube. Calculations have shown that to avoid multipacting problems in the synchroscan operation of streak tubes, the gaps between deflector plates and ground surfaces should avoid the region of 1.5 mm to 20 mm within which multipacting may be initiated when operating at frequencies up to 500 MHz. This can be

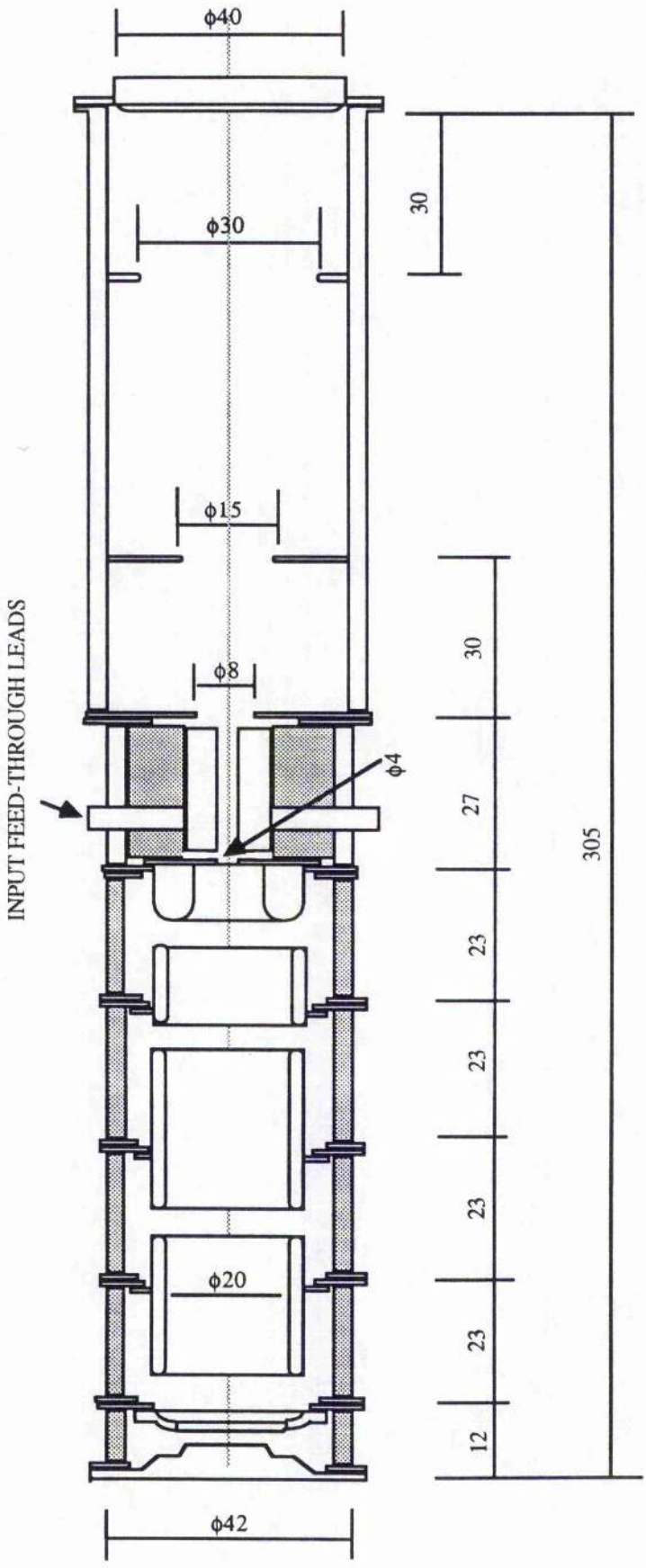

Fig.4.6.1 The configuration of the Photochron V streak tube

achieved by using a ceramic slab to support the deflector plates. To limit the related increase in the capacitance of the system, the diameter of the leadthroughs is maximised and the amount of ceramic between the back of the deflector plates and the envelope wall is minimised.

The construction of the Photochron V streak tube together with the deflector assembly is displayed in Fig. 4.6.1. Its overall length is 305mm and the outer diameter is 42 mm. As illustrated, the tube construction uses a metal-ceramic fabrication technology.

4.7 Power supply and image intensifier requirements

To determine the requirement for the performance of a power supply, computer-aided design studies have been carried out. The results have indicated that the power supply ripple tolerance required for single-shot operation is of the order of ±0.5% provided that all of the operating voltages are derived from the same source and so will vary proportionately. However, for the synchroscan operation, this requirement is much higher because the power supply ripple will induce fluctuations in the transit times of different pulses. For instance, a power supply ripple of 0.1% can give rise to a synchronisation time variation of up to ± 130 fs. Thus, to ensure that a time resolution of 300 fs or less can be achieved in the synchroscan operation, it is necessary to have a power supply with a minimum ripple (eg. less than 0.05%).

To minimise space-charge effects and enhance the dynamic range, an intensifier with high gain and good spatial resolution is generally required in single-shot operating mode and it is necessary for the intensifier to have performance features such as a gain of better than 10^4, good S/N ratio, a spatial resolution of no less than 30 lp/mm, an input working area of Φ30-40 mm and Fibre-optic input and output faceplates. In practice, most of these conditions can be satisfied by an electrostatically-focused microchannel plate intensifier.

4.8 Image readout system and its optical coupling lens

A spatial resolution of 70 lp/mm at photocathode predicted for a Photochron V image tube is equivalent to a FWHM resolution element around 22 μm on the phosphor screen given that

the electron-optical magnification of the streak tube is X3. The available OSA or CCD detectors have a pixel size of 22 μm thereby implying a spatial resolution of 22 lp/mm whenever crosstalk between pixels can be neglected. To prevent the readout system from becoming a limiting factor to the achievement of the best time resolution, an optical lens with a suitably large magnification is desirable for the coupling between phosphor screen of the streak tube or the intensifier and readout target. Normally an optical lens with magnification of x 2-3 is used which produces 2-3 pixels on the readout system for each limiting spatial resolution element of the streak tube. If the streak tube is operating at the streak speed equal to the speed of light, one pixel will correspond to a time duration of 25-35 fs. A 200 fs limiting time resolution of the streak tube will produce a spatial dimension of 60 μm on the tube phosphor screen which represent 6-9 pixels on the readout device. This introduces an error of around 15% into the evaluation value of the tube time resolution and may be considered to be acceptable since the tube is normally used for applications in timescales that are several times the limiting time resolution.

4.9 Experiment evaluations of Photochron V prototype tube

4.9.1 The static test of a pre-prototype streak tube

A pre-prototype Photochron V streak tube has been made and its overall appearance is displayed in Fig. 4.9.1. Pending the manufacture of the tube housing, static spatial resolution tests were carried out on the unmounted tube. A voltage resistor divider chain was constructed and set to give the computer predicted operating voltages. A Brandenburg 807R power supply having 0.01% peak-to-peak ripple at maximum 30 kV output was used to provide the required overall voltage. Starting at a low value, the overall voltage applied to the tube was progressively increased until at 5 kV electrical discharge was observed in the photocathode mesh section. For this first tube, the correctly profiled mesh-photocathode assembly was not available at the time of manufacture and hence the overall design voltage of 10 kV was not achievable. The photocathode sensitivity given by the manufacturer (Photek Ltd., UK) was 70

μA/lumen which was adequate for the wavelengths around 800 nm used for this preliminary test.

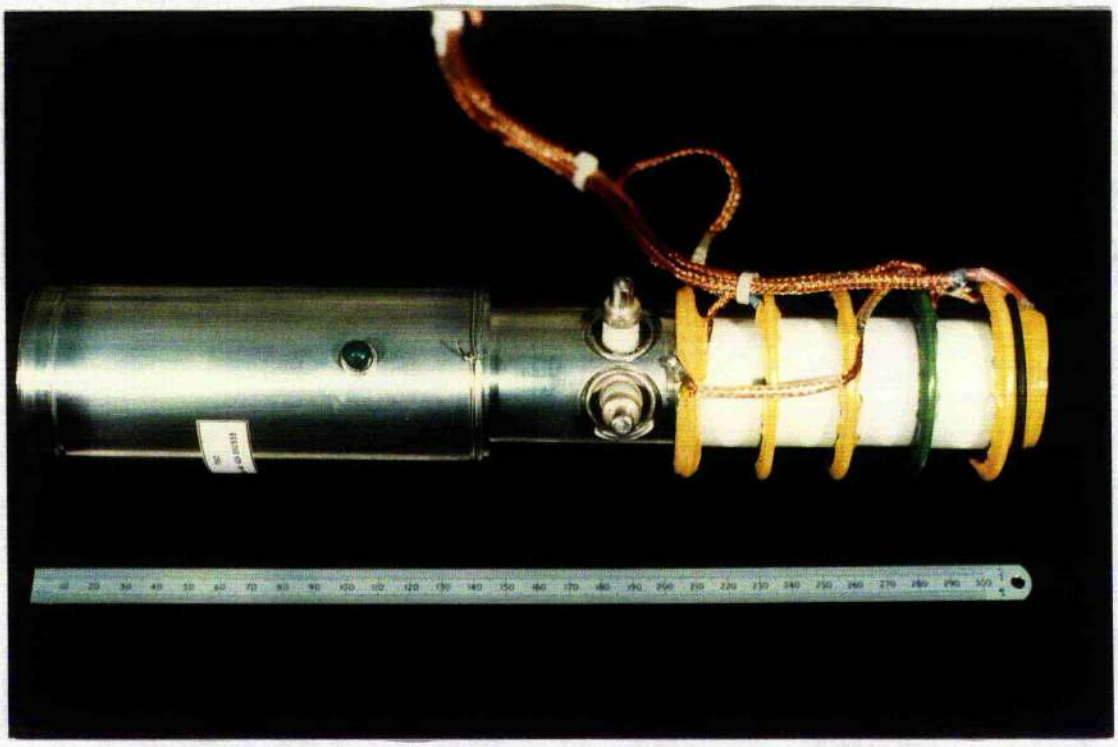

Fig.4.9.1 The experimental version of the Photochron V tube

A static test has been carried out to determine the spatial resolution across phosphor screen of this prototype tube. At the proportionately reduced operating voltage of 4.7 kV, the tube proved to be in correct focus at theoretically predicted electrode voltages. The spatial resolution at the centre of the phosphor screen was measured to be 60 lp/mm whilst at the edge of the screen the spatial resolution was around 50 lp/mm in the streak direction and 30 lp/mm in the orthogonal direction. (The fact that the spatial resolution in the nondeflection direction is worse than that in the other may be caused by the magnetic disturbance from the power supplies, which were beside the streak tube during the test, and the acceleration mesh interference). The electron-optical magnification was measured to be X 3. The deflection voltage required for a full-screen scanning was 220 V which corresponds to a deflection sensitivity of 16.7 cm/kV as predicted from computation.

It was observed that the spatial resolution was limited by the existence of the acceleration mesh because its image tended to appear and interfere with the test chart. By arranging a mesh line orientation of 45° to the deflection direction, some improvement could be obtained.

4.9.2 The deflector assembly

The deflector assembly incorporated in this prototype tube was assessed to detect multipacting problems and it appears to have acceptably low RF losses and frequency drift with temperature (less than 100 kHz) when driven at 20 W at a frequency of 170 MHz. No detectable multipacting effects were observed in the deflection region when 20 W RF power was applied. The operating frequency range used on this tube was in the range of 100-500 MHz.

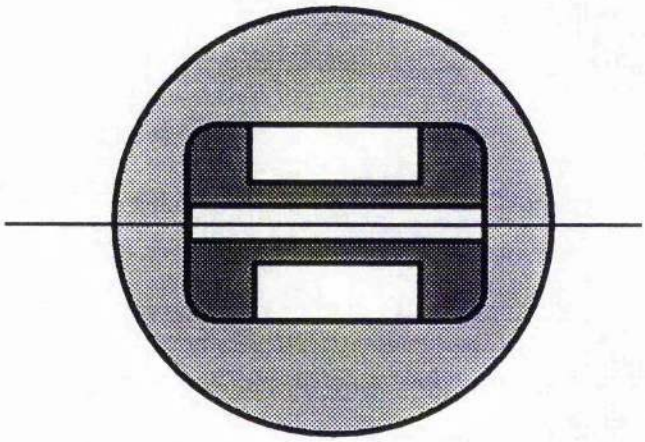

Fig.4.9.2 The cross-section of the deflector assembly

The capacitance of the system was higher than that in Photochron IV tube (3 - 4 pF) and measured to be 6 pF which is close to the calculated figure of about 7 pF. Calculations indicated that about half of the capacitance was due to the very thick section of ceramic at the back of the deflector plates. It is possible to reduce this capacitance by taking away the rear of the plates as shown in Fig.4.9.2 thereby providing an additional vacuum gap. Supposing that an area of 6 mm wide and 5 mm high along the plates is removed, then the total capacitance can be reduced to about 3 pF which will also reduce the RF dielectric loss. It is essential that the capacitance be reduced if operation at higher frequencies than 500 MHz is to be obtained and it would be more efficient to operate the system with the above modification at 500 MHz.

4.9.3 Preliminary dynamic test for synchroscan operation

4.9.3.1 Experimental setup

The dynamic testing of this tube in a synchroscan mode of operation was undertaken at the reduced overall operating voltage of 4.7 kV using a commercial mode-locked titanium-sapphire laser system (Spectra Physics, Tsunami). This laser was operated at a pulse repetition rate of approximately 82 MHz with 100 fs duration at a wavelength around 830 nm. Of interest here, is the fact that the dynamic sensitivity of the deflection system operating at 164 MHz was such that only around 500 mW of RF power was required to give full-screen scanning (± 20 mm). The test signal for calibration was obtained by utilising the reflection from the front and back surfaces of a 1.15 mm thick glass slide that provides two pulses separated by 11.7 ps.

When carrying out these tests, a 40 μm slit size was used. The input optical lens had a demagnification of 3 and so the input slit size on the photocathode was about 14 μm which is comparable with the tube resolution limit (i.e. ~ 8 μm). Thus the ultimate resolution size on the screen was determined by both input slit size and the resolution of the tube itself. Taking into account an electron-optical magnification X3 of the tube, the image size on the screen of the tube can be worked out to be 50 μm. The optical lens coupling the OSA had an optical magnification of about 1.6 and so the image size on the OSA is ~80 μm. As the pixel size of the OSA is 25 μm, the spatial resolution element of the entire system should take about 3-4 channels. In our experiment, the best resolution obtained was 6 pixels.

4.9.3.2 Dynamic results and discussion

The streaked images were recorded on a B&M Spectronik Analyser OSA500 and are reproduced in Fig. 4.9.3. Although the above results do not provide the specified design performance, as a first attempt the experiments have indicated some promising aspects. The static tests have confirmed that computer programs are capable of giving reliable predictions for the tube performance. The tube manufacturing accuracy appear to meet the design specification adequately and the photocathode transfer technology can provide a uniform and sensitive S25

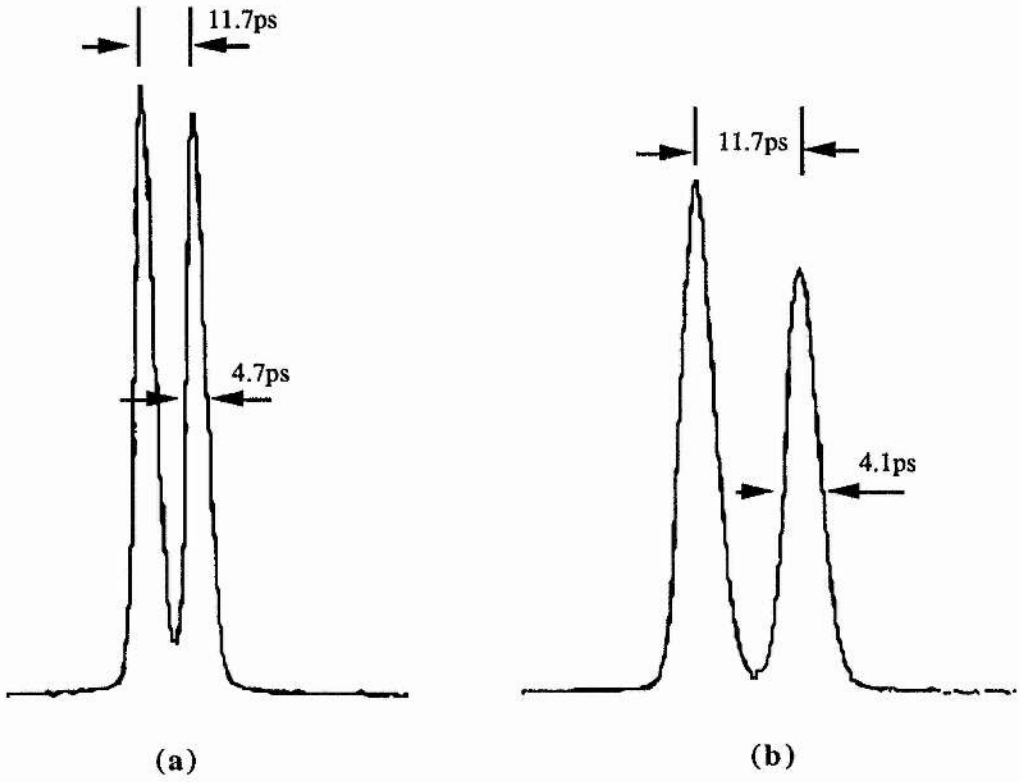

Fig.4.9.3 Recorded intensity profiles of a pair of laser pulses separated by 11.7ps, **(a)** 0.5 W RF deflection power at real time **(b)** 2.5 W RF deflection power at real time **(c)** 2.5 W RF deflection power at 1ms shutter speed

photocathode. The deflection assembly design appeared to have overcome multipacting discharge problems since no evidence of multipacting or ionisation was observed up to a maximum applied RF power of 20W. When operating the tube at a low overall voltage 5 kV a time resolution of less than 4 ps (2.5 ps time duration were actually recorded later but its hardcopy was not produced) can be provided by using RF deflection power of 0.5 W. (An increase of applied RF power beyond 2.5W did not result in an improved streak performance for this particular system arrangement)

It should be emphasised that these results may not represent the limiting resolution of the tube used in its present form as computer studies have indicated that a time resolution of less than 2 ps should be achievable. It is expected that a properly-profiled cathode and mesh construction will allow the specified photocathode-to-mesh electric field and hence improved time resolution to be achieved. For future work on the experimental tubes, we will use our inhouse-designed self-mode-locked titanium-sapphire laser with a cavity-frequency referencing scheme which is less noisy than CPM lasers[10,11].

4.10 Summary

In order to demonstrate a femtosecond time resolution for synchroscan operation, an improved design of a streak image tube _ Photochron V has been developed. The principal design specifications have included optimised focusing and deflection systems which can provide minimum time dispersions and spatial aberrations, maximum deflection sensitivity with adequate frequency bandwidth and avoidance of multipacting problems. Theoretical predictions have indicated that the tube has a limiting time resolution of 250 fs when a S1 photocathode is illuminated near its long wavelength threshold (i.e. 1.06 μm).

The influence of parameters such as input slit, photocathode electric field strength, initial energy spread, streak speed, electronic and laser noise in synchroscan operation on the performance of the system have been investigated. With moderate adaptation, this new streak tube can be universally used for different operation modes such as single-shot, circular scan and framing. With regard to single-shot operation of the tube, the focusing system has a

shorter photoelectron transit time than that of the Photochron IV tube and a proportionate increase of operating voltages will allow further reduction in the photoelectron transit time. The availability of such a tube can thus make it possible to achieve a time resolution of around 300 fs for both synchroscan, single-shot and circular-scan streak operations.

The tube has been manufactured and a prototype version has been produced. The preliminary experimental evaluations have confirmed that the key feature of the tube design have been achieved and the new tube has outstanding merits of high deflection sensitivity, good spatial resolution and improved time resolution. In this regard, the suite of computation computer programs used to establish such designs have proved to be successful and accurate. It has also confirmed that the multipacting analysis can provide correct information and instructive guidance for appropriate deflector construction design. Preliminary streak results of 3.8 ps have been obtained from this prototype tube in synchroscan operation when a Ti:sapphire mode-locked laser was used. Potentially, time resolution of less than 2 ps should be achievable from this tube when the laser cavity stabilisation scheme is adopted.

4.11 References

1 Fujimoto J G, Salour M M, SPIE Vol. 322, Picosecond Lasers and Applications, pp.137-165 (1982)

2 Campillo A J, Shapiro S L, IEEE J. Quantum Electronics, Vol. QE-19 (4), pp.585-603 (1983)

3 Sibbett W, Proc. 15th ICHSPP, SPIE Vol. 348, pp. 15-26 (1982)

4 Finch A, Liu Y, Sleat W E, Sibbett W, Chen G, Proc. 18th ICHSPP, SPIE., Vol. 1032, pp. 97-104 (1988)

5 Walker D R, Crust D W, Sleat W E, Sibbett W, IEEE J. Quantum Electron., Vol. 28 (1), pp. 289-296 (1992)

6 Finch, A., Liu, Y., Niu, H., Sleat, W.E., Sibbett, W., Yang, Q.L., Zhang, H., Proc. 18th ICHSPP, SPIE Vol. 1032, pp.622-627 (1988)

7 Hamamatsu Photonic Systems (advertisement), Laser Focus World, Vol.26 (5), p.220 (1990)

8 Sibbett W, Sleat W E, Taylor J R, Krause W, Proc. of 16th ICHSPP SPIE Vol.491, pp.76-81 (1984)

9 Johnson C B, Nevin S, Bebris J, Abshire J B, Appl. Opt., Vol.19 (20), pp.3491-3495 (1980)

10 Spence D E, Evans J M, Sleat W E, Sibbett W, Opt. Lett., Vol.16 (22), pp.1762-1764 (1991)

11 Son J, Rudd J V, Whitaker J F, Opt. Lett., Vol.17 (10), pp.733-735 (1992)

Chapter 5

SINGLE-SHOT STREAK CAMERAS AND EVALUATIONS

5.1 Introduction

With the rapid development of research related to ultrafast phenomena, increasingly high demands have been placed upon the instrumental performance of single-shot streak cameras and this has stimulated significant progress in their development. Dramatic improvement in the time resolution of single-shot streak cameras has been made during the past twenty years[1,2], but, further improvement of the time resolution has encountered difficulties associated with the limited dynamic range and deflection speed of the available deflection systems. Schemes aimed at overcoming these problems have become key issues in single-shot camera studies.

5.2 Single-shot operation of streak cameras

The operation of a streak camera in a single-shot mode implies that only a single light event is recorded. Such operation is normally achieved by applying a single ramp voltage to the deflection system of the streak tube in synchronisation with a single input light event. The fact that the input light signal consists of only one single light event leads to the need for sufficiently high intensity of the incident light pulse. But a high light signal intensity can give rise to a degradation in the temporal performance for subpicosecond /femtosecond time scales due to the induced space-charge effects[3]. The use of internal or external intensification can alleviate the severity of such effects to some extent, but the dynamic range still tends to be very low or too low to provide useful information. Under the constraints of an adequate dynamic range requirement, the ultimate time resolution tends to be limited to a picosecond regime. Furthermore, the achievement of a high streak speed requires a high deflection sensitivity as

well as a fast deflection ramp voltage which contains a broad range of frequency components. This implies that a deflection system having a broad frequency bandwidth is desirable. Therefore, minimising the space-charge effects and providing fast deflection has become the challenging joint tasks in the single-shot streak camera development. The objectives in this chapter are the investigation of efficient deflection systems and the mechanism of space-charge effects so as to seek the practical ways to improve the performance of single-shot cameras.

5.3 Generation of deflection ramp voltage

The generation of high ramp voltage for picosecond/femtosecond streak cameras has been achieved by means of several techniques which include laser triggered spark-gap[4,5,6], krytron valve circuits[7], avalanche transistor stacks[1,8,9,10], hybrid avalanche transistor-krytron circuits[11,12] and photoconductive switches[13,14,15,16]. The laser-triggered spark gaps and krytron valves are effective in producing high voltage ramps with subnanosecond rise times but their jitter can be relatively large eg. 0.5 ~ 1.0 ns. Also, laser triggered spark-gaps require relatively high optical pulse energy. Using hybrid avalanche-krytron circuits, voltage ramps of 3 kV/ns with ± 50 ps jitter were generated but it was not stable and in practice it is difficult to construct a krytron based ramp generator with low jitter and a long operational life. Avalanche transistor ramp generator has been utilised successfully in picosecond streak cameras to provide sweep speeds of ~ 10^{10} cm/s (2 kV/ns) and trigger jitters of less than ± 20 ps[17,18,19] without the need of a high intensity optical trigger signal. For higher sweep speed and lower jitter operation, laser illuminated photoconductive switches are more appropriate when the adequate laser energy is available. They have been applied in both single-shot and framing cameras to provide sweep speeds of 4 x 10^{10} cm/s with typical jitters of < 15 ps[20]. Unfortunately, they require high optical power since low jitter can be achieved only if the switch is saturated every shot by the activating pulse having an energy of 20 - 100 μJ. Without high power lasers, avalanche transistor circuits have generally proved to be more practical. Although they tend to have higher jitter (20 ~ 100 ps) compared with semiconductor switches, a strict selection procedure for the avalanche transistors can lead to adequately fast rise time (1.5 kV/ns) and relatively low jitter circuitry(± 20 ps). The best single-shot results obtained so

far were from avalanche transistor stack ramp generators. Hence it is still considered to be a reliable means of producing fast writing speeds for single-shot streak cameras.

5.4 High frequency deflection

The general performance of a deflection system is judged on the basis of its deflection sensitivity and frequency bandwidth. The deflection sensitivity is defined as the spatial shift of an electron on the phosphor screen caused by unity deflection voltage applied to the deflection system. The frequency bandwidth of a deflection system is given by the 3 dB roll-off frequency of its deflection response to a single frequency sinusoidal signal relative to its DC deflection. In order to achieve high streak speed, it is imperative for a deflection system to provide both high deflection sensitivity and broad frequency bandwidth which allow the application of fast ramp voltage.

5.4.1 DC deflection

Commonly-used conventional deflectors consist of a pair of parallel metal plates. When a DC voltage is applied to such a deflection system, the deflection sensitivity (DS) can be easily deduced by neglecting the fringing-fields at the edges of the deflector plates:

$$DS = \frac{l}{dV_a}\left(\frac{l}{2} + L\right) \tag{5.4.1}$$

where l is the length of the plate, d is the separation between the two plates, V_a is the anode voltage relative to the photocathode and L is the distance between the exit of the deflector plates and the phosphor screen. It indicates that the deflection under static conditions varies linearly with deflection voltage for a deflector with given deflector structure parameters and the anode voltage.

5.4.2 High frequency deflection response of capacitive metal-plate deflectors

Under dynamic operating conditions, the deflection signal is time-varying and thus the frequency response of the system must be considered. When a parallel-plate deflector is used,

a sinusoidal waveform signal applied induces an instantaneous electric field which can be expressed as

$$E = \frac{V_d}{d}\sin(\omega t) \tag{5.4.2}$$

Under such an electric field, the deflection sensitivity of an electron can be derived by the integration of the equation of the motion of the electron as

$$DS_f = \frac{l}{2dV_a}\cdot\mathrm{sinc}(\frac{\theta}{2})\cdot\{L\cdot\cos\frac{\theta}{2} - \frac{l}{2}\cdot\mathrm{sinc}(\frac{\theta}{2})\} \tag{5.4.3}$$

where

$$\mathrm{sinc}(\frac{\theta}{2}) = \frac{\sin(\frac{\theta}{2})}{\frac{\theta}{2}},$$

$$\theta = \frac{\omega l}{v_z},$$

v_z is the velocity of the electron,

D_0 is the DC deflection, i.e. DS x V_d,

v_z is determined by the anode voltage V_a (typically 10 - 20 kV), i.e. $\sqrt{\frac{2eV_a}{m}}$.

It is seen that the deflection sensitivity in this case is a function of the deflection signal frequency. The increase of frequency induces a loss in the deflection sensitivity relative to the DC deflection conditions. This is referred to as the electron transit time effect. It gives rise to difficulties in achieving high streak speed and as a result it may limit the improvement of the ultimate time resolution.

As an example, the deflection response of the metal-plate deflector used in the Photochron V tube has been calculated and is plotted in Fig.5.4.1. It can be seen that the frequency bandwidth of this deflector is limited to 580 MHz for 10 kV anode voltage and 780 MHz for

18 kV anode voltage. A broader frequency bandwidth can only be attained at the expense of a deflection sensitivity by reducing the length of the deflector plates.

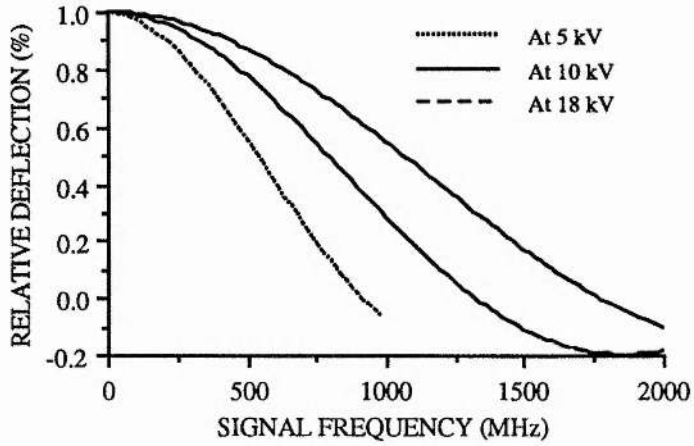

Fig.5.4.1 The deflection response of the metal-plate deflector for a Photochron V streak tube

Also the metal-plate deflectors as a whole are a capacitive load and therefore its impedance changes with frequency. Hence its response time is intrinsically restricted by the rise time of the deflection system including the inductive feedthrough leads. Because of these defects in metal-plate deflectors, the use of travelling-wave deflectors have been considered where the input deflection signal is dealt with as a continuously travelling-wave.

5.4.3 Travelling-wave deflectors

Widely used travelling-wave deflectors in cathode ray tubes (CRT) and microwave tubes include resonant cavity type[21], helical type[22], trough-type[23], meander-type[24] and stripline-type[25]. The high-Q factor resonant cavity type can operate at very high frequencies but it has poor deflection sensitivity and very narrow bandwidth. Helical type deflectors have been widely used in oscilloscopes and can provide adequate bandwidth and deflection sensitivity. They appear to have low phase velocity and are difficult to construct. Trough-type deflectors have the same problem and are even more complicated in construction. Stripline type and meander-type deflectors have both been used in streak image tubes. The former is based on the parallel plate construction with input and output impedance matching. Although it does not

solve velocity mismatching problem, the limitation to the application of fast ramp voltages can be reduced considerably with consequent improvement in streak speed. The latter has been indicated to be appropriate for streak tube operation so far as it can provide adequate frequency bandwidth and velocity matching with high deflection sensitivity. The analysis of these two deflector types will be given below.

5.4.3.1 Impedance-matched stripline type deflectors

When the metal-plate deflectors are constructed with impedance-matched feed-through leads and properly terminated, the deflection input signal can be taken as a TEM travelling-wave. In general, the TEM wave should obey the Maxwell relations:

$$\nabla \cdot \mathbf{E} = \frac{\rho}{\varepsilon_o} \tag{5.4.4a}$$

$$\nabla \times \mathbf{E} = -\frac{\partial \mathbf{B}}{\partial t} \tag{5.4.4b}$$

$$\nabla \cdot \mathbf{B} = 0 \tag{5.4.4c}$$

$$\nabla \times \mathbf{B} = \frac{1}{c^2}\left(\frac{\mathbf{j}}{\varepsilon_o} + \frac{\partial \mathbf{E}}{\partial t}\right) \tag{5.4.4d}$$

where all bold letters represent vector variables, **j** is the current density in the space, ρ is the charge density, **E** and **B** are the electric and magnetic field vectors. In streak image tubes, the number of photoelectrons is very small such that the current density **j** and charge density ρ can be ignored.

As the input signal can be fed to the deflectors either from the entrance or from the exit of the deflectors, the deflection wave can be assumed to travel in either the same (i.e. forward) or opposite (i.e. backward) direction of the electron propagation and the deflection electric field can be written as:

$$E = E_y = \frac{V_d}{d} \exp\left(j\omega\left(t \pm \frac{z}{v_s}\right)\right) \tag{5.4.5}$$

where the *plus* sign applies when the wave travels in the opposite direction to the electron propagation, v_s is speed of the travelling-wave. From equation (5.4.4b), the magnetic field induced by the time-varying electric field can be obtained as $B = B_x = -\frac{E}{v_s}$.

The motion of an electric charge moving in an electromagnetic field can be generally described by

$$\mathbf{F} = q(\mathbf{E} + \mathbf{v} \times \mathbf{B}) \tag{5.4.6}$$

where **E, B** are the electric and magnetic fields applied to the charge, and **v** is the velocity of the charge considered. Substituting E_y and B_x into this equation, the following equation of motion can be deduced:

$$m\frac{d^2y}{dt^2} = e\left(1 \pm \frac{v_z}{v_s}\right) E_y \tag{5.4.7}$$

Integration of this equation leads to the deflection sensitivity response expression:

$$DS = \frac{\beta l}{2dV_a} \cdot \mathrm{sinc}\left(\frac{\beta\theta}{2}\right) \cdot \left\{L \cdot \cos\frac{\beta\theta}{2} - \frac{l}{2} \cdot \mathrm{sinc}\left(\frac{\beta\theta}{2}\right)\right\} \tag{5.4.8}$$

where $\beta = 1 \pm \frac{v_z}{v_s}$, the *minus* sign denotes the forward wave while the *plus* sign applies to the backward wave. In vacuum, v_s is equal to the speed of light, c. The deflection responses of the deflector used in a Photochron V streak tube at 10 kV and 18 kV for both forward and backward wave deflections are presented in Fig. 5.4.2 on the assumption that it has input and output impedance matching.

It is seen that the difference between the electron velocity and the signal phase velocity causes the reduction in the deflection sensitivity at high frequencies. The existence of magnetic field leads to further reduction in the forward wave deflection but an increase in the backward wave deflection. From the deflection sensitivity point of view, the improvement provided by such a variation is not great but the input and output impedance matching construction should allow faster input signal to be applied.

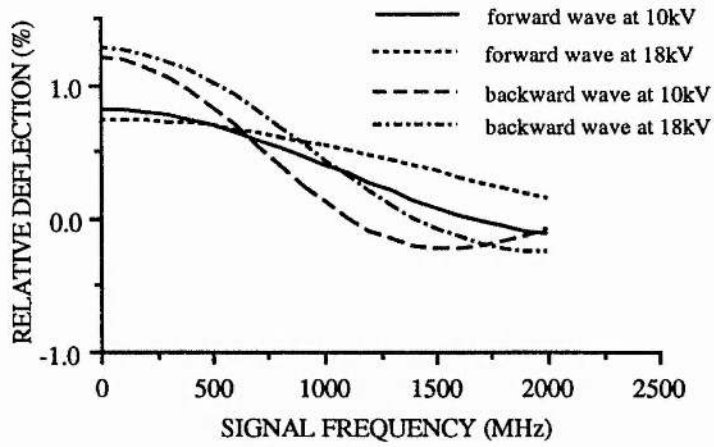

Fig.5.4.2 The deflection response of impedance-matched metal-plate deflector for a Photochron V streak tube

5.4.3.2 Meander-type TWDs

Theoretical analyses and simulation of meander-type travelling-wave deflectors (TWDs) for streak tube applications have been previously carried out in detail by the author elsewhere[26]. It suffices to briefly describe the theory and simulation here. The parameters for describing the characteristics of TWDs include characteristic impedance, phase velocity dispersion and deflection response. When incorporated into a streak tube, its temporal and spatial performance also needs to be considered.

A. Electromagnetic field distributions

The schematic and cross-section of a typical meander-type travelling-wave deflector are shown in Fig. 5.4.3 where the coordinates are defined. When an RF signal is applied, a time-varying electromagnetic field is established which can be obtained from the general Maxwell's equations. In the deduction of the distributions of the electromagnetic field, simplifications are made by assuming that (i) the space charge density and the conducting current density in the deflectors are negligible, (ii) the RF electromagnetic wave propagating along the deflectors is TEM wave in the finger length direction (i.e. x direction) and (iii) the input and output connections of the deflectors are impedance matched so that the reflection losses are negligible. Under these assumptions, the potential distribution on the deflectors can be expressed as

$$V(x,y,z,t) = F(y,z)\, e^{-jk_0 x}\, e^{j\omega t} \tag{5.4.9}$$

where k_0 is the wave constant in vacuum, x, y, z are the coordinates as shown in Fig. 5.4.3.

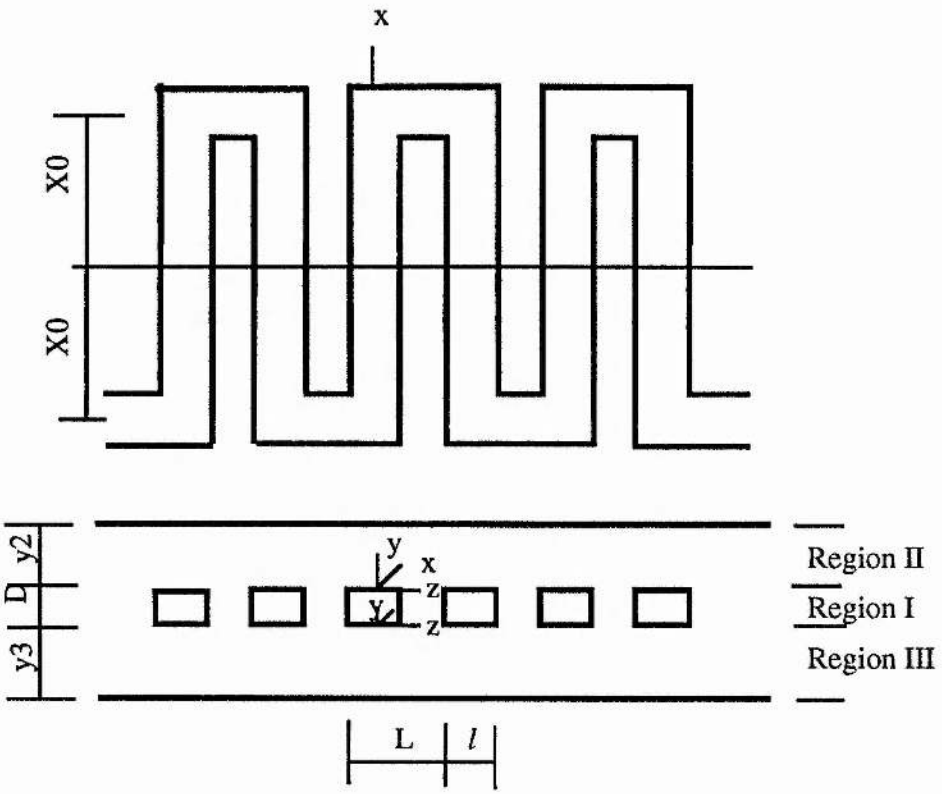

Fig.5.4.3 The schematic and cross-section of a meander-type deflector

F(y,z) satisfies equation:

$$\frac{\partial^2 F(y,z)}{\partial^2 y} + \frac{\partial^2 F(y,z)}{\partial^2 z} = 0 \tag{5.4.10}$$

This equation should satisfy the Maxwell equations and can be solved by using either space harmonic analysis[27] or numerical finite difference methods[26]. To solve equation (5.4.10) analytically, further simplification needs to be made by assuming that the length of the deflector along the electron propagation direction is infinite (i.e. the discontinuities at the ends of the deflectors are ignored) and the fields between the sides of the fingers are homogeneous. Equation (5.4.10) can also be numerically computed by using the techniques described in chapter 2. Knowing the boundary conditions and the nature of the periodical structure, the

electromagnetic field distributions can be readily obtained either analytically or numerically and details have been given in Ref. 26.

B. Impedance and velocity dispersion properties

Basically, a meander-type TWD is a transmission line. To ensure the achievement of broad frequency bandwidth, it is very important to be impedance matched with their resistive loads. The impedance of a transmission line is generally defined as the ratio of the voltage to the current on the fingers.

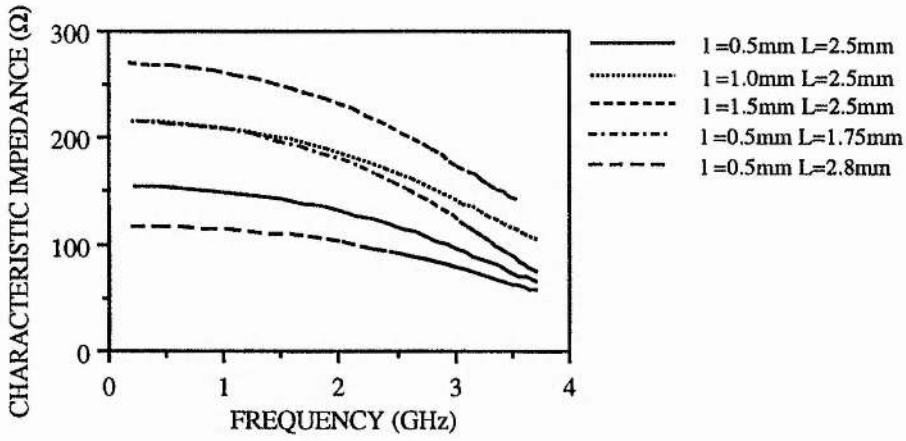

Fig.5.4.4 The characteristic impedance of the designed meander-line deflection system versus frequency

Using the analytical expressions of electromagnetic fields on the surrounding surfaces of the fingers, the characteristic impedance of a meander-type transmission line can be easily deduced as follows:

$$Z(\theta) = \frac{\sqrt{\mu_0/\varepsilon_0}}{(\Theta_1+\Theta_2+\Theta_3)} \tag{5.4.11}$$

where

$$\Theta_1 = 4\frac{D}{l}\sin^2(\frac{\theta}{2})$$

$$\Theta_2 = \sum_{n=-\infty}^{\infty}\frac{2l}{L}\sin\frac{\theta}{2}\frac{\sin(\frac{\Gamma_n l}{2})}{(\frac{\Gamma_n l}{2})^2}\coth(\Gamma_n y_2)\sin(\frac{\Gamma_n l}{2}-\frac{\theta}{2})$$

$$\Theta_3 = \sum_{n=-\infty}^{\infty} \frac{2l}{L} \sin\frac{\theta}{2} \frac{\sin(\frac{\Gamma_n l}{2})}{(\frac{\Gamma_n l}{2})^2} \coth(\Gamma_n y_3) \sin(\frac{\Gamma_n l}{2} - \frac{\theta}{2})$$

The calculated data of the characteristic impedance for a particular set of structure parameters are displayed in Fig.5.4.4. It can be seen that the characteristic impedance of such a deflector system decreases with the increase of frequency. This may cause nonlinear response to a linear deflection ramp applied to it and thus reduce the streak speed. Nevertheless, within a frequency bandwidth of up to 2GHz the discrepancy from linearity should be negligible.

By applying Kirchhoff's law and boundary conditions in the X direction, phase velocity dispersion equations can be obtained:

$$\mathrm{tg}^2\frac{\theta}{2} = \frac{Y(\theta)}{Y(\theta+\pi)} \mathrm{tg}^2\frac{\Phi_0}{2} \qquad (5.4.12a)$$

$$\mathrm{tg}^2\frac{\theta}{2} = \frac{Y(\theta)}{Y(\theta+\pi)} \mathrm{ctg}^2\frac{\phi_0}{2} \qquad (5.4.12b)$$

where θ is the phase shift of the electromagnetic wave propagating through one pitch along the deflector longitudinal axis, $\Phi_0 = k_0 x_0$, and $Y(\theta)$, $Y(\theta+\pi)$ are the characteristic admittances.

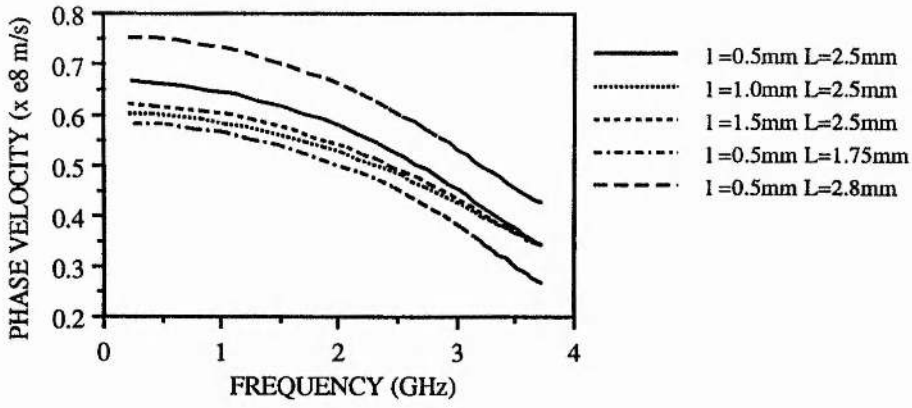

Fig.5.4.5 The phase velocity of the deflector versus frequency

Because of the periodical feature of the deflector structure, many space-harmonic waves can generally propagate along it and they travel at different phase velocities for a fixed fundamental frequency, only one of these phase velocities can be chosen to match with that of

photoelectrons. Normally the phase velocity of the fundamental given by $v_p = 2\pi f\frac{L}{\theta}$ is selected and the higher order harmonics are neglected. The velocity dispersion characteristics are illustrated in Fig.5.4.5 for the design used in Fig.5.4.4. It reveals that the phase velocity rolls off with increasing signal frequency and this is mainly due to the interactions between the fingers. At frequencies lower than 2 GHz, the velocity reduction is less than 30%.

C. Deflection characteristics

Knowing the electromagnetic field distributions, the equations of the motion of the photoelectrons can be solved by using fourth-order Runge-Kutta method under assumptions of both phase velocity and impedance matching. The typical results of the relative deflections as a function of frequency under different anode voltages are displayed in Fig. 5.4.6.

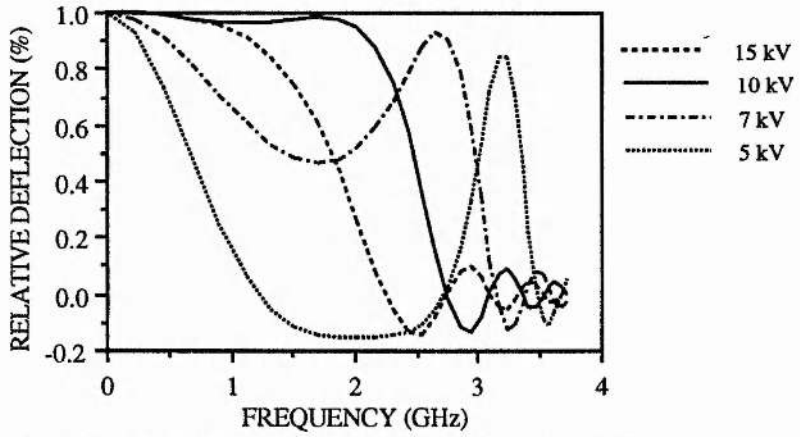

Fig.5.4.6 Frequency responses of deflection for different anode voltages

It is observed that the deflection decreases with the increase of the signal frequency more significantly at frequencies above 1 GHz and an optimum anode voltage exist where the deflection frequency response provides a maximum frequency bandwidth. This implies that an alteration in anode operating voltage requires a change in deflector parameters so that velocity matching can be achieved. Nevertheless, it indicates that the use of such a TWD system should provide the outstanding advantage of having simultaneously broad frequency bandwidth and high deflection sensitivity over the conventional metal-plate deflectors.

D. The design of a TWD system for Photochron V

The design of a TWD deflection system has been accomplished for the Photochron V tube at both 10 kV and 18 kV anode voltages. The design parameters for this TWD system at 10 kV anode voltage are as follows: L= 2.5 mm, l = 0.5 mm, thickness = 0.5 mm, X_0 = 10.5 mm, y_2= 2.2 mm, y_3 = 1 mm, m = 20. Its DC deflection sensitivity is calculated to be up to 10 cm/kV and its frequency bandwidth is 2.5 GHz. For a anode voltage of 18 kV, the width, X_0, of the transmission lines should be reduced to 8.2 mm to maintain velocity matching and it also gives a frequency bandwidth of 2.5 GHz. If a higher deflection sensitivity is required for the 18 kV anode voltage, the number of pitches, m, can be increased to 28 (i.e. 70 mm in length) to compensate for the induced deflection sensitivity loss and a DC deflection sensitivity of 7.3 cm/kV can be achieved. The characteristic impedance of the deflection system is in the range of 90 Ω–120 Ω over its entire bandwidth.

E. Spatial and temporal performance of a streak tube with a meander-type deflector system

A theoretical evaluation of the spatial and temporal performance of a Photochron V streak tube incorporating this meander-type deflection system has been carried out for 10 kV anode voltage. Since a fast ramp voltage signal consisting of multiple frequency components is very complicated to model, a sinusoidal waveform was used instead in the calculation. The different streak speed values were obtained by changing the voltage amplitude. The spatial and temporal MTF results for different streak speeds at 170 MHz for a 5 μm input slit are plotted in Fig.5.4.7. Due to the discontinuities at the ends of the deflector transmission lines where considerable fringe-fields can exist, the best time resolution does not appear when the phase velocity of the deflection signal matches the velocity of the photoelectrons precisely. Instead, a slight velocity mismatch is required to achieve the best performance. For example, at 170 MHz the phase velocity of the electric signal was 0.537 x 10^8 m/s while the velocity of photoelectrons was 0.595 x 10^8 m/s. As a result of the fringe-field influence, the upper limit of the streak speed was restricted to 3 x 10^8 m/s for this particular design. For an input slit size of

10 μm, the lower side of the streak speed range is seen to be 0.8 x 10^8 m/s. Within this range of streak speed, the limiting time resolutions were ~ 260 - 300 fs.

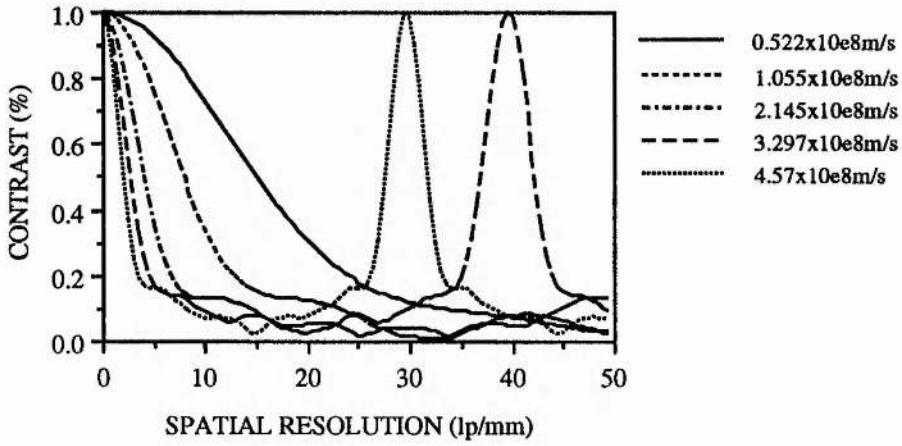

(a) Spatial MTF profiles

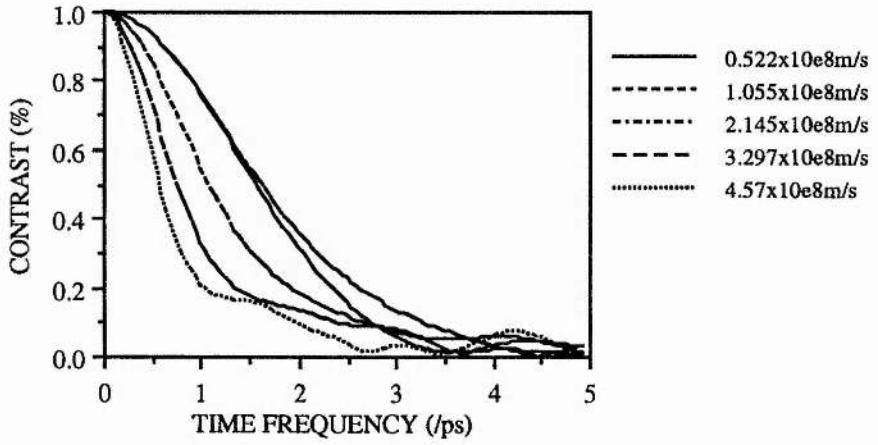

(b) Temporal MTF profiles

Fig.5.4.7 Spatial and temporal MTFs of the Photochron V tube with a meander-type TWD system

The prominent advantage of using a TWD system is that a constant deflection sensitivity can be achieved over a broad deflection frequency. At frequencies up to 1.3 GHz, the streak speed increases almost linearly with the increase of voltage amplitude and the limiting time resolution remains around 300 fs. This is very important for single-shot operation as it ensures a linear relationship between the deflection response and the applied voltage ramp signal. This

merit has been demonstrated in our early experiments during which a temporal resolution of 300 fs was recorded by a streak tube having a TWD system in single-shot operation[1].

One of the problems existing in using TWD systems is that there tends to be a noticeable loss in the spatial resolution along the nonstreak direction and this loss becomes more severe when the streak speed increases as seen in Fig.5.4.7 (a). In the streak speed range of 0.8×10^8 m/s to 3×10^8 m/s, the spatial resolution varies from 44 lp/mm to 17 lp/mm. This is due to the magnetic fields in TWD systems that give rise to additional sagittal aberrations. Normally, the sagittal aberrations are only caused by sagittal trajectories, i.e. the trajectories are two-dimensional curves. But, in a TWD system the magnetic fields induce three dimensional effects to the photoelectron trajectories. The other problem arises from the nonuniform electromagnetic field distributions inherent in these deflectors which induce additional aberrations in the streak direction and thus degrade the temporal MTF characteristic. This may give rise to difficulties in the achievement of a time resolution better than 200 fs and further detailed investigation in the performance and optimisation of such TWD systems is necessary.

5.5 The theoretical simulation and analysis of the dynamic range of Photochron V image tube

5.5.1 Definition of dynamic range

As mentioned earlier, the dynamic range of a streak camera is most commonly defined as the ratio of the upper limit to the lower limit of the incident light intensity at the photocathode of the streak tube i.e.

$$DR = \frac{I_U}{I_L} \tag{5.5.1}$$

The upper limit, I_U, of the input light intensity is defined as the level where the measured time duration on the phosphor screen is 20% greater than that of the incident pulse at the photocathode. The lower limit, I_L, of the incident current density is normally determined by the background or noise intensity level of the system.

In general, the lower limit I_L is dependent upon the factors including photoelectron statistical noise, specific type of photocathode and its processing technique, vacuum conditions, the type of phosphor screen, the streak tube structure and the intensifier (if used) as well as the noise level of the readout device. The upper limit ,I_U, is primarily determined by the input slit size, input pulse duration, streak tube configuration and the current saturation levels of the intensifier and readout system. To estimate the dynamic range of a camera system, the knowledge of both the lower and upper limits is desired.

5.5.2 The lower limit of the dynamic range

There can be two criteria which determine the lower limit of the current density I_L. One is given by the entire system noise level which is dependent upon the optical coupling methods, photocathode thermal emission, magnifications of the streak tube and intensifier, intensifier noise figure and the noise level of the chosen readout system. The other is set by the minimum signal-to-noise ratio (i.e. snr) due to statistical noise required for the system to record meaningful information.

First, consider the noise level of a typical system consisting of a streak image tube fibre-optically coupled onto an intensifier which in turn is lens-coupled onto the photocathode of a readout system. Assume that the streak tube has a phosphor screen with conversion efficiency of η_p (in photons/electron) and an acceleration mesh with a transmission of T_m, the intensifier has a gain of G_1 and the readout system provides a gain of G_2 with photocathode sensitivity of η_{rp} (in electrons/photon). The fibre-optical coupling efficiency is taken as α_1 and the lens coupling efficiency is denoted by α_2. Suppose that the noise level of the entire system is N_r electrons per resolution element of dimensions x and y on the SIT of the readout system, then the minimum current density I_L referred to 1 cm^2 photocathode area of the streak tube can be readily derived as

$$I_{Lr} = \frac{eN_r M_1^2 M_2^2 M_3^2}{\tau T_m \eta_p \eta_{rp} \alpha_1 \alpha_2 G_1 G_2 xy} \qquad (5.5.2)$$

where M_1, M_2, M_3 are respectively magnifications of the streak image tube, the image intensifier and the coupling lens between intensifier and the readout system, τ is the time duration of the input pulse.

Assuming $M_1 = 3$, $M_2 = 1$, $M_3 = 1.5$, $T_m = 0.5$, $\eta_p = 400$ photons/electron for P11 phosphor at 15 kV photoelectron energy, $\eta_{rp} = 0.1$, $\alpha_1 = 0.25$ for fibre-optic coupling, $\alpha_2 = 0.04$ for optical lens coupling, then the minimum current density I_L can be derived as

$$I_{Lr} = 101.2\frac{eN_r}{\tau G_1 G_2 xy} \qquad (5.5.3)$$

Taking an intensifier with gain of 10^3 and an SIT vidicon readout system with resolution element size of 25 μm x 25 μm, a gain of 150 and N_r of 40 electrons, then

$$I_{Lr} = 4.3 \times 10^3 \frac{e}{\tau} (A/cm^2) \qquad (5.5.4)$$

This definition has been used by other researchers[12,28] but it may give a rather optimistic estimation. This is due to the fact that the input pulse intensity equal to this noise level can not yet be discriminated. It is certain that the signal intensity level has to be higher than this to be diagnosed but there is no exact data for how much higher the signal level is required to be for an acceptable signal-to-noise level. Suppose a signal-to-noise level of 3 is necessary, then the system background noise limited minimum current density can be given as

$$I_{Lr} = 1.3 \times 10^4 \frac{e}{\tau} (A/cm^2) \qquad (5.5.5)$$

This estimation may still not give a realistic value as it is based on the assumption that enough photoelectrons are present in the measured signals such that the statistical noise is not considered and also it does not include the effect of spatial resolution loss due to optical coupling components. In some cases, the number of photoelectrons is so small that statistical noise becomes significant and the criterion set by the minimum signal-to-noise ratio (snr) under statistical fluctuation limit must be considered.

The statistical noise-limited snr is normally given as $\sqrt{N}$ per resolution element assuming that the photoemission process obeys a Poisson probability. Obviously, it is essential for the minimum snr to be equal to or greater than unity, i.e. 1 photoelectron per spatial resolution

element, in order to provide an output carrying any signal information on the output phosphor screen of the streak tube. Considering the mesh transmission factor, T_m, the minimum photoelectron number required on the photocathode should be greater than 1. For a streak tube with resolution size of h (height in mm) by w (width in mm), then the lower limit I_L at photocathode required for a minimum signal-to-noise ratio value of 1 can be given as

$$I_{Ls} = 10^2 \frac{e}{\tau T_m h w} \text{ A/cm}^2 \qquad (5.5.6)$$

Taking a resolution size of 20 x 25 μm and mesh transmission of 0.5, then we can have

$$I_{Ls}=4x10^5 \frac{e}{\tau} \text{ A/cm}^2 \qquad (5.5.7)$$

This indicates that the minimum current density I_{Ls} is nearly 30 times higher than that required by the readout system. However, this criterion may be pessimistic because it cannot take into account the advantages of using a high efficiency phosphor screen, image intensifier and recording medium which can influence the ultimate dynamic range significantly[12]. The minimum detectable value for a practical system is more likely to lie in between these two criteria.

It can be seen from the definition of dynamic range that a higher dynamic range can be achieved by minimising the lower limit of the current density. This suggests that it will be necessary to reduce the system noise level, optical magnification and to increase the overall gain, phosphor screen conversion efficiency and coupling efficiency. However, high gain may induce high noise level, the smaller magnification demands that the readout system has smaller resolution element size. Therefore, a trade-off is required among these parameters.

In situations where spatial resolution in the slit direction is not required, an integration of photoelectrons along the slit direction can be made to enhance the output signal so that the snr can be increased. For example, if a slit size of 20 μm wide and 1 mm long is used, then the lower limit can be reduced considerably and so the dynamic range of the system can be improved.

5.5.3 The upper limit of the dynamic range __ space-charge effects

Influential factors in determining the upper limit of the input current density I_U include space charge effects, photocathode resistivity, phosphor saturation level, the intensifier and readout system used. In a single-shot or framing mode of operation, very high photocurrent density (in the order of $1A/cm^2$ or higher) could be drawn from the photocathode when illuminated by a pico/femtosecond light event. It has been experimentally observed and theoretically proved that with such a high current density, the time resolution degrades significantly whilst the spatial resolution along the slit remains essentially unaltered[29,30]. In the femtosecond regime, this has become a key limiting factor. Recent studies of the dynamic range of single-shot streak cameras have revealed[31,32,33] that in the picosecond/femtosecond time scale the upper limit of the input current density is dominated by space-charge effects due mainly to the temporal broadening. In order to quantify this upper limit of incident current density, a detailed evaluation of intensity-dependent temporal broadening in a streak tube has been carried out by simulating the actual trajectories of photoelectrons travelling in a streak image tube under the influence of space-charge effects.

5.5.3.1 Space-charge induced electric fields

The temporal broadening induced by space-charge effects can be understood as follows. When the photocathode of a streak tube is illuminated by an ultrashort light pulse as a narrow slit image, a burst of photoelectrons is emitted. During their propagation in the streak tube, the photoelectrons experience the electric fields produced by the electrodes as well as the fields induced by the surrounding photoelectrons. Due to the repulsive interactions between photoelectrons, the leading electrons are accelerated while the trailing ones are decelerated and this results in a temporal broadening in the recorded pulse duration. For a particular incident light pulse, the relative temporal broadening rises with the increased levels of the incident current densities and for shorter duration light pulses such effects are more pronounced.

As the photoelectrons are moving at a relatively high speed, the induced electric fields vary with time and may produce magnetic fields according to the general electromagnetic theory, i.e. Maxwell's equations. The electric field and magnetic field can be expressed respectively by a scalar potential and a vector potential:

$$\mathbf{E} = -\nabla\phi - \frac{\partial \mathbf{A}}{\partial t} \tag{5.5.8a}$$

$$\mathbf{B} = \nabla \times \mathbf{A} \tag{5.5.8b}$$

where the scalar potential ϕ is the sum of potentials induced by the electron-optical lens electrodes and by the existing space charges whilst the vector potential **A** is merely due to the motion of space charges.

To simulate space-charge induced electromagnetic fields, simplifications are made as follows. (i) External magnetic fields are assumed to be negligible and the external electric field is static; (ii) electron collisions with remnant gas atoms in the tube are negligible considering the system dimensions to be small as compared with the corresponding free path length; (iii) the distribution of the external potential, determined by solving Laplace's equation, is not altered by the space charge potential because the distances between the photoelectron packet and the electrodes are much larger (typically several millimetres) than those between photoelectrons (from a few micrometres to less than a millimetre); (iv) considering that the number of photoelectrons is generally small and the photoelectron packet only occupies a small spatial extent, the current density **j** and charge density ρ should be negligible. (v) in each step of photoelectron trajectory calculation, the photoelectron distribution is assumed to be constant; (vi) the time dispersion caused by the photoemission process in the photocathode is ignored.

Based on the above simplifications and the superposition law of electric potentials, the total potential, ϕ, can be expressed as a summation of the external potential produced by the electrodes and space-charges induced potential, i.e. $\phi = \phi_L + \phi_q$. The two different potentials ϕ_L, ϕ_q, can be dealt with separately. The external potential, ϕ_L, satisfies Laplace equation $\nabla^2\phi_L=0$ and can be solved by conventional numerical method, for example, over-relaxation iterative method. The corresponding electric field can be given by $\mathbf{E}_L = -\nabla\phi_L$. As for the space-

charge induced potential, ϕ_q, because the space charges associated with the ultrashort pulses only occupies a very small dimension of space and the charge density and position are a function of time, the use of either the Gauss's theorem or the static Coulomb's law seems inappropriate. Fortunately, the actual number of photoelectrons at an acceptable photocurrent density level is relatively small and in practice they can be treated individually. That is to say, the entire space-charge induced potential, ϕ_q, can be obtained by summing up the potentials produced by each individual photoelectron.

In general, the potential at point (x_0, y_0, z_0) produced by a point charge q at point (x_1, y_1, z_1) moving at any velocity can be described by

$$\phi(r, t) = \frac{q}{4\pi\varepsilon_o(r - \frac{\mathbf{v}\cdot\mathbf{r}}{c})} \tag{5.5.9a}$$

$$\mathbf{A}(r, t) = \frac{qv_q}{4\pi\varepsilon_o(r - \frac{\mathbf{v}\cdot\mathbf{r}}{c})} \tag{5.5.9b}$$

where $\mathbf{r}$ is the distance vector from point (x_1, y_1, z_1) to point (x_0, y_0, z_0), i.e. $\mathbf{r} = (x_0-x_1)\mathbf{e}_x + (y_0-y_1)\mathbf{e}_y + (z_0-z_1)\mathbf{e}_z$ and its absolute value $r = ((x_0-x_1)^2 + (y_0-y_1)^2 + (z_0-z_1)^2)^{1/2}$, $\mathbf{v}_q$ is the velocity vector of the moving charge which can be given as $\mathbf{v}_q = v_{qx}\mathbf{e}_x + v_{qy}\mathbf{e}_y + v_{qz}\mathbf{e}_z$ and $v_q=(v_{qx}^2 + v_{qy}^2 + v_{qz}^2)$. Both position coordinates, x_1, y_1, z_1, and the velocity components v_{qx}, v_{qy}, v_{qz}, are the functions of time, t', which is described by (t-r/c). Since the charge at (x_0, y_0, z_0) is also moving, position coordinates, (x_0, y_0, z_0), should be the function of time t. But the derivatives for the field expressions become extremely complicated. Regarding that the velocity $\mathbf{v}$, in the term $\frac{\mathbf{v}\cdot\mathbf{r}}{c}$ of equations (5.5.9a) and (5.5.9b), is the relative velocity between two charges and that the photoelectrons are travelling at very similar speeds, the term $\frac{\mathbf{v}\cdot\mathbf{r}}{c}$ should be very small compared to r and thus can be neglected. By substituting equation (5.5.9a), (5.5.9b) into equation (5.4.4a), (5.4.4b), (5.4.4c) and taking all the derivatives, the space-charge induced electromagnetic fields $\mathbf{E}_q$ and $\mathbf{B}_q$ can be deduced as:

$$\mathbf{E}_q = \frac{q}{4\pi\varepsilon_o r^2}\left(\frac{\mathbf{r}}{(r - \frac{\mathbf{v}_q\cdot\mathbf{r}}{c})} - \frac{\mathbf{r}}{c^2}\mathbf{a}_q\right) \tag{5.5.10a}$$

$$\mathbf{B}_q = \frac{q}{4\pi\varepsilon_o r\left(r-\frac{\mathbf{v}_q\cdot\mathbf{r}}{c}\right)}\left(\frac{\mathbf{a}_q}{c^2}-\frac{\mathbf{v}_q}{cr}\right)\times\mathbf{r} \qquad (5.5.10b)$$

For streak image tubes, the charges are photoelectrons i.e. q=-e.

The entire electromagnetic fields can then be expressed as:

$$\mathbf{E}_{total}=\mathbf{E}_L+\mathbf{E}_q \qquad (5.5.11a)$$

$$\mathbf{B}_{total}=\mathbf{B}_q \qquad (5.5.11b)$$

5.5.3.2 The calculation of photoelectron trajectories under space-charge influence

When the relativistic effect is taken into account, the equation of the motion of an electron should be expressed as:

$$\frac{d}{dt}\left(\frac{m_o v_x}{(1-v^2/c^2)^{1/2}}\right)=q(E_x+(v\times B)_x) \qquad (5.5.12a)$$

$$\frac{d}{dt}\left(\frac{m_o v_y}{(1-v^2/c^2)^{1/2}}\right)=q(E_y+(v\times B)_y) \qquad (5.5.12b)$$

$$\frac{d}{dt}\left(\frac{m_o v_z}{(1-v^2/c^2)^{1/2}}\right)=q(E_z+(v\times B)_z) \qquad (5.5.12c)$$

where c is the speed of light.

After taking all the derivatives, the appropriate expressions for the above equations of motion can be established to be:

$$\frac{d^2x}{dt^2}=\frac{q}{m_o}\left(E_x\left(1-\frac{v_x^2}{c^2}\right)+(v_yB_z-v_zB_y)-\frac{v_xv_y}{c^2}E_y-\frac{v_xv_z}{c^2}E_z\right)\left(1-\frac{v^2}{c^2}\right)^{1/2} \qquad (5.5.13a)$$

$$\frac{d^2y}{dt^2}=\frac{q}{m_o}\left(E_y\left(1-\frac{v_y^2}{c^2}\right)+(v_zB_x-v_xB_z)-\frac{v_xv_y}{c^2}E_x-\frac{v_yv_z}{c^2}E_z\right)\left(1-\frac{v^2}{c^2}\right)^{1/2} \qquad (5.5.13b)$$

$$\frac{d^2z}{dt^2}=\frac{q}{m_o}\left(E_z\left(1-\frac{v_z^2}{c^2}\right)+(v_xB_y-v_yB_x)-\frac{v_xv_z}{c^2}E_x-\frac{v_yv_z}{c^2}E_y\right)\left(1-\frac{v^2}{c^2}\right)^{1/2} \qquad (5.5.13c)$$

To simulate these equations for photoelectrons, the initial conditions of photoelectron emission, i.e. x, y, z, v_x, v_y, v_z, at t = 0 at photocathode, can be simulated by Monte-Carlo method as described in chapter 2. In order to take their emission time differences, it is considered that the photoelectrons are emitted in temporal sequence at the photocathode such that at the emission of the first electron there is no space-charge influence and the second one will experience the repulsive field from the first one and so on. Consequently, the photoelectrons appear spatially-dispersed along the axis of the streak tube corresponding to their initial emission time differences.

The photoelectron trajectories can be calculated by using Runge-Kutta method depicted in chapter 2. However, because equations (5.5.13a), (5.5.13b), (5.5.13c) for one photoelectron are correlated with those of all the others due to the interactions between photoelectrons, the calculation procedure is much more complicated. As the photoelectron packet propagates, the distribution of the photoelectrons in the packet and the size of the packet will change with time and thus the space-charge induced fields must be recalculated for all the photoelectrons in each numerical step. The method to determine the step size here is similar to that described in chapter 2 except that a smaller step size is desired for an adequately accurate calculation. To keep CPU time and memory space for data minimal, a compromise has to be made with regard to the grid size for potential distribution and the step size for trajectories. The maximum temporal step size used here is 500 fs and the potential grid size is 0.125 x 0.125 mm for the focusing region and 0.1 x 0.125 mm for the deflection region.

5.5.3.3 Calculated results

The temporal performance of the Photochron V streak tube design, considering space-charge effects, has been evaluated under the following operating conditions. The overall operating voltage was 10 kV and the electric field at the photocathode was 5 kV/mm. A limiting time resolution of 250 fs was obtained at a streak speed of 2.84 x 10^8 m/s with a photoelectron emission energy spread (FWHM) of 0.2 eV without considering space-charge effects.

It should be appreciated that because the photoelectrons have random initial photoemission conditions, streak images from identical input optical pulses could give different output streak durations under the same operating conditions. This is especially true when only a small number of photoelectrons are involved and thus the recorded image profiles in single-shot experiments appear to be relatively random. Therefore, the specification of the instrumental time resolution and dynamic range of a streak camera should be provided by taking the average of the durations of many recordings under the same operating conditions. As only qualitative information is required here, the following numerical results were produced by taking the average of only two shots and thus the irregularities shown in these figures are inevitable.

Examples of the computed results for various operating parameters are shown in Fig.5.5.1-Fig.5.5.5. The resultant output duration denoted by **tp'** was obtained when space-charge effects, over the region between the photocathode and the exit of the deflectors, were included and that denoted by **tp** was produced when space-charge effects were excluded.

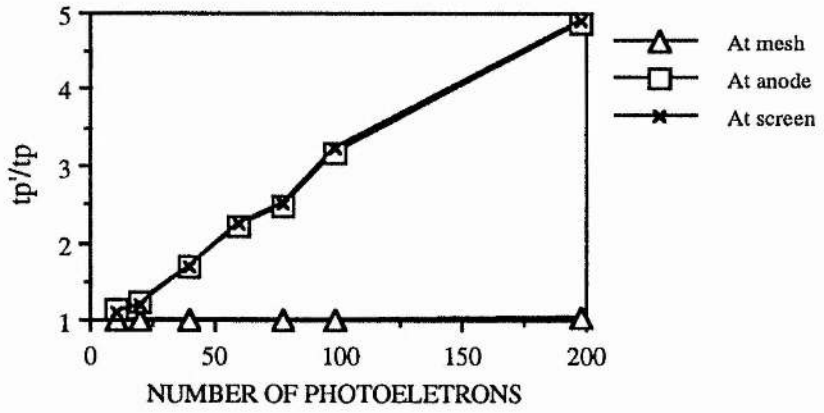

Fig.5.5.1 Relative output pulse duration tp'/tp at mesh, anode and phosphor screen of the streak tube for a slit size of 10 μm x 200 μm and a pulse duration of 200 fs.

Fig. 5.5.1 illustrates the output time durations of photoelectrons respectively at the mesh, anode and phosphor screen when considering space-charge effects for a slit size of 10 μm x 200 μm and an input pulse duration of 200 fs. It is seen that the temporal broadening due to space-charge effects is mainly induced in the mesh-anode section. This is because the transit time in this region is much longer than that in the other regions. Thus, the space-charge effects

are dependent upon the transit time of photoelectrons rather than specific locations within the tube. In the deflector-screen region, the space-charge effects are insignificant because the size of the photoelectron packet becomes large after temporal-spatial conversion and spatial dispersion due to space-charge interactions should be relatively small. Hence, in the following calculations space-charge effects were only considered up to the exit of the deflectors.

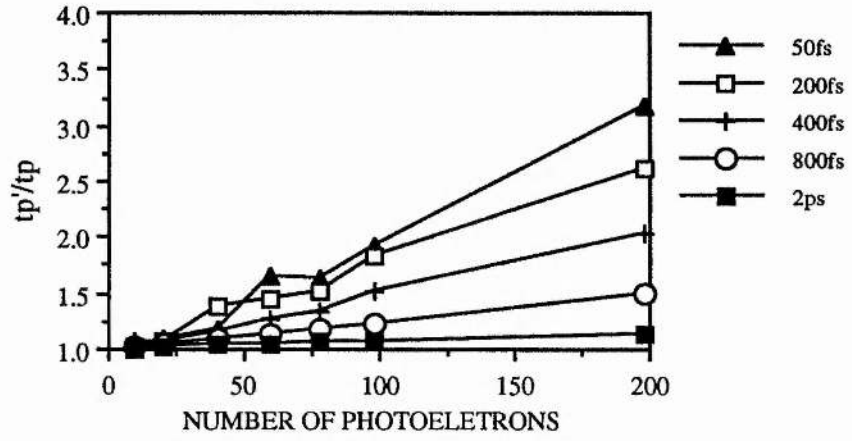

Fig.5.5.2 Relative output pulse durations corresponding to different input pulse durations for a slit size of 20 μm x 500 μm

Fig. 5.5.2 demonstrates the relation between space-charge related time broadening and input pulse duration for a slit size of 20 μm x 500 μm. It shows clearly that the space-charge induced temporal broadening increases with the reduction of input pulse duration and such tendency has also been revealed by experiments[33]. This is because for shorter input pulse durations, the spatial size of the photoelectron packet is smaller and thus stronger space-charge interactions will result. This is why the dynamic range of a streak tube tends to be lower for the recording of pulses with shorter durations. In other words, the achievement of a high time resolution is unfortunately accompanied by a severe lack of dynamic range.

Fig.5.5.3 indicates the influence of the input slit size on the output pulse duration that can be measured by a streak tube. It can be seen that an increase in slit length can alleviate the space-charge effects in the tube if the output signal can be integrated along the slit whereas a change in the slit width has little effect on the duration of the output streak image. This is obvious since the repulsive force between two charges is inversely proportional to their spatial

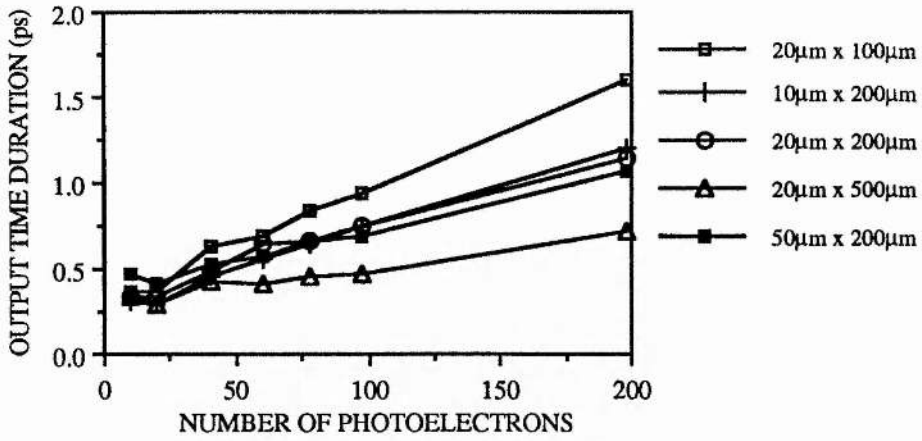

Fig.5.5.3 Output pulse duration as a function of the number of photoelectrons with different slit sizes for an input pulse duration of 200 fs.

separation. For very small slit widths, the photoelectrons are distributed mainly along the length direction and the distances between photoelectrons are governed by the slit length dimension. Thus, although the current densities for the slit sizes of 10 μm x 200 μm and 20 μm x 100 μm are the same, the resultant temporal broadening is greater for the latter case. But, for large slit widths such effects are covered by the slit size influence on the resultant pulse durations.

To speculate the optimum operating conditions for the streak tube, the influence of streak speed on the temporal performance has also studied under space-charge constraints. The resultant output streak durations as a function of the number of photoelectrons under different streak speed are plotted in Fig. 5.5.4. It indicates that as space-charge effects are dominant in determining the resultant output duration, the output image duration appears to be relatively insensitive to the variation of streak speed when space charge effects is included. Only when the streak speed is considerably low or high (e.g. less than 1.5 x 10^8 m/s or higher than 4 x 10^8 m/s for a 20 μm input slit), the influence of input slit size or the deflector fringe field effects will have noticeable contribution to the output pulse duration. Thus the choice of a specific streak speed is not necessarily critical under such operating conditions.

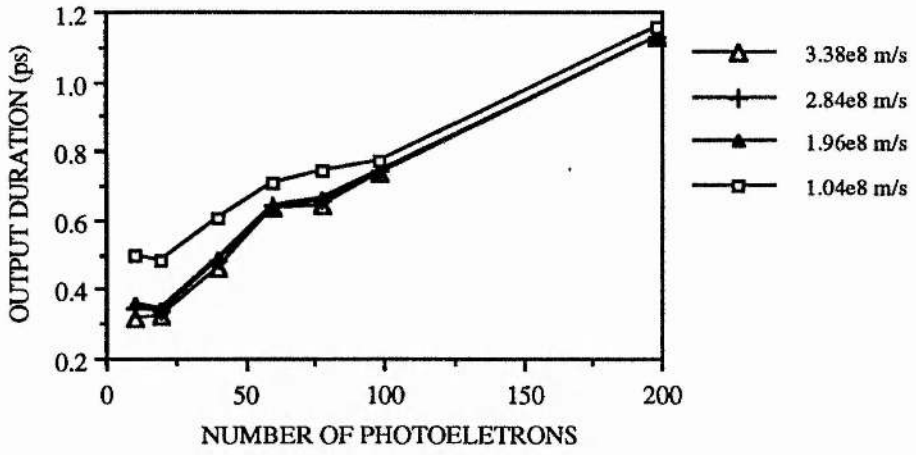

Fig.5.5.4 Output pulse duration under space-charge effects at different streak speeds for the slit size of 20 μm x 200 μm and the input pulse duration of 200 fs

Since the space-charge induced temporal broadening is dependent upon the photoelectron transit time in the tube, it may be worthwhile increasing the overall operating voltage at the expense of the deflection sensitivity. The space-charge induced temporal broadening at different operating voltages has also been investigated and the results are displayed in Fig.5.5.5 for the same operating conditions as those for Fig.5.5.1-3.

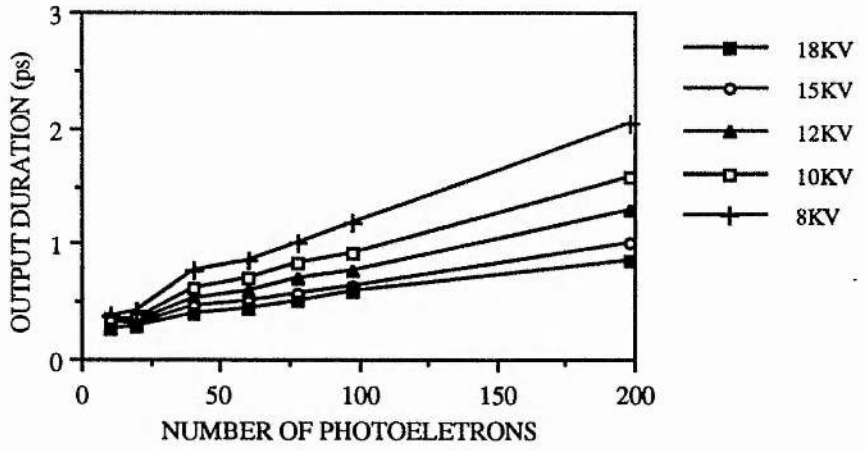

Fig.5.5.5 Output pulse durations for different overall operating voltages with a slit size of 20 μm x 100 μm, an input pulse duration of 200 fs and a streak speed of 2.8 x 10^8 m/s.

These data show that a proportionate increase of operating voltages on the streak tube electrodes leads to a reduction of the space-charge related temporal broadening. Indeed an increase of operating voltages can, to a certain extent, improve the dynamic range of a streak tube despite of the degradation of deflection sensitivity and streak speed. For operating voltages higher than 15 kV, such improvement is less pronounced. Thus, there is a compromise between space-charge effects and streak speed. The results are in good general agreement with those obtained experimentally by other researchers[34].

5.5.4 Theoretical simulation results of the streak tube dynamic range

On the basis of the analysis described in the previous two sections, theoretical simulation of the dynamic range of a streak image can be readily carried out. In doing so, the lower limit, set both by the statistical noise (see equation (5.5.7)) and by the system noise level (see equation (5.5.5)), were used. The upper limit was obtained from space-charge effect calculations. The variation of the dynamic range as a function of input pulse duration have been calculated for both Photochron V and Photochron IV and the results are shown in Fig.5.5.6 which were produced when using a resolution element size of 20 μm in width and 25 μm in length at the photocathode and taking one electron as the statistical-limited minimum number in the resolution area. The initial rms energy spread was assumed to be 0.2 eV and the photocathode electric field was chosen to be 5 kV/mm. The Photochron V tube was operating respectively at 10 kV anode voltage which gave rise to a sweep speed of 2.86×10^8 m/s and at 18 kV overall operating voltage at which the sweep speed was 1.67×10^8 m/s for a deflection ramp voltage of 2 kV/ns. The Photochron IV streak tube was operating at 15 kV anode voltage which produced a sweep speed of 1.51×10^8 m/s. As the number of the photoelectrons is generally small, the value of the output time duration tends to fluctuate due to statistical effects. In order to smooth out such statistical influence, the value of ultimate output duration was obtained by averaging the output durations of many shots. The number of shots was determined by the ultimate total number of photoelectrons which was chosen to be 500. To

reduce the CPU time demand, the slit length in the calculation was chosen to be 200 μm or less.

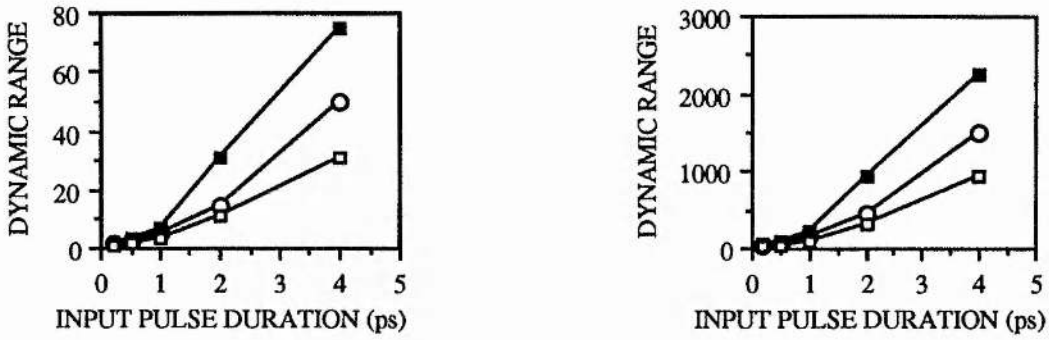

Fig.5.5.6 The predicted dynamic range versus input pulse duration **(a)** dynamic range set by statistical noise limitation, **(b)** dynamic range derived from system noise level limitation. The curves labelled by circles are for Photochron V at 10 kV, the curves labelled by solid squares are for Photochron V at 18 kV and the ones labelled by hollow squares are for Photochron IV at 15 kV.

It is seen from Fig.5.5.6 that the Photochron V tube clearly has a higher dynamic range at a lower anode voltage than that of Photochron IV and an increase of overall voltage to 18 kV can enhance the dynamic range considerably. For example, for an input pulse of 2 ps the dynamic range at 18 kV is double that at 10 kV. For shorter pulse durations, the difference is smaller. If the photoelectrons are integrated along the output slit image, the dynamic range can be significantly increased provided that time distortions can be eliminated through an image processing technique or using a specially-designed input optical lens. A reduction of the slit width from 20 μm to 10 μm only had negligible influence on the dynamic range value. This suggests that it may be beneficial to choose a minimal slit size since it will reduce the requirement for a high streak speed.

The dynamic range data shown in fig.5.5.6 (a) were obtained by using the lower limit of input pulse intensity set by the statistical noise criterion while Fig.5.5.6 (b) were produced by using the system noise level limitation. The later excluded the dynamic range limits of the image intensifier and the readout system which will limit system dynamic range to 150[31]. The difference in the two sets of dynamic range data is in an order of magnitude. In practice, the

dynamic range of a streak camera system is very much dependent upon the performance and combination of its component parts and it is very difficult to produce a model which can cover every configuration. Nevertheless, such theoretical model is necessary and it offers a very useful tool for design optimisation and performance evaluation to complement experimental measurements.

5.6 Experimental evaluation of a single-shot streak camera with TWD deflectors

5.6.1 Description of the streak image tube

A new streak tube[35] was developed and tested in conjunction with Xian Institute of optics and Precision Mechanics, Xian, PR. China which was specifically designed for single-shot operation. The streak tube consisted of a photocathode, an accelerating mesh, focusing electrodes, a TWD deflection system and phosphor screen.

Aiming for a femtosecond time resolution, high spatial resolution and maximum dynamic range, this streak tube is featured with the following aspects. As the time dispersion and spatial aberrations in a streak tube are highly dependent upon the photoelectron initial emission conditions, among which the initial energy spread is one of the influential factors, a specially thin photocathode having large energy bandgap was used in order to achieve a reduction in energy spread. Possible cause of electrode contamination in the photocathode processing was prevented by using the transfer technique so as to improve the signal to noise ratio of the tube. The focusing system was constructed by four cylinder electrodes and optimised for minimum time dispersions and spatial aberrations. To alleviate space charge effects, the electron transit time was minimised by using a short focusing system. To ensure a high streak speed, a meander-type TWD system was employed as it can provide a high dynamic deflection sensitivity over a broad frequency bandwidth. At the ends of the transmission lines, impedance matching structures were employed for the input and output leads of the TWD deflector to reduce RF reflection loss due to the structure discontinuity.

From theoretical analyses, the limiting time resolution was estimated to be 300 fs when the photocathode field strength was 6 kV/mm and the initial energy spread of the photoelectrons is 0.05 eV. The dynamic deflection sensitivity of the TWD system can be as high as 10 cm/kV with frequency bandwidth of 1.8 GHz.

5.6.2 Experimental arrangement and evaluation

To evaluate the performance of this streak image tube in single-shot operation experimentally, a suitable setup was built as shown in Fig.5.6.1. The laser system used was a

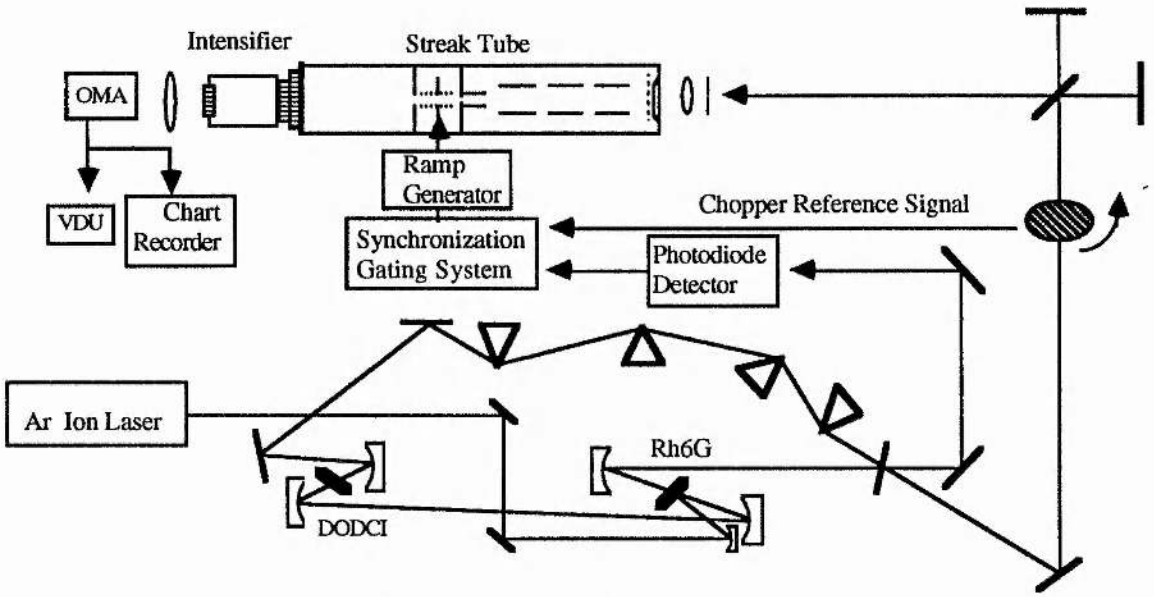

Collide-Pulse Mode-Locked Ring Dye Laser

Fig.5.6.1 The CPM dye laser based experimental setup for single-shot operation of the streak tube with a meander-type travelling-wave deflector

colliding-pulse mode-locked Rh6G ring dye laser which can provide a variety of femtosecond laser pulses. In this experiment, the light signal consisting of 200 fs pulses were used to illuminate the photocathode of the camera via a 50 μm slit and a relay lens having a demagnification of 3. A mircochannel plate (MCP) intensifier, giving a gain of 10^3 and a limiting spatial resolution of 50 lp/mm, was fibre-optically coupled onto the output screen of the streak tube in order to obtain adequate output image intensity. The ramp voltage signal of 1.5 kV/ns, applied to the deflector, was generated by an avalanche transistor circuit and the deflector was suitably terminated to prevent RF reflection. To obtain a synchronised triggering

signal for the ramp circuit, the 200 MHz electrical pulse train from the photodiode was applied to an input of an AND gate circuit. The chopper synchronising signal was also applied to the AND gate via a divide-by-ten network. This allowed sufficient time for the avalanche to recover between sweeps. The streak rewrite due to the trailing edge of the deflection pulse was overcome by applying a 10 kV gating pulse to the photocathode of the camera. This deflection circuitry has the merit of avoiding the need of amplifying the light pulse from the dye laser which is necessary for a photoconductive switch circuit.

It was observed in this experiment that space-charge effects were significant and to reduce such effects the input signal intensity was minimised. But at low input light levels, the background noise became a significant factor which limited the minimum recordable input light intensity. In order to reduce the background noise, the operating time window of the system was required to be of the order of 400 μs or less and this was achieved by using a chopper with a 0.5 mm open slit rotating at 10 - 20 Hz speed. For streak speed calibration, a pair of pulses separated by 6.7ps was provided by an optical delay line comprising a 50/50 beam splitter and two mirrors. The output image of the camera was recorded by a SIT vidicon readout system as mentioned previously.

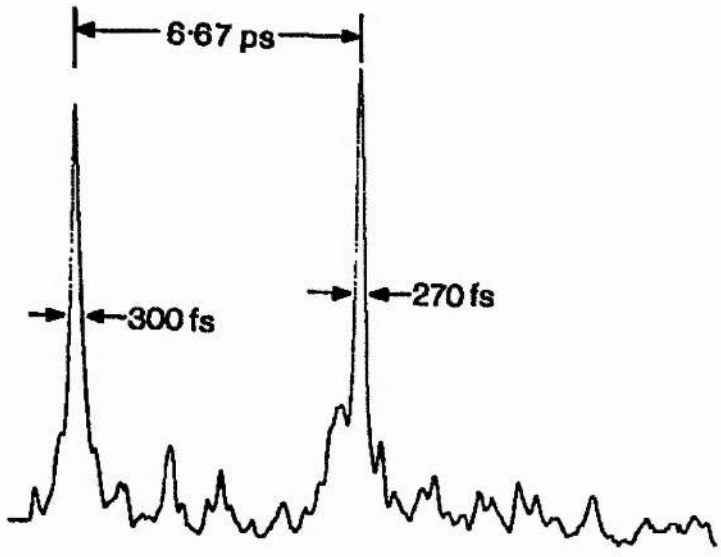

Fig.5.6.2 The recorded best single-shot result indicating a 300 fs time duration

This experiment produced, for the first time, a recorded streak output duration of 300 fs under operating conditions of 8 kV overall voltage and 4 kV/mm photocathode field strength and it continues to be the best time resolution yet reported[1]. The result is shown in Fig.5.6.2. It was recorded at a minimum detectable input light intensity and even at this level it was observed that any increase in the input light intensity caused an increase in the recorded streak image duration. A shorter measured time duration would therefore require a further reduction in input light intensity which may be possible if a low noise image intensifier with higher gain becomes available.

5.6.3 Discussion

During this experiment, it was observed that the time durations of streak images varied from shot to shot in the range of 250 fs to 500 fs. This phenomenon may be caused partly by the fluctuations in the light signal intensity which results in variation of space-charge effects and mostly by the statistical fluctuations in the photoelectron emission since the number of the photoelectrons in each shot was small. It is not possible to justify that 300 fs time duration represents the instrumental time resolution of the system in general and it can only be evaluated by taking the average of a large number of shots. Due to the lack of a sufficiently high-gain intensifier and limited experimental period, the dynamic range of this tube was not measured and space-charge effects were, therefore, the primary factor limiting the measurement of a shorter time resolution for this tube.

Nevertheless, this experiment has proved, for the first time, that a meander-type travelling wave deflector is appropriate for single-shot streak image tubes because it can provide a high deflection sensitivity over broad frequency range. To acquire the predicted limiting resolution, further experiments need to be carried out with the considerations that include higher ramp speed (e.g.. 3 kV/ns), higher electric field strengths at photocathode(through the application of a fast electric gating pulse to the photocathode-mesh electrode), lower jitter(less than 40 ps) and an intensifier with higher gain. It is also worthwhile to consider a completely new streak tube structure which will obviate the need for mesh electrodes and also be able to overcome the initial energy and angle spread limitation.

5.7 Summary

To obtain comprehensive temporal information using a streak camera, it is required to have a high dynamic range. The achievement of an adequate dynamic range has been one of the more important objectives in the development of ultrafast electron-optical streak cameras in single-shot /framing operation in the picosecond/femtosecond regime. Theoretical investigations of the factors limiting the dynamic range of streak image tubes have been carried out where particular attention has been paid to the consideration of space charge effects.

An attempt has been made to theoretically simulate the influence of photoelectron interactions by a method free from priori-model assumptions. This has enabled us to monitor the behaviour of photoelectrons in a streak tube subject to space-charge effects and provided useful additional insight into the mechanisms that limit the tube performance. The influence of various operating parameters, such as slit size, electrode configuration, operating voltages, magnification and type of phosphor screen, on the dynamic range of a streak tube has been studied and the calculated results agree clearly with the available experimental data. It has been shown that the space-charge effects are accumulated during the transit time of photoelectrons throughout the streak image tube. When shorter input pulse durations are involved, more pronounced space-charge effects are observed to arise.

The assessment of streak tube dynamic range has indicated that its upper limit is primarily due to the space-charge interactions within the tube, especially in the mesh-anode area while the lower limit is set by the intrinsic statistical noise of photoemission. It can be generally concluded that in single-shot operation of streak tubes, space-charge effects are the main limiting factors in the achievement of femtosecond time resolutions with a good dynamic range. The calculations of dynamic range have shown that the Photochron V streak tube offers a much higher dynamic range than that of the Photochron IV. For an 1 ps input pulse, a Photochron V at 10 kV can provide a dynamic range of around 5 under the statistical limit and 150 under a system noise-level criterion whereas a Photochron IV at 15 kV can only give dynamic range of respectively 3 and 93.

As a result of this work, it is suggested that a refined optimisation procedure should be considered with regard to a better design of femtosecond streak camera systems. For instance, to alleviate the space-charge effects and enhance the dynamic range of a streak tube, an electron-optical focusing system having minimum photoelectron transit time (i.e. shorter lengths, higher operating voltages) and a reduced electron-optical magnification is required in addition to a phosphor screen with a fully optimised electron/photon conversion efficiency. It is also important to use an image intensifier, with higher signal-to-noise ratio and higher gain, and a two-dimensional readout system, which can accumulate information along the slit length and enhance the signal-to-noise ratio of the output image.

A high streak speed in a single-shot streak tube may be achieved by using travelling-wave deflectors which can offer a high deflection sensitivity over a broad frequency bandwidth. This has been confirmed by the experimental evaluation of a streak tube having a travelling-wave deflector that has recorded an output streak duration of 300 fs. This result, together with the analyses described in this chapter, thus implies that liming time resolutions of less than 300 fs are feasible in a fully optimised streak camera design.

5.8 Reference

[1] Finch A, Liu Y, Niu H, Sibbett W, Sleat W E, Walker D R, Yang Q L Zhang H, Proc. 18th ICHSPP, SPIE Vol. 1032, pp.622-626 (1988)

[2] Kinoshita K, Ito M, Suzuki Y, Rev. Sci. Instrum., Vol. 58, pp.932-938 (1987)

[3] Friedman W, Jackel S, Seka W, Proc. 12th ICHSPP, SPIE Vol.97, pp.544-548 (1976)

[4] Bradley D J, Bryant S F, Taylor J R, Sibbett W, Rev. Sci. Instrum., Vol.49 (2), pp.215-219 (1978)

[5] Bradley D J, Higgins J F, Key M H, Appl. Phys. Lett., Vol. 16, pp.53-55 (1970)

[6] Milam D, Gallagher C C, etc., Rev. Sci. Instrum., Vol. 43, pp. 1482-1484 (1972)

[7] Sleat W E, PhD Thesis, The Queen's University of Belfast (1974)

[8] Thomas S W, Tripp G R, Coleman L W, Proc. 10th ICHSP, pp.127-130 (1972)

[9] Tsuchiya Y, Inuzuka E, Suzuki Y, Yu W, Proc. 13th ICHSPP, pp.517-520 (1978)

[10] Cunin B, Miehe J A, Sipp B, Lompre L A, Mainfray G, Thebault J, Proc. 12th ICHSP, SPIE Vol. 97, pp.3-10 (1976)

[11] Bradley D J, Sibbett W, Appl. Phys. Lett., Vol. 27, pp.382-384 (1975)

[12] Bryant S F, PhD Thesis, Imperial college of Science and Technology, University of London (1978)

[13] Auston D H, Appl. Phys. Lett., Vol. 26, pp. 101-103 (1975)

[14] Mourou G, Knox W, Appl. Phys. Lett., Vol. 35, pp. 492-495 (1979)

[15] Auston D H, Johnson A M, Smith P R, and Dean J C, Appl. Phys. Lett., Vol. 37, pp.371-373 (1980)

[16] Margulis W, Sibbett W, Opt. Commun., Vol. 37 (3), pp.224-228 (1984)

[17] Tsuchiya Y, Takeshima A, Inuzuka E, Suzuki K, Koishi M, Kinoshita K, Proc. 16th ICHSPP, SPIE Vol.491, pp.86-94 (1984)

[18] Eagles R T, PhD Thesis, Imperial College, University of London (1986)

[19] Jackson M C, Long R D, Lee D, Freeman N J, Laser and Particle Beams, Vol.4 (1), pp.145-156 (1986)

[20] Margulis W, Sibbett W, Opt. Commun., Vol. 51 (2), pp.91-94 (1984)

[21] Korobkin V V, Stepanov B M, Fanchenko S D, Schelev M Ya, Optical and Quantum Electronics, Vol.10 (5), pp.367-381 (1978)

[22] Devilbiss A J, Electronics, Vol. 42, pp.190-192 (1969)

[23] Fukushlma M, US Patent No. 3504222 (1970)

[24] Owaki K, Terahata S, Hada T, Nakanura T, Pro. IRE, Vol.38, pp.1172-1176 (1950)

[25] Schelev M Ya, Proc. 13th ICHSPP, pp.142-150 (1978)

[26] Liu Y, MSc Thesis, Xian Institute of Optics and Precision Mechanics, PR. China (1985)

[27] Yamada I, Takagi T, IEEE trans. Electron Devices, Vol. ED-19 (2), pp. 204-213 (1972)

[28] Majamada J, Proc. 13th ICHSPP, pp.821-824 (1978)

[29] Niu H, Sibbett W, Rev. Sci. Instrum., Vol. 52 (12) pp. 1830-1836 (1981)

[30] Bradley D J, Bryant S F, Sibbett W, Rev. Sci. Instrum., Vol. 51 (6), pp.824-831 (1980)

[31] Hull D R, Freeman N J, J. Phys. E: Sci. Instrum., Vol.13, pp.685-690 (1980)

[32] Bradley D J, Rev. Sci. Instrum., Vol. 51 (6), pp.824-831 (1980)

[33] Suyama M, Kinoshita K, Proc. 18th ICHSPP, SPIE Vol. 1032, High Speed Photography and Photonics, pp.448-452 (1988)

[34] Takiguchi Y, Kinoshita K, Suyama M, Inagaki Y, Tsuchiya Y, SPIE Vol.693 High Speed Photography, Videography, and Photonics IV, pp.105-110 (1986)

[35] Niu H, Zhang H, Yang Q L, Liu Y, Wang Y C, Reng Y A, Zhou J L, Proc. 18th ICHSPP, SPIE Vol.1032, pp.472-280 (1988)

Chapter 6

THE OUTPUT RESPONSE FIDELITY STUDY OF A PHOTOCHRON V STREAK TUBE

6.1 Introduction

As streak cameras are developed particularly for the study of the temporal structures of ultrashort laser signals, or the luminous phenomena induced by them, it is desirable to ensure the fidelity of the measurement provided by such instruments. Increasingly stringent demands placed upon streak cameras by research applications have led to extensive studies of their time resolving capability in order to optimise their temporal performance[1,2,3,4,5]. In the previous chapters, the spatial and temporal performance of synchroscan and single-shot streak cameras have been studied by using the concept of limiting spatial and time resolutions. Based on these studies, the design of the Photochron V streak tube has been accomplished to provide a limiting time resolution of 250 fs. To extend their usefulness and obtain unambiguous interpretation of the experimental data provided by them, it is necessary to specify the minimum time-scale which can be measured by such instruments with adequate fidelity. Such information can be achieved by examining the output responses of a streak tube for input signals having a variety of temporal profiles such that the temporal-information borne by photoelectrons can be inspected.

6.2 The limiting time resolution

As described in chapter 2, the limiting time resolution can be specified using one of two criteria[6]. One is the full width at half maximum (FWHM) of the output temporal response of the streak tube to a delta-function-like input signal, which is commonly used both in theoretical and experimental evaluations. The other is given by Rayleigh limit Δt such that a 20% contrast

(or modulation) is shown in the output response to a signal consisting of two delta function pulses separated in time by Δt. To illustrate the two criteria, the temporal responses of the Photochron V streak tube respectively to a 10 fs pulse and to a signal consisting of two 10 fs pulses separated by 250 fs are displayed in Fig.6.2.1. These profiles were obtained for a S1 photocathode illuminated at its long wavelength threshold (i.e. 0.2 eV rms value of initial energy spread), a slit width of 10 μm at the photocathode. A ramp voltage of 2 kV/ns was applied to the deflectors giving a streak speed of 2.86×10^8 m/s and influence of the synchroscan noise, timing jitter and space-charge effects are excluded.

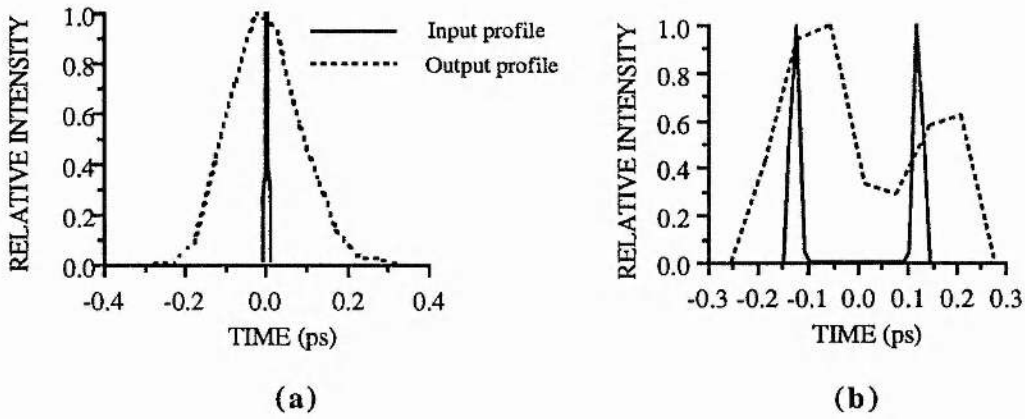

Fig.6.2.1 Temporal responses for time resolution evaluation

Fig.6.2.1a indicates a time resolution of around 200 fs whereas Fig.6.2.1b illustrates a modulation of over 20% for 250 fs separation but it is significantly influenced by the photoelectron emission conditions which give rise to intensity difference in the two output subpulses. This implies that the second criterion is more critical than the first one and a limiting time resolution of 250 fs can just be specified. It can be seen clearly in fig.6.2.1 that the output response is completely governed by the streak tube performance and thus the inherent temporal performance of the streak tube is revealed. This limiting time resolution is set by factors such as time-related dispersive photoemission processes in the photocathode, the initial spreads in the emission energies and angles of the photoelectrons, the spatial size of the input slit, the limited spatial resolution of the phosphor screen and deflector performance.

To understand how the temporal performance of a streak tube influences the time information of photoelectrons during their propagation, the output temporal profiles at different stages in a Photochron V streak tube have been studied and are displayed in fig.6.2.2 for an input signal with a time duration of 300 fs.

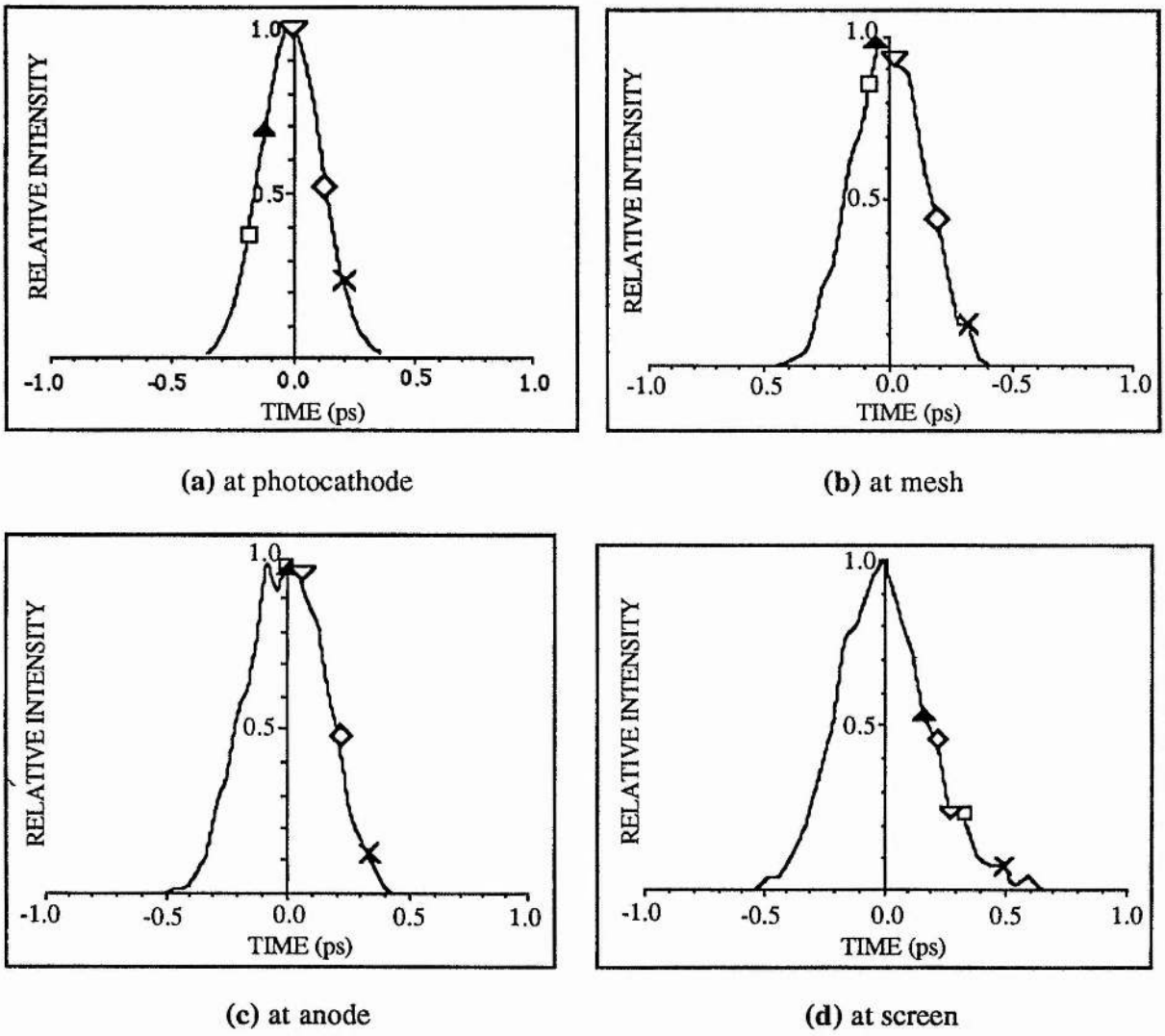

Fig.6.2.2 The temporal profiles of photoelectrons for an input pulse with 300 fs time duration at photocathode, mesh, anode and phosphor screen

The five different marks on the curves represent five temporally-distinct photoelectrons which are arbitrarily selected from the photoelectron pulse at the photocathode in order to inspect the evolution of their time sequencing and to understand the mechanism of the temporal information loss caused by the streak tube. It shows that some photoelectrons tend to deviate

significantly from their original temporal locations. For example, those in the trailing edge of the original temporal profile appear near the temporal centre of the profile at the mesh, move into the leading edge in an altered time order relative to each other at the phosphor screen. Other photoelectrons may remain nearly at the same temporal locations as where they were initially at the photocathode such as the ones in the leading edge. Although these photoelectrons are arbitrarily chosen as an example, it does illustrate generally that due to the inherent differences in the initial emission conditions, photoelectrons emitted simultaneously from a finite spatial area on the photocathode travel at different velocities and thus arrive at different times and are dispersed spatially at locations such as mesh, anode and phosphor screen. The temporal dispersions are mainly induced in the photocathode-mesh region, accentuated slightly in the focusing region and then mixed with spatial dispersions by the deflection section at the phosphor screen. Thus the spatial dimension of the resultant output image displayed on the phosphor screen, which ultimately determines the limiting time resolution, is a mixture of temporal and spatial dispersions, induced in the tube, combined with the input slit size effect. The time information of the output response from the streak tube is essentially scrambled. Therefore, the limiting time resolution only represents a latitude of error induced by the time response characteristic of the streak tube.

For input signals having time durations longer than the limiting time resolution, the streak tube can only provide an estimation of the input pulse duration by means of deconvolving the time resolution value from the full width half-maximum (FWHM) value of the output profile. It can just discriminate substructures separated by more than 250 fs with a modulation depth around 100% but not with low modulation. In other words, the output responses of the streak tube cannot represent, in a linear manner, the input signals in a time regime comparable to the limiting temporal resolution. This leads to a question as to the minimum time-scale on which the output responses of the streak tube can offer high-fidelity and unambiguous information that can be directly related to the optical input signal. Obviously, measurements on a longer time-scale will provide higher fidelity. But more specified information on the exact value of the minimum time-scale which can be resolved with adequate fidelity is of practical importance in situations where their maximum capability and precise interpretation is required.

To be able to specify this minimum timescale which can be resolved with adequate fidelity, for example less than 10% error, an investigation has been made to assess the output responses of our Photochron V streak tube for pulse-pair input signals having a variety of pulse durations and separations as displayed in Fig.6.2.3 (a)-(j).

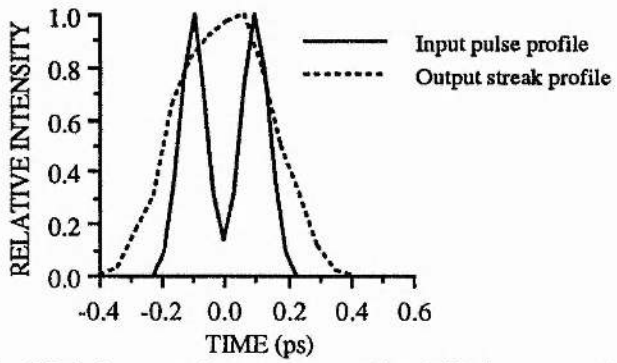

(a) 100 fs input pulses separated by 200 fs

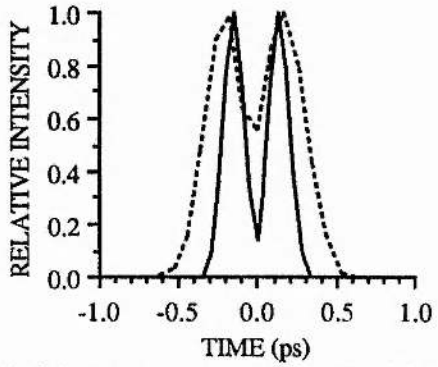

(b) 150 fs input pulses separated by 300 fs

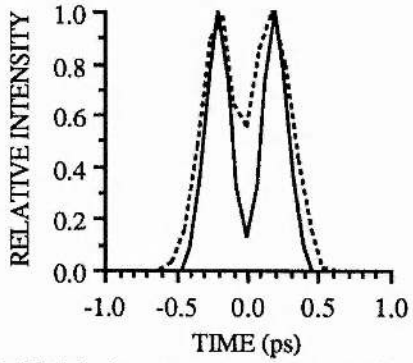

(c) 200 fs input pulses separated by 400 fs

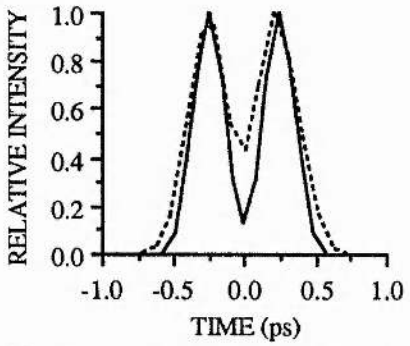

(d) 250 fs input pulses separated by 500 fs

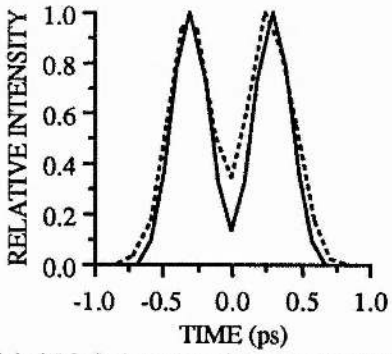

(e) 300 fs input pulses separated by 600 fs

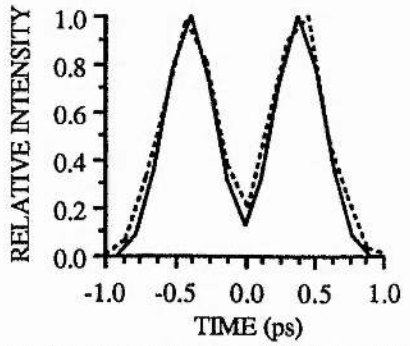

(f) 400 fs input pulses separated by 800 fs

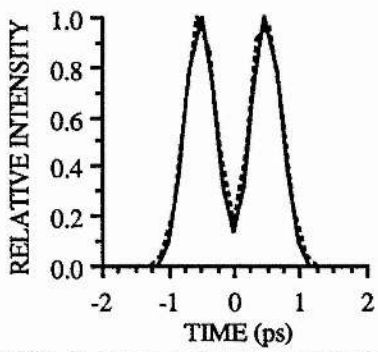

(g) 500 fs input pulses separated by 1 ps

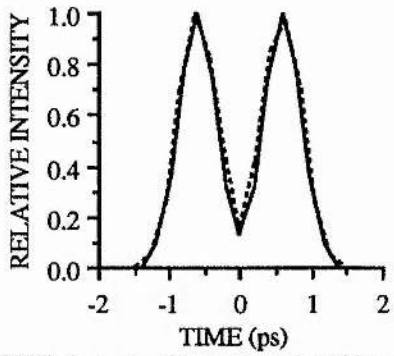

(h) 600 fs input pulses separated by 1.2 ps

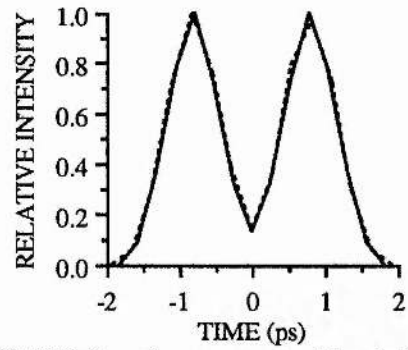

(i) 800 fs pulses separated by 1.6 ps

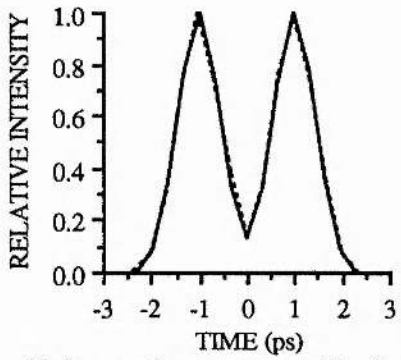

(j) 1 ps pulses separated by 2 ps

Fig.6.2.3 The output streak responses of the streak tube for optical pulse-pairs having various pulse duration and separations

It can be readily seen from Fig. 6.2.3 that the output profiles deviate from the input profiles substantially due to the influence of the streak tube for the photoelectron signals having durations or separations less than 500 fs. Such deviations decrease as the input pulse durations and separations are increased. For instance, when the input pulse duration is less than 500 fs, the percentage of output profile deviation from the original input profile ranges from 15% for 500 fs up to 60% for 250 fs. In this case, the pulse durations of the input signals can be estimated and a modulation of 10% can be observed in the output responses that relate to input signals having 100% modulation depth. The entire pulse shape tends to be distorted due to the modulation loss and individual pulse expansion. For the input pulse signals in the range of 400 fs to 800 fs, the pulse duration deviations are reduced gradually from 15% to 5% and the modulation loss from 10% to 2% such that a qualitative recognition of the original signal

becomes possible. For input signals having durations of 800 fs and separation of 1.6 ps or above, the output responses can reproduce the input profiles with less than 5% deviations in both pulse duration and modulation. As the information fidelity improves gradually with the increase of input signal timescales, there is no clear distinction of the time-scale which can be defined as the minimum time unit for high fidelity time measurement. Its specification is very much dependent on the requirement of actual applications. For this particular streak tube, if a less than 5% deviation in both time duration and modulation is required then the timescale can be claimed as ≥ 800 fs where an unambiguous identification of optical input signals can be achieved.

It should be noticed that the above analysis was carried out under ideal operating conditions. In practice, the laser and electrical noise in synchroscan operation and space-charge effects in single-shot operation are always present as described in chapters 3 and 5 respectively and these factors can have significant influence on the temporal performance in timescales below 500 fs. It is therefore more realistic to examine the output response features with consideration of these factors.

6.3 The output responses in synchroscan operation

As stated in chapter 3, in the synchroscan operation of streak cameras the time resolution is degraded due to phase and amplitude noise in the laser and RF electronic sources which lead to perturbation in the streaked image superimposition. Therefore, it is worth studying the output responses to different input signals under these noise effects to demonstrate how well the temporal information of photoelectrons is transferred under noise constraints.

To begin with, the output temporal responses for Gaussian photoelectron pulses having time durations of 10 fs, 250 fs, 500 fs, 1 ps, 2 ps are examined and are reproduced in Fig.6.3.1. These data were obtained for two selected synchroscan operating conditions. These are zero timing jitter with 80 dB signal-to-noise ratio (abbreviated as snr in the figure), 0.1 ps timing jitter with 120 dB signal-to-noise ratio. From the available experimental data given by publications on laser noise characterisations and synchroscan streak camera studies, 80 dB snr

for active synchronisation operation of streak camera is a realistic figure[7] and a timing jitter of less than 0.2 ps accompanying 120 dB snr may be possible for synchroscan operation using electronic feedback stabilisation techniques[8]. As a comparison, the output profiles without synchronisation noise influence are also provided.

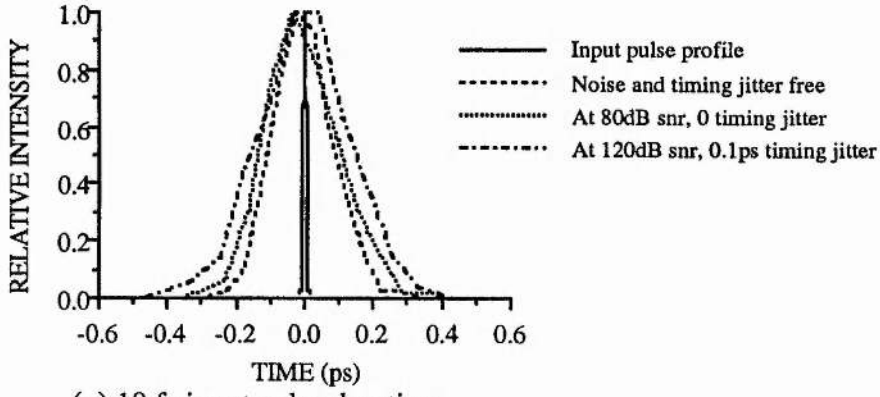

(a) 10 fs input pulse duration

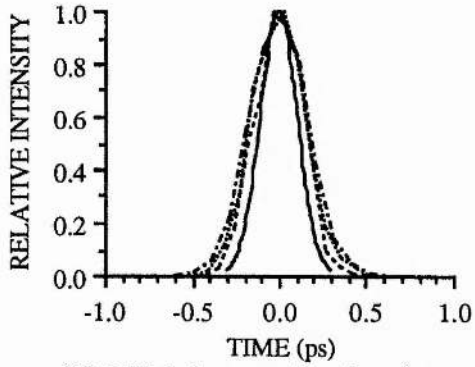

(b) 250 fs input pulse duration

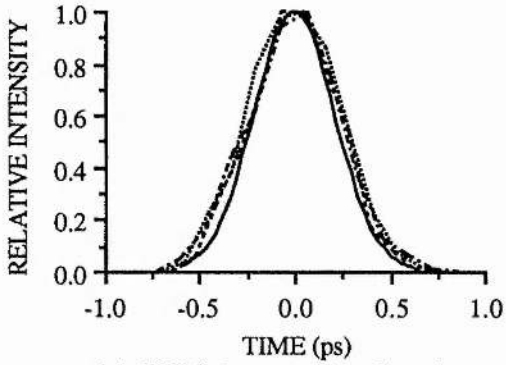

(c) 500 fs input pulse duration

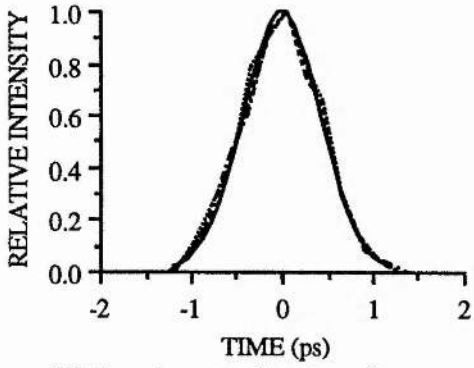

(d) 1 ps input pulse duration

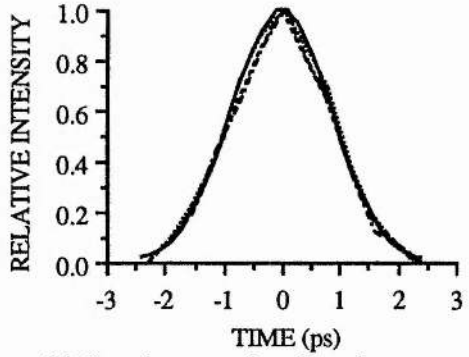

(e) 2 ps input pulse duration

Fig.6.3.1 Output temporal response profiles for Gaussian input pulses under conditions with and without synchroscan noise and jitter influence

It can be seen that the inclusion of noise and timing jitter leads to an increase in the time durations of the recorded output profiles but it does not alter the profile shapes. For the condition of 80 dB snr with a zero timing jitter, the ultimate time resolution is degraded to 280 fs whereas for the condition of 120 dB snr with 0.1 ps timing jitter, the ultimate time resolution is deteriorated to 350 fs. For 500 fs input pulses, the output time duration deviations are 20% and 25% respectively.

In general applications, the measured events often have unknown temporal structures. Using symmetrical profiles as input photoelectron signals to quantify the temporal performance of a streak tube could, therefore, be regarded as unsatisfactory. To ensure a generally valid evaluation, input signals having rectangular profiles have been considered and the output profiles are shown in Fig. 6.3.2.

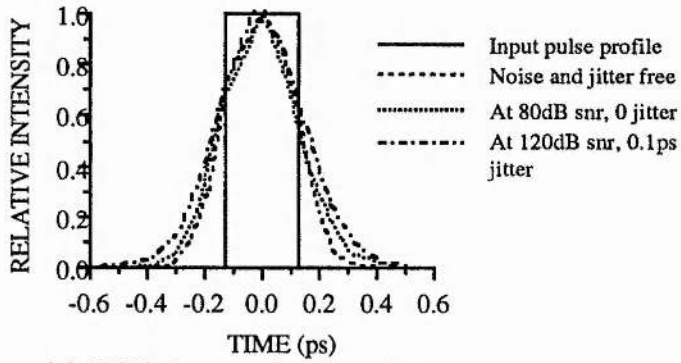

(a) 250 fs input pulse duration

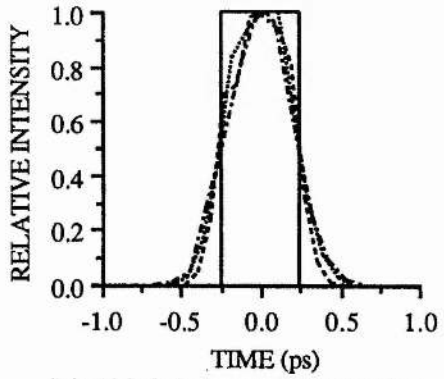

(b) 500 fs input pulse duration

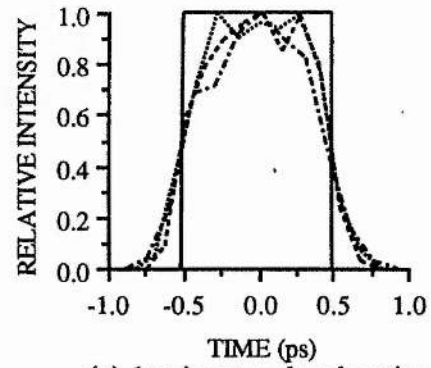

(c) 1ps input pulse duration

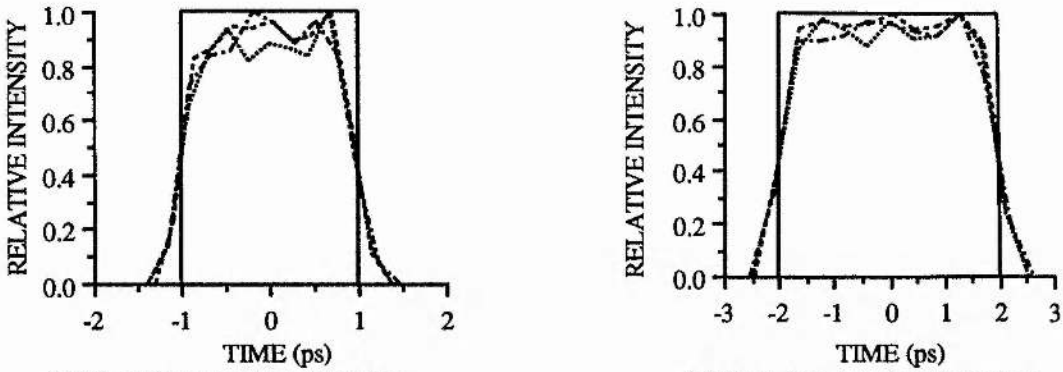

(d) 2 ps input pulse duration (e) 4 ps input pulse duration

Fig.6.3.2 Output streak profiles for rectangular-shaped optical input pulses under conditions with and without synchroscan noise and jitter effects

It is obvious that for the input signal with 250 fs time duration, instead of rectangular shape, the streak output profile is characterised more closely by a Gaussian profile. For the 500 fs input pulse, some evidence of a flat top emerges in the output profiles but the sharp corners have been smoothed out. As the input pulse duration is increased to 1 ps, the output profile starts to show more of the original rectangular feature with a time duration error of 5%. Extended leading and trailing edges of around 400 fs are the inevitable evidence of the tube limiting time resolution effect. This suggests that the tube can be used to diagnose light signals in a time-scale $\geq$ 1 ps under the given noise and timing jitter conditions with 5% or less infidelity.

Further demonstration of the tube ability to diagnose the temporal signatures of light signals can be provided by simulating the output responses for input signals consisting of two Gaussian pulses differing in intensity and with preselected time intervals under the same conditions as the above and the results as plotted in Fig. 6.3.3. Evidently, the existence of the RF noise and optical pulse timing jitter induces output time duration broadening and a modulation depth loss for time-scales less than 1 ps. For time-scales $\geq$ 1 ps, the discrepancy of the output temporal structure from that of the original input pulse is reduced to less than 5% for the 80 dB snr case and 7% for the 120 dB snr and 0.1 ps timing jitter case. This confirms that

the minimum time-scale, on which high fidelity time information can be provided, can be estimated to be around 1 ps for the given operating conditions.

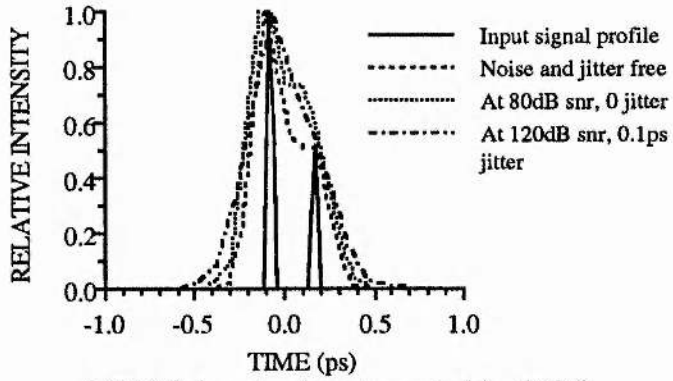

(a) 10 fs input pulses separated by 250 fs

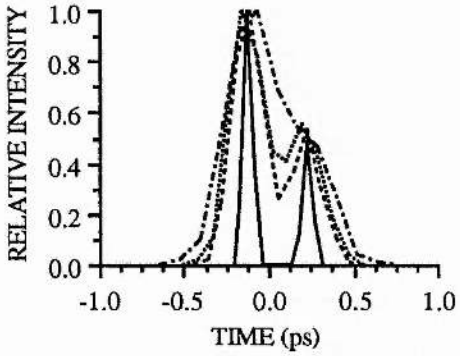

(b) 50 fs pulses separated by 350 fs

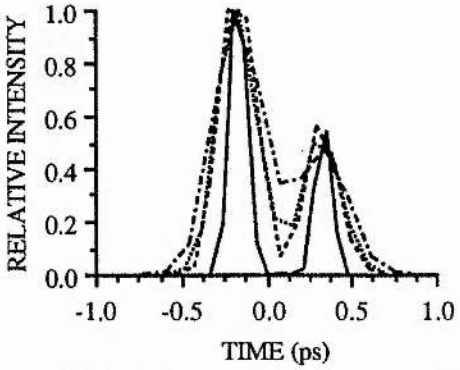

(c) 100 fs pulses separated by 500 fs

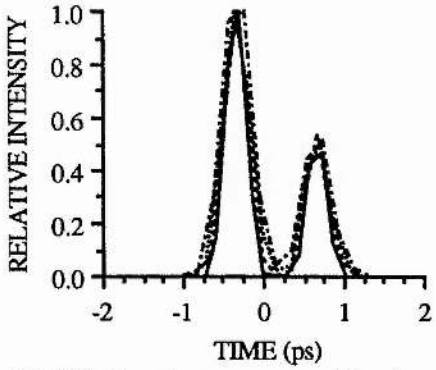

(d) 250 fs pulses separated by 1 ps

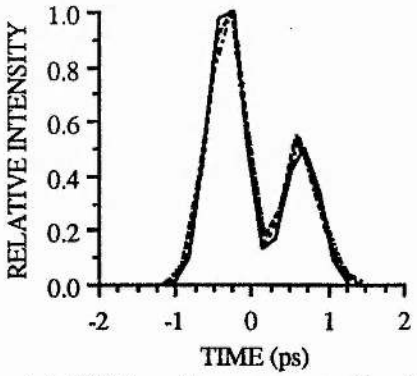

(e) 500 fs pulses separated by 1 ps

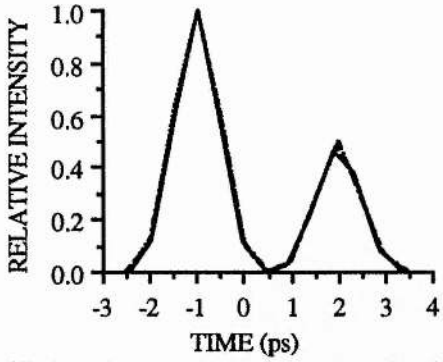

(f) 1 ps input pulses separated by 3 ps

Fig.6.3.3 The output streak profiles for pulse-pair signals under conditions with and without synchroscan noise and timing jitter effects

6.4 The output response profiles in single-shot streak operation

In single-shot streak operation, the space-charge effects are the main concern which tends to limit the maximum acceptable number of photoelectrons. The influence of this factor on the output response profiles for several selected input signals have been assessed under the same tube operating conditions as those employed in section 6.2 except that space-charge effects are included and the number of photoelectrons is chosen to be that which produces an input current density near the upper limit of the dynamic range of the tube. Since the number of photoelectrons is very small, an integration of photoelectrons is made along the selected slit length direction so as to produce relatively smooth temporal profiles. The slit lengths used are respectively 400 μm for 250 fs, 500 fs pulses, 100 μm for 1 ps, 2 ps pulses and 25 μm for 4 ps pulse. The output response profiles without space-charge influence are also presented in order to inspect the pure influence of space-charge effects. The output streak profiles for Gaussian input pulses with selected time durations are illustrated in Fig.6.4.1. It is seen that the output temporal profiles where space-charge effects were included tend to have some irregularities for time durations shorter than 1 ps and this is because a very limited number of photoelectrons are involved. This should be improved by the utilisation of image intensification. The 20% time duration broadening shown in the output profiles with space-charge effects is in accordance with the dynamic range definition. The inspection of these profiles reveals that for timescales shorter than 1 ps, the output streak profiles are very much

affected by the statistical noise of the photoelectrons and for timescales ≥ 1 ps, the streaked temporal profiles under space-charge influence start to follow the shapes of the space-charge-free output profiles.

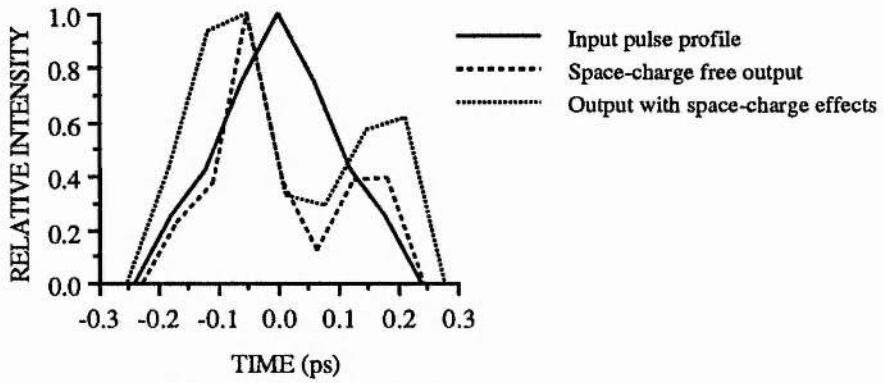

(a) 250 fs input pulse duration

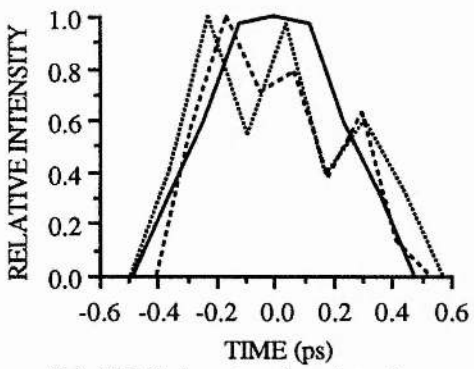

(b) 500 fs input pulse duration

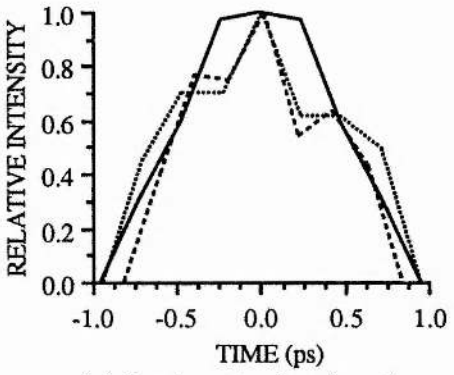

(c) 1ps input pulse duration

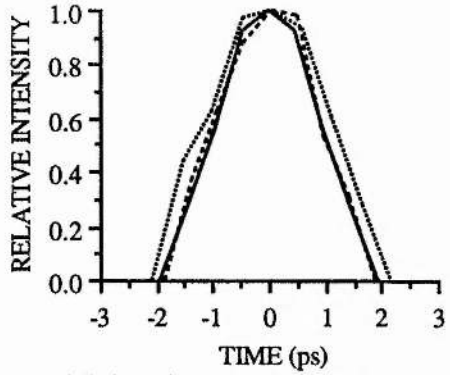

(d) 2 ps input pulse duration

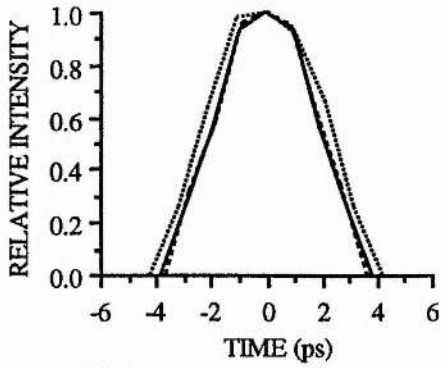

(e) 4 ps input pulse duration

Fig.6.4.1 The output streak responses for Gaussian input pulses where space-charge effects have been included

To determine the high fidelity minimum timescale with confidence, rectangular pulses and pulse-pair profiles with different time durations and separations have been taken as input signals and the obtained output responses are shown in Fig.6.4.2 and Fig.6.4.3 respectively.

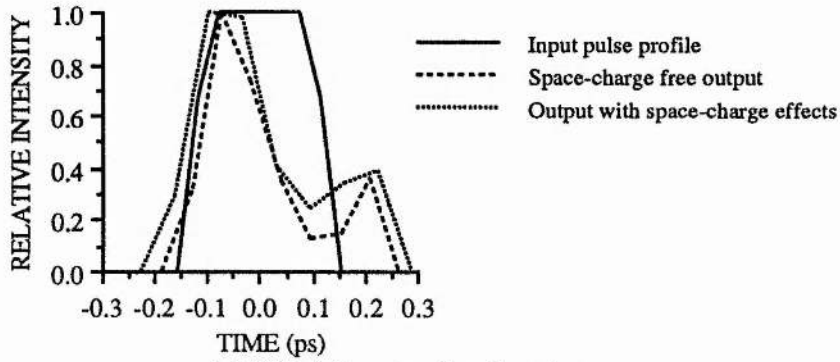

(a) 250 fs input pulse duration

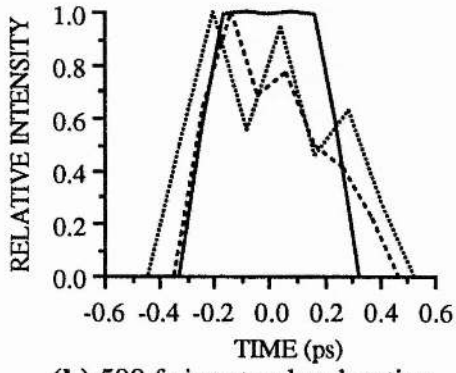

(b) 500 fs input pulse duration

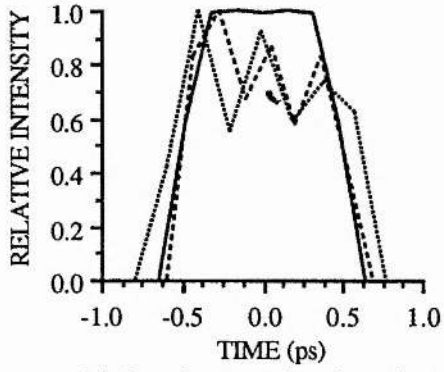

(c) 1 ps input pulse duration

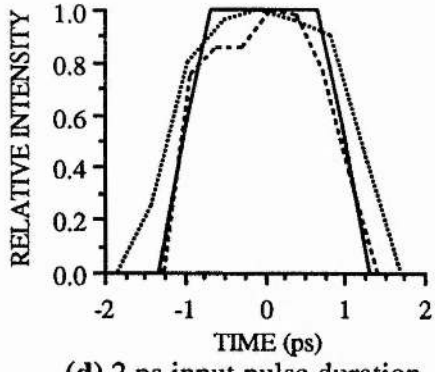

(d) 2 ps input pulse duration

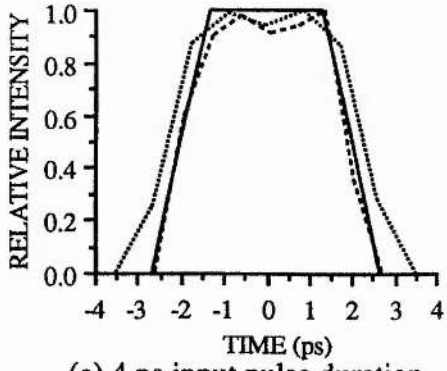

(e) 4 ps input pulse duration

Fig.6.4.2 The output responses for rectangular input pulses where space-charge effects have been considered

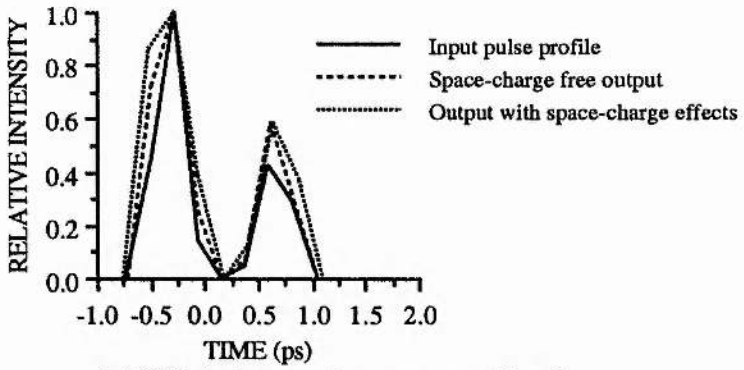

(a) 250 fs input pulses separated by 1 ps

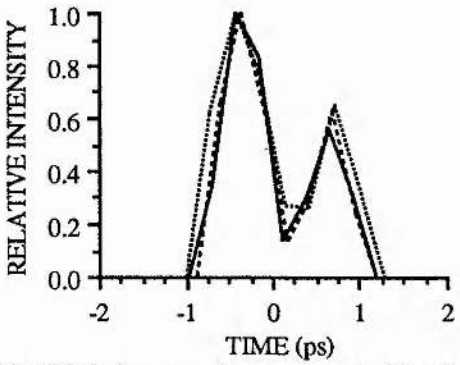

(b) 500 fs input pulses separated by 1 ps

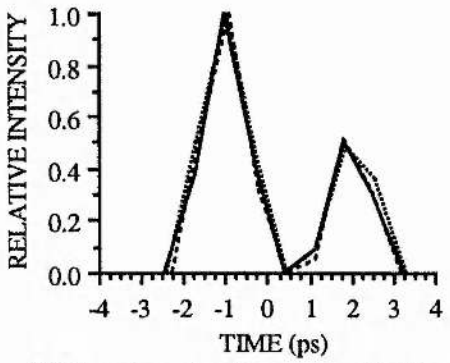

(c) 1 ps input pulses separated by 3 ps

Fig.6.4.3 The output responses for pulse-pair signals where space-charge effects were included

These results indicate that the minimum timescale for high fidelity information assessment can be limited by the acceptable number of photoelectrons and provided that this is not a problem, then the minimum time-scale can be specified to be around 1 ps. Without using intensification, it will be limited to more than 2 ps. As only a limited number of selected cases were taken for the pulse-pair signal case, it may require a wider range of study to adequately illustrate the ultimate time resolving ability of the streak tube under the influence of space-charge effect.

6.5 Summary

In this chapter, particular attention has been given to the fidelity assessment of the time-resolved information provided by a streak tube. A computationally-based theoretical investigation of the temporal response characteristics has been carried out for a range of chosen

photoelectron signals under practical operating conditions for a Photochron V tube. This theoretical approach, aimed at the precise determination of the temporal resolving characteristics of streak cameras, provides a direct demonstration of their temporal performance which is more compatible with the experimental evaluation results. These studies have indicated that the time dispersions and spatial aberrations inherent in a streak tube on the whole cause a scrambling effect in the temporal information of photoelectrons when the time-scale involved is comparable to the limiting time resolution. To accurately identify the time profiles, the timescales of the input light signals are required to be much longer than the tube limiting time resolution. It has been suggested that a minimum time-scale can be specified where the temporal scrambling effect will be negligible and where appropriate fidelity in its output responses can be ensured. For this reason, the output responses of a Photochron V streak tube configuration, which has a calculated limiting time resolution of 250 fs (FWHM), have been examined. It has been shown that this minimum time data has been estimated to be ~800 fs when synchronisation noise (and jitter) and space charge effects are excluded. When the synchronisation noise and timing jitter in synchroscan operation are considered, this value is increased. For example, for 80 dB snr with zero timing jitter or 120 dB snr with 0.1 ps timing jitter, this minimum timescale is increased to around 1 ps. Similarly, when space-charge effects in single-shot operation are taken into account in the output profiles, the minimum timescale required for a linear display of the input signals is estimated to be > 1 ps.

It follows from this type of considerations that specifications of streak camera performance should not just relate to the limiting time resolution and dynamic range. The timescale within which pulse profile information can be unambiguously displayed must also be determined. This latter timescale can be substantially in excess of the limiting time resolution.

6.6 References

1 Zavoisky E K, and Fanchenko S D, Applied Optics, Vol. 4, No. 9, PP. 1155-1167, (1965)

2 Niu H, Sibbett W and Baggs M R, Rev. Sci. Instrum., 53 (5), pp.563-569 (1982)

3 Kinoshita K, Ito M and Suzuki Y, Rev. Sci. Instrum., 58 (6) pp. 932-938 (1987)

4 Niu H, Degtyareva V P, Platonov V N, Prokhorov A M, Schelev M Y, Proc. of 18th ICHSPP, SPIE vol. 1032, pp.79-85 (1988)

5 Finch A, Liu Y P, Niu H, Sibbett W, Sleat W E, Walker D R, Proc. of 18th ICHSPP, SPIE. vol. 1032, pp. 622-626 (1988)

6 "Workshop on picosecond streak cameras", 16th Proc. of ICHSPP, SPIE Vol.491, pp.374-375 (Strasbourg 1984)

7 Finch A, Liu Y, Sleat W E, Sibbett W, Chen G, Proc. 18th ICHSPP, SPIE., Vol. 1032, pp. 97-104 (1988)

8 Spence D E, Evans J M, Sleat W E, Sibbett W, Opt. Lett., Vol.16 (22), pp.1762-1764 (1991)

Chapter 7

DESIGN AND ASSESSMENT OF PICOSECOND FRAMING CAMERAS

7.1 Introduction

The ultrafast diagnostic techniques described in previous chapters are developed to access time-resolved one-dimensional information of light events. However, in research areas such as laser-induced fusion and laser plasma physics, atomic and radiation physics[1], two-dimensional ultrafast diagnostics having moderate spatial resolution and short exposure times (typically < 1ns) are desirable. For example, in inertial confinement fusion (ICF) experiments an essential requirement for the achievement of inertial confinement fusion using laser drivers is that the D-T fuel be compressed symmetrically with minimum increase in entropy. Consequently, the study of the hydrodynamics of fuel-pellet implosions under realistic conditions, e.g., nonuniform laser drivers and imperfect targets, becomes very important. It is imperative to allow direct observation of hydrodynamic instabilities and asymmetries that can degrade the performance of a fuel-pellet implosion. The laser-produced plasmas radiate in the spectral region of 0.1-10 keV range.

By X-ray spectroscopy or X-ray imaging, the detailed structure and evolution of laser produced plasmas can be obtained. However, the plasmas are usually 100-1000 μm in size and have very high density gradients, particularly at early times. Thus it is desirable that the imaging system be able to resolve structure on a spatial scale of ~ 1-10 μm. Considering that the expansion velocities are generally in excess of 10^7 cm/s, exposure times of less than 100 ps are needed to avoid significant blurring. Therefore, time-resolved two-dimensional imaging systems with short exposure time (less than 100ps) and high spatial resolution (≥ 10 lp/mm) are required so as to provide a direct means of studying the evolution of temperature and

density profiles of plasma, as well as the hydrodynamics which govern its expansion and compression. Present laser pulses of interest to ICF are typically one to several ns in duration, multiple frames with readily adjustable time intervals between frames are necessary to record the complete period of the evolution process.

There are also other emission sources requiring directly two-dimensional imaging with picosecond temporal resolution. These include parametric scattering process(e.g. stimulated Brillouin scattering, stimulated Raman scattering, half-harmonic emission) or thermal emission, which appears in visible to near-UV regions of the spectrum. Studies of the deposition of laser energy into solid materials require one to observe directly the appearance of shock waves breaking through the target.

Regarding these applications, the performance requirements for the diagnostics are (1) frame exposure times ≤ 100ps, (2) interframe periods ≤ 250ps and adjustable, (3) dynamic spatial resolution ≥ 10 lp/mm, (4) spectral response coverage for spectrum of X-ray/UV/visible/NIR/IR, (5) sufficiently high dynamic range, (6) adequate frame size. To fulfil these requirements, several framing techniques have already been developed. These techniques are principally operated in a shutter mode through mechanical/optical/electrical/electro-optical control so that the ultrafast events can be temporally dissected with required time resolutions.

7.1.1 Mechanical framing cameras

The simplest and most direct technique to receive time-resolved two-dimensional images is to use a rotating mirror or prism to scan images across a stationary recording medium. It is relatively slow because of the limitation of the rotating speed of the mirror caused by the limited material strength. For the best structural material, the maximum rotating speed is 5×10^5 mm/s without its destruction by centrifugal forces[2]. Combining with moving recording medium, the best result obtained by this technique is 10^{-7} s framing time[3]. It has been very useful in research areas where relatively slow phenomena are involved but it is far too slow for the applications mentioned above.

7.1.2 Electro-optic Kerr shutters

By applying external time-dependent electric fields[4] to induce a birefringence in Kerr cell medium, 0.5 ns exposure time has been claimed[5] and yet difficulties in generating high voltage electrical pulses (~10KV) having short rise time (~100ps) have impeded the achievement of shorter frame times. The use of polarised light pulses in lieu of electrical pulses[6] has provided a frame exposure time of 5 ps by using CS_2 as Kerr cell medium in conjunction with an image streak camera[7]. In this method the limitation to exposure time is predominantly set by the relaxation time of the Kerr material, gating pulse duration and group velocity mismatch between the gating and gated beams. For Kerr material CS_2, the relaxation time was measured to be 2.1±0.3 ps[8]. By suitable choice of active medium, this optical gating technique may be extended to the femtosecond regime[9]. This gating technique has been adapted for single-shot recording using crossed-beam or echelon technique[10] and also applied in many applications[11,12]. However, it has very poor transmission efficiency (typically a few percent), consequently low contrast and requires very high laser power density to induce an acceptable degree of birefringence in Kerr medium.

7.1.3 Holographic techniques

These techniques are accomplished by using shadowgraphic or interferometric principles. With the aid of multireflex or multiplexer, results of four frames with 20 ps frame exposure times[13] and six frames with 3ps frame exposure times[14] having spatial resolution of 1μm have been achieved. However, their complicated optical arrangements and image reconstruction plus the requirement of laser amplification have limited their applications significantly. Efforts have also been made to utilise light-in-flight holographic technique to carry out ultrafast diagnostics providing two dimensional images with a continuous temporal information by changing the angle of the reference reading beam continuously[15]. With this approach, it is claimed that a frame time equal to the reference pulse duration should be obtainable. But the specified spatial resolution is merely submilimeter. Also it requires sufficiently high laser power and collimated

illumination to ensure unambiguous results. Its image reconstruction requires critical alignment and stable environments and can be time consuming.

7.1.4 Electron-optical framing techniques

Electron-optical framing cameras have demonstrated the capacity to provide single/multiple subnanosecond/picosecond exposure times and high sensitivities over broad spectral response. Their applicability to plasma studies and to temporally/spatially-resolved photobiological investigations in the water window spectral region around 2.3- 4.4 nm has made framing techniques an important subject in the development of modern instrumentation.

According to its operation principles, this technique can be classified into photocathode-gated type and deflection shuttering type. In the former category, the ultrafast gating action is accomplished by switching the electron beam on and off within very short time by means of applying an ultrafast voltage pulse onto the photocathode. Within this category, it can be further classified into gated image intensifiers and electron-optical lens focusing image tubes.

Gated image intensifiers being used for gating operation was first reported in late sixties presenting 1ns gating time[16]. Because of the simple structure and intensifying nature, it has been one of the important developing interests in framing techniques and numerous publications on this technique have emerged since[17]. The development of this technique has primarily focused on aspects such as (1) better tube construction, (2) faster gating techniques, (3) MCP structure with reduced resistivity and minimum photoelectron transit time, (4) compact system. The limitations on the gating speed of image intensifiers include the gating pulse duration, electron transit time from photocathode to MCP, the propagating time of electric pulse wave across image area on the photocathode, limited conductivity of the gating electrodes and the inevitable large capacitance between them. By adopting a microstrip transmission line construction for the gating electrodes, the limitation on the charging speed between photocathode and MCP input face or between MCP input and output faces, imposed by the capacitance and surface resistance, can be alleviated[18,19]. By matching the impedance of the transmission line to the feed-through cables the charging RC time limits can be avoided. A

good conductivity of gating electrodes is provided by coating a thin layer of Au on the gating electrodes[20], thus the power loss due to Ohmic loss can be minimised. When using MCP gating, the transit time of photoelectrons in MCP can be reduced 50 ps by using thinner MCP[21]. The direct excitation of phosphor screen by X-rays transmitted through photocathode can be alleviated by tilting MCP tubelets a few degrees from normal direction. The production of fast high voltage switching pulses has been made possible by utilising photoconductive switches or avalanche breakdown of p-n junctions[22] which can provide a 5 kV electric pulse with 100 ps duration. The incorporation of CCD directly into such devices replacing phosphor screen add the advantage of high spatial resolution easy data access and compact construction[23]. With these modifications, The single frame result of 50 ps frame exposure time with 20 lp/mm spatial resolution and 8.6 x 12.8 mm^2 frame size have been obtained. It is also possible to achieve multiple frames by manufacturing either several separate windows[24] or several transmission lines with independent electrical gatings[22,25], or a meander line[26] on the MCP input face or photocathode. With appropriate pinhole camera arrangements, more than ten frames with 100 ps frame exposure times and 50 ps interframe times, 6 x 5 mm^2 image area and better than 10 lp/mm spatial resolution have been reported[25,26]. The disadvantage of this technique is that the inevitable transmission of X-ray through photocathode causes serious background noise despite of adopting tilted MCP tubelet and the minimum gating time is limited by the transit time spread of photoelectrons in MCP.

In the photocathode-gated image tube, the photocathode is gated with repetitive pulses to get multiple frame exposures and the different exposures are positioned by applying staircase waveform signals to the two orthogonally-oriented deflectors[27,28]. With this method, so far the best obtained results are four frames with 400 ps exposure times, 5 ns frame interval, 7 x 7 mm^2 image size and dynamic spatial resolutions were inspected to be 5 lp/mm. Its performance was limited by the difficulties of producing fast gating pulses and ideal staircase waveforms. With this technique, faster gating can be obtained by using travelling-wave deflectors (TWDs) instead of conventional plate deflectors in the absence of electric gating on photocathode[29]. This is because the application of TWDs with impedance-matching feed through leads allows faster rise time of the staircases and so the exposures between stair steps are very weak

compared to the exposures on the flat steps. Such modification has led to experimental results of two frames with 500 ps frame times, 70 ps interframe times and spatial resolution of 4 lp/mm. But it tends to have low image contrast and also difficulties in producing short staircases with reasonably flat steps have restricted further improvement of frame time and spatial resolution

In deflection shutter type, electron-optical focusing image tubes are used where the gating action is provided by incorporating one or more than pairs of deflectors to which high speed voltage ramp signals are applied. One approach is to use a conventional streak camera and computer software such that a discrete matrix of objects points selected by a mask is optically relayed to the photocathode of a streak image tube and the streaked image is digitised using either microdensitometer or a TV system which are fed to a computer for image construction processing[30]. By doing this, 5 frames with 13 ps frame exposure times were obtained. But they suffer poor spatial resolution, which was 2 lp/mm, due to the requirement of adequate distances between the object points and it involves too much post data-processing work.

Another technique is the so-called dissector/storer image tube which is based on the line dissection of an electron image swept through a slit aperture by a set of deflectors (so-called dissector) to which a fast ramp voltage is applied[31]. Using this technique, three frames with 250 ps frame exposure times and 400 ps interframe times have been produced when employing Nd:YAG mode-locked laser which provides pulses with duration of 1.5 ns[32]. The problem with this technique is that the system consists of two sets of electron-optical lenses and deflectors and it is very difficult to manufacture with adequate accuracy so as to achieve complete restoration of image lines and the dynamic resolution tends to be poor. Also the frame exposure times are dependent upon the frame sizes and the dissecting speed which tends to be low. Furthermore, the resultant image formation is not completed at one time and the top line and bottom line of the frame has a time difference of the frame exposure time. Because the whole image is dissected into line and the exposure time of each line is only a fraction of the total frame exposure time, the use of incident light intensity is very inefficient and it requires

high incident light intensity. This manifests more serious space-charge effects and so low dynamic range.

To overcome the disadvantages in the previous technique, a simpler design has been suggested where instead of photoelectron image the crossover of photoelectrons is swept across a small aperture by a set of deflectors and restored by a second set of deflectors[33]. An unsmeared image can be obtained on the phosphor screen without the use of a second set of electron-optical lens. The resultant image can be formed at one time over the exposure period and so the dynamic range can be higher. Also the frame time can be shorter since it depends upon the crossover size and aperture size rather than image size. This type of framing cameras is designated as Picoframe type.

To date, the frame times of this type of camera have been reported to be 100 ps (FWHM) in single-frame operation[34], 120 ps in double-frame operation[35] and 250 ps in four-frame operation[36] with limiting spatial resolutions (i.e. 5% modulation depth) of 8 lp/mm for ultraviolet (UV) and 5 lp/mm for X-ray illuminations. Although gated intensifiers have been able to provide multiple frames with frame times of less than 100 ps and spatial resolution of better than 10 lp/mm, they suffer from X-ray transmission directly through photocathode. Picoframe cameras are immune to this problem and also have the advantage of being able to provide adjustable number of frames and frame times. Therefore, it has been one of the important framing techniques. Full detail of the design and improvement of this type of camera will be presented in the following sections.

7.2 Operating principle and theoretical simulation

Theoretically, Picoframe image tubes were designed for providing frame times of 100 ps with dynamic spatial resolution of 10 lp/mm. A schematic diagram of a Picoframe I image tube is included as Fig.7.2.1. It basically consists of a photocathode C, mesh electrode M, electrostatic focusing lens electrodes, phosphor screen P, two apertures A_1, A_2 and two pairs of deflectors D_1, D_2. Deflector, D_1 is used for the framing (or shuttering) operation and deflector, D_2 is for compensating the image 'smear' caused by the framing deflectors. The

original design concepts have been discussed in detail elsewhere[37]. It, therefore, suffices to include a brief review of the basic operating principle involved.

The operating principle of this tube is similar to that of streak cameras and the difference is in that the first pair of deflectors together with the framing aperture function as a shutter and the second pair of deflector is used to recover the streak effect of the first one so that a static image can be obtained on the screen.

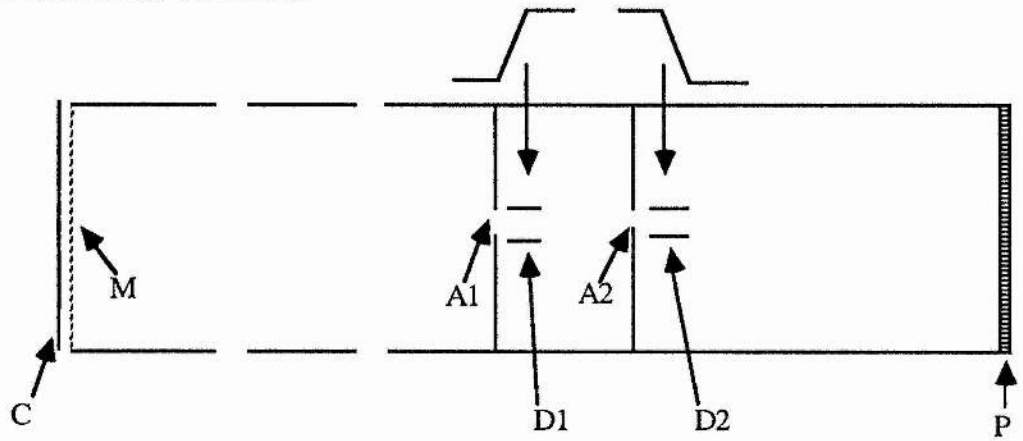

Fig.7.2.1 Schematic diagram of a Picoframe I image tube, C, photocathode, M, mesh, A1, anode aperture, A2, framing aperture, D1, framing deflectors, D2, compensating deflectors, P, phosphor screen

When a linear, time-varying voltage ramp is applied to the so-called 'framing' deflectors D_1, the photoelectrons are swept across the aperture A2 (framing aperture) and a short temporal exposure is defined by the finite size of the framing aperture. The imposed temporal smear on the image caused by framing deflection is then eliminated by applying an identical and suitably phased inverse-polarity voltage ramp to the compensating deflectors D_2.

In theory, the overall frame exposure time t of the image (or frame) defined by aperture A_2 can be expressed as:

$$t = 2Va\ A\ d/(K\ a(a/2+L)) \qquad (7.2.1)$$

where *Va* is the anode voltage, *A* equals to the framing aperture diameter plus photoelectron beam diameter at the framing aperture, *d* is the separation of the framing deflector plates, *K* is the gradient of the deflection voltage ramp (V/s), *a* is the length of the framing deflectors and *L*

is the distance from the exit of the framing deflectors to the framing aperture. In practice, fluctuations in the photoelectron emission conditions make the actual diameter, A, of the photoelectron beam inconsistent and it is thus difficult to measure the photoelectron beam diameter, A , accurately. Usually the parameter, A, is estimated to a first approximation by the full width at the half maximum of the convolution function between the aperture diameter and the photoelectron beam cross-section profile. Experimentally, a specified exposure time is given by the full width of the half maximum exposure temporal transmission profile through the framing aperture. This gives rise to values for the frame exposure time t that may differ from those predicted by the above equation- usually shorter than that defined by the above formula. To understand the limiting factors to their frame exposure times and dynamic resolution and to provide a practically optimum design, a thorough theoretical simulation of the camera is required.

In most instances, the theoretical design of a framing tube is undertaken on the basis of theoretically predicted parameters under static operating conditions and the dynamic performance can only be obtained from experiments. The latter can be time-consuming and costy because the static performance does not necessarily represent the optimum dynamic performance which is the most important aspect in the practical design considerations of a framing tube. In fact it has been noticed that the spatial resolution in dynamic mode is significantly degraded compared to that under static conditions. To overcome such degradation and thereby to ensure an optimised design of a framing tube under dynamic operating conditions, more realistic theoretical modelling techniques for ultrafast framing cameras in dynamic operation have become imperative. By using the computer programs developed for streak camera simulations with small alterations, the dynamic operation of both Picoframe I and Picoframe II framing tubes can be simulated such that parameter data including optimum image positions, magnification, beam-crossover position and beam size, spatial and temporal modulation transfer functions (MTF), deflection sweep speed and photoelectron transmission through the framing aperture can be provided. For the UV and X-ray illuminations used in the following sections, 0.6 eV and 4.0 eV of photoelectron emission energies were assumed for a gold cathode on suitable substrates under 266 nm and 0.6 – 1.2 nm radiations respectively.

The experimental results presented here for comparison with theoretical data were produced by Dr. David Walker at AWE, Aldermaston.

7.3 Evaluation of Picoframe I camera in single/double frame operations

7.3.1 Single-frame operation

In the single frame mode of the Picoframe I camera operation, two linear, time-varying voltage ramps of inverse polarities are applied respectively to the two sets of deflectors so that the photoelectrons are swept across the framing aperture according to their time sequences. The framing aperture functions as a 'time window' to establish the temporal transmission of the photoelectrons through the time window. For calculations, this temporal transmission is defined by the transverse positions of photoelectrons at the framing aperture plate. Only the photoelectrons located within the framing aperture area can proceed to the second deflection region. By suitably adjusting the synchronisation of the deflection signal on the compensating deflectors with respect to that on the framing deflectors, a properly framed image can be obtained on the centre of the phosphor screen. The calibration of the sweep speeds provided by the deflectors is accomplished by deliberately providing a pair of photoelectrons with the same conditions of photoelectron emission but differing only in the time (e.g. 10ps) of liberation at the photocathode (the same is taken for double-frame operations).

Fig.7.3.1 shows graphically a number of randomly-selected photoelectron trajectories in the original Picoframe I image tube design at a single-frame mode with reference to the sweep direction where the phosphor screen is located at the static focus plane. The sweep speed provided by the framing deflectors at the framing aperture was 0.18×10^8 m/s at a deflection ramp speed of 2 kV/ns and a deflection sensitivity of 0.95 cm/kV (referred to the framing aperture) for an input light pulse duration of 100 ps (FWHM). Calculation results indicate that in the non-sweep direction, the optimum focus image-plane remains the same as that in the static mode and so the dynamic spatial resolution is unchanged. In the sweep direction, however, the framing action advances the focusing plane about 50 mm closer to the deflectors.

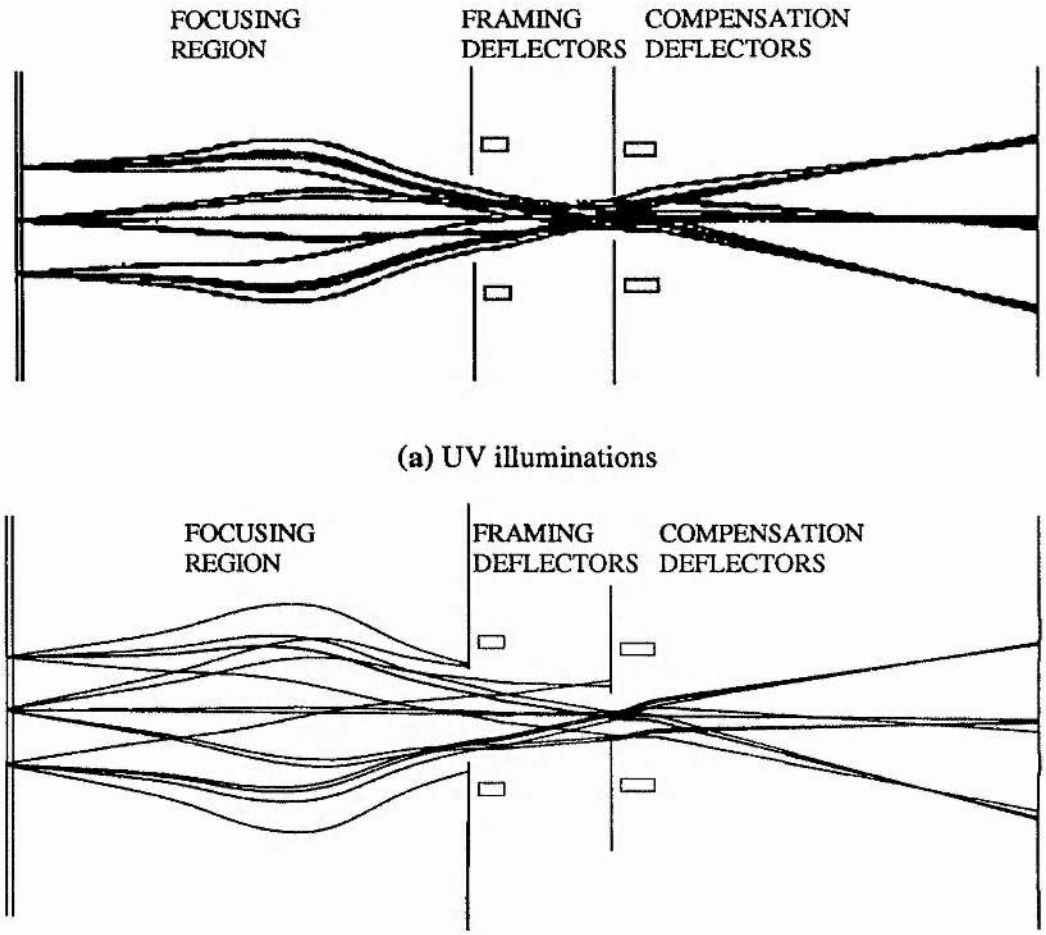

Fig.7.3.1 Photoelectron trajectories in a Picoframe I image tube in single-frame operation

This causes image astigmatism and gives rise to a significant degradation in the spatial resolution and a theoretically simulated limiting dynamic spatial resolution of less than 3 lp/mm for UV illumination was obtained in the sweep direction at the photocathode.

Such a dynamic relocation of the optimum focal plane is due mainly to the dynamic fringing-field effects that arise in conventional metal plate deflectors. Because the velocity of the photoelectrons travelling between the deflectors is only about one-fifth of the velocity at which the electrical deflection signal propagates along the metal deflector plates, the deflection voltage applied on the photoelectrons is changing while the photoelectrons are propagating along the deflectors such that a so-called finite transit time effect arises. In order to synchronise

the photoelectrons with the deflection waveforms in such a way that the photoelectrons pass through both apertures and reach the centre of the phosphor screen, account must be taken of the electron transit time within the deflection section. This, inevitably, introduces non-zero and opposite voltages at the entrance and exit of the deflectors as illustrated in Fig.7.3.2. This

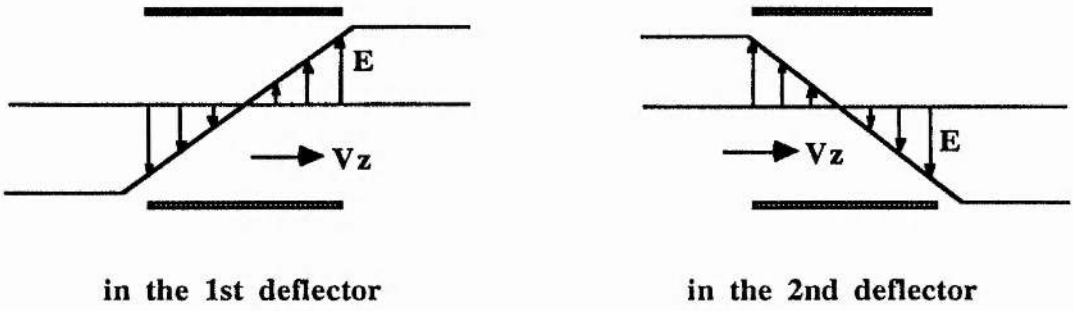

Fig.7.3.2 Time-varying electric fields experienced by photoelectrons travelling in the deflection section

implies that the photoelectrons experience deflection fields that change from positive to negative or vice versa. Because the field strengths at the two ends reach a maximum, they cause the so-called fringing-field effects. Typical operating conditions of a Picoframe camera yield a

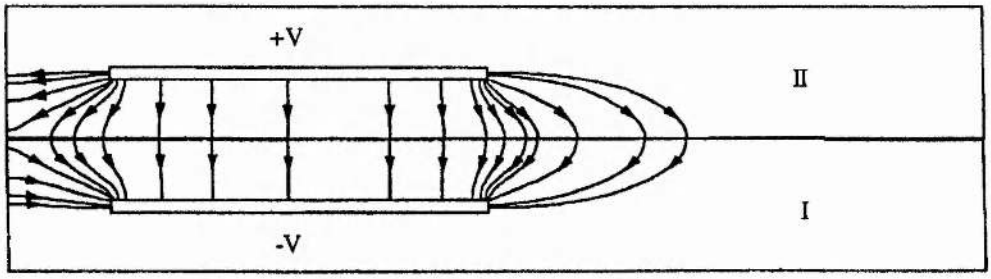

FRAMING DEFLECTION REGION

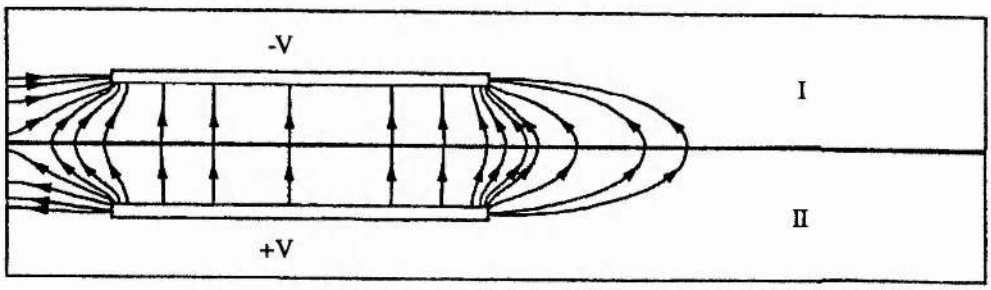

COMPENSATION DEFLECTION REGION

Fig.7.3.3 Deflection field distributions in the framing and compensation deflectors of a Picoframe I image tube in single-frame operation

deflection potential difference of up to 550 V between the entrance and exit of the deflectors during the propagation of the photoelectrons. This has the same effect as that if a DC bias voltage is applied to the deflectors and it varies along the deflectors. Because symmetrical ramp voltages(+/-) are applied to the two deflectors, their combined function essentially leads to a cylindrical lens effect. This effect can be readily explained by the graphics of the fringing-field distributions in both the framing and compensation deflectors under framing operating conditions as displayed in Fig.7.3.3. The fringe-fields in the regions labelled, I, constitute a convergent cylindrical lens and those in the regions labelled, II, represent a divergent cylindrical lens for the photoelectrons. Their combination is equivalent to an electrostatic cylindrical lens which has a focusing effect on the photoelectrons. For higher sweep speeds, this effect becomes more pronounced.

By adjusting the voltages on the main electrostatic focusing lens section of the image tube, a compromised focusing condition can be achieved between sweep and non-sweep directions. Theoretical evaluations have demonstrated that under the same sweep conditions as considered previously, the limiting dynamic spatial resolutions on the phosphor screen were obtained to be 7 lp/mm for UV illumination and 3 lp/mm for X-ray illumination assuming that 100 photoelectrons (the same applies to the following calculations) were emitted from a point at the centre of a photocathode illuminated with a 120 ps duration light pulse. The frame times of approximately 95 ps (FWHM) for UV and 110 ps (FWHM) for X-ray illumination were deduced from the temporal transmission profile through the framing aperture and the corresponding spatial modulation transfer functions are plotted in Fig.7.3.4 (i.e. labelled as curve 1). Considering that the magnification of the image tube was 1.5, spatial resolutions of 10.5 lp/mm for UV illumination and 4.5 lp/mm for X-ray illumination at the photocathode can be derived. The transmissions of the photoelectrons through the apertures were 66% for UV and 50% for X-ray illumination. When the photoelectrons were emitted from a point that was 2 mm away from the photocathode centre, the transmissions were reduced to 60% for UV and 40% for X-ray illumination and the spatial resolutions were degraded compared to those from the centre of the photocathode. These theoretical evaluations agree with the experimental results (see Fig.7.3.5) where limiting dynamic spatial resolutions of 8 lp/mm for UV and 6 lp/mm for

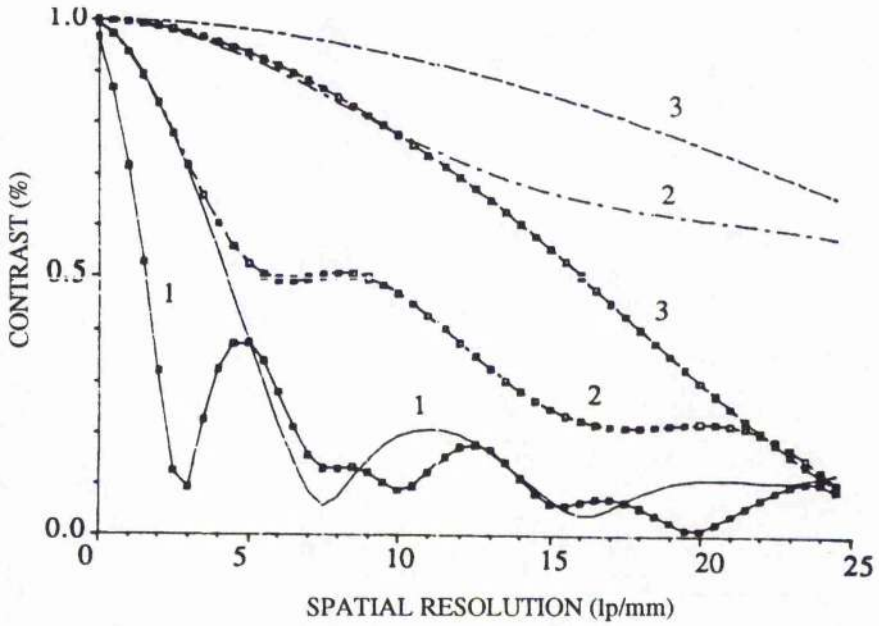

Fig.7.3.4 Theoretically calculated SMTF data for Picoframe I camera in single-frame operation where curves labelled **1** are for the original tube design, curves labelled **2** are for a Picoframe tube with an extra cylindrical lens and curves labelled **3** are for a Picoframe I tube with TWD system, curves with square symbols are for X-ray illumination and the others for UV illuminations

X-ray (referred to the photocathode) were measured. The experimental data were obtained from a Picoframe framing camera which incorporated an image intensifier (Mullard XX1330A microchannel plate device) having a limiting spatial resolution of 20 lp/mm.

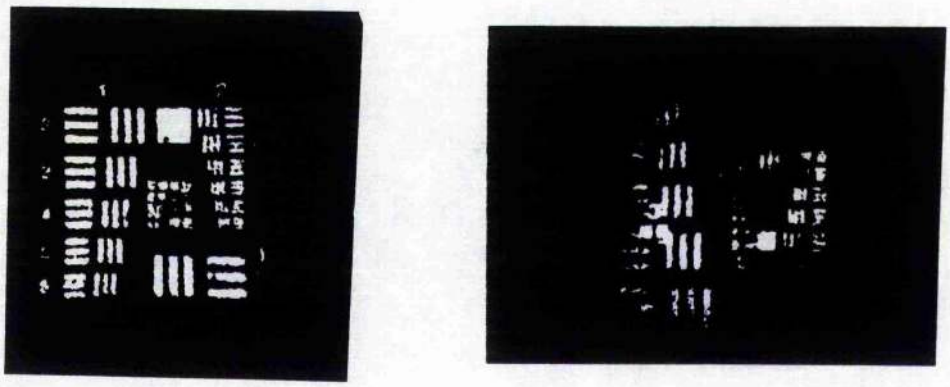

(a) UV illumination **(b)** X-ray illumination

Fig.7.3.5 Experimental single-frame results recorded on a Picoframe I camera

7.3.2 Double-frame operation

To achieve multiple frames, alternative techniques can be applied. One approach is to operate a Picoframe I camera with deflection signals of reverse-polarity symmetrical triangular waveforms. Another approach involves the use of a multiple framing aperture plate together with more than one set of compensating deflectors. In both options a pair of shift plates can be incorporated at an orthogonal orientation to these framing/compensation deflectors so that a sequence of multiple frames can be produced. In this section the former has been discussed.

In order to get two frames in a Picoframe I tube, a triangular deflection waveform is applied to the framing deflectors so that two separate frames can be achieved by sweeping the photoelectrons twice across the framing aperture. Image 'smear' can be eliminated by applying an identical but inverse-polarity waveform to the compensation deflectors. The spatial discrimination of the two resultant frames on the phosphor screen is provided by suitably adjusting the relative phase between the framing and compensation deflection waveforms. The operating principle is depicted schematically in Fig.7.3.6.

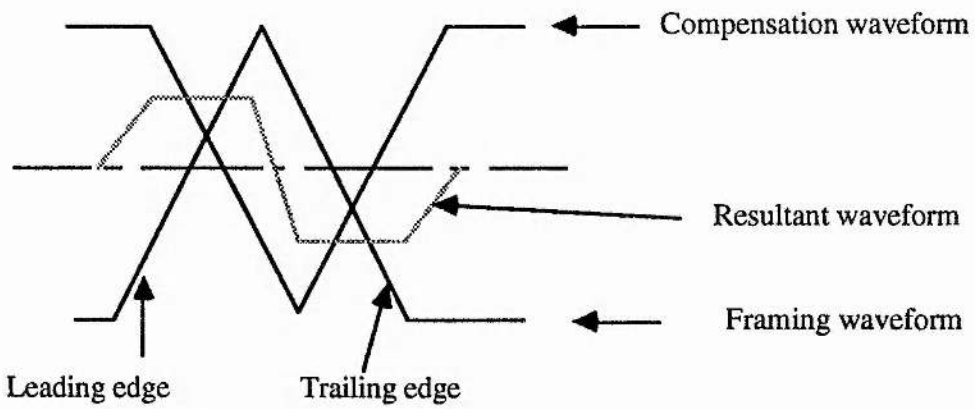

Fig.7.3.6 Deflection voltage waveforms for double-frame operation of a Picoframe I image tube

Consider firstly the leading edges of the waveforms. If the relative timing between the waveforms applied to the framing and compensation deflectors is less than the transit time of the photoelectrons between the two deflectors, then a net differential deflection of the resultant image at the phosphor screen will occur. The second frame generated on the trailing edges of

the waveforms is shifted by an equal and opposite amount relative to the first one at the phosphor screen, thus a desired spatial separation can be provided without resulting in additional deflection waveforms.

A theoretical simulation for this double-frame operation is somewhat similar to the single-frame counterpart. The only difference is that the deflection signals have triangular waveforms and the beam of photoelectrons is subdivided into two sequential frames. For simplicity, it was assumed that the triangular deflection waveforms have identical rising and falling edges. In the computation process, only one frame was considered at a time and so a method of calculation similar to that for the single-frame operation can be used for both frames.

In Fig.7.3.7 some randomly-selected trajectories are illustrated for photoelectrons propagating through the entire Picoframe I tube when operated in a double-frame mode. It reveals that the photoelectron beam expands considerably in the region of the compensation deflectors and is very close to the exit edge of the deflectors where strong fringe-fields exist. The focal positions are, therefore, shifted according to the emission locations of the photoelectrons to an extent which is greater than that for the single-frame counterpart. Consequently, the image qualities are non-uniform across the image areas and the dynamic performance is usually inferior to that in single-frame operation for similar operating conditions.

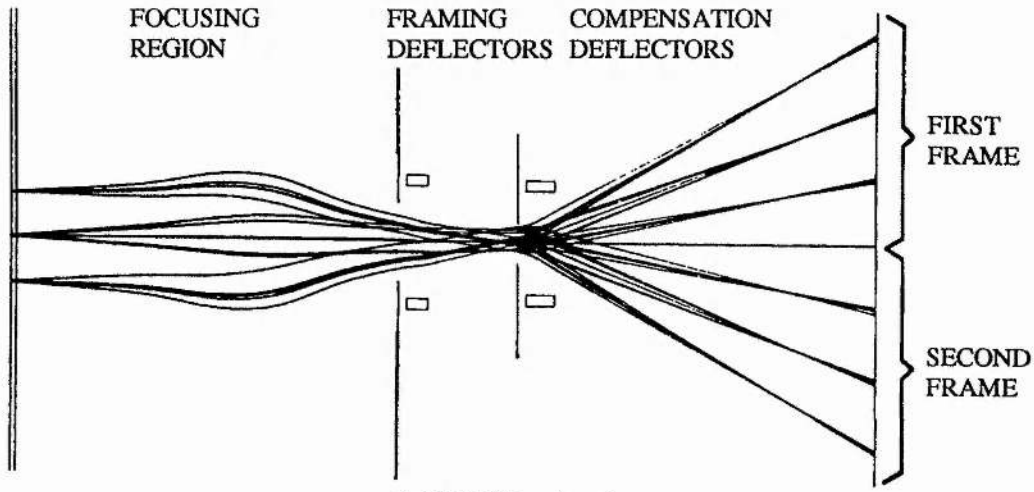

(a) UV illuminations

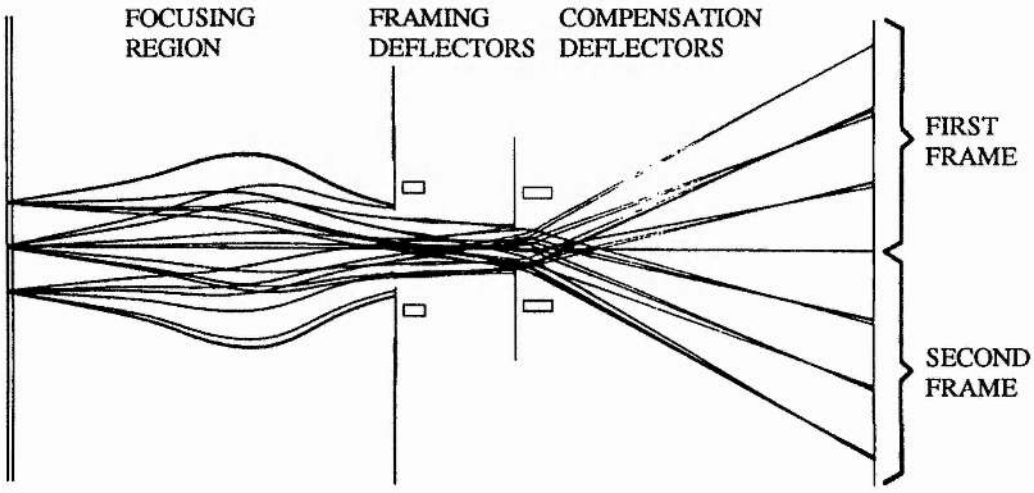

(b) X-ray illuminations

Fig.7.3.7 Photoelectron trajectories in a Picoframe I image tube in double-frame operation

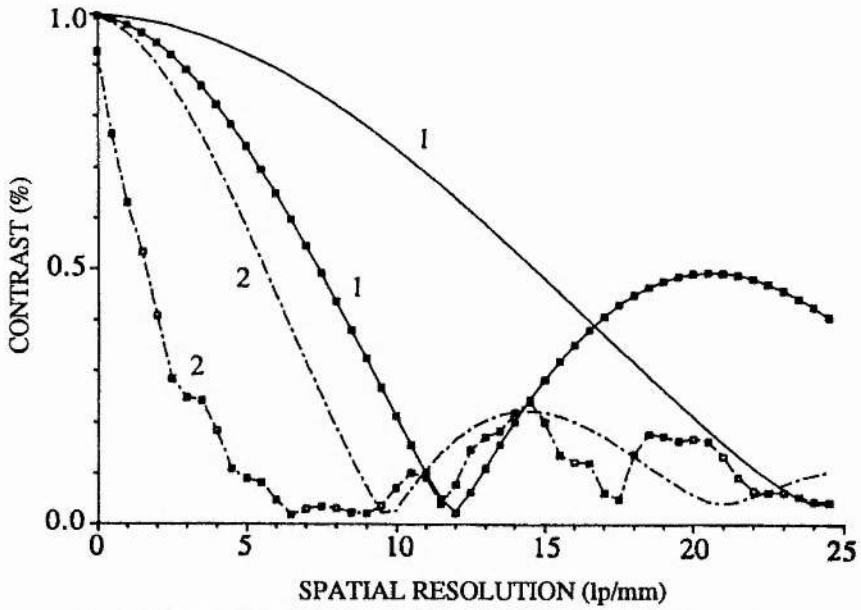

Fig.7.3.8 Theoretical spatial MTF results for Picoframe I & II in double-frame operations where curves labelled 1 are for Picoframe I tube and curves labelled 2 are for Picoframe II tube, curves with square symbols are for X-ray illuminations and the others are for UV illuminations

Theoretical predictions have indicated that under suitably-compromised operating conditions, the dynamic limiting spatial resolutions at the phosphor screen were 22 lp/mm for UV and 11 lp/mm for X-ray illumination at frame times of 250 ps (FWHM), a sweep speed of 7.5 x10^7 m/s at the framing aperture which was obtained at a framing deflection speed of 0.8

kV/ns. This corresponds to 33 lp/mm for UV illumination and 16.5 lp/mm for X-ray illumination respectively at the photocathode when considering the electron-optical magnification of 1.5. The calculated spatial modulation transfer functions (SMTF) are given in Fig. 7.3.8 (see curve 1). For comparison a reproduction of some typical experimental double-frame results is included in Fig.7.3.9 which provided limiting spatial resolutions of 8 lp/mm for UV and 5 lp/mm for X-ray at the photocathode when using an image intensifier having a 20 lp/mm limiting spatial resolution. The poorer experimental data is due to the practical difficulties in producing fast triangular waveforms with identical rising and falling edges and two identical waveforms.

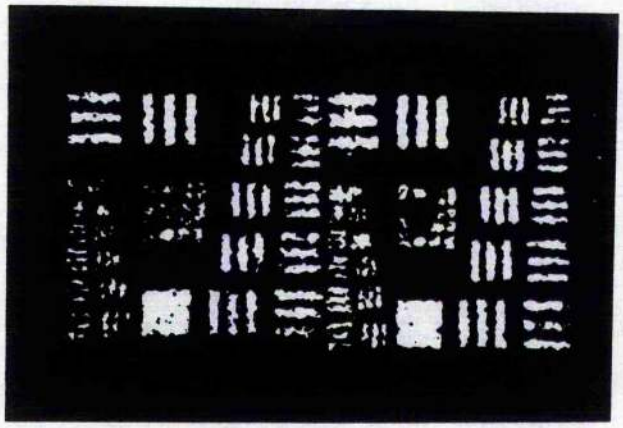

(a) UV illumination

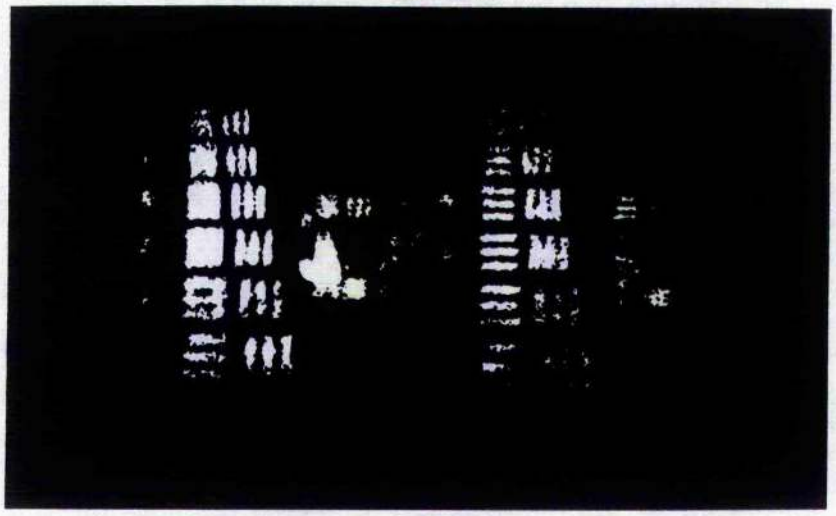

(b) X-ray illuminations

Fig.7.3.9 Experimental double-frame results recorded by a Picoframe I camera

It is seen from both the theoretical evaluations and the experimental data that the spatial resolutions for X-ray illumination are inferior to that for UV or visible illumination in both single- and double- frame operations. It is more obvious when the sweep speed is increased, for example, in the single-frame case. It is also found that the focal plane for X-ray illumination is slightly different from that for UV illumination under the same operating conditions. This is primarily due to the large initial energy spread of the photoelectrons from an X-ray sensitive gold photocathode. For X-ray illuminations, the photoelectron beam diameter is increased and more serious fringe-field effects arise. From the expression for the frame time given in Eq. (7.2.1), a larger beam diameter implies an increased frame period and a further reduction in the transmission of photoelectrons through the apertures. Consequently, to maintain the required image contrast ratio at the phosphor screen, the input light intensity at the photocathode has to be increased to compensate for the intercepted photoelectrons. This leads to a requirement for higher photoelectron current densities in the electrostatic focusing lens of the camera and this in turn lead to more deleterious space charge effects. An effective way to improve the dynamic performance for x-ray illumination would therefore be to incorporate an X-ray sensitive photocathode having a minimum secondary electron emission energy spread, such as potassium iodide[38]. It is noted that the dynamic spatial resolution is influenced by the sweep speed of framing and compensating deflectors. This causes some difficulty in reducing the frame times of the Picoframe type of camera.

7.4 Evaluation of Picoframe II camera in double-frame operation

As mentioned in the previous section, an alternative to a Picoframe I camera for the achievement of multiple frames is to use a double-aperture image tube design designated as the Picoframe II[39]. As illustrated in Fig.7.4.1, in this framing tube the applied linear framing deflection signal sweeps the photoelectrons across two apertures in turn and so two photoelectron transmissions are defined. To spatially separate the two frames and to eliminate any temporal smearing effects in the two frames, a set of compensation deflector plates is arranged behind each aperture and an identical but inverse-polarity linear ramp is applied to

each compensation deflectors. The separation of the two frames on the phosphor screen is provided by adjusting the synchronisation of the compensating waveforms with the photoelectron arrival time at the framing aperture in much the same way as that already described in section 7.3.1. The interframe time is determined by centre-to-centre distance between the two framing apertures and the sweep speed provided by the framing deflectors at the framing aperture plate.

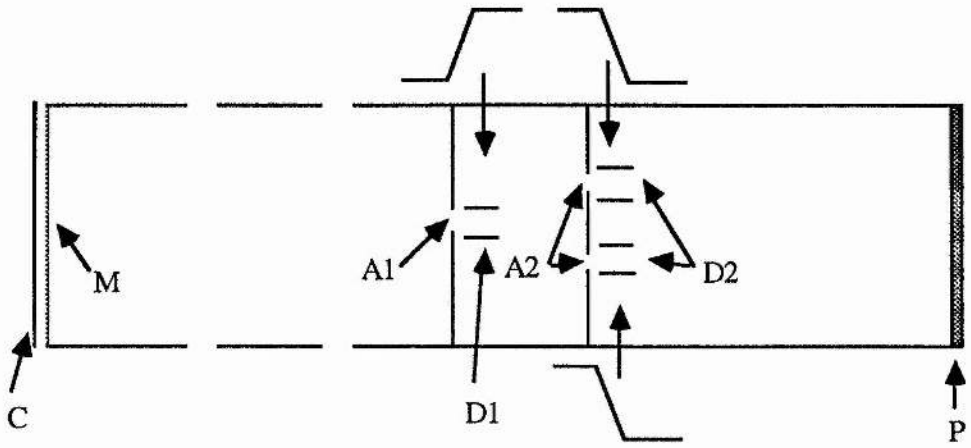

Fig.7.4.1 Electrode configuration of Picoframe II image tube with a double aperture where C, photocathode, M, mesh, A1, anode aperture, A2, framing aperture, D1, framing deflectors, D2, compensating deflectors, P, phosphor screen

For the theoretical evaluation of the performance of this framing camera design, the computer programs used in the trajectory computation of the Picoframe I camera were modified so that the parameters that include the transverse and axial positions, centre-to-centre distance of the two apertures and of the compensating deflectors can be conveniently controlled. The computation of trajectories for each frame was then carried out separately assuming that the voltage ramps applied to the two sets of compensating deflectors are identical.

Some calculated trajectories of photoelectrons along the entire image tube are shown in Fig. 7.4.2 with respect to the sweep direction. It is seen that when the photoelectron beam is swept across the two framing apertures, it is spread from the lower plate exit edge to the upper plate exit edge of the framing deflector plates where the fringe-fields are very strong. This gives rise to deleterious effects, whereby the combined lensing influences of the deflectors become more pronounced than these in the single-frame Picoframe I camera under the same sweeping

conditions and the spatial performance is significantly degraded. In addition, because the photoelectrons near the upper plate edge and near the lower plate edge experience different fringing-field effects, the optimum focusing plane varies both with frames and the emission coordinates of the photoelectrons as illustrated in Fig.7.4.2.

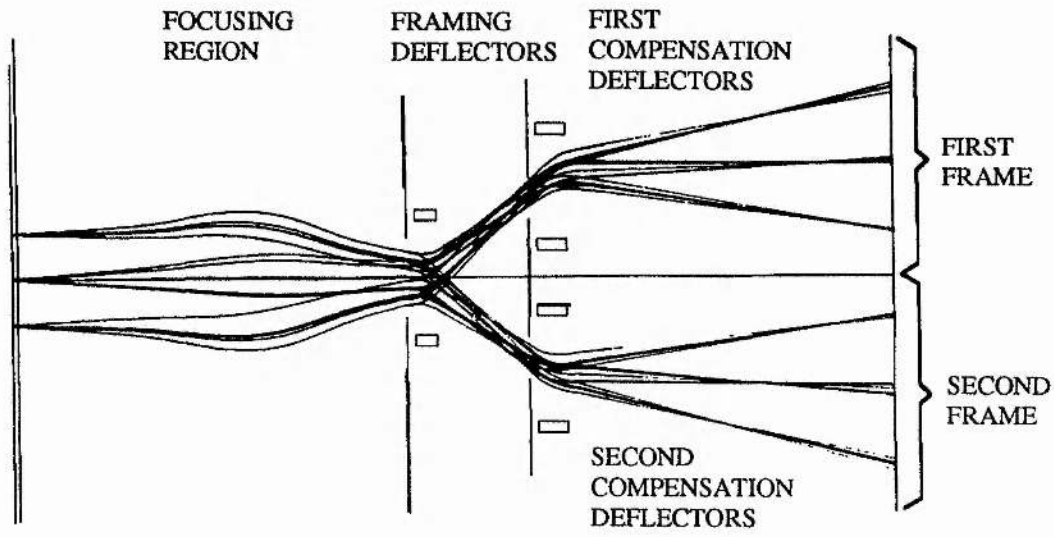

(a) UV illuminations

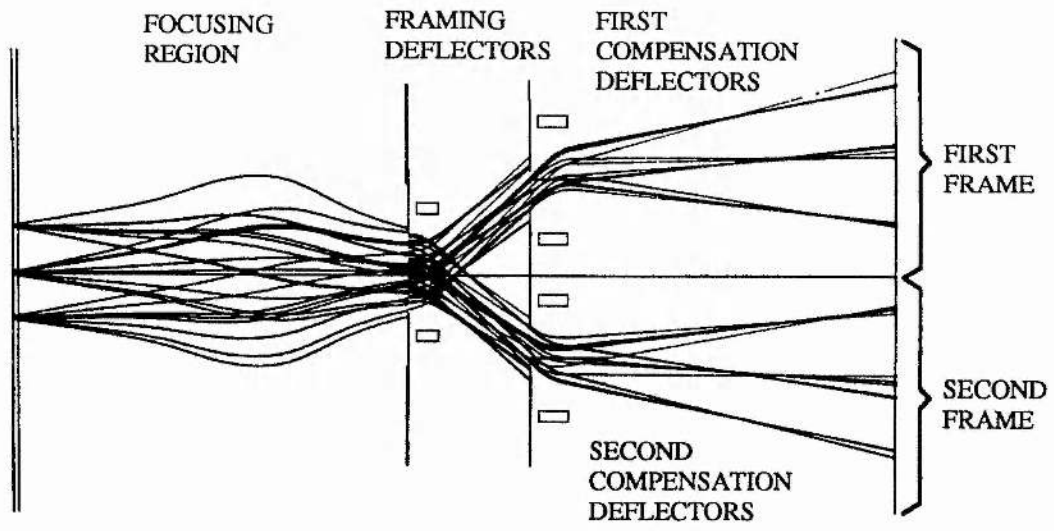

(b) X-ray illumination

Fig.7.4.2 Photoelectron trajectories in a Picoframe II image tube in double-frame operation

The computed limiting dynamic spatial resolutions at the phosphor screen for one frame are 9 lp/mm for UV and 4 lp/mm for X-ray illumination as shown in Fig.7.3.8 (curve 2) but for the second frame are 6 lp/mm for UV and 3 lp/mm for X-ray illumination. The frame times are 115 ps (FWHM) for UV illumination and 130 ps (FWHM) for X-ray illumination for a sweep speed of 1.7 x 10^7 m/s at the framing aperture and framing voltage slope of 1.85 kV/ns. These figures agree with the experimental results that demonstrate limiting dynamic spatial resolutions of 8 lp/mm for UV and 4.5 lp/mm for X-ray illumination under similar sweep conditions (Fig.7.4.3).

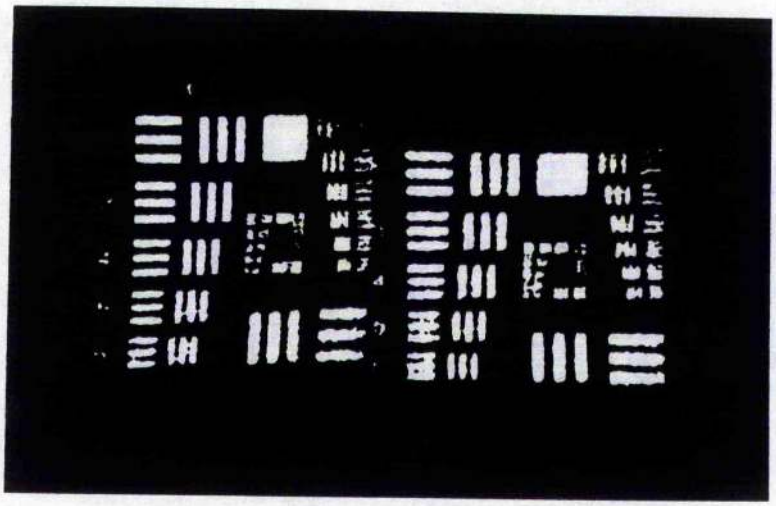

(a) UV illumination

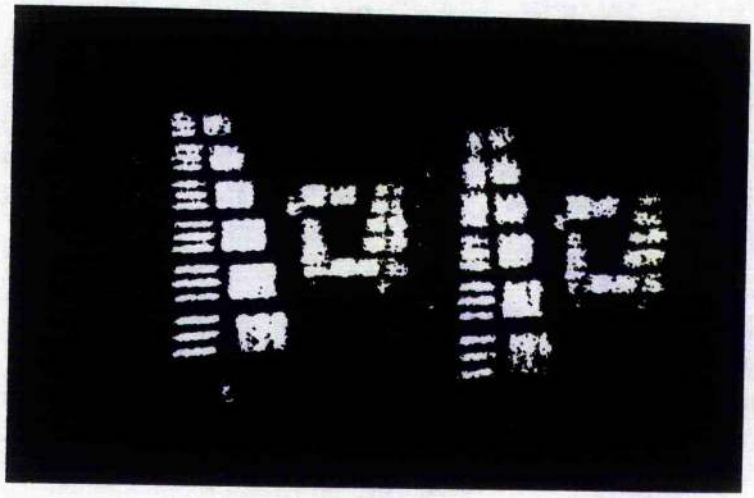

(b) X-ray illumination

Fig.7.4.3 Experimental double-frame results recorded with a Picoframe II framing camera

7.5 The refinements of the Picoframe I tube design

It is clearly not possible to eliminate the inequality of the focusing abilities in the two directions by simply adjusting the voltages on the electrostatic lens electrodes and the arrangement of the two sets of deflectors. More practical approaches must be introduced to overcome this undesired lensing effect[40].

One approach towards alleviating the fringing-field effects involves the use of an extra electrostatic cylindrical lens (orientation orthogonal to the deflection direction) between the framing deflector and aperture. The main electrostatic lens is adjusted in the dynamic mode such that the focusing plane in sweep direction is located at the required position and the focusing condition in non-sweep direction is then re-established by adjusting the voltage on the extra cylindrical focusing lens. It follows, therefore, that the focusing conditions in the sweep and non-sweep directions can be adjusted separately and can thus be independently optimised. By doing this, theoretical limiting dynamic spatial resolutions referred to phosphor screen have been estimated for conditions similar to those described previously to be better than 30 lp/mm for UV illumination and 18 lp/mm for X-ray illumination at the centre of the photocathode (See Fig.7.3.4 curve 2). A preliminary experiment has been carried out for UV illuminations using

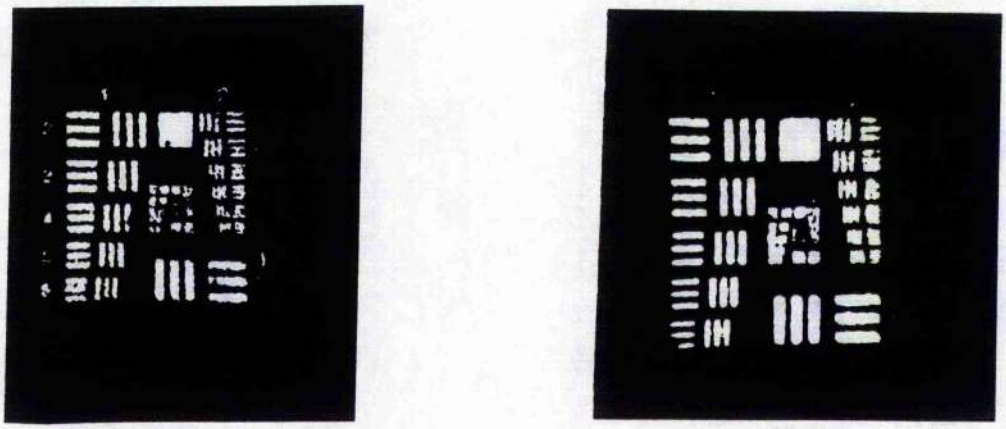

(a) Using an extra cylindrical lens **(b)** Using TWD systems

Fig.7.5.1 Improved single-frame experimental results recorded by a Picoframe I camera for UV illuminations

this regime and a limiting dynamic spatial resolution of better than 9 lp/mm has been recorded as shown in Fig.7.5.1(a). The result was obtained when employing about 55 V to the electrostatic cylindrical lens that gave a deflection sensitivity of 0.9 cm/kV at the phosphor screen when it was used as a deflector. A disadvantage of this approach is that the photoelectron beam diameter tended to be larger than that for the optimum static focusing condition of the main electrostatic focusing system due to its defocused operating condition. This leads to longer frame times and a reduction in the transmission of photoelectrons by the apertures. For example, the theoretical computation suggests that the photoelectron transmission is reduced to 40% and the beam diameter at the framing aperture is increased from 2.5 mm to 3.1 mm for X-ray illuminations. Furthermore, it makes the manufacture of the tube more difficult and results in a difference of electron-optical magnification in the two image directions.

An alternative to the above approach is to use travelling-wave deflectors (i.e. TWDs)[41] such that finite transit time effects can be avoided. This type of deflector geometry has been successfully applied in a single-shot streak camera[42] and has the advantage that its dynamic operation does not alter the focusing conditions of the electrostatic focusing lens. Thus the design of a framing tube with travelling-wave deflectors can be optimised under static conditions and the achievement of shorter frame times becomes possible. The configuration of the entire tube can thus be simpler and smaller beam sizes can be obtained. Moreover, it has the advantage of enhanced deflection sensitivity and frequency bandwidth such that faster linear ramp voltages can therefore be applied without giving rise to waveform distortions. From theoretical simulations, it has been indicated that under the same sweep conditions the limiting dynamic spatial resolutions in this case are similar to those in the previous instance (as seen curve 3 in Fig. 7.3.5) but has a smaller reduction in the number of photoelectrons reaching the phosphor screen.

A preliminary experimental attempt has been made to incorporate TWDs in a Picoframe I framing camera and a limiting dynamic spatial resolution of 10 lp/mm in both directions for UV illumination has been achieved as illustrated in Fig.7.5.1(b). Unfortunately, there can be some

difficulties in providing high speed voltage deflection ramps with travelling-wave deflectors because of the demanding impedance matching requirements. A frame time of 180 ps FWHM which is almost twice as long as that when using the metal-plate deflectors can be attributed to the absence of voltage multiplication associated with the standard system at the high impedance deflector/feed cable interface[43].

7.6 New design considerations

7.6.1 Frame time

From Eq. (7.2.1), it can be seen that the shortening of the frame time requires a smaller electron beam size and framing aperture diameter, lower anode voltage V_a, faster deflection voltage gradient K, longer separation between apertures A1, A2 and optimum design of framing plates. The electrostatic focusing lens has therefore been redesigned and optimised which has a minimised electron beam diameter and increased framing speed by moving the beam crossover position further from the anode aperture A1 (80 mm between the two apertures) and reducing the anode voltage to 8 kV (from 15 kV). To prevent severe space charge effects, the length of the focusing region was decreased. The configuration of the framing plates was also modified for less fringe-field effects and to be fully compatible with the compensation deflectors.

7.6.2 Spatial resolution

Under framing conditions, the fringing-field effects of the deflectors play a very important role in determining the image quality. In particular, with regard to the compensating deflectors, the spatial spread of the electron beam becomes significant due to the temporal extent of the illuminating pulse. Thus the beam size becomes large and may propagate very near to the edges of the compensating deflectors where the fringe-field effects are serious. From this point of view, the fringe-field effects should be minimised and the image 'smear' caused by the framing deflectors should be eliminated completely by suitably-designed compensating plates.

7.6.3 Theoretical performance of the improved design

According to the above design considerations, an improved design of a framing tube has been developed using either conventional or travelling-wave deflectors.

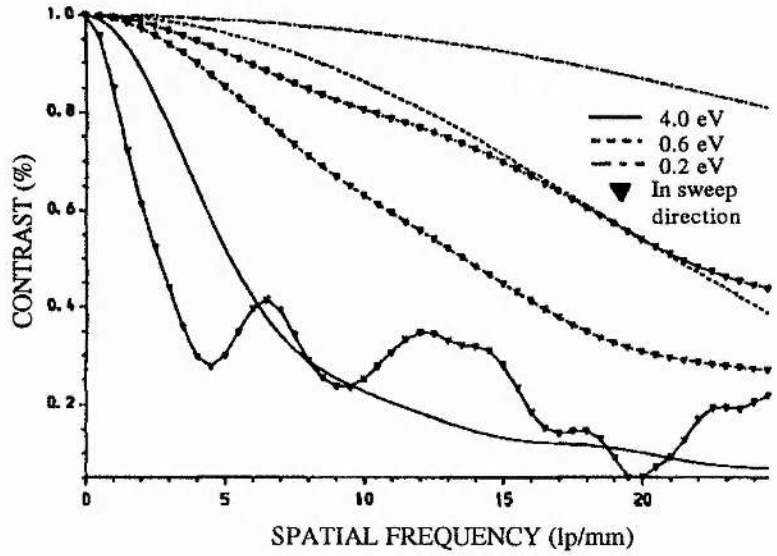

(a) The use of metal-plate deflectors

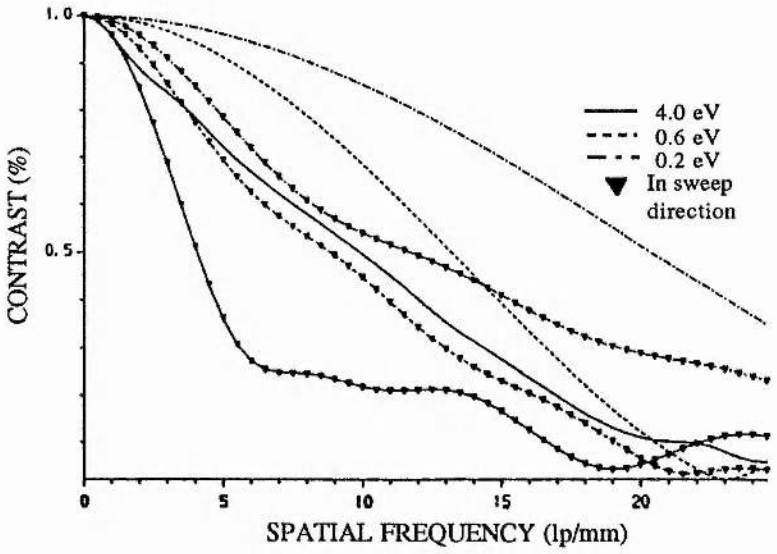

(b) The use of TWD systems

Fig.7.6.1 Theoretically predicted spatial MTF performance in sweep and orthogonal directions for the proposed framing tube design

In this modified design, the deflection sensitivity is increased by three times for the tube version having conventional deflectors and by four times for the tube with travelling wave

deflectors as compared to the original Picoframe I tube. Because of the shorter focusing system, the working area on the photocathode is reduced from 6 x 6 mm to 4 x 4 mm. To achieve complete compensation between the two deflections at shorter frame times, the voltage ramps applied to them are made different to compensate for their deflection sensitivity difference. The frame times for UV illuminations are predicted to be approximately 60 ps (FWHM) for the conventional deflector version and less than 50 ps FWHM for the travelling-wave deflection design at a deflection speed of +/- 1.6 kV/ns. The calculated spatial modulation transfer functions are shown in Fig.7.6.1a & b for conventional and travelling-wave deflectors respectively when using different radiation sources. The dynamic spatial resolution referred to the photocathode is estimated to be 15 lp/mm for UV light sources and 10 lp/mm for X-ray radiation source at a modulation depth ≈ 20%. The magnifications of the tube with metal-plate deflectors in the sweep and orthogonal directions are x1.8 and x1.4 respectively and those for the tube having travelling-wave deflectors are x1.8 in both directions. It should be noted that the above approaches can also be employed in the improvement of double-frame operations.

7.7 Summary

To improve the dynamic performances of picosecond-resolution framing cameras, detailed theoretical evaluations of Picoframe I, II type framing cameras in both single-frame and double-frame operation have been accomplished and the theoretically-predicted performance characteristics have been compared with the corresponding experimental data. These results have enabled us to have a better understanding of the mechanism of this type of framing cameras. For comparison related experimental measurements have been presented. Particular emphasis has been directed towards Picoframe cameras having ultraviolet and X-ray spectral sensitivities.

The illustrations of photoelectron trajectories in the entire image tube under dynamic framing conditions have revealed that the electron-optical focusing characteristics are influenced significantly by the dynamic fringe-field effects within the deflectors which give rise to different optimum image planes in the two orthogonal spatial directions. It has been shown that it is this factor that limits the dynamic spatial resolutions and frame times for these particular

designs of framing cameras. It has also been confirmed that for X-ray applications, the frame exposure time is longer and the number of photoelectrons reaching the phosphor screen is smaller compared to UV illuminations due to the high secondary electron energy spread of X-ray excitation. To overcome these problems, refinements have been made to provide an optimised focusing system having a better electron beam quality and a longer drift region. A reduced exposure(or frame) time has been made possible applying a lower anode voltage and increasing the distance between the anode aperture and the framing aperture. The defocusing effect due to the deflections has been elliviated by either introducing an extra cylindrical lens between the two deflectors or employing travelling-wave deflectors. An improved design of a framing tube has been devised and it can provide frame times of about 60 ps (FWHM) when using conventional deflectors together with an extra cylindrical lens and less than 50ps (FWHM) when travelling-wave deflectors are employed. Theoretically predicted dynamic spatial resolutions referred to photocathode are respectively 10 lp/mm for X-rays and over 15 lp/mm for UV and visible radiations.

With ongoing and future research, substantial improvements in framing camera performance will be a primary objective so as to catch up with the rapid development of ultrafast phenomena studies. For instance, the provision of a larger photocathode working area, higher dynamic spatial resolution, shorter frame time and larger dynamic range will all be relevant to many new application areas.

7.8 References

1 Key M H, Phil. Trans. R. Soc. Lond. A, Vol.298, pp.351-364 (1980)

2 Zavoisky E K and Fanchenko S D, Applied Optics, Vol.4 (9), pp.1155-1167 (1965)

3 J. S. Courtnet-Pratt, Applied Optics, Vol. 3, No. 11, pp. 1201-1209 (1964)

4 M. Blanchet, Proc. 6th ICHSP, pp.313-316 (1962)

5 Blanchet M, Proc. 9th ICHSP, pp.112-115 (1970)

6 Duguay M A, Hansen J, Appl. Phys. Lett., Vol.15, pp.192-194 (1969)

7 Richardson M C, and Sala K, Appl. Phys. Lett., Vol.23, pp.420-422 (1973)

8 Ippen E P, Shank C V, Appl. Phys. Lett., Vol.26, pp.92-94 (1975)

9 Etchepare J, Grillon G, Migus A, Martin J L and Hamoniau G, Appl. Phys. Lett., Vol.43, pp. 406-408 (1983)

10 Topics in Applied Physics Vol.18, Ultrafast light pulses, picosecond techniques and applications, Editor: S. L. Shapiro, Springer-Verlag, Berlin, Heidelberg, (New York, 1978)

11 Duguay M A and Mattick A T, Appl. Opt., Vol.10 (9), pp. 2162-2170 (1971)

12 Billman K W, Burnham D C, Rev. Sci. Instum., Vol.41 (12), pp.1837-1838 (1970)

13 Busch G E, Shepard C L, Siebbert L D, Tarvin J A, Rev. Sci. Instrum., Vol.56 (5), pp. 879-884 (1985)

14 Maaswinkel A G, Sigel R, Baumhacker H, Brederlow G, Rev. Sci. Instrum., Vol.55 (1), pp.48-51 (1984)

15 Valdmanis J A and Abramson N H, Laser Focus World, Vol.27 (2), pp.111-117 (1991)

16 Eschord G and Polaert R, Adv. Elect. & Elect. Phys., Vol. 28B, pp.989-998 (1969)

17 Lunddy A S, Iverson A E, SPIE Vol.348, High Speed Photography, pp.178-189 (San Diego, 1982)

18 Clement G, Adv. Elect. & Elect. Phys., Vol. 33B, pp. 1131-1136 (1972)

19 Pfeiffer W, Wittmer D, SPIE Vol.491, High Speed Photography, pp.254-256 (Strasburg, 1984)

20 Young B K F, Stewart R E and Woodwark J G, Bailey J, Rev. Sci. Instrum., Vol.57 (11), pp. 2729-2732 (1986)

[21] Bell P M, Hammel B A, Kilkenny J D, and Turner R E, SPIE. Vol.1155, Ultrahigh Speed Photography, Photonics and Videography '89, pp.415-421 (San Diego, 1989)

[22] Kilkenny J D, Bell P, Hanks R, Power G, Turner R E, Wiedwald J, Rev. Sci. Instrum., Vol. 59 (8), pp.1793-1796 (1988)

[23] Sterns D G, Wiedwald J D, Cook B M, Hanks R L, Landen O L, Rev. Sci. Instrum., Vol.60 (3), pp.363-367 (1989)

[24] Fleurot N, Gex J P, Rostocing M, Sauneuf R, SPIE. Vol.348, High Speed Photography, pp.772-776 (San Diego, 1982)

[25] Katayama M, Nakai M, Yamanaka T, Izawa Y, Nakai S, Rev. Sci. Instrum., Vol.62 (1), pp.124-129 (1991)

[26] Bell P M, Kilkenny J D, Power G and Bonner R, SPIE. Vol.1155, Ultrahigh Speed and High Speed photography, Photonics and Videography '89, pp. 430-438 (1989)

[27] Ludikov V V, Prokhorov A M and Chevokin V K, Adv. Elect. & Elect. Phys., Vol. 74, pp. 239-246 (1988)

[28] Huston A E, Proc.15th ICHSPP., SPIE Vol.348, pp. 251-253 (San Diego, 1982)

[29] N. Finn, Hall T A and McGoldrick E, Appl. Phys. Lett., Vol.46 (8), pp. 731-733 (1985)

[30] Niu H, Chao T and Sibbett W, Rev. Sci. Instrum., Vol. 52 (8), pp.1190-1192 (1981)

[31] Kalibjian R, Rev. Sci. Instrum., Vol.49 (7), pp.891-896 (1978)

[32] Kalibjian R, Thomas S W, Rev. Sci. Instrum., Vol. 54 (12), pp.1626-1628 (1983)

[33] Sibbett W, Baggs M R, Niu H, SPIE Vol.348, High Speed Photography, pp.267-270 (San Diego, 1982)

[34] Eagles R T, Freeman N J, Allison J M, Sibbett W, Sleat W E, Walker D R, Proc. 32nd International Symposium on Optical and Optoelectronic Applied Science and Engineering, pp.193-220 (San Diego, 1988)

[35] Eagles R T, Sibbett W, Sleat W E, Walker D R, Allison J M, Freeman N J, Adv. Elect. and Elect. Phys., Vol. 74, pp.209-217 (1988)

[36] Sibbett W, Walker D R, Sleat W E, Eagles R T, Freeman N J, Proc. 33rd International Symposium on Optical and Optoelectronic Applied Science and Engineering, SPIE Vol. 1155, pp.406-414 (San Diego, 1989)

[37] Sibbett W Baggs M R, Niu H, Proc. of 15th ICHSPP., SPIE Vol.348, pp.267-270 (San Diego, 1982)

[38] Henke B L, Liesegang J, Smith S D, Physical Reviews B, Vol.19 (6), pp.3004-3021 (1979)

[39] Eagles R T, PhD Thesis, Imperial College of Science and Technology (London, 1986)

[40] Liu Y, Sibbett W, Walker D R, Proc. 33rd International Symposium on Optical and Optoelectronic Applied Science and Engineering, SPIE Vol.1155, pp.398-405 (San Diego, 1989)

[41] Yamada I, Takagi T, IEEE Trans. on Electron Devices, ED-19 (2), pp. 204-213 (1972)

[42] Finch A, Liu Y, Niu H, Sibbett W, Sleat W E, Walker D R, Yang Q L, Zhang H, Proc. 18th ICHSPP., SPIE Vol.1032, pp.622-626 (Xi'an, 1988)

[43] Walker D R, PhD thesis, The J F Allen Physics Research Lab., Department of Physics and Astronomy, University of St. Andrews (1989)

Chapter 8

FUTURE PROSPECTS

8.1 Introduction

In the previous chapters, detailed studies of streak image tubes in streak (synchroscan, single-shot) and framing modes of operation have been described. It has been revealed that limitations to the performance of these cameras arise mainly from laser and RF noise for synchroscan operation, space-charge effects for single-shot operation and poor dynamic spatial resolution for framing operation. Future developments of electron-optical cameras are required to overcome these factors and to extend their applications in a wider range of research fields.

8.2 New design considerations for a better dynamic range

Although the incorporation of an extraction mesh electrode into the streak tubes[1] opened up a new era for ultrafast streak cameras and made it possible to achieve femtosecond time resolution[2,3], its existence induces additional problems which have become increasingly pronounced as the time resolution reaches the femtosecond timescale. One of the problems is the limited transmission of the mesh which significantly reduces the number of photoelectrons reaching the screen and effectively increases the required input light intensity. Another problem is that some of the photoelectrons are scattered by the mesh and constitute a background noise thus degrading the signal-to-noise ratio. Furthermore, because it is close to the photocathode, in addition to its microlensing effects, it may be imaged on the screen and thereby can compromise the signal image resulting in the degradation of the spatial resolution. Also, the mesh electrode can make the streak tube more susceptible to mechanical damages and adds to difficulties of the tube manufacture. These disadvantages have led researchers to devise new tube designs which do not require such a mesh and which might provide temporal and spatial

resolution similar to or better than existing streak tubes[4]. Based on the design given in reference 4, a new tube design has been evaluated which consists of five pairs of parallel planar electrodes. A narrow rectangular shaped photocathode is located at the inner space of the first electrode so that a high electric field can be formed near photocathode surface and can be relatively uniform close to its centre. The arrangement of the focusing lens (with dimensions) is shown in Fig.6.2.1.

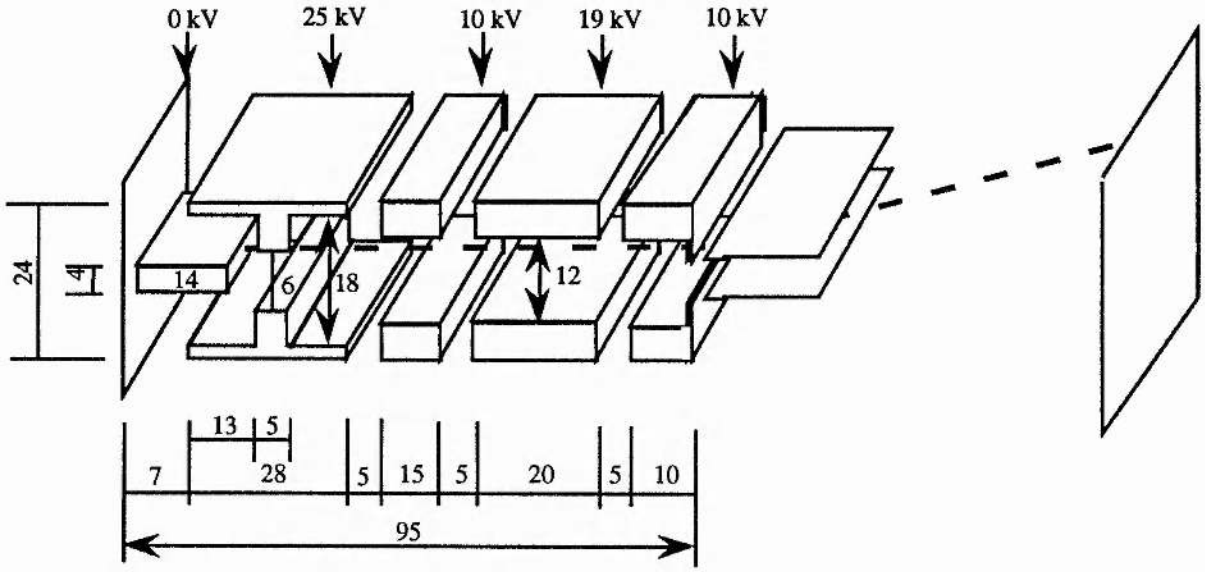

Fig.8.2.1 The configuration of an experimental meshless cylindrical tube

It is noticeable that the anode has the lowest operating voltage and the distance from the photocathode to the anode in the focusing system is only 81 mm. This gives a transit time of photoelectrons from photocathode to the anode as short as 1.1 ns which is only half of that in the Photochron V tube described in chapter 4. Thus when used for single-shot operation, the space-charge effects can be reduced dramatically. The total length of the tube is 300 mm with a magnification of x2.5. A deflection sensitivity of greater than 8 cm/kV is achievable for the metal-plate deflector configuration used in the Photochron V tube and can even be higher if a TWD system is used. As the photocathode is located within the first electrode to which a very high voltage is applied, a electric field as high as 5 kV/mm can be produced near the photocathode and this ensures that the tube provide good spatial and temporal resolutions. Due to the nonuniformity of the electric field across the width direction of the photocathode, the usable area of the photocathode in this direction is limited to 200 μm. This should not matter

much since the input object has a dimension of only several tens of micrometers and the object should be easily aligned at the centre of the photocathode. The calculation of its temporal and spatial resolutions has revealed that a temporal resolution of less than 200 fs is achievable with a spatial resolution of better than 60 lp/mm at the centre of the photocathode.

Although this new tube can only provide one dimension resolution and has a very small photocathode working area in the streak direction, still it is very attractive due to its outstanding advantages created by eliminating the extraction mesh electrode such as enhanced spatial resolution, 30%-50% higher response efficiency to input signal, high deflection sensitivity, very short transit time, freedom from time distortion, improved signal-to-noise ratio and high dynamic range. For single-shot operation, it is desirable to integrate the output along the slit so that an adequate dynamic range can be obtained and the absence of time distortions along the slit dimension makes such data processing much easier to implement.

8.3 Synchronous framing technique ____ potential application for breast cancer diagnosis

One of the potential applications of electron-optical cameras is for medical research where ultrashort time processes are of interest. Early diagnosis of breast cancer is one of the examples.

As the death rate of women caused by breast cancer is increasingly high, the early diagnose has become very important to reduce the mortality rate. X-ray mammography is the commonly used medical diagnostic method which has been employed for routine clinical screening at present. Although its effectiveness of detection is about 80-90% of breast cancers that should be detectable and has been proved to be clinically worthwhile[5,6,7,8], it is far from being perfect as it is not equally accurate in diagnosing carcinoma in each breast type. Particularly it fails to identify malignant tumours embedded in dysplastic (abnormal) tissue of a radiodense breast. Such failure is due to factors such as inadequate image qualities, difficulties and errors in interpreting mammograms, and problems with imaging the architecture and tissue/fat composition of the breast itself[9,10,11,12]. Also, it has caused concern about exposing patients

to ionising radiation which may actually induce cancer[13]. It is highly desirable to have a precise detection method based on examination of tissues by a non-ionising form of radiation that carries no risk to the patient.

This has led to interest by researchers in developing alternative techniques for breast imaging[14]. Among these is transillumination light scanning or diaphanography, a method of cancer detection that relies on non-ionising radiation of visible red and near infrared wavelengths. It is a diagnostic modality based on the characteristic absorption of light in malignant tumours owing to the surrounding neova scularization. In this technique, the light is incident on one side of the breast and a shadow image of the tumour is recorded on the other side. It has been considered to be a valuable supplement to the mammography technique for the clinical examination of breasts[15,16,17,18]. However, it also has the principal weakness of inability to differentiate malignant from benign breast masses reliably and to detect very small and deep-seated cancers[19,20,21]. Such limitations have restricted its clinic usefulness[22,23]. Such failure is mainly due to random light scattering around lesions since in visible red or infrared wavelength region, the dominating attenuating effect is not absorption but scattering[24]. The scattering coefficient in breast tissues is of the order of 10 mm^{-1} whereas the absorption coefficient is of order of 0.1 mm^{-1}. The high scattering coefficient induces pronounced multiple scattering in tissue and degrades image contrast when breast transillumination is performed. This limits transillumination technique to a spatial resolution of > 1 cm with 54% detection efficiency[25]. When the tumour is either too small (~mm) or lies deep inside the breast, it cannot be observed by this technique.

Studies in understanding how light migrates in a random medium has shown that after experiencing multiple scattering, the exiting light is composed of three components: ballistic (coherent), snake-like (quasi-coherent) and diffuse (incoherent)[26,27,28] as illustrated in Fig. 8.3.1. The ballistic photons result from the coherent interference of light scattered in the forward direction and they propagate straight through the medium. The ballistic component is always present, but its intensity is reduced considerably by scattered away from the forward direction. In an inhomogeneous medium such as biological tissues, photons follow the

continuous variation of refractive index along the line of least optical path, so the ballistic component may be temporally broadened slightly but retain all the signal information. Some photons are scattered slightly off the straight line path and zigzag through the medium such that they form the snake-like component and retain some information. Diffuse component attributes to photons which experience multiple scattering and follow a random walk through the medium. Diffuse photons lose all the signal information they carried on entering the medium and form noise background in the image plane. In a highly scattering medium such as breast tissues or dense clouds, the diffuse light is the dominant component which smears out any shadow of the tumour and makes it very difficult to detect. As the diffuse light travels furthest and takes much longer time than that for the snake or ballistic light to pass through the material, the ballistic light reaches the detector first and produces a sharp image. For example, the propagation of a 100 fs laser pulse through a 10 mm thick scattering medium induces a ballistic light with a duration of a few tens of picoseconds and a diffuse light lasting a few hundred picosecond up to nanosecond[29]. Such properties have lead to the adoption of time-gating techniques in the transillumination diagnosis by selecting only the ballistic light.

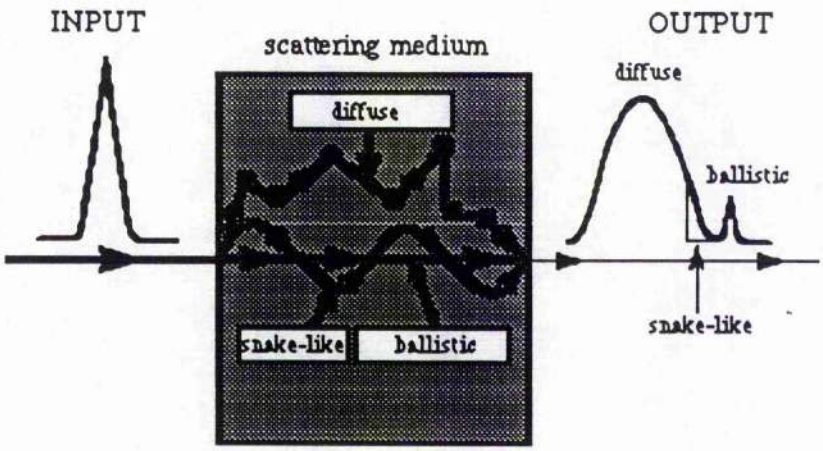

Fig.8.3.1 The migration of a laser pulse through a scattering medium

A number of techniques have been used to provide time-gated imaging so far. These include electronic gating which provides time resolution of 80 ps[30], streak cameras which provide time resolution of 10 - 40 ps[31], optical Kerr gates which gating time of the order of 8 ps[32], holography using short pulses[33] or long-pulse broadband radiation[34] having down to

150 fs time resolution, the stimulated Raman amplification providing time resolution of 1 ps-150 fs and spatial resolution of 150 μm[35]. All these systems have been utilised to produce time-gated images with subnanosecond time resolution and each has its own limitations. Systems based on streak cameras do not provide direct two-dimensional images and the signal must be built up from points or scanlines. In systems based on femtosecond holography, the fringe visibility can be washed out if the energy in the delayed part of the signal is too strong relative to the energy in the forward-scattered component. Electronic gating has relatively low time resolution. The stimulated Raman scattering amplification requires amplification of the laser sources and a high gain Raman cell.

An ideal system is the one that has a short time gate (of the order of picoseconds or less), high detection sensitivity and capability of providing direct, high resolution, two-dimensional information. It should provide substantial discrimination against the time-delayed diffusive light since it contains most of the light energy and causes significant noise or loss of image contrast. Apart from having high signal-to-noise, the system should also provide high spatial resolution and two-dimentional images with a minimum of signal processing. To meet such needs, we have pursued a new technique which uses a synchronous framing camera operating in a repetitive mode at a frequency of a few tens of megahertz. The operating principle of the proposed system is shown in Fig.8.3.2. The operation of the system resembles that of a synchroscan streak camera system. The difference is that the framing tube requires a two-dimensional object and two deflection signals fed to the two pairs of deflectors with an appropriate time delay. The light pulse signal at a repetition rate of a few ten MHz produced by a mode-locked NIR laser is directed to a beam splitter. A fraction of the beam is directed onto a photodetector which produces a electrical signal for the deflection unit. The main part of the light signal is collimated and then used to illuminate the object under examination. The transmitted light from the object is then optically imaged onto the photocathode of the framing tube. By adjusting the synchronisation time between the deflection signals and the light signal, framing images can be superimposed on each other precisely at a repetition rate of the light pulses. Obviously, this technique has the merits of direct two dimensional imaging and extremely high gain as well as high signal-to-noise ratio.

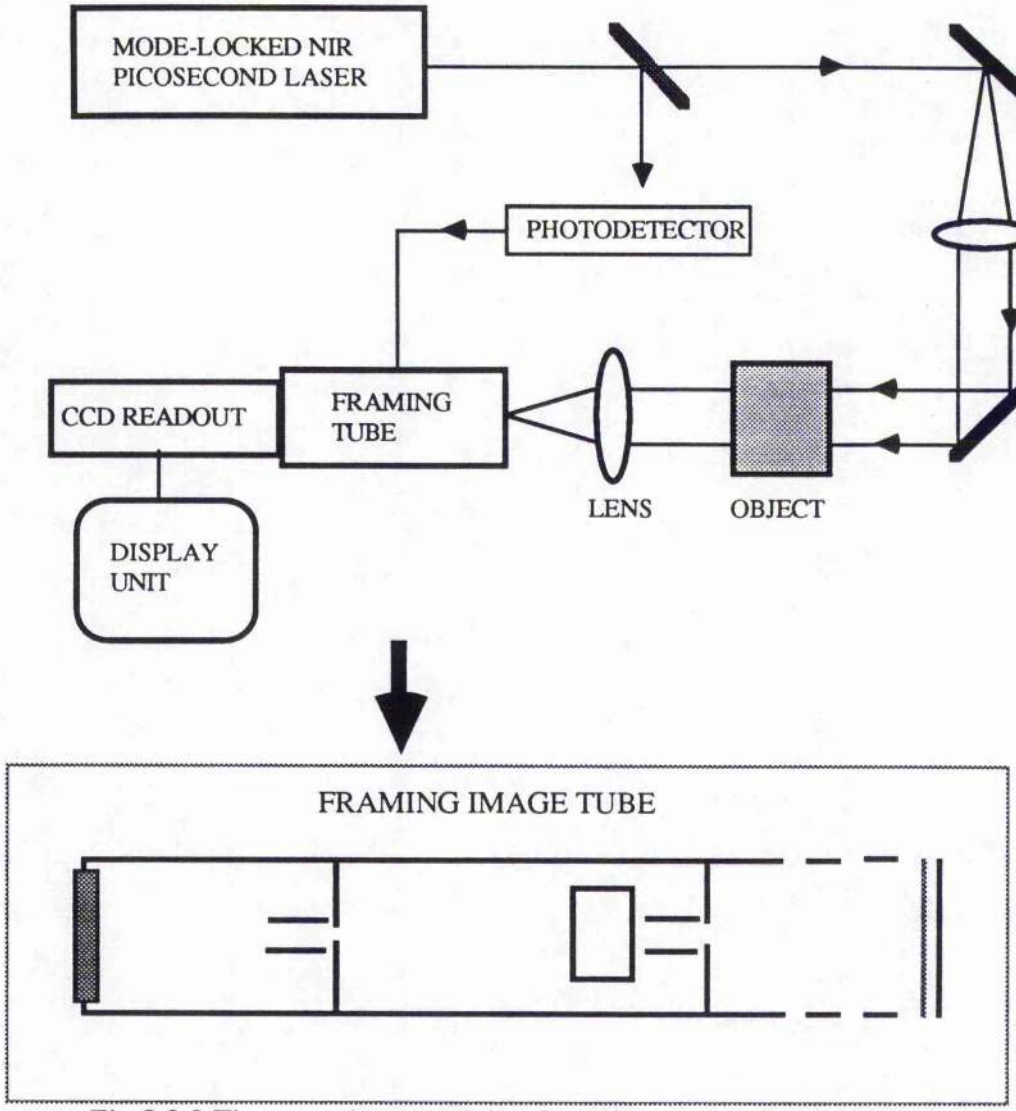

Fig.8.3.2 The operating principle of synchronous framing technique

The preliminary design of the framing tube has been carried out based on Picoframe I tube configuration[36]. In order to reduce the exposure time down to less than 10 ps, the beam diameter at the framing aperture is considerably reduced so that the aperture size can be much smaller. As the tube operates in synchronous mode, input signal intensity can be extremely low. Thus the operating voltage can be reduced to 5 kV without giving rise to space charge effects. By doing this, a very high deflection sensitivity can be attained and the sweep speed can be increased dramatically. To further increase the sweep speed, the framing aperture is located further away from the anode aperture to provide adequately long free space length.

As in dynamic operation, the focusing conditions are significantly influenced by the deflection operating conditions. Rearrangement of the focusing voltages is necessary. This can be accomplished by preconditioning the sweep direction into focus at the static image position and adding a cylindrical lens in the nonsweep direction so that focusing conditions in two directions can be satisfied independently.

A preliminary design of such a tube which has been assessed consists of an extraction mesh and four cylinder electrodes with a total length of 250 mm. Its photocathode working area is 4 mm with magnifications of X4.7 in the sweep direction and X2.7 in the non-sweep direction. It can provide exposure time of less than 10 ps and spatial resolutions of 500 μm in sweep direction and 50 μm in non-sweep direction for visible and NIR light sources. Such a device incorporating with a two dimensional CCD readout system should provide a convenient, high resolution and fast data acquisition diagnostic instrument. Further development of such techniques is still on-going.

8.4 References

1 Bradley D J, Liddy B, Sleat W E, Opt. Commun., Vol. 2, p.39 (1971)

2 Finch, A., Liu, Y., Niu, H., Sleat, W.E., Sibbett, W., Yang, Q.L., Zhang, H., Proc. 18th ICHSPP, SPIE Vol.1032, pp.622-627 (1988)

3 Hamamatsu Photonic Systems (advertisement), Laser Focus World, Vol.26 (5), p.220 (1990)

4 Walker D R, PhD thesis, J F Allen Research Lab., Physics and Astronamy Department, University of St. Andrews, (1989)

5 Kopans D B, J. Natl. Cancer Inst., Vol. 84, pp.745-747 (1992)

6 Meyer J E, Kopans D B, Oot R, Radiology, Vol.147, pp.93-94 (1983)

7 Law J, The British J. Radiol., Vol.65, pp.50-55 (1992)

8 Adami H O, Malker B, Rutqvist L E, Persson I, Ries L, J. Natl. Cancer Inst., Vol.76, pp.653-659 (1986)

9 Ma L, Fishell E, Wright B, et al, J. Natl. Cancer Inst., Vol. 84, pp.781-785 (1992)

10 Holland R, Hendriks J H, Mravunac M, Cancer, Vol.52, pp.1810-1819 (1983)

11 News, J. Natl. Cancer Inst., Vol.83, pp.1444-1445 (1991)

12 Feig G A, Shaber G S, Patchefsky A, et al, Am. J. Roentgenol., Vol. 128, pp.403-408 (1977)

13 Mole R H, Brit. J. Radiol., Vol.51, p.401 (1978)

14 Feig S A, Mclelland R, eds., Breast carcinoma: Current diagnosis and treatment. New York: Masson, pp.233-250 (1983)

15 Ohlsson B, Gunderson J, and Nilsson D M, World J. Surg., Vol.4, p.701 (1980)

16 Hussey G, MacDonald A F, Nichols D and Watmough D J, Brit. J. Radiol., Vol. 54, p.163 (1981)

17 Wallberg H, Acta Radiol. Diagnosis, Vol. 26, pp.271-276 (1985)

18 Watmough D J, Acta Radiol. Oncology, Vol.21, pp.11-15 (1982)

19 Sickles E A, Am. J. Roentgenol., Vol.142, pp.841-844 (1984)

20 Monsees B, Destouet J M, Gersell D, Radiology, Vol.163, pp.467-470 (1987)

21 Drexler B, Davis J L, Schofield G, Radiology, Vol.157, pp.41-44 (1985)

22 Jarlman O, Andersson I, Balldin G, Larsson S A, Acta Radiologica, Vol.33, pp.69-71 (1992)

23 Watmough D J, Radiology, Vol.147, pp.89-92 (1983)

24 Wilson B C, Patterson M S, Flock S T and Wyman D R, in Photon Migration in Tissue, Chance B, ed., Plenum, New York (1989)

25 Geslien G E, Fisher J R, Delaney C, Am. J. Roengetnol., Vol.144, pp.619-622 (1985)

26 Wang L, Ho P P, Liu C, Zhang G, Alfano R R, Science, Vol.253, pp.769-771 (1991)

27 Yoo K M, Alfano R R, Opt. Lett., Vol.15 (6), pp.320-322 (1990)

28 Alfano R, Ho P P, Yoo K M, Physics World, Vol.66 (1), pp.37-40 (1992)

29 Andersson-Engels S, Berg R, and Svanberg S, Opt. Lett., Vol.15 (21), pp.1179-1181 (1990)

30 Anderson-Engels S, Berg R, Svanberg S, Jarlman O, Opt. Lett., Vol.15, pp.1179-1181 (1990)

31 Hebden J C, Kruger R A, Wang K S, Appl. Opt., Vol.30, pp.788-794 (1991)

32 Wang L, Liu Y, Ho P P, Alfano R R, Conference on Lasers and Electro-Optics, Vol.10 of 1991 OSA Technical Digest Series, p.102 (optical Society of America, Washington, D C, 1991)

33 Chen H, Chen Y, Dilworth D, Leith E, Lopez J, Valdmanis J, Opt. Lett., Vol.16, pp.487-489 (1991)

34 Spears K G, Serafin J, Zhu X, Bjelkhagen H, Instrum. Eng., Vol.1090, p.29 (1989)

35 Duncan M D, Mahon R, Tankersky L L, Reintjes J, Opt. Lett., Vol.16 (23), pp.1868-1870 (1991)

36 Sibbett W, Baggs M R, Niu H, Proc. 15th ICHSPP, SPIE Vol. 348, pp.267-270, (San Diego, 1982)

Chapter 9

GENERAL CONCLUSIONS

The rapid development of ultrashort light sources has placed stringent demands upon the performance of ultrafast diagnostic techniques. The outstanding merits of high speed electron-optical cameras providing direct, linear and multi-dimensional information have established their important role in the ultrafast research areas that require picosecond/subpicosecond time resolutions[1]. As the number of their applications is still increasing, it is necessary to understand the operation and performance limitations of these devices so as to further improve their properties and to extend their usefulness.

To identify the main factors that limit the performance feature of streak cameras, the properties of all component parts including input optics, streak image tube, image intensification and readout system have been analysed in substantial details. It is recognised that the streak image tube is the principal element that ultimately determines the instrumental performance of such camera systems.

The theoretical analyses of the performance characterisations of streak image tubes in different operating modes have been accomplished by using a tailored suite of computer programs. The computing evaluations include the simulations of potential distributions and photoelectron trajectories, the characterisation of static image qualities, temporal and spatial properties in terms of both aberrations and MTFs in dynamic deflection operations. For MTF evaluations, the statistics of photoelectron emission have been taken into account by using Monte-Carlo simulations. The results of theoretical investigations clearly show that the initial energy and angle spreads of photoelectrons and deflection-related fringe-field effects inherent

---

1 Tsuchiya Y, IEEE J. Quantum Electron., QE-20 (12), pp.1516-1528 (1984)

in streak tubes are the fundamental limiting factors to their overall spatial and temporal performance.

With regarding to the different modes of streak tube operations, additional problems arise. Specifically, in synchroscan operation, amplitude and phase noise inherent in laser sources and in electronic circuitry tend to degrade the overall time resolution of the system. Multipacting effects induced in the deflection section increase the background noise and restrict the deflection speed. In single-shot operation, space-charge effects have always been a key factor which limits the dynamic range of the system. The requirement for a high speed linear ramp voltage signal leads to another difficulty. For framing operation, in addition to dynamic range requirements, methods by which short frame times with good dynamic spatial resolution can be achieved have been of the major concern. Theoretical studies of these problems have been discussed in this thesis and the modelling results agree clearly with the experimental data obtained to date.

The analysis of synchroscan operation of streak tubes indicates that as the time resolution of a streak tube reaches femtosecond timescale, the amplitude and phase noise inherent in the laser source and electric deflection signal are the factors that limit the overall time resolution to a picosecond regime. For instance, for a streak tube having a 300 fs time resolution, the achievement of an instrumental time resolution of better than 500 fs requires the signal-to-noise ratio of the electric deflection signal to be better than 80 dB and the synchronisation timing jitter to be less than 200 fs. Therefore, to achieve a time resolution in a femtosecond timescale, it is necessary to improve the laser and electronic circuitry stability.

The simulation of space-charge effects in single-shot operation of streak tubes indicates that the temporal broadening caused by space-charge effects is accumulative during the transit time of photoelectrons from the photocathode to the entrance of the deflectors. For shorter input pulse durations more pronounced space-charge effects arise and variation in input slit width has little influence on space-charge effects. With the aid of simulations that have taken space-charge effects into account, the characterisation of the dynamic range of streak tubes has been accomplished. It indicates that the enhancement of dynamic range demands a minimum transit

time of photoelectrons in the focusing section of the tube and highly efficient phosphor screen in conjunction with the use of an image intensifier as well as a readout system with a suitably high signal-to-noise ratio. To obtain high speed ramp voltage, travelling-wave deflection systems have been assessed for application in single-shot streak tubes and have demonstrated the capability of maintaining a high deflection sensitivity over a broad frequency bandwidth (e.g.. 2.5 GHz). A meander-type travelling wave deflector has been introduced into a streak tube. Experimental tests on such a tube have been carried out where an output image duration of 300 fs was obtained and this confirms the practicality of the travelling-wave deflectors in streak tubes.

As a result of theoretical simulations of streak tube, an improved design of a streak image tube, the Photochron V, has been completed and constructed which has fully-optimised focusing and deflection systems. It is theoretically predicted that when using a S1 photocathode near its long wavelength threshold at 1064 nm a limiting time resolution of 250 fs can be obtained from this streak tube under practical operating conditions. Compared with a Photochron IV tube, this Photochron V provides better time resolution, higher deflection sensitivity (7.8 cm/kV) and higher dynamic range at a lower operating voltage (10 kV) and shorter overall tube length (300 mm). Theoretical evaluations also show that in synchroscan operation of the tube an overall time resolution of 300 fs can be achieved if the RF signal-to-noise ratio is greater than 90 dB and the timing jitter is less than 100 fs. When operating in a single-shot mode, linear high speed deflection can be provided by the use of a travelling-wave deflector and it is predicted that a streaked pulse duration of 300 fs is achievable under space-charge constraints provided that a intensifier with adequate gain and sufficiently low noise is available.

An experimental Photochron V tube has been manufactured and preliminary tests have been performed. When operating at a 5 kV overall voltage (design figure 10 kV) the tube has a static spatial resolution of over 50 lp/mm (referred to photocathode) and it has a distinctively high deflection sensitivity (i.e.14.7 cm/kV). This indicates that the simulation programs can provide adequately accurate design parameters. The dynamic evaluation of the streak tube in

synchroscan operation has also been attempted by using a modelocked titanium:sapphire laser as a light source at a repetition rate of 166 MHz. A streaked time duration of 3.8 ps has been recorded and a time duration of 2.5 ps has been observed. Indeed, it is possible to improve this to less than 2 ps for this tube if refinements are made to the laser system.

It is expected that a Photochron V tube with fully specified design configuration in conjunction with a less noisy laser system (eg. less than 100 fs timing jitter) for synchroscan operation and an image intensifier and readout device with high gain and low noise for single-shot operation should provide a time resolution of less than 500 fs towards the predicted value of 250 fs.

Normally, the time resolving ability of a streak tube is specified in terms of its limiting time resolution as stated in chapter 2. From this definition, it can be readily understood that this time resolution figure is only a measure of temporal error induced by the streak tube itself. It therefore follows that the streak tube cannot identify the time signature of input signals in this timescale. In order to specify the timescale on which the identification of the temporal structure of input signals can be provided by a streak tube with a given limiting time resolution, output temporal responses of the Photochron V streak tube for different input temporal profiles have been investigated on a theoretical basis. The results indicate that for input signals with time durations $\geq$ 1 ps the tube can reproduce their temporal profiles with adequate fidelity in both synchroscan and single-shot operations and can still provide some intensity-time information for input signals with durations between 400 fs and 1 ps.

Theoretical simulations of Picoframe I and II framing tube have also been conducted in order to improve their dynamic performance and to meet the needs of even more exacting applications. The simulation results suggest that the main limiting factor to the dynamic spatial resolution is the fringe-field effects of the deflectors. The refinements of the framing tubes towards a better dynamic spatial resolution and shorter frame times are possible by the optimisation of the focusing lens system and the addition of an cylindrical lens between the framing deflection and the compensation deflection systems. Frame times of around 60 ps with dynamic spatial resolutions of over 15 lp/mm for UV illuminations and 10 lp/mm for x-ray

radiations are theoretically predicted for the improved design. Based on these studies of farming tubes, the design of a framing tube providing frame times shorter than 10 ps for NIR /visible light sources has been made possible in synchronously repetitive mode of operation and it may have an important impact on medical diagnosis, such as breast cancer, where the requirement for high sensitivity, two-dimensional diagnostic techniques with short frame time and good spatial resolution has recently emerged. It is expected that with the availability of adequate information on the interaction of light with biological tissues, such applications will be put in practice in the near future.

For the future development of streak cameras, a new streak tube design that avoids the use of an acceleration mesh has been proposed which can provide a limiting time resolution comparable with that of the Photochron V tube. Although it can only provide one dimensional information (temporal only), it has the advantages of having lower background noise and better spatial resolution due to the elimination of the mesh electrode. Also its shorter transit time implies a better dynamic range and the lack of time distortion along the slit will allow signal integration along the slit so as to further enhance its dynamic range.

It should be pointed out that the work described in this thesis mainly focuses on performance characterisations of the electron-optical cameras. The designs of streak tubes presented are based on the grounds of being practically achievable and compatible with currently available operating conditions. Without practical limitation considerations, the performance of the Photochron V tube can be further improved. For example, if a fast gating pulse is applied across its photocathode and mesh, an electric field of 10 kV/mm may be achieved without a significant background noise increase. Also, if a thin photocathode having a large energy bandgap is used near its long wavelength response threshold, then the initial energy spread of photoelectrons can be reduced to 0.05 eV. Under such conditions, it would be possible to reduce the limiting time resolution towards 100 fs.

As a result of this work, a powerful simulation tool for evaluating and designing a variety of electron-optical image devices has become available and it has provided a thorough insight into the instrumental limitations of ultrafast electron-optical cameras. No doubt, this will play

an important role in the future development in ultrafast diagnosis techniques and applications in this research field.

ACKNOWLEDGEMENTS

I would like to express my sincere thanks to my supervisor, Professor W. Sibbett, for providing me with the opportunity of studying for the degree of PhD and for his patient supervision, firm support and encouragement throughout the course of this work.

I am very grateful to Dr. Bill Sleat for his tireless help and invaluable advice during my study and for his patient proof reading of this thesis.

Thanks are due to all the technical staff for their kind help. I would also like to thank all my colleagues and friends for their support and understanding during the period of this study. In particular, I would like to thank Dr. David Walker for his practical assistance and useful discussions.

I am also indebted to the University of St. Andrews for the postgraduate studentship and the Oversea Research Scholarship.

PUBLICATIONS

Finch A, Liu Y, Niu H, Sibbett W, Sleat W E, Walker D R, Yang Q L, Zhang H, "Development and Evaluation of a new Femtosecond Streak Camera", Proc. 18th ICHSPP, SPIE. 1032, p.622-626 (Xi'an, 1988)

Finch A, Liu Y, Sleat W E, Sibbett W, Chen G, "Phase Noise Limitations in Synchroscan Streak Tube Operation", Proc. 18th ICHSPP, SPIE., Vol. 1032, pp. 97-104 (1988)

Liu Y, Sibbett W, Walker D R, "Theoretical analyses and design considerations of a picosecond framing tube", Proc. 33rd International Symposium on Optical and Optoelectronic Applied Science and Engineering, SPIE Vol. 1155, pp.398-405 (San Diego, 1989)

Liu Y, Sibbett W, Walker D R, " Theoretical and Experimental Performance Evaluations of Picoframe Framing Cameras", Proc. 19th ICHSPP, SPIE Vol.1358, pp.290-299 (Cambridge, 1990).

Liu Y, Sibbett W, "Profile-related Time Resolution for a Femtosecond Streak tube", Proc. 19th ICHSPP, SPIE Vol.1358, pp.503-510 (Cambridge, 1990).

Liu Y, Sibbett W, " A Theoretical Analysis of the Dynamic Range of a Streak Image tube", Proc. 9th Conf. on Photoelectronic Image Devices, pp. 305-310 (London, 1991).

Liu Y, Sibbett W, and Walker D R, " Picosecond (Picoframe) Framing Camera Evaluations", Applied Optics, Vol.31 (7), pp.926-934 (1992)

a reprint from Applied Optics

Picosecond (picoframe) framing camera evaluations

Y. Liu, W. Sibbett, and D. R. Walker

Detailed theoretical evaluations of picoframe-I- and II-type framing cameras are presented, and predicted performance characteristics are compared with experimental results. The methods of theoretical simulations are described, and a suite of computer programs was developed. The theoretical analyses indicate that the existence of fringe fields in the vicinity of the deflectors is the main factor that limits the dynamic spatial resolutions and frame times of these particular designs of framing camera, and possible refinements are outlined.

Key word: Framing camera.

Introduction

In several related research areas, such as laser-induced fusion and laser plasma interactions,[1] two-dimensional ultrafast diagnostic techniques with moderate spatial resolution and short frame times (typically <1 ns) are desirable. In order to fulfill this requirement, several kinds of framing technique have been reported.[2–5] Among these, the picoframe type of framing camera has demonstrated the capacity to provide single–multiple subnanosecond frames, and it has been a subject of development and applications of framing techniques. To date, the frame times of this type of camera have been demonstrated to be 100-ps FWHM in a single-frame operation,[6] 120-ps FWHM in double-frame operation,[7] and 250 ps FWHM in four-frame operation[8] with limiting spatial resolutions (i.e., 5% modulation depth) of 8 line pairs/mm (lp/mm) for UV and 5 lp/mm for x-ray illuminations. However, for some applications, higher spatial resolutions and shorter frame times are required so that appropriately quantitative information can be obtained. For this reason, further improvements to the dynamic performance of this type of framing camera have been investigated by using theoretical simulations.

Some modeling of a picoframe-I camera has been performed, and a few design refinements have been discussed.[9] More detailed theoretical analysis of both picoframe-I- and picoframe-II-type framing cameras are presented in this paper, and theoretical data are related to the available experimental measurements. From this, it can be concluded that the fringe field effects of the deflection systems represent the major limitation to the frame times and the dynamic spatial resolutions of these camera systems.

Theoretical Modeling Scheme

A schematic of a picoframe-I image tube is reproduced in Fig. 1, and its design concepts are discussed in detail in Ref. 10. It therefore suffices to include a brief review of the basic operating principle involved.

The photoelectrons emitted from the photocathode are accelerated in the photocathode–mesh region and then focused by an electro-optical lens. When a linear, time-varying voltage ramp is applied to the so-called framing deflectors, the photoelectrons are swept across the aperture, A2 (framing aperture), and so a short temporal exposure is defined by the framing aperture. The imposed temporal smear on the image is canceled by applying an identical and properly phased inverse-polarity voltage ramp to the compensating deflectors.

The overall frame exposure time t of the image (or frame) can thus be expressed as

$$t = 2V_a Ad/[Ka(a/2 + L)], \quad (1)$$

where V_a is the anode voltage, A is the sum of the framing aperture diameter and the photoelectron beam diameter at the framing aperture, d is the separation of the framing deflector plates, K is the gradient of the deflection voltage ramp (V/s), a is the length of the framing deflectors, and L is the distance from the exit of the framing deflectors to the framing

The authors are with the J. F. Allen Physics Research Laboratory, University of St. Andrews, St. Andrews, Fife KY16 9SS, UK.

Received 12 March 1990.
0003-6935/92/070926-09$05.00/0.

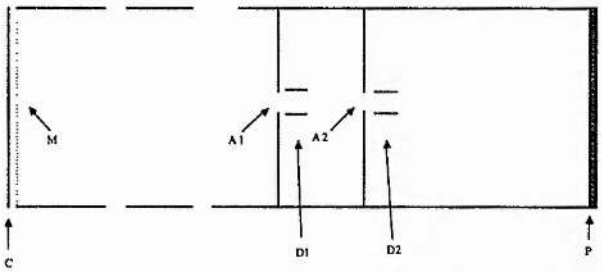

Fig. 1. Schematic of a picoframe-I image tube: C, photocathode; M, mesh; A1, anode aperture; A2, framing aperture; D1, framing deflectors; D2, compensating deflectors; P, phosphor screen.

aperture. In practice, variations in the conditions associated with photoelectron emission make it difficult to determine the actual diameter of the photoelectron beam. Usually the parameter A is estimated to the first approximation at FWHM of the convolution function of the aperture diameter and the photoelectron beam cross-section profile. This gives rise to values for the frame exposure time t that differ—usually shorter—from those predicted by Eq. (1).

In most instances, the design of a framing tube is undertaken on the basis of the parameters that are predicted under conditions of a static (or focus) mode of operation. However, the achievement of the optimum dynamic performance is the most important aspect in the design of a framing tube. It has been found, in practice, that in the framing mode, the spatial resolution is significantly degraded compared with that under static conditions. To overcome this problem, one must apply more realistic theoretical modeling techniques for this kind of framing camera in dynamic operation.

When an optical signal with a finite time duration illuminates the photocathode of a framing tube, a photoelectron replica with an identical temporal duration should be emitted if the time dispersion of the photoelectrons within the photocathode can be neglected. Knowledge of the conditions of this photoemission process is required to achieve quantitative characterization of the behavior of the photoelectron signal within an image tube. The associated parameters include the temporal relationship between individual photoelectrons and the emission angles and energies of the liberated photoelectrons. With regard to the photocathode microstructure, the photoelectron emission process is statistically random such that when considering a particular photoelectron, its initial energy, time, and angles of emission are random parameters. When a large number of photoelectrons are taken into account, such parameters may be described by appropriate distribution functions. In many cases, the intensity temporal profile of the incident-light signal can be assumed to be a Gaussian distribution, where the variance is given by the time duration of the light pulse and the initial energy spread can be modeled by a beta function.[11] The angles of emission corresponding to directions that are normal and parallel to the photocathode plane can be dealt with, respectively, as variables of cosine and uniform distributions. The determination of specific values of these statistical variables is accomplished by using the Monte Carlo method,[12] where a multiplicative generator is used to generate random numbers distributed uniformly over the interval (0, 1). The required variables are then generated by means of acceptance–rejection techniques with the aid of uniform random numbers.

Potential distributions in both focusing and deflection regions are presented by an overrelaxation iterative solution of a finite difference Laplace equation from which the electric field distributions can be simulated by using Lagrange interpolation and numerical differentiation techniques. In the photocathode–mesh region, assuming a perfectly planar and parallel photocathode–mesh geometry and ignoring the field spread near the extremity (or fringe) of the photocathode–mesh region, the equations of motion of the photoelectrons can be solved analytically for conditions of nonrelativistic motion. In the mesh-to-phosphor-screen region, the equations of motion of photoelectrons can be numerically solved by a three-step Runge–Kutta method.[13] The error introduced in each step of such a calculation is checked by estimating the third-order term truncated in the Taylor series. If the given accuracy is satisfied, the step is accepted, otherwise the step is rejected and a smaller step length is chosen. At the same time, the conservation of energy for each photoelectron is used as a cross check on the accuracy of the calculation. The relativistic effects are considered in this region because the operating voltage of the tube is relatively high (typically 15 kV). In this case, the equations of motion become somewhat more complicated, and more numerical computing errors are introduced because of the additional arithmetic calculations involved and the limited capacity of the computer. To reduce these computation errors, we used double precision for all variables and constants in the program and the order of the calculation of the variables was rearranged such that the subtraction or division of two variables having a small difference could be avoided. As a result, the available digits of the computer can be utilized most effectively, and the errors introduced during the entire simulation process can be minimized.

Simulation of Single-/Double-Frame Operation of a Picoframe-I Camera

Single-Frame Operation

For the simulation of picoframe-I framing camera performance, a complete suite of computer programs was developed on the basis of the simulation techniques mentioned above. These programs can provide data that relate to image position, magnification, spatial aberrations, transit-time dispersions, deflection sweep speeds, spatial and temporal modulation transfer functions, and photoelectron transmission through the apertures. In the framing mode, two linear time-varying voltage ramps of inverse polarity

are applied, respectively, to the two sets of deflectors. For simplicity, the finite transit times of deflection signals propagating along the deflector plates are neglected (the same approximation is made for double-frame operation). Because of the limited memory capacity of the computer, the potential distributions in the focusing and deflecting regions are calculated separately. In the deflection regions, the existence of the apertures is ignored. The UV and x-ray illuminations mentioned below refer, respectively, to 0.6 and 4.0 eV of photoelectron emission energies obtained from a gold cathode on suitable substrates under 266- and 0.6–1.2-nm radiation. Under dynamic operation, the photoelectrons are swept across the framing aperture according to their time sequences where the framing aperture is functioning as a time window. To determine the temporal transmission of the photoelectrons through the time window, one must consider the transverse position of each photoelectron on the framing aperture plate. Only the photoelectrons located within the framing aperture area can proceed to the second deflection region. By suitably adjusting the synchronization of the deflection signal on the compensating deflectors with respect to that on the framing deflectors, one can obtain a properly framed image on the center of the phosphor screen. The calibration of the sweep speeds provided by the deflectors is accomplished by deliberately providing a pair of photoelectrons with the same conditions of photoelectron emission but differing only in the time (e.g., 10 ps) of liberation at the photocathode.

A number of randomly selected photoelectron trajectories, traced in the original picoframe-I image tube design in a single-frame mode, are reproduced graphically in Fig. 2 with reference to the sweep direction. The phosphor screen is located at the static in-focus plane. The sweep speed of the framing deflectors at the framing aperture is 0.18×10^8 m/s under conditions of the framing deflection ramp of 2 kV/ns; the deflection sensitivity is 0.95 cm/kV (referring to the framing aperture); and the input light pulse duration is 100 ps (FWHM). The calculations indicate that in the nonsweep direction, the focused image plane remains the same as that in the static mode and so the dynamic spatial resolution is unchanged. In the sweep direction, however, the framing action advances the focusing plane approximately 50 mm closer to the deflectors. This causes image astigmatism and gives rise to a significant degradation in the spatial resolution, and a theoretically simulated limiting dynamic spatial resolution of less than 3 lp/mm for UV illumination is obtained for the sweep direction at the photocathode. Such a dynamic relocation of the optimum focal plane is mainly due to the dynamic fringe field effects that arise with conventional metal plate deflectors. It occurs because the velocity of the photoelectrons traveling between deflectors is only approximately one fifth of the velocity at which the electrical deflection signal propagates along the metal deflector plates. Consequently, the deflection voltage changes while the photoelectrons propagate between the deflectors such that a so-called finite transit-time effect arises. Typical operating conditions of a picoframe camera yield a deflection potential difference of up to 550 V between the entrance and the exit of the deflectors that the photoelectrons encounter, and so the synchronization between the deflection and the photoelectron signals must be adjusted to allow the photoelectrons to reach the center of the phosphor screen. This inevitably introduces nonzero and opposite voltages at the entrance and the exit of the deflectors that give rise to fringe fields between the ends of the deflectors and the apertures or boundaries of the regions. The fringe field distributions in both the framing and the compensation deflectors are shown in Fig. 3. It can be seen that the fringe fields in regions I constitute a convergent cylindrical lens and those in regions II represent a divergent cylindrical lens for the photoelectrons. The overall influence is equivalent to an electrostatic cylindrical lens that produces an enhanced focusing

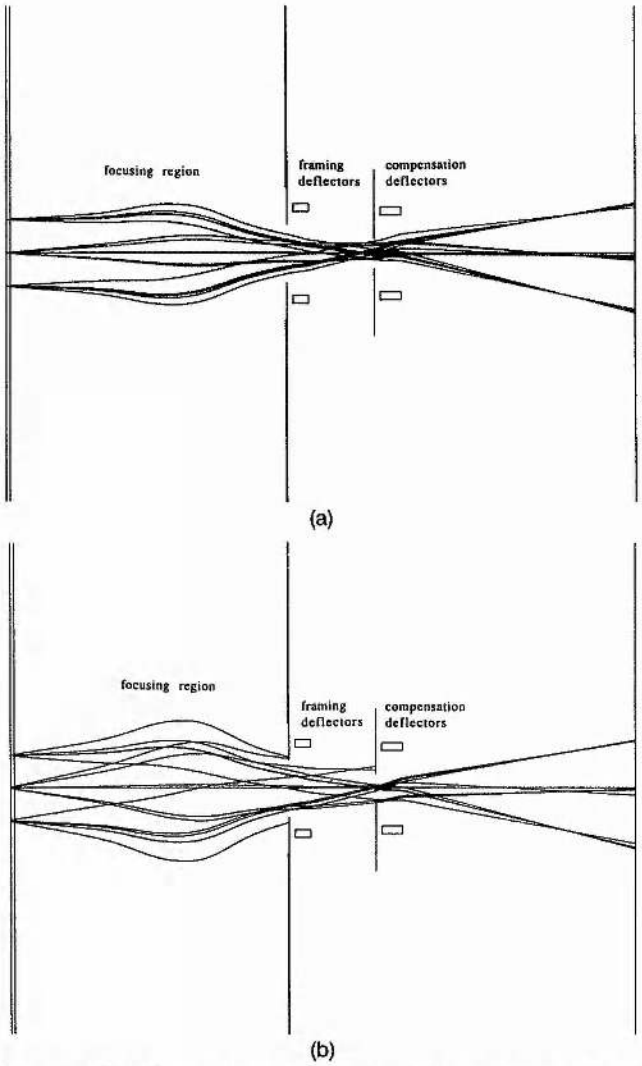

Fig. 2. Photoelectron trajectories in a picoframe-I image tube in single-frame mode of operation: (a) UV illumination, (b) x-ray illumination.

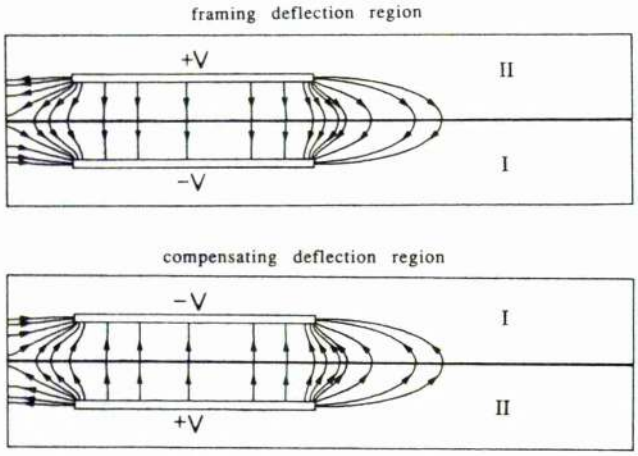

Fig. 3. Fringe field distributions in the framing and the compensating deflectors of a picoframe-I image tube in a single-frame mode of operation.

effect. For higher sweep speeds, this effect becomes more pronounced.

By adjusting the voltages on the main electrostatic focusing lens section of the image tube, one can achieve a compromised focusing condition. Theoretical evaluations demonstrated that, under the same sweep conditions as those considered previously, the limiting dynamic spatial resolutions on the phosphor screen are 7 lp/mm for UV illumination and 3 lp/mm for x-ray illumination, assuming that 100 photoelectrons (the same for the calculations below) are emitted from a point at the center of a photocathode illuminated with a 100-ps (FWHM) light pulse. The frame times of approximately 95 ps (FWHM) for UV and 110 ps (FWHM) for x-ray illumination are deduced from the temporal transmission profile through the framing aperture, and the corresponding spatial modulation transfer functions (SMTF's) are plotted in Fig. 4. Considering that the magnification of the image tube is 1.5×, spatial resolutions of 10.5 lp/mm for UV illumination and 4.5 lp/mm for x-ray illumination at the photocathode can be derived. The transmissions of the photoelectrons through the apertures in the dynamic mode of operation are 66% for UV and 50% for x-ray illumination. When the photoelectrons are emitted from a point that is 2 mm from the photocathode center, the transmissions reduce to 60% for UV and 40% for x-ray illumination, and the spatial resolutions are degraded compared with those from the center of the photocathode. These theoretical predictions agree with the experimental results (see Fig. 5), where limiting dynamic spatial resolutions of 8 lp/mm for UV illumination and 6 lp/mm for x-ray illumination were measured on the photocathode. These experimental data apply to a framing camera that incorporated an image intensifier (Mullard XX1330A microchannel plate device) with a limiting spatial resolution of 20 lp/mm.

It is clearly not possible to eliminate the inequality of the focusing abilities in the two directions by a simple adjustment of the voltages applied to the electrostatic lens. More practical approaches must be introduced to minimize this undesired lensing effect.[9]

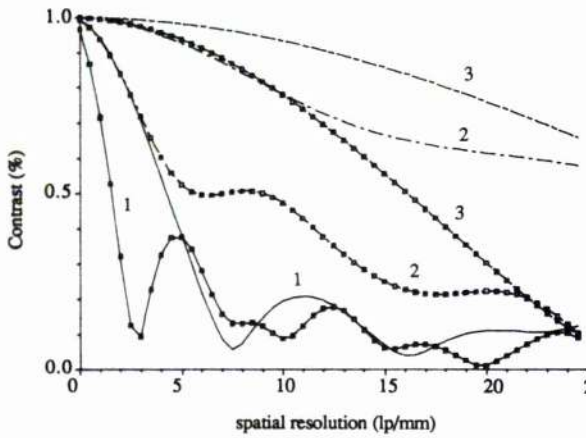

Fig. 4. Theoretical SMTF data for a picoframe-I camera in a single-frame mode of operation. Curve 1, an original picoframe-I tube; curve 2, a picoframe-I tube with a compensating cylindrical lens. Curves labeled by boxes are for x-ray illumination, and the other are for UV illumination.

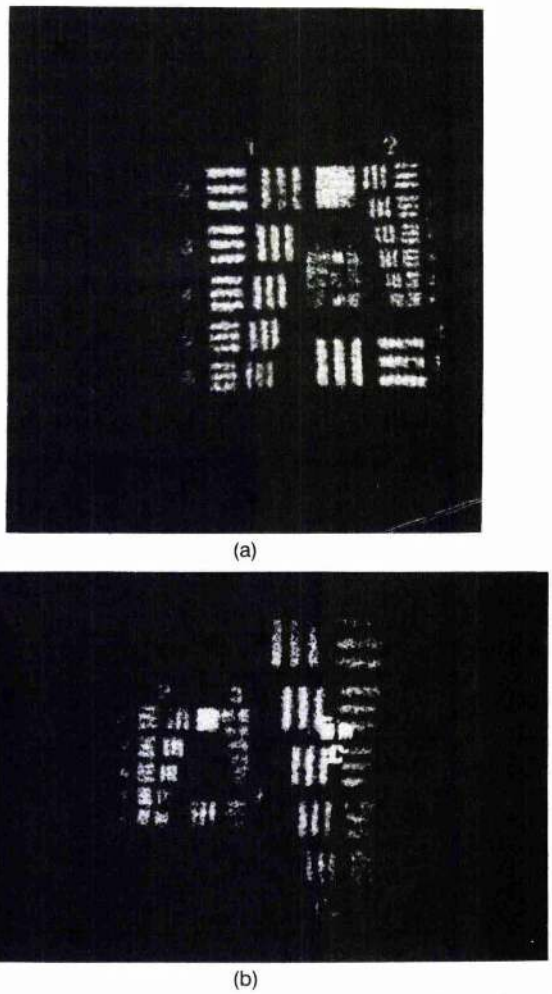

Fig. 5. Experimental single-frame results for UV and x-ray illuminations recorded with a picoframe-I camera: (a) UV illumination, (b) x-ray illumination.

One approach involves the inclusion of an extra electrostatic cylindrical lens (orientation orthogonal to the deflection direction) between the framing deflector and the aperture. The main electrostatic lens is deliberately defocused in the static mode such that the focusing condition in the dynamic operation can be reestablished in the sweep direction by a combination of the main focusing lens and the dynamic fringe field effects of the deflectors. In the nonsweep direction, the effects of the main focusing lens and the inserted cylindrical lens are suitably combined. It follows, therefore, that the focusing conditions in the sweep and the nonsweep directions can be adjusted separately and, thus, optimized independently. By doing this, we estimated the theoretical limiting dynamic spatial resolutions on the phosphor screen for conditions similar to those described above to be better than 30 lp/mm for UV illumination and 18 lp/mm for x-ray illumination from the center of the photocathode (see Fig. 4). A preliminary experiment was carried out with UV illumination, and a limiting dynamic spatial resolution of better than 9 lp/mm was recorded, as shown in Fig. 6, when we applied approximately 55 V to the electrostatic cylindrical lens, giving a deflection sensitivity of 0.9 cm/kV at the phosphor screen when the lens is used as a deflector. A disadvantage of this approach is that the photoelectron beam diameter tends to be larger than that for the optimum static focusing condition of the main electrostatic focusing system because of its defocused operating condition. This leads to longer frame times and a reduction in the transmission of photoelectrons by the apertures. For example, the theoretical computation indicates that the photoelectron transmission is reduced to 40% and the beam diameter at the framing aperture is increased from 2.5 to 3.1 mm for x-ray illumination.

An alternative and preferred design refinement involves the use of traveling-wave deflectors[14] (i.e., TWD's), such that finite transit-time effects can be avoided. This type of deflector geometry has been successfully applied in a single-shot streak camera[15] and has the advantage that the focusing condition of the electrostatic focusing lens can be optimized under static conditions and shorter frame times are possible. From the theoretical simulation, under the same sweep conditions the limiting dynamic spatial resolutions are similar to those in the above case but there is a less serious reduction in the number of photoelectrons reaching the phosphor screen. A preliminary experimental attempt was made to incorporate TWD's in a picoframe-I framing camera, and a limiting dynamic spatial resolution of 10 lp/mm in both directions for UV illumination was achieved, as is illustrated in Fig. 7. Unfortunately, there can be some difficulties in providing high-speed voltage deflection ramps with TWD's because of the impedance matching requirements. A frame time of 180 ps FWHM, which is almost twice as long as that when metal plate deflectors are used, can be attributed to the absence of voltage multiplication that is associated with the standard system at the high-impedance deflector–feed-cable interface.[16]

Double-Frame Operation

To operate a picoframe-I camera in a double-frame mode, one must apply a triangular deflection waveform to the framing deflectors so that two frames can be achieved by sweeping the photoelectrons twice across the framing aperture. Image compensations can be achieved by applying an identical but inverse-polarity waveform to the second set of deflectors. To obtain a spatial discrimination of the two resultant frames on the phosphor screen, one must suitably adjust the relative phase between the framing and the compensation deflection waveforms. Consider first the leading edges of the waveforms. If the relative timing of the waveforms applied to the framing and compensation deflectors is less than the transit time of the photoelectrons between the two deflectors, then a net differential deflection of the resultant image at the phosphor screen will occur. The second frame generated on the trailing edges of the waveforms is deflected by an equal and opposite amount at the phosphor screen, thus providing the desired spatial separation without resulting in additional deflection waveforms. This technique is depicted schematically in Fig. 8.

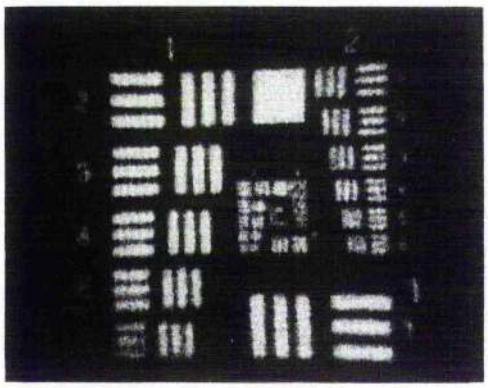

Fig. 6. Experimental recorded single-frame result for UV illumination with a picoframe-I camera with electrostatic cylindrical lens compensation.

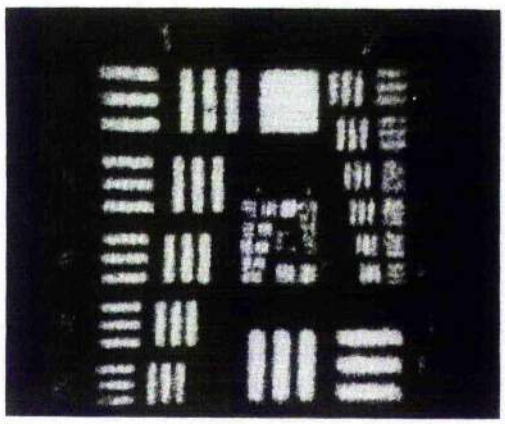

Fig. 7. Experimental single-frame result for UV illumination recorded with a picoframe-I camera with TWD's.

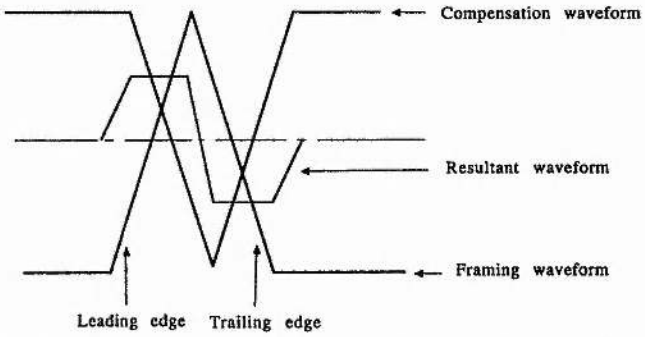

Fig. 8. Deflection voltage waveforms in the double-frame mode of operation of a picoframe-I framing camera.

A theoretical simulation for this double-frame operation is somewhat more complicated than the single-frame counterpart in that the deflection signals have triangular waveforms and the beam of photoelectrons is subdivided into two sequential frames. For simplicity, it is assumed that the triangular deflection waveforms have identical rising and falling edges. In the computation process, only one frame is considered, and a method of calculation similar to that for single-frame operation is used for both frames.

The calculations of the photoelectron trajectories reveal that the photoelectron beam expands considerably in the region of the compensation deflectors and is close to the exit edge of the deflectors where strong fringe fields exist. The focal position is, therefore, shifted according to the emitting plane of the photoelectrons to an extent that is greater than that for the single-frame counterpart. As a compromise, the image quality is nonuniform across the image area, and the dynamic performance is usually inferior to that in the single-frame operation for similar operating conditions. This effect can be seen in Fig. 9, which illustrates some randomly selected trajectories of photoelectrons through the entire picoframe-I tube when operated in a double-frame mode.

Theoretical predictions indicated that under suitable operating conditions, the limiting dynamic spatial resolutions at the phosphor screen are 22 lp/mm for UV and 11 lp/mm for x-ray illumination at frame times of 250 ps (FWHM), a sweep speed of 7.5×10^7 m/s at the framing aperture, and a framing deflection slope of 0.8 kV/ns. This corresponds to 33 and 16.5 lp/mm, respectively, at the photocathode when the electro-optical magnification of 1.5 is taken into account. The calculated SMTF's are given in Fig. 10, and, for comparison, a reproduction of a typical experimental double-frame result is presented in Fig. 11. The inspection of the original photographic negative reveals limiting spatial resolutions of 8 lp/mm for UV and 5 lp/mm for x ray at the photocathode when using an image intensifier with a 20-lp/mm limiting spatial resolution in the experimental camera system. The poor experimental data are due to the practical difficulties of producing faster triangular waveforms with identical rising and falling edges.

It is seen from both the theoretical evaluations and

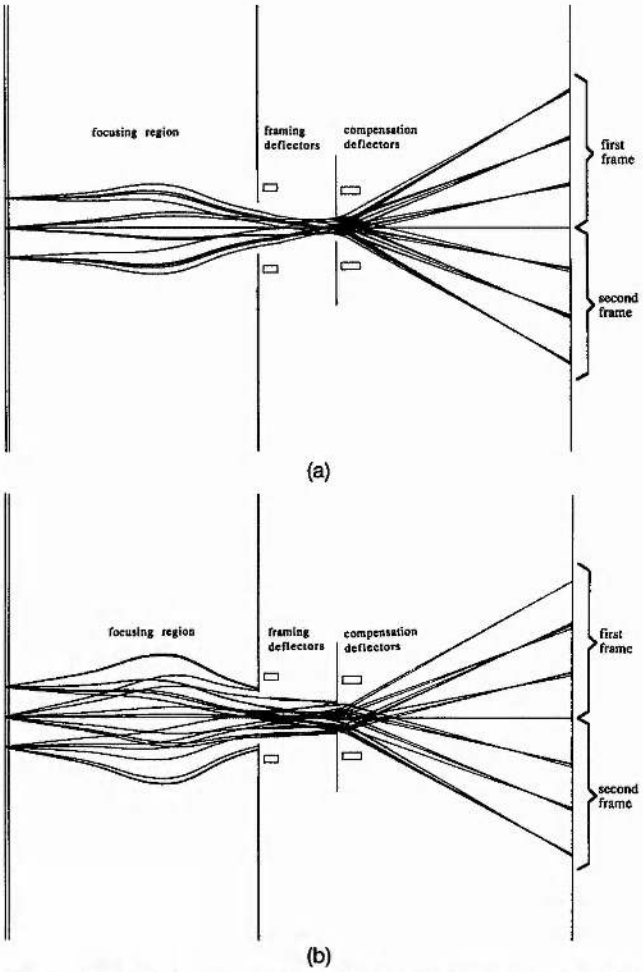

Fig. 9. Photoelectron trajectories for double-frame operation of a picoframe-I image tube for (a) UV and (b) x-ray illuminations.

the experimental data that the spatial resolutions for x-ray illumination are inferior to those for UV or visible illumination in both single- and double-frame operations. This is more obvious when the sweep speed is increased, for example, in the single-frame case. It is also found that the focal plane for x-ray illumination is different from that for UV illumination. This is primarily because of the large initial energy spread of the photoelectrons from an x-ray sensitive gold photocathode. Thus, for x-ray illumination, the photoelectron beam diameter is increased and more serious fringe field effects arise. From the expression for the frame time given in Eq. (1), a larger beam diameter implies an increased frame period and a further reduction in the transmission of photoelectrons through the apertures. Consequently, to maintain the required image contrast ratio at the phosphor screen, the input light intensity at the photocathode has to be increased to compensate for the intercepted photoelectrons. This leads to a requirement for higher photoelectron current densities in the electrostatic focusing lens of the camera, and this, in turn, leads to more deleterious space-charge effects. An effective way to improve the dynamic perfor-

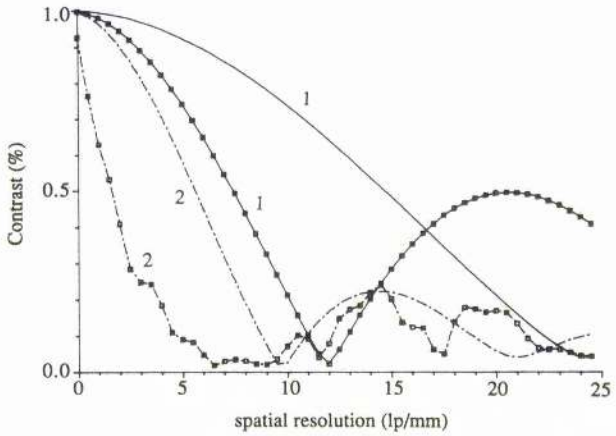

Fig. 10. Theoretical SMTF results in picoframes I and II in a double-frame mode of operation. Curve 1, a picoframe-I image tube in a double-frame operation; curve 2, a picoframe-II image tube in a double-frame mode of operation. Curves labeled by boxes are for x-ray illumination, and the others are for UV illumination.

mance for x-ray illumination would therefore be to incorporate an x-ray sensitive photocathode, such as potassium iodide,[17] having a minimum secondary electron emission energy spread. It is noted that the dynamic spatial resolution is influenced by the sweep speed of framing and compensating deflectors. This causes some difficulty in reducing the frame times of the picoframe type of camera.

Evaluation of Picoframe-II Camera Double-frame Performance

An alternative to the double-frame operation of a picoframe-I camera is to use a double-aperture image tube design (designated as the picoframe II)[18] illustrated in Fig. 12.

In the picoframe-I image tube, the framing deflectors sweep the photoelectrons across the two apertures in turn when a linear ramp voltage is applied, and so two photoelectron transmissions are defined.

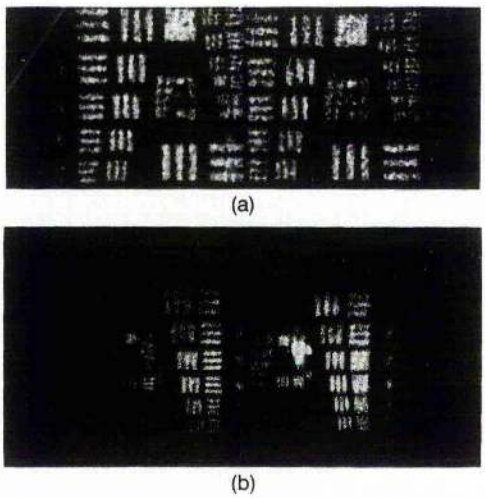

Fig. 11. Experimental double-frame results for (a) UV and (b) x-ray illumination recorded with a picoframe-I camera.

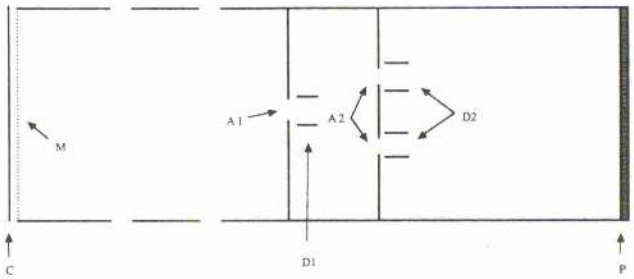

Fig. 12. Electrode configuration of a picoframe-II image tube: C, photocathode; M, mesh; A1, anode aperture; A2, framing aperture; D1, framing deflectors; D2, compensating deflectors; P, phosphor screen.

To separate the two frames spatially and to eliminate any temporal smearing effects in the two frames, we arranged a set of compensation deflector plates behind each aperture. The separation of the two frames on the phosphor screen is provided by adjusting the synchronization of the compensating waveforms with the photoelectron arrival time at the framing aperture in much the same way as that described above. The interframe time is determined by the center-to-center distance between the two framing apertures and by the sweep speed provided by the framing deflectors at the framing aperture plate.

For the theoretical evaluation of the performance of this type of framing camera (the computer programs developed for the trajectory computation of the picoframe-I camera are modified so that the parameters include the transverse and the axial positions), the center-to-center distance of the two apertures and of the compensating deflectors can be conveniently controlled. The computation of trajectories for each frame is carried out separately, assuming that the voltage ramps applied to the two sets of compensating deflectors are identical.

Some calculated trajectories of photoelectrons along the entire image tube are shown in Fig. 13 with respect to the sweep direction. It is seen that, when the photoelectron beam is swept across the two framing apertures, it is spread from the lower plate exit edge to the upper plate exit edge of the framing deflector plates, where the fringe fields are strong. This gives rise to deleterious effects, whereby the combined lensing influences of the deflectors become more pronounced than those in the single-frame Picoframe-I camera under the same sweeping conditions, and the spatial performance is significantly degraded. In addition, because the photoelectrons near the upper plate edge and the lower plate edge experience different fringe fields, the optimum focusing plane varies both with the frames and the emitting positions of the photoelectrons, as illustrated in Fig. 13. The computed limiting dynamic spatial resolutions at the phosphor screen for one frame are 9 lp/mm for UV and 4 lp/mm for x-ray illumination, but for the second frame they are 6 lp/mm for UV and 3 lp/mm for x-ray illumination, as shown in Fig. 10. The frame times are 115 ps (FWHM) for UV illumina-

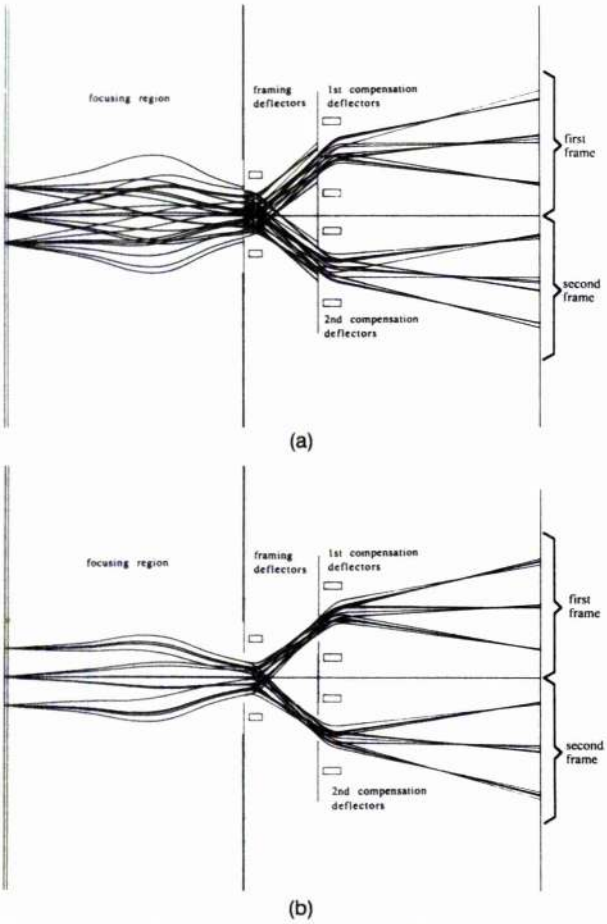

Fig. 13. Photoelectron trajectories in a picoframe-II image tube in a double-frame mode of operation: (a) UV illumination, (b) x-ray illumination.

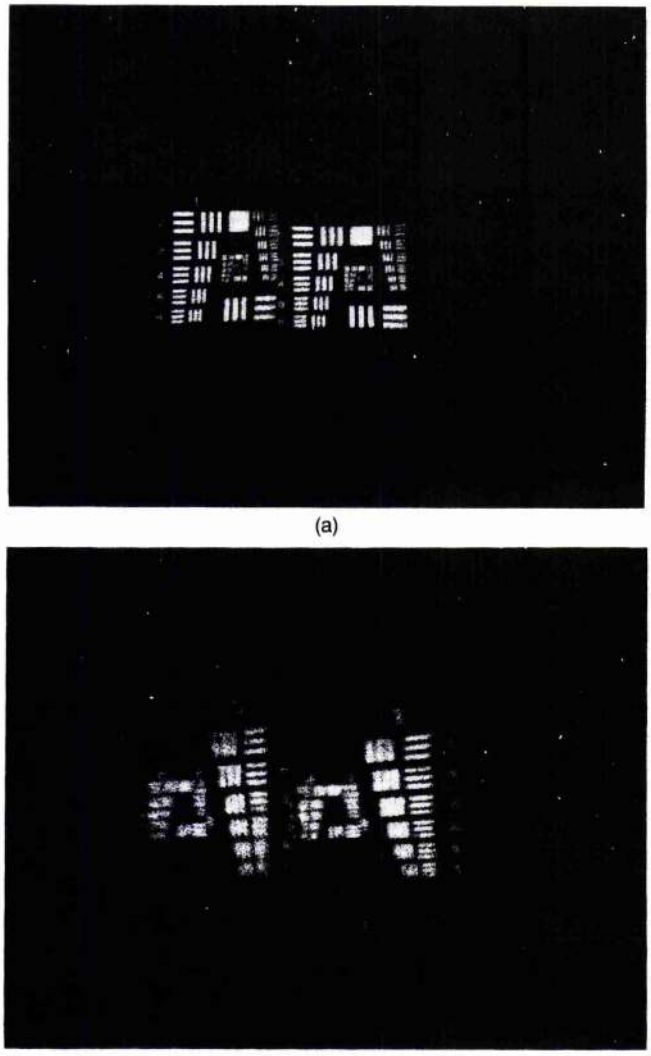

Fig. 14. Experimental double-frame results for (a) UV and (b) x-ray illumination recorded with a picoframe-II camera.

tion and 130 ps (FWHM) for x-ray illumination for a sweep speed of 1.7×10^7 m/s at the framing aperture and a framing voltage slope of 1.85 kV/ns. These figures agree with the experimental results that demonstrate limiting dynamic spatial resolutions of 8 lp/mm for UV and 4.5 lp/mm for x-ray illumination under similar sweep conditions (Fig. 14). Similarly, the elimination of the combined lensing effects of the deflectors in double-frame operation can be realized by the methods described in the section above for single-frame operation.

Conclusions

A thorough evaluation of picoframe I and picoframe II types of camera in single-/double-frame operations has been presented. From a systematic theoretical assessment of the framing operations, it can be concluded that the fringe field effects of the deflectors play a major role in determining the dynamic spatial characteristics. Methods by which these fringe field effects can be overcome have been evaluated, and improved dynamic spatial resolutions have been shown by both theoretical simulations and preliminary experiments. With ongoing and future research, substantial improvements in framing-camera performance will be a primary objective. For instance, the provision of a large photocathode working area, a higher dynamic spatial resolution, a shorter frame time, and a larger dynamic range will be relevant to many new application areas.

The financial support of the Paul Instrument Fund of the Royal Society and the Science and Engineering Research Council (SERC) is gratefully acknowledged. Acknowledgement is also made by Y. Liu for a University Studentship from the University of St. Andrews. D. R. Walker is supported by a SERC Research Assistantship.

References

1. M. H. Key, "Some topical issues in research on short-pulse laser produced plasmas," Philos. Trans. R. Soc. London Ser. A **298,** 351–364 (1980).
2. R. Kalibjian and S. W. Thomas, "Framing camera tube for subnanosecond imaging applications," Rev. Sci. Instrum. **54,** 1626–1628 (1983).
3. J. D. Kilkenny, P. Bell, R. Hanks, G. Power, R. E. Turner, and

J. Wiedwald, "High speed gated x-ray imagers," Rev. Sci. Instrum. **59,** 1793–1796 (1988).
4. M. C. Richardson and K. Sala, "Picosecond framing photography of a laser-induced plasma," Appl. Phys. Lett. **23,** 420–422 (1973).
5. M. R. Baggs, R. T. Eagles, W. Margulis, W. Sibbett, and W. E. Sleat, "A picosecond framing camera for single or multiple frames," Adv. Electron. Electron Phys. B **64,** 627–636 (1984).
6. R. T. Eagles, N. J. Freeman, J. M. Allison, W. Sibbett, W. E. Sleat, and D. R. Walker, "100ps UV/x-ray framing camera," presented at the Thirty-Second International Symposium on Optical and Optoelectronic Applied Science and Engineering, San Diego, Calif., 22–26 August 1988.
7. R. T. Eagles, W. Sibbett, W. E. Sleat, D. R. Walker, J. M. Allison, and N. J. Freeman, "Multiple-frame UV/x-ray picosecond framing camera," Adv. Electron. Electron. Phys. **74,** 209–217 (1988).
8. W. Sibbett, D. R. Walker, W. E. Sleat, R. T. Eagles, and N. J. Freeman, "Four-frame UV/x-ray picoframe II framing camera," in *Ultrahigh Speed and High Speed Photography, Photonics, and Videography '89: Seventh in a Series,* G. L. Stradling, ed., Proc. Soc. Photo-Opt. Instrum. Eng. **1155,** 406–414 (1989).
9. Y. Liu, W. Sibbett, and D. R. Walker, "Theoretical analyses and design considerations of a picosecond framing tube," in *Ultrahigh Speed and High Speed Photography, Photonics, and Videography '89: Seventh in a Series,* G. L. Stradling, ed., Proc. Soc. Photo-Opt. Instrum. Eng. **1155,** 398–405 (1989).
10. W. Sibbett, M. R. Baggs, and H. Niu, "Picosecond framing image tube," in *15th International Congress on High Speed Photography and Photonics,* L. L. Endelman, ed., Proc. Soc. Photo-Opt. Instrum. Eng. **348,** 267–270 (1982).
11. H. Niu, W. Sibbett, and M. R. Baggs, "Theoretical evaluation of the temporal and spatial resolutions of Photochron streak image tubes," Rev. Sci. Instrum. **53,** 563–569 (1982).
12. R. Y. Rubinstein, *Simulation and the Monte Carlo Method* (Wiley, New York, 1981).
13. C. Weber, *Analogue and Digital Methods for Investigating Electron–Optical Systems,* Philips Res. Reps. Suppl. 6 (Philips Research Laboratories, Eindhoven, The Netherlands).
14. I. Yamada and T. Takagi, "A new type of travelling wave deflection system," IEEE Trans. Electron Devices **ED-19,** 204–213 (1972).
15. A. Finch, Y. Liu, H. Niu, W. Sibbett, W. E. Sleat, D. R. Walker, Q. L. Yang, and H. Zhang, "Development and evaluation of a new femtosecond streak camera," in *18th International Congress on High Speed Photography and Photonics,* W. Daheng, ed., Proc. Soc. Photo-Opt. Instrum. Eng. **1032,** 622–626 (1988).
16. D. R. Walker, "Ultrafast electron-optical visible/x-ray sensitivity streak and framing cameras," Ph.D. dissertation (University of St. Andrews, St. Andrews, Fife, UK, 1989).
17. B. L. Henke, J. Liesegang, and S. D. Smith, "Soft-x-ray-induced secondary-electron emission from semiconductors and insulators: models and measurements," Phys. Rev. B **19,** 3004–3021 (1979).
18. R. T. Eagles, "Electron-optical cameras with ultrafast time resolution in one or two spatial dimensions," Ph.D. dissertation (Imperial College of Science and Technology, London, 1986).